Formation and behavior of nanoparticles in a plasma: Dusty plasma instabilities.

Hagop Tawidian

UNIVERSITÉ D'ORLÉANS

ÉCOLE DOCTORALE ENERGIE - MATÉRIAUX - SCIENCES DE LA TERRE ET DE L'UNIVERS

LABORATOIRE GREMI

THÈSE présentée par : / **THESIS** presented by :

Hagop-Jack TAWIDIAN

soutenue le: **24 Octobre 2013**

pour obtenir le grade de : **Docteur de l'Université d'Orléans**
Discipline: Physique des Plasmas

Formation et comportement de nanoparticules dans un plasma: Instabilités dans les plasmas poudreux.

Formation and behavior of nanoparticles in a plasma: Dusty plasma instabilities.

THÈSE dirigée par/supervised by :
Maxime MIKIKIAN Docteur, CNRS Orléans, France

RAPPORTEURS/EXAMINERS :
Uwe CZARNETZKI Professor, Ruhr-Universität Bochum, Germany
François RENIERS Professeur, Université Libre de Bruxelles, Belgique

---

JURY :
Chantal LEBORGNE Professeur, Université d'Orléans, France
Uwe CZARNETZKI Professor, Ruhr-Universität Bochum, Germany
François RENIERS Professeur, Université Libre de Bruxelles, Belgique
Cécile ARNAS Docteur, CNRS Aix-Marseille, France
Holger KERSTEN Professor, Christian-Albrechts-Universität zu Kiel, Germany
Hubertus THOMAS Doctor, Max-Planck-Institut, Germany
Maxime MIKIKIAN Docteur, CNRS Orléans, France

I can do all this through him who gives me strength

Phil. 4:13

Acknowledgments

I would like to thank many people who made this thesis possible and a wonderful experience for me.

First of all, I would like to express my deepest gratitude to my supervisor, Dr. Maxime Mikikian, for his valuable guidance, patience, encouragement and providing an excellent atmosphere for doing research throughout the course of these 3 years. It is his full support that allowed me to complete my thesis on time and with European label. I sincerely appreciate his enthusiasm in helping me to understand the concepts of plasma physics.

I would like to thank the former director Dr. Jean-Michel Pouvesle for welcoming me at GREMI, and Prof. Chantal Leborgne the current director for providing her full support during my PhD journey.

I would like to thank also all members of the jury for having accepted to assess my thesis, Prof. Chantal Leborgne the president of the jury, Prof. Uwe Czarnetzki and Prof. François Reniers the rapporteurs of my thesis, Dr. Cécile Arnas, Prof. Holger Kersten, Dr. Hubertus Thomas and of course Dr. Maxime Mikikian the members of the jury.

In order to achieve an European label PhD, experiments were performed in many research labs. For this purpose, I would like to thank Dr. Hubertus Thomas, Dr. Slobodan Mitic and Dr. Lisa Wörner for the opportunity to work with them at the Max-Planck Institute for Extraterrestrial Physics (Garching, Germany). Also I would like to thank Prof. Holger Kersten, Dr. Maik Fröhlich, Dr. Sven Bornholdt, Alexander Spethmann...for welcoming me at IEAP (Kiel, Germany).

Back to GREMI, thank you to all my colleagues "the GREMIst" for these 3 years.

First, I would like to thank the administrative staff constituted of Sylvie Jauffrion and Christophe Dubois for their kindness help and specially concerning the "paperasse"! Also the office colleagues, Pierre Audier ("the inventor" of A+ in the bus!) and Lu Xie ("the Chinese Chef"), we really had a good time during these 2-3 years, it was FUN.

A special thanks for our engineer Thomas Lecas, who has always the good humor "et maintenant les oiseaux à la..." et continu tes voyages (Laponie..?!) et tes blagues :). I would like to thank also Jacky Mathias, Bernard Dumax, Guy Coudrat for their help.

Without forgetting our GREMI football team, we have a pretty good team (Hervé R., Maxime, Sostaine...), keep moving.

I would like also to thank Eva Kovacevic, Johannes Berndt, Titaina Gibert, Isabelle Géraud-Grenier, Véronique Massereau-Guilbaud and Jean-François Lagrange for their fruitful discussions. Also, I would like to thank the PhD students and the PostDocs: Ibrahim (The Khlooney!), Fatou (alors le moteur...), Mukesh (next destination?), Stéphane (grateful to meet you), Amer (compatriot), Delphine, Grégoire, Hervé H., Perrine, Ismaël, Thien, Dai, Marie, Valentin, Lucile, Thibault L., Nicolas, Thibault D., Laurent, Ahmad, Tayeb, Mireille, Wassim... "Good Luck" for the new PhD students: Thomas, Elodie, Cyril and Mariem. It's a fast journey, just enjoy it. I would like to thank some friends for their support during these 3 years: Serge K., Sahar A., Samuel....

Now, a new Chapter of my life will begin. They say: The end is nothing but an opportunity for a new beginning ! So let's go for it.

Last but not least, I would like to extend my deepest gratitude to my family for their support throughout my life. Thank you for all of the advice and wise words you have provided me over the last several years...

Hagop Tawidian
November, 2013

Contents

List of Figures

Nomenclature

α	degree of ionization
b	impact parameter
$b_{\pi/2}$	impact parameter for 90 ° scattering
b_c	critical impact parameter
$\boldsymbol{E}$	electric field
e	elementary charge
ϵ_0	vacuum permittivity
$\boldsymbol{F_E}$	electrostatic force
$\boldsymbol{F_g}$	force of gravity
$\boldsymbol{F_i}$	ion drag force
$\boldsymbol{F_{i-coll}}$	collection force
$\boldsymbol{F_{i-or}}$	orbit force
$f_i(v_i)$	ion velocity distribution function
$\boldsymbol{F_n}$	neutral drag force
$\boldsymbol{F_T}$	thermophoretic force
Γ	Coulomb logarithm
I_a	currents entering and leaving the dust particle
I_e	electron charging current

I_i	ion charging current
k_B	Boltzmann constant
κ_{tr}	translational part of the thermal conductivity of the gas
λ_D	Debye length
m_e	electron mass
m_i	ion mass
m_n	mass of the neutral gas
$\boldsymbol{\nabla}\ T_n$	temperature gradient in the neutral gas
n_d	number density of the dust particle
n_e	number density of the electrons
n_i	number density of the ions
n_n	number density of the neutral particles
ϕ	electrical potential
ϕ_d	final potential
ϕ_s	dust particle surface potential
Q	electric charge
Q_d	charge of the dust particle
r	Length scale
r_d	radius of the dust particle
ρ	mass density
σ_{c_e}	cross section for electron collection
σ_{c_i}	cross section for ion collection
τ	charging time
T_e	electron temperature

T_i	ion temperature
T_n	neutral gas temperature
$\mathbf{v}_d$	average velocity of the particle
v_e	initial velocity of the electrons
v_i	initial velocity of the ions
$v_{i,gr}$	velocity of the ion after its grazing collision
$\mathbf{v}_n$	average velocity of the gas
V_p	plasma potential
v_s	mean velocity of the ions moving towards the dust particles
v_{th_e}	electron thermal mean velocity
v_{th_i}	ion thermal mean velocity
v_{th_n}	neutral thermal mean velocity
Z_d	mean number of elementary charges on each dust particle

Chapter 1

Introduction

1.1 Plasmas and dusty plasmas: history and characteristics

In general, three states of matter can be evidenced: solid, liquid and gas. A fourth state of matter, called plasma, can also be observed. The plasma is similar to gas but some of the particles are ionized: In addition to atoms and molecules, it contains also positive (or negative) ions and free electrons. Almost the whole universe around us is made of plasma [1]. Stars are huge luminous spheres of hot plasma. The inner part of stars burns through the process of fusion. During this process, two ions are accelerated to energies high enough to overcome the repelling electrostatic force between them, allowing them to come close together. The nuclear force binds them together to form a heavier element, and a gain in energy is released. The closest star to the Earth is the Sun. Its corona spreads out in the space to create what is called the solar wind which is constituted of a stream of charged particles [2]. On the Earth, the solar wind can be observable when it is strong enough to trigger phenomena such as the aurora and geomagnetic storms. The high luminosity of the aurora is due to the highly energetic particles coming from the solar wind interacting with molecules in the Earth upper atmosphere (ionosphere). The ionosphere is a layer that extends from 85 to 600 km, it is a result of the ionization of oxygen, nitrogen and nitric oxide by ultraviolet and X-ray radiation coming from the Sun. The amount of the ionization varies with the amount of the radiation received from the Sun. Thus, seasonal effect (winter, summer) and geographical location (polar, equatorial regions) can play a massive role. Another example of a natural plasma observed on the Earth is the lightning (Fig. 1.1) triggered by the charging of the vapor inside the cloud. It is due to the electrical discharge

between oppositely charged regions, the cloud and the ground. The light produced is a result of the ionization of the air.

At the beginning of the 20^{th} century, the "plasma" field has started to become more and more famous with Tonks and Langmuir when they spread the terms sheath [3] and plasma [4, 5] (1920s). Artificially produced plasmas find applications in many fields of research, industry and technology. For instance, surface treatments such as plasma spraying (coating), metal cutting [6], etching in microelectronics. For the future, the application of plasma devices for controlling and enhancing aerodynamic phenomena encountered in atmospheric flight vehicles is under investigations. Plasma medicine is an innovative and emerging field which combines plasma physics, life sciences and clinical medicine to use physical plasmas for therapeutic applications [7]. Thermonuclear fusion is also a field of investigation to create a clean energy. For this purpose, an international facility, called ITER, is aiming to prove the practicability of continuous fusion energy production at the industrial scale.

Figure 1.1: Lightning: an example of plasma found on Earth.

The detection of small solid (dust) particles in the plasma during astrophysical observations caused the birth of a new field of research: dusty plasmas [8]. Since the discovery, the astrophysicists are highly interested in this field. The dust particles acquire an electrical charge by capturing the charged particles from the plasma or by photo-emission. Dust particles are strongly affected by the presence of electromagnetic fields, and change drastically the behavior of the plasma. These dusty plasmas are found in many astrophysical environments like comet tails, planetary nebulae and rings [9, 10]. The comet Hale-Bopp shown in Fig. 1.2 is constituted of two different tails. A

blue plasma tail is always pointed straight away from the Sun and the white dust tail is curved away along its orbit. The angle between these two tails is due to the light pressure induced by photons emitted by the Sun. In the 80s, the Voyager spacecraft has observed radial features called spokes, in Saturn's ring [10–13]. These spokes observed in Fig. 1.3 are constituted of ice dust particles levitating above the ring by electrostatic repulsion and traveling all around. The spokes disappeared for almost two decades and were re-detected by Cassini spacecraft. They appear dark in the backscattered light and bright in forward scattered light. The formation and the evolution of the spokes are widely detailed in [9, 13]. In 1924, Irving Langmuir in his paper "A new type of electric discharge: the streamer discharge" [14] described the formation of particles by sputtering a tungsten cathode. This report is considered as the first laboratory dusty plasma experiment.

Figure 1.2: The Hale-Bopp comet close to the Sun. Two tails are visible: the blue plasma tail, and the bright white dust tail.

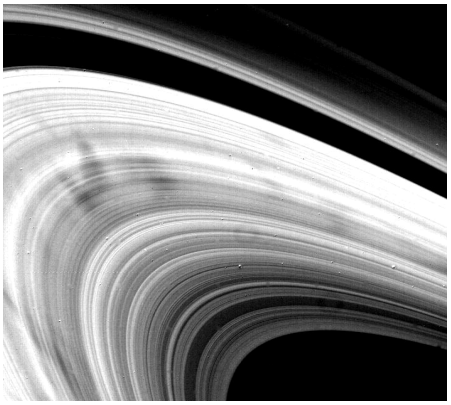

Figure 1.3: Dark radial spokes were observed in Saturn's B-ring during the fly-by of the Voyager 1 spacecraft.

1.2 Dusty plasmas in laboratory: nowadays

Few experiments were performed concerning the influence of dust particles on the plasma after Langmuir's first work. Afterwards and for decades, the presence of the particles was neglected. In the 70s, the presence and the effect of negatively charged dust particles in a DC positive column was studied [15, 16]. It was deduced that the effect of dust particles is similar to the effect of negative ions in electronegative discharges. In 1974, T. C. Anestos and C. D. Hendricks [17] described a method to

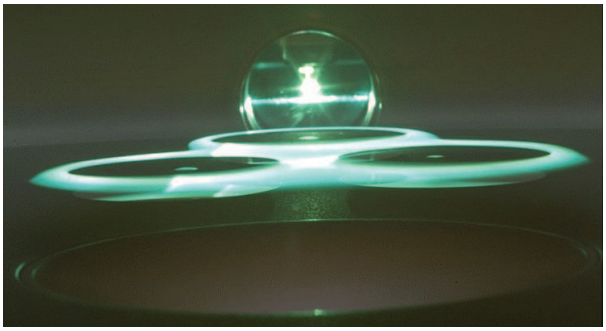

Figure 1.4: Rings of dust particles encircling silicon wafers in a plasma processing device.[18]

measure the electron temperature in a plasma by calculating the charge acquired by dust particles injected into the plasma. Afterwards, the huge change in the history of dusty plasmas was in the late 80s when dust particles were detected in industrial plasma processes (Fig. 1.4) [18]. In microelectronics, plasmas are widely used. Etching, surface processing and computer chip fabrication encountered a significant problem due to the presence of these dust particles in the plasma. Once the discharge is switched off, dust particles fall on wafers and can affect seriously semiconductor device performances [19, 20]. Studies were developed in order to understand the origin of these dust particles in the discharge [21].

In the late 90s, the presence of dust particles in fusion devices became an important subject to investigate [22–25]. These dust particles are produced by sputtering and sublimation of the wall material [25–27]. The presence of these particles can cause serious issues in the development of the ITER project currently under construction in Cadarache (France).

Whereas these nanosized particles are harmful in many processes, nowadays they are considered for several applications like solar cells [28], and memories [29]. Other applications include, the production of a hard wear-resistant coating [30], the enhancement of adhesive, mechanical and protective properties of powder particles for sintering processes in metallurgy [31], and the production of color pigments for paints.

Due to these applications, it is necessary to study dusty plasmas in laboratories. Dust particles can be easily grown in laboratory experiments using reactive gases [32–38], by sputtering different types of materials [39–42], or simply by injecting particles into the discharge [43–48]. In reactive plasmas, dust particle growth by nucleation and agglomeration is a well-known process [49], widely studied in silane discharges [21, 50–52]. Once these dust particles are grown, a dust cloud can be observed in the discharge.

In this cloud, many phenomena can be studied like wave phenomena [53–59]. Due to the strong interaction between these charged dust particles, self-organized structures (plasma crystals) are observed in capacitively coupled radio frequency discharges [44, 60], in DC discharges [61, 62], and in nuclear-induced plasmas [63].

Many types of investigations have been performed (and are still in progress) in the dusty plasma field, like on inter-particle interactions, dust particle charges and on the major forces acting on dust particles. In the experiments performed on ground (Earth), micrometer size dust particles can levitate only close to the bottom sheath of the plasma where the electric field, due to the potential difference between the wall and the plasma bulk, is strong enough to balance the gravitational force. Nevertheless, it is possible to trap the dust particles in the plasma bulk by applying an upward thermophoretic force to balance gravity. This force moves the dust particles from the hot regions to the cold ones. To reduce the effect of the gravity, it is also possible to use smaller dust particles (often grown in the plasma). In this case, one of the main drawbacks is their more difficult observation. To study the behavior of micrometer size dust particles without forcing the system, microgravity experiments are necessary. Under these conditions, three dimensional quasi-isotropic dusty plasmas can be clearly formed, and the dust particle cloud is distributed in the whole plasma bulk. Experiments under microgravity conditions were launched in the 90s. Experiments were performed on board parabolic flights or using rocket launches as for the TEXUS program [64, 65]. A research program on plasma crystals named PKE-Nefedov (Plasma Kristall Experiment), started between the Max-Planck Institute for Extraterrestrial Physics in Garching (Germany) and the Institute for High Energy Densities in Moscow (currently known as Joint Institute for High Temperatures of the Russian Academy of Sciences) (Russia) in 1998. PKE-Nefedov was the first dusty plasma experiment designed for the International Space Station [66]. In 2001, the first experiment on board the ISS was performed by injecting micrometer sized melamine formaldehyde dust particles. In the late 2000, the GREMI (Orléans, France) joined the collaboration to study the growth of particles by sputtering previously injected dust particles [67]. In 2005, a new dusty plasma experiment was installed on the International Space Station, the PK-3 Plus [68]. The next project on board will be the PK-4, a DC discharge. To prepare these future on board the ISS experiments, works are currently performed on parabolic flights and on ground with injected or grown dust particles [69–72].

1.3 Contribution of this thesis

This thesis focuses on dust particle growth and behavior in hydrocarbon based plasmas. For this purpose, experiments have been performed in different setups and laboratories. In Orléans, the sputtering of a polymer material led to the growth of carbonaceous dust particles. In Bourges (France) and Garching (Germany), hydrocarbon gases like methane and acetylene were used to induce polymerization reactions in the gas phase. Finally in Kiel (Germany), the chemistry of aluminium tri-isopropoxide (containing carbon) in a plasma has been investigated.

In the major part of this thesis, the experiments are performed in the PKE-Nefedov reactor [66] where dust particles are grown by sputtering a polymer layer. During their growth, dust particles acquire a negative charge by capturing electrons. This loss of free electrons can lead to a disturbance of the plasma equilibrium. Unstable behaviors can be observed like dust particle growth instabilities (DPGI). This type of instability was reported in the late 90*s* [40, 41]. The actual work is in the continuity of Mikikian's *et al*. experiments [67, 73, 74] where argon was used as the sputtering gas. The aim was to better understand the effect of dust particle growth on the discharge and plasma parameters. During these instabilities, the plasma glow can experience several outstanding behaviors [75]. Beside DPGI, various interesting behaviors were studied like successive generation instabilities [76, 77], the void and the heartbeat [78, 79]. The void, a dust free region in the center of the discharge, is still an outstanding behavior to study. Few theoretical models explaining the formation and stability of the void were proposed, among them Avinash *et al*. [80] and Tsytovich *et al*. [81]. First numerical studies on void formation have been performed by Akdim and Goedheer [82]. In this thesis, the instabilities triggered by the presence of dust particles in the plasma and the evolution of their characteristics are investigated. For this purpose, electrical and optical (high speed imaging and Laser Induced Fluorescence) measurements are performed and compared. The void is investigated thanks to the Laser Induced Fluorescence diagnostic.

In the last part of this thesis, investigations are performed in the ATILA reactor where Aluminium Tri-Isopropoxide "ATI" is used. ATI has been widely used to prepare thin films and coatings of alumina as a protection against corrosion and oxidation. For these purposes, CVD and PECVD are used to deposit the alumina films [83–86]. In this thesis, the chemistry is studied thanks to the Fourier Transform Infrared (FTIR) spectroscopy. The experiments presented are performed in IEAP Kiel (Germany) with Prof. Holger Kersten and Dr. Maik Fröhlich, in collaboration with INP Greifswald

(Germany) with Prof. Jürgen Röpcke and Dr. Marko Hübner, and GREMI Orléans (France).

I would like to mention that, during one month, some experiments were performed in the Max Planck Institute for Extraterrestrial Physics (Garching, Germany) thanks to Prof. Gregor Morfill and Dr. Hubertus Thomas. With the assistance of Dr. Slobodan Mitic and Dr. Lisa Wörner, experiments were performed in the PK-4 reactor using methane-argon and acetylene-argon plasmas to create dust particles. Some plasma instabilities were observed by recording the plasma luminosity. Due to the short period, we were unable to complete our investigations concerning the growth of the particles.

Some discussions also were performed with our colleagues of GREMI located in Bourges (France) (Prof. Véronique Massereau-Guilbaud and Dr. Isabelle Géraud-Grenier) concerning the growth of dust particles in an classical planar radio-frequency reactor in nitrogen-rich methane at low pressure. The results are not presented in this thesis, however the published paper can be found in the appendix.

The present thesis is organized as follows: In Chapter 2, some basic notions of plasmas and dusty plasmas are reviewed, as dust particle charging process, and the major forces acting on a dust particle. Dust particle growth, and the formation of the void are also detailed. In Chapter 3, the experimental setups and diagnostics used in this work are described. Then, the experimental results are presented and discussed in Chapters 4, 5, 6 and 7.

- In Chapter 4, the work presented is in the continuity of previous experiments performed in the PKE-Nefedov reactor (GREMI, Orléans). Krypton is used to study the dust particle growth and the related instabilities. Electrical diagnostics are used to investigate the influence of the dust particles on the discharge characteristics. During DPGI, various regimes are identified. The main instability characteristics are determined as a function of the gas pressure. A particular attention is paid to the changes of the instability appearance time, duration and frequencies. These parameters can provide some insights on dust particle size and number density. The instability appearance time is the first parameter that can be easily measured during an experiment. It is shown that it can be used to predict the instability evolution and its other main characteristics. In order to emphasize DPGI phases, the electrical signal is analyzed through the variation of its oscillation amplitude as a function of the pressure. Argon gas is also used to compare the instability evolution with the one obtained using krypton.

- In Chapter 5, high-speed imaging allows to investigate the plasma glow evolution at the beginning and during DPGI. Several phenomena are discussed concerning the

spatiotemporal oscillations of the plasma luminosity. Particularly, the characterization of plasma spheroids appearing in the center of the discharge and/or at the vicinity of the electrodes is performed. These plasma spheroids consist of small plasma regions with an enhanced emission. Several cases are discussed: 1) a single spheroid rotation around the electrode, 2) complex behavior of spheroids close to the electrodes and 3) interesting interaction behaviors between the plasma spheroids.

- In Chapter 6, Laser Induced Fluorescence (LIF) is used to characterize different phenomena occurring in an argon dusty plasma. Firstly, LIF is used to follow dust particle growth and the corresponding instabilities. Secondly, LIF is used to obtain the spatial profile of the excited species in the presence of a void in the plasma center.

- In Chapter 7, the experiments are performed in ATILA where aluminium tri-isopropoxide (ATI) is injected as a gas phase in the plasma. The aim of the study is to characterize the dissociation of ATI and the formation of the reaction products in the plasma.

1.4 French summary

En général, trois états de la matière peuvent être mis en évidence: solide, liquide et gaz. Un quatrième état de la matiére appelé plasma, peut également être observé. Durant la phase plasma, une partie des particules sont ionisés. Ainsi, un plasma contient des atomes, des molécules, des ions et des électrons libres. Presque tout l'univers qui nous entoure est constitué de plasma. Les étoiles, comme notre soleil, sont des énormes sphères lumineuses de plasma chaud. Un autre exemple de plasma naturel observé sur la terre est la foudre. Elle est due à une décharge électrique entre des régions de charge opposées, le nuage et le sol. La lumière produite est le résultat de l'ionisation de l'air.

Au début du 20^{ieme} siècle, le terme "plasma" est devenu de plus en plus répandu, notamment grâce à Tonks et Langmuir dans les années 1920. Les plasmas produits artificiellement trouvent des applications dans de nombreux domaines de la recherche, de l'industrie et de la technologie. Par exemple, dans les traitements de surfaces et la gravure en microélectronique. De nouvelles applications des plasmas sont en cours de développement comme le domaine medical ("plasma médecine") domaine émergent qui combine la physique des plasmas, les sciences de la vie et la médecine pour l'utilisation des plasmas à des fins thérapeutiques. La fusion thermonucléaire est également un champ d'investigation pour créer une énergie propre. Un complexe international appelé ITER, vise à prouver la possibilté de production d'énergie de fusion en continu à l'échelle industrielle.

La détection de petites particules solides dans les plasmas astrophysiques a donné naissance à un nouveau domaine de recherche: les plasmas poudreux. Ces plasmas poudreux sont observés dans de nombreux environnements astrophysiques comme les queues de comètes, les nébuleuses et les anneaux planétaires. Dans les années 80, la sonde spatiale "Voyager" a observé des bandes sombres, appelés spokes, dans les anneaux de Saturne. Ces spokes s'avèrent être constitués de poussières.

En laboratoire, Irving Langmuir en 1924 a décrit dans son papier, la formation de poudres par pulvérisation d'une cathode de tungstène. Par la suite et pendant des décennies, la présence des poudres a été négligée. Le grand changement dans l'histoire des plasmas poudreux s'est produit à la fin des années 80, lorsque les poudres ont été détectées dans les procédés plasma industriels. En effet, en microélectronique, les plasmas sont largement utilisés pour la gravure, le traitement de surfaces et la fabrication de puces d'ordinateur. La présence de poussiéres est alors un véritable problème car elle affecte la performance des dispositifs fabriqués.

A la fin des années 90, la présence de poudres dans les réacteurs expérimentaux de fusion est devenue un sujet important à étudier. Ces poudres sont produites par la pulvérisation de la matière constituant la paroi des réacteurs. C'est un des problèmes majeurs dans le développement du ITER actuellement en construction à Cadarache (France).

Tandis que les poudres sont considérées comme nuisibles dans de nombreux processus, de nos jours elles sont prises en considération pour de nouvelles applications comme les cellules solaires, et les mémoires. Dans les laboratoires, les particules peuvent être créer en utilisant des gaz réactifs ou par pulvérisation des différents matériaux.

Depuis, de nombreuses études sont réalisées dans le domaine des plasmas poudreux, notammant sur les interactions entre le plasma et les poudres, la charge électrique des poudres et sur les principales forces en présence. Dans les expériences de laboratoire, des poudres micrométriques peuvent être piégées en suspension près de la gaine où le champ électrique est assez fort pour équilibrer la force de la gravité. Il est également possible de piéger ces poudres au centre du plasma en appliquant une force de thermophorèse pour équilibrer la gravité. Pour réduire l'effet de la gravité, il est également possible d'utiliser des poudres nanométriques qui sont le plus souvent créées dans le plasma lui-même. Pour étudier le comportement de poudres micrométriques sans forcer le système, des expériences en microgravité sont nécessaires. Les premières furent réalisées à bord de vols paraboliques et de fusées. A la fin des années 90, un programme de recherche nommé PKE (Plasma Kristall Experiment) a été lançé entre le Max-Planck Institute for Extraterrestrial Physics (Allemagne) et l'Institute for High

Energy Densities (actuellement: Joint Institute for High Temperatures of the Russian Academy of Sciences) en Russie. PKE-Nefedov était la première expérience sur les plasmas poudreux conçue pour la Station Spatiale Internationale. En 2000, la GREMI (Orléans, France) a rejoint la collaboration pour étudier la croissance de poudres par pulvérisation des poudres injectées précédemment. En 2005, une nouvelle expérience de plasmas poudreux a été installé sur la Station Spatiale Internationale, le PK-3 Plus. Le prochain projet à bord sera le PK-4. Pour préparer les futures expériences sur la Station, des travaux sont actuellement effectués sur des vols paraboliques et en laboratoire avec des poudres injectées ou créées dans le plasma.

Cette thèse se concentre sur la croissance des poudres et sur leur comportement dans des plasmas à base d'hydrocarbures. Des expériences ont été réalisées dans différents réacteurs et laboratoires. A Orléans, la pulvérisation d'un matériau de polymère conduit à la croissance de poudres carbonées. A Bourges (France) et à Garching (Allemagne), des gaz hydrocarbonés tels que le méthane et l'acétylène ont été utilisés pour induire des réactions de polymérisation en phase gazeuse. Enfin à Kiel (Allemagne), la chimie de l'aluminium tri-isopropoxide (contenant du carbone) dans un plasma a été étudiée.

Dans une grande partie de cette thèse, les expériences sont réalisées dans le réacteur PKE-Nefedov au GREMI où les poudres sont créées par pulvérisation d'une couche de polymère. Durant leur croissance, les poudres acquièrent une charge négative en capturant les electrons. Cette perte d'électrons libres peut entrainer une perturbation de l'équilibre du plasma. Des comportements instables peuvent alors être observés comme des instabilités pendant la croissance des poudres. Ce travail est dans la continuité des expériences menées par Mikikian *et al.* où l'argon est utilisé comme gaz de pulvérisation. D'autres comportements intéressants sont également observés comme l'apparition et la dynamique du void. Le void est une région dépourvue de poudres au centre de la décharge. Des modèles théoriques expliquant la formation et la stabilité du void ont été proposés, parmi lesquels les travaux de Avinash *et al.*, et Tsytovich *et al.*. Les premières simulations sur la formation du void ont été effectuées par Akdim et Goedheer. Dans la dernière partie de cette thèse, des études sont effectuées dans le réacteur ATILA où l'Aluminium Tri-Isopropoxide "ATI" est utilisé. L'ATI a été largement utilisé pour préparer des couches minces et des revêtements d'alumine comme protection contre la corrosion et l'oxydation. Ces expériences ont été réalisées à l'IEAP à Kiel (Allemagne) avec le Prof. Holger Kersten et le Dr. Maik Fröhlich en collaboration avec le Prof. Jürgen Röpcke et le Dr. Marko Hübner de l'INP Greifswald (Allemagne).

Durant un mois de ma thèse, des expériences ont été réalisées au Max Planck Institute à Garching (Allemagne) grâce au Prof. Gregor Morfill et au Dr. Hubertus Thomas. Ces expériences ont été réalisées avec l'aide du Dr. Slobodan Mitic et du Dr. Lisa Wörner sur le réacteur PK-4 en utilisant des mélanges méthane-argon et acétylène-argon pour créer les poudres. En raison de la courte durée passée à Garching, les résultats obtenus sont trop préliminaires et ne seront pas présentés dans ce manuscrit.

Des discussions ont également été menées avec nos collègues du GREMI situé à Bourges (Prof. Véronique Massereau-Guilbaud et Dr. Isabelle Géraud-Grenier) concernant la croissance de poudres dans un réacteur radio-fréquence en azote-méthane à basse pression. Les résultats ne sont pas présentés dans cette thèse, mais le papier publié se trouve en annexe.

Cette thèse est organisée comme suit: Dans le chapitre 2, quelques notions de base des plasmas et des plasmas poudreux sont presentés, comme les processus de charge des poudres, et les forces principales agissant sur une poudre. La croissance des poudres et la formation du void sont également détaillés. Dans le chapitre 3, les montages expérimentaux et les diagnostics utilisés dans cette thèse sont décrits. Les résultats expérimentaux sont présentés et discutés dans les chapitres 4, 5, 6 et 7.

Dans le chapitre 4, le travail présenté s'inscrit dans la continuité des expériences antérieures réalisées sur le réacteur PKE-Nefedov (GREMI, Orléans). Le krypton est utilisé pour étudier la croissance des poussières et les instabilités. Un diagnostic électrique est utilisé pour étudier l'influence des poudres sur les caractéristiques de décharge. Cette analyse a permis de mettre en évidence l'existence de différents régimes pendant l'instabilité. Les principales caractéristiques de l'instabilité sont alors déterminées en fonction de la pression du gaz. Une attention particulière est accordée au temps d'apparition de l'instabilité, à la durée de l'instabilité et à ses fréquences caractéristiques. Ces paramètres peuvent fournir des indications sur la taille et la densité des poudres. Les différents régimes de l'instabilité sont également analysés par la variation de l'amplitude d'oscillation du signal électrique en fonction de la pression. L'argon est également utilisé pour comparer l'évolution de l'instabilité avec celle obtenue en krypton.

Dans le chapitre 5, l'évolution de la luminosité du plasma au début et durant les instabilités est étudiée à l'aide d'une caméra rapide. Plusieurs phénomènes sont discutés en ce qui concerne les oscillations spatio-temporelles de la luminosité du plasma. En particulier, la caractérisation de petites boules de plasma (sphéroides) apparaissant au centre de la décharge et/ou au voisinage des électrodes est effectuée. Les sphéroides de plasma sont de petites régions de plasma à forte émission lumineuse. Plusieurs cas sont

analysés: 1) un sphéroide circulant autour de l'électrode, 2) le comportement complexe des sphéroides à proximité des électrodes et 3) des phénomènes d'interaction (fusion, séparation) entre les sphéroides.

Dans le chapitre 6, la fluorescence induite par laser (LIF) est utilisée pour caractériser différents phénomènes se produisant dans un plasma d'argon poudreux. La LIF est notamment utilisée pour suivre la croissance des poudres et les instabilités correspondantes. La LIF permet également d'obtenir le profil spatial des espèces excitées en présence du void au centre du plasma.

Dans le chapitre 7, les expériences sont réalisées dans ATILA où l'aluminium triisopropoxide (ATI) est injecté en phase gazeuse dans le plasma. L'objectif de l'étude est de caractériser la dissociation de l'ATI et d'étudier les réactions du polymérisation dans le plasma.

Chapter 2

Theoretical aspects

2.1 Some properties of plasmas and dusty plasmas

2.1.1 Weakly ionized plasmas, Quasi-neutrality

The presence of dust particles in a plasma can drastically change the main plasma characteristics. Dusty plasma experiments are mostly involved in weakly ionized plasmas [87]. The degree of ionization α is defined as the ratio of the number density of electrons (n_e) or ions (n_i) to the total density (n_n represents the number density of the neutral particles).

$$\alpha = \frac{n_i}{n_i + n_n} \tag{2.1}$$

In the field of dusty plasmas, the degree of ionization α is $\ll 1$. Weakly ionized plasmas have several features: these plasmas are driven electrically, charged particle collisions with neutral gas molecules are dominant, ionization of neutrals sustains the plasma in a steady state and the electrons are not in a thermal equilibrium with the ions. The applied power in these discharges heats the mobile electrons, while the heavy ions efficiently exchange energy by collisions with the background gas, thus $T_e \gg T_i$. The ion temperature is equal to the neutral gas temperature which is near to the ambient temperature.

The most important feature of a plasma is its ability to reduce electric fields very effectively. This shielding effect is explained by using a single charge $+Q$ "injected" into a large plasma [88]. This plasma has an equal densities of electrons and positive ions $n_{e0} = n_{i0}$. Electrons and ions will be attracted or repelled regarding to the injected charge $+Q$. It results the observation of a space charge created nearby of $+Q$. The shielding action is not static, and is governed by the thermal motion of the plasma

electrons and ions. In order to simplify the description, the Boltzmann factor [88] is used. If we assume that Q is a positive charge, in the repulsive potential case, the Boltzmann factor presents the number of particles in a thermal distribution that have overcome the electric potential ϕ. In the attractive potential case, the density is greater than the equilibrium value. In the following equations the densities are presented:

$$n_e = n_{e0} exp\left(+\frac{e\phi(r)}{k_B T_e}\right) \tag{2.2}$$

$$n_i = n_{i0} exp\left(-\frac{e\phi(r)}{k_B T_i}\right) \tag{2.3}$$

where e is the positive elementary charge, k_B the Boltzmann constant and ϵ_0 is the vacuum permittivity.

Assuming that there is no considerable disturbances due to the presence of the "injected" charge, the densities can be simplified into:

$$n_e \approx n_{e0}\left(1 + \frac{e\phi(r)}{k_B T_e}\right) \tag{2.4}$$

$$n_i \approx n_{i0}\left(1 - \frac{e\phi(r)}{k_B T_i}\right) \tag{2.5}$$

The electric potential can be deduced by using the Poisson's equation

$$\Delta\phi = -\frac{1}{\epsilon_0}(-en_e(r) + en_i(r) + Q\delta(r)) \tag{2.6}$$

and by replacing $n_e(r)$ and $n_i(r)$ by eq. 2.4 and 2.5, the equation 2.6 becomes:

$$\frac{\partial^2\phi}{\partial r^2} + \frac{2}{r}\frac{\partial\phi}{\partial r} - \frac{1}{\lambda_D^2}\phi = -\frac{Q}{\epsilon_0}\delta(r) \tag{2.7}$$

where λ_D is the Debye length defined as:

$$\frac{1}{\lambda_D} = \left(\frac{e^2 n_{e0}}{\epsilon_0 k_B T_e} + \frac{e^2 n_{i0}}{\epsilon_0 k_B T_i}\right)^{1/2} \tag{2.8}$$

The Debye length is a combination of the shielding action of electrons $\lambda_{De} = (\epsilon_0 k_B T_e / e^2 n_{e0})^{1/2}$ and ions $\lambda_{Di} = (\epsilon_0 k_B T_i / e^2 n_{i0})^{1/2}$. The solution is the Debye-Hückel potential that can be written as

$$\phi(r) = \frac{Q}{4\pi\epsilon_0 r} exp\left(-\frac{r}{\lambda_D}\right) \tag{2.9}$$

At the vicinity of the "injected" charge (r $\rightarrow$ 0), the potential is equal to the Coulomb potential. Far away from the charge, the exponential part of the equation is dominant and the potential drops in a fast way. The equation can be approximated as

$$\phi(r) = \begin{cases} \frac{Q}{4\pi\epsilon_0 r}, & \text{r} \leq \lambda_D. \\ \\ 0, & \text{r} > \lambda_D. \end{cases} \tag{2.10}$$

The existence of dust particles in a plasma modify some behaviors of the plasma particles. Ions and electrons hit the dust particles and transform them into charged particles. Due to the mass difference between the electrons and ions, the electrons have a higher mobility than the ions. Therefore, the dust particles acquire a negative charge. The presence of these charged dust particles initiates new interactions in the plasma. These particles are involved in the quasineutrality equation

$$n_i - n_e - n_d Z_d = 0 \tag{2.11}$$

where $Z_d = Q_d/e$ is the mean number of elementary charges on each dust particle, Q_d the charge of the dust particle and n_d the dust density .

2.1.2 Dust Particle charging: The Orbital Motion Limited Theory

Dust particles in a plasma behave like isolated probes. Beside the collection of electrons and ions from the plasma, various charging mechanisms can be involved like photoemission and secondary emission. In the case of photoemission and secondary emission, the dust particles can be charged positively as more commonly encountered in astrophysical environments. However in typical laboratory dusty plasmas, ion and electron collection dominates the charging process. The dust charging equation is defined as

$$\frac{dQ_d}{dt} = \sum_a I_a \tag{2.12}$$

with I_a denotes the different currents entering and leaving the particle.

The Orbital Motion Limited (OML) theory [89–92] is developed and used to explain the charging of the particles. An isolated spherical dust particle of radius r_d is considered in a plasma. This particle is smaller than the linearized Debye length λ_D ($r_d \ll \lambda_D$). As $v_{th_e} \gg v_{th_i}$, where $v_{th_{e(i)}} = \sqrt{(8k_B T_{e(i)})/(\pi m_{e(i)})}$ is the electron (ion) thermal mean velocity with m_e and m_i the electron and ion mass respectively, the

electron reach the dust particle surface in a faster way. Therefore, more electrons are collected and the dust particle surface potential ϕ_s is negative relatively to the plasma. The final potential that is reached is $\phi_d = \phi_s$ - V_p where V_p is the plasma potential. Once these particles are charged negatively, the positive ions will be attracted to ensure that the net current flowing onto the particle surface becomes zero at equilibrium

$$\frac{dQ_d}{dt} = I_i - I_e = 0 \tag{2.13}$$

where I_e and I_i are the electron and ion charging currents to the dust particle. The surface charge Q_d on the particle can be obtained from the capacitance model $Q_d = C\phi_d$. The dust particle is supposed to be a spherical capacitor with $C = 4\pi\epsilon_0 r_d$. The polarization of the plasma increases the capacitance [93] into

$$C = 4\pi\epsilon_0 r_d \left(1 + \frac{r_d}{\lambda_D}\right) \tag{2.14}$$

Since $r_d \ll \lambda_D$, the charge Q_d can be defined as

$$Q_d = 4\pi\epsilon_0 r_d \phi_d \tag{2.15}$$

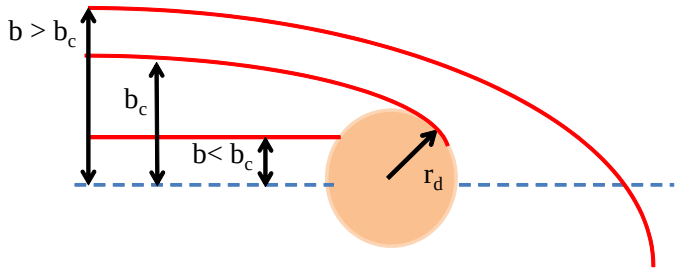

Figure 2.1: Interaction of ions with a dust particle.

In the OML theory, it is assumed that the mean free path of electron-neutral and ion-neutral collisions is larger that the width of the positive ion sheath around the dust particle. It means that the sheath around the dust particle is collisionless. Once an ion enters the dust particle sheath, the effect of the electrostatic field surrounding the charged particle acts on the ion trajectory. The ion can be deflected or collected. As shown in Fig. 2.1, b_c represents the critical impact parameter [88]. The ion enters in contact with the charged particle when $b < b_c$, while the ion is just deflected in the

electric field of the dust particle when $b > b_c$. At the critical impact parameter b_c, the ion is collected by the dust particle at grazing incidence. The conservation of angular momentum and energy for $b = b_c$ can be defined as

$$m_i v_i b_c = m_i v_{i,gr} r_d \tag{2.16}$$

$$\frac{1}{2} m_i v_i^2 = \frac{1}{2} m_i v_{i,gr}^2 + e\phi_d \tag{2.17}$$

where v_i is the initial velocity of the ions and $v_{i,gr}$ is the velocity of the ion after its grazing collision with the dust particle. Thanks to these equations, the conservation of energy is written as

$$\frac{1}{2} m_i v_i^2 = \frac{1}{2} m_i v_i^2 \left(\frac{b_c^2}{r_d^2} + \frac{e\phi_d}{\frac{1}{2} m_i v_i^2} \right) \tag{2.18}$$

From this equation, the expression of b_c is deduced as a function of the initial ion energy, ϕ_d and the radius of the dust particle:

$$b_c^2 = -r_d^2 \left(\frac{2e\phi_d}{m_i v_i^2} - 1 \right) \tag{2.19}$$

and the cross section for ion collection is defined as follows:

$$\sigma_{c_i} = \pi b_c^2 = -\pi r_d^2 \left(\frac{2e\phi_d}{m_i v_i^2} - 1 \right) \tag{2.20}$$

The ion current I_i is deduced by using the Maxwell-Boltzmann distribution function $f_i(v_i)$:

$$I_i = e \int v_i \sigma_{c_i} f_i(v_i)\, d^3 v_i. \tag{2.21}$$

and $f_i(v_i)$ is supposed to be Maxwellian:

$$f_i(v_i) = n_i \left(\frac{m_i}{2\pi k_B T_i} \right)^{\frac{3}{2}} exp \left(-\frac{m_i v_i^2}{2 k_B T_i} \right) \tag{2.22}$$

The charging current for the ions can be defined as

$$I_i = \pi r_d^2 n_i e \sqrt{\frac{8 k_B T_i}{\pi m_i}} \left(1 - \frac{e\phi_d}{k_B T_i} \right) \tag{2.23}$$

Concerning the repulsive case, the electron current is calculated in the same way as the

attractive case. The cross section for electron collection is defined

$$\sigma_{c_e} = \pi b_c^2 = \pi r_d^2 \left(\frac{2e\phi_d}{m_e v_e^2} + 1 \right) \tag{2.24}$$

and the electron current I_e can be written

$$I_e = \pi r_d^2 n_e e \sqrt{\frac{8k_B T_e}{\pi m_e}} exp\left(\frac{e\phi_d}{k_B T_e} \right) \tag{2.25}$$

by replacing eq. 2.23 and eq. 2.25 in eq. 2.13, it becomes

$$n_e exp\left(\frac{e\phi_d}{k_B T_e} \right) = n_i \sqrt{\left(\frac{m_e T_i}{m_i T_e} \right)} \left(1 - \frac{e\phi_d}{k_B T_i} \right) \tag{2.26}$$

2.1.3 Charging time

Since the dust particles are negatively charged, the ions surround the dust particle to sustain the equilibrium. It means that the heavy and slow ions define the final equilibrium. The ion current is used to determine the charging time τ_i [88, 94]:

$$\frac{dQ_d}{dt} = I_i = \pi r_d^2 n_i e \sqrt{\frac{8k_B T_i}{\pi m_i}} \left(1 - \frac{e\phi_d}{k_B T_i} \right) \tag{2.27}$$

$Q_d(t)$ has a solution of the form $Q_d(t) = k_1 exp(-t/\tau_i) + k_2$. It represents a capacitor charging equation with $\tau_i = RC$. The equation above is rewritten as:

$$\frac{dQ_d}{dt} = \pi r_d^2 n_i e \sqrt{\frac{8k_B T_i}{\pi m_i}} \left(1 - \frac{eQ_d}{4\pi\epsilon_0 r_d k_B T_i} \right) \tag{2.28}$$

$$\frac{dQ_d}{dt} = -\frac{1}{\tau_i} k_1 exp\left(-\frac{t}{\tau_i} \right) = \pi r_d^2 n_i e \sqrt{\frac{8k_B T_i}{\pi m_i}} \left(1 - \frac{e\left(k_1 exp\left(-\frac{t}{\tau_i} \right) + k_2 \right)}{4\pi\epsilon_0 r_d k_B T_i} \right) \tag{2.29}$$

$t \to \infty$ gives the constant k_2, as $k_2 = 4\pi\epsilon_0 r_d k_B T_i / e$. The solution for the charging time τ_i can be written as

$$\tau_i = 4\pi\epsilon_0 r_d \frac{k_B T_i}{e} \frac{1}{\pi r_d^2 e n_i \sqrt{\frac{8k_B T_i}{\pi m_i}}} \tag{2.30}$$

The dependence of the charging time on the size of the dust particle follows $C \propto r_d$ (from the capacitance model) and $R \propto r_d^{-2}$, which makes $\tau = RC \propto r_d^{-1}$. Therefore, large grains have a much shorter charging time than small grains. For instance, a dust particle of $r_d = 1$ μm in a typical laboratory plasma with electron temperature T_e= 3

eV, ion temperature $T_i = 0.03$ eV and density $n_i = 10^9$ cm^{-3} has a charging time of τ=18 μs.

2.2 Forces acting on dust particles

Charged dust particles in a plasma experience several forces. In laboratory discharges, dust particles in the micrometer range are in general massive enough to experience a significant gravitational force. As they are charged, they are subject to electrostatic forces. In the following sections, the forces that can have an effect on dust particles are detailed.

2.2.1 Gravity

Dust particles are influenced by the force of gravity given by :

$$\boldsymbol{F_g} = \frac{4}{3}\pi r_d^3 \rho \boldsymbol{g} \tag{2.31}$$

With $\boldsymbol{g}$ the gravitational acceleration on Earth, and ρ the mass density of the dust particles. This force scales with the volume of the particle. It can be neglected for nanometer sized particles, while it can play a huge role on micrometer sized particles.

2.2.2 Electrostatic force

The electrostatic force acting on the dust particle is

$$\boldsymbol{F_E} = Q_d \boldsymbol{E} \tag{2.32}$$

The electric field is much larger in the sheaths adjacent to the plasma-wall boundary than in the plasma bulk due to the quasineutrality condition. This force pushes the negatively charged particles from the electrodes towards the plasma center, causing the trapping of the dust particles in the discharge. For nano sized particles, this force is the most dominant one. Micrometer sized particles can levitate at the vicinity of the sheath where the electric field balances the gravity force. Hamagushi *et al.* [95] discussed about the positive Debye sheath surrounding the dust particle, which shields its long range Coulomb field. In the presence of an external electric field, the Debye shielding does not diminish the magnitude of this field at the particle location by, for example, a redistribution of the particle sheath charges. Daugherty *et al.* [96] developed an expression for the electric force, assuming that the sheath is not deformed by the

applied electric field:

$$\boldsymbol{F_E} = Q_d \boldsymbol{E} \left(1 + \frac{\left(\frac{r_d}{\lambda_D}\right)^2}{3\left(1 + \frac{r_d}{\lambda_D}\right)} \right) \tag{2.33}$$

The first part of equation 2.33 describes the electrostatic force that a dust particle would experience in a field $\boldsymbol{E}$ in the vacuum. The term between the brackets represents the polarization of the dust charge by the plasma, which provides additional small electric field at the dust particle surface. When $r_d \ll \lambda_D$, the electrostatic force is written as $Q_d\ \boldsymbol{E}$.

2.2.3 Thermophoresis

The thermophoretic force appears due to a temperature gradient in the neutral gas. Neutral gas atoms from the hotter side hitting the dust grain transfer a larger momentum to the dust than atoms from the colder side. Therefore, a force towards regions of colder gas is created

$$\boldsymbol{F}_T = -\frac{32}{15} \left(\frac{\pi m_n}{8 k_B T_n} \right)^{\frac{1}{2}} r_d^2 \kappa_{tr} \boldsymbol{\nabla} T_n \tag{2.34}$$

where $\boldsymbol{\nabla}\ T_n$ is a temperature gradient in the neutral gas, κ_{tr} is the translational part of the thermal conductivity of the gas and m_n is the mass of the neutral gas. Jellum *et al.* [97, 98] have observed thermophoresis effects in a radio frequency glow discharge. By using heated or cooled electrodes, the thermophoretic force has also been used to levitate dust particles in discharges [99, 100].

2.2.4 Neutral drag force

The ionization fraction in typical laboratory experiments is small. Therefore, the most important constituent is the neutral gas. Dust particles moving through the background gas encounter collisions with neutral gas atoms/molecules. Using the kinetic gas theory, Graves *et al.* [101] approximated the neutral drag force as:

$$\boldsymbol{F}_n = -\frac{4}{3} \pi r_d^2 n_n m_n v_{th_n} (\mathbf{v}_d - \mathbf{v}_n) \tag{2.35}$$

where $\mathbf{v}_d$ represents the average velocity of the particle and $\mathbf{v}_n$ the average velocity of the gas. The neutral drag is the resistance experienced by a particle moving through a gas, and when $\mathbf{v}_n = 0$ the neutral drag force simply acts as a damping force on the velocity of the particles. This force is proportional to r_d^2.

2.2.5 Ion drag force

The ion drag force characterizes the interaction between a dust particle and the ions. Positive ions driven by the electric field towards the plasma sheaths can transfer their momentum to the dust particles. Ions can be collected or scattered. This force is constituted of two parts: the collection force $\boldsymbol{F}_{i-coll}$ due to the direct impact of positive ions with the dust particle and the orbit force $\boldsymbol{F}_{i-or}$ due to the electrostatic interactions between the ions and the dust particle. The ion drag force is written:

$$\boldsymbol{F}_i = \boldsymbol{F}_{i-coll} + \boldsymbol{F}_{i-or} \tag{2.36}$$

In laboratory experiments, this force plays a huge role in the field of dusty plasmas and specially in the formation of the void which is a dust-free region in the center of the plasma bulk. Also, it is present in the rotation of dust clusters in magnetic field [102]. The ion drag force is obtained under the assumption that no ion interaction with dust particle is taken into consideration outside the Debye length of the particle. The collection force is given in [103] as:

$$\boldsymbol{F}_{i-coll} = n_i m_i v_i v_s \pi b_c^2 \tag{2.37}$$

with v_s the mean velocity of the ions moving towards the dust particles.

$$v_s = \left(\frac{8 k_B T_i}{\pi m_i} + v_i^2 \right)^{1/2} \tag{2.38}$$

The collection parameter b_c based on the OML theory is given by eq. 2.19.

The second part of the force, the orbit force is:

$$\boldsymbol{F}_{i-or} = n_i m_i v_i v_s 4\pi b_{\pi/2}^2 \Gamma \tag{2.39}$$

where $b_{\pi/2}$ is the impact parameter for 90° scattering:

$$b_{\pi/2} = \frac{eQ_d}{4\pi\epsilon_0 m_i v_s^2} \tag{2.40}$$

and the Coulomb logarithm integrated over the interval b_c to λ_D is :

$$\Gamma = \frac{1}{2} \ln \left(\frac{\lambda_D^2 + b_{\pi/2}^2}{b_c^2 + b_{\pi/2}^2} \right) \tag{2.41}$$

Different expressions for the ion drag force are proposed in literature. Kilgore *et al.* [104] have given a different expression for the orbital ion drag force in case of monoenergetic ions and cut-off Coulomb potential. Khrapak *et al.* [105] have shown that due to the high charge on the dust, ion scattering outside the Debye sphere will increase the strength of the ion drag force.

In Fig. 2.2, an overview of the different forces acting on a dust particle in a capacitively coupled discharge is shown.

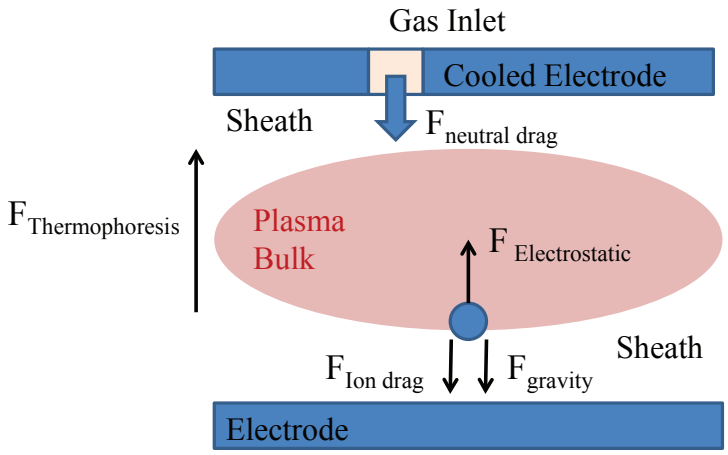

Figure 2.2: Schematic of different forces acting on a dust particle.

2.3 Formation and growth of dust particles and the dust void

In laboratories, dust particles can be either injected into the plasma or can be formed by the plasma itself. Dust particles can be easily formed in plasmas containing chemically active species. In gases such as silane or methane the growth of dust particles is easily obtained. Dust particles can also be formed in plasmas when molecules or atoms from the electrodes or walls are sputtered by ion bombardment. Dust particle growth occurs in several phases: 1) nucleation, 2) coagulation, and 3) surface growth. During the nucleation, parent gas monomers are transformed into macromolecules and small clusters due to the chemical reactions in the gas phase. The size of the particles can reach 5 nm [106], and the particles have only a few elementary charges. This process is called the gas phase polymerization. The next phase of growth is the coagulation or agglomeration of the particles. During this phase, two particles collide to form a bigger

particle ($r_d < 50$ nm). As the particle size grows they collect more and more negative charges that prevents further agglomeration due to the mutual Coulomb repulsion. This coagulation phase is followed by the surface growth process where the particles continue to grow thanks to the plasma radicals that stick to the particles.

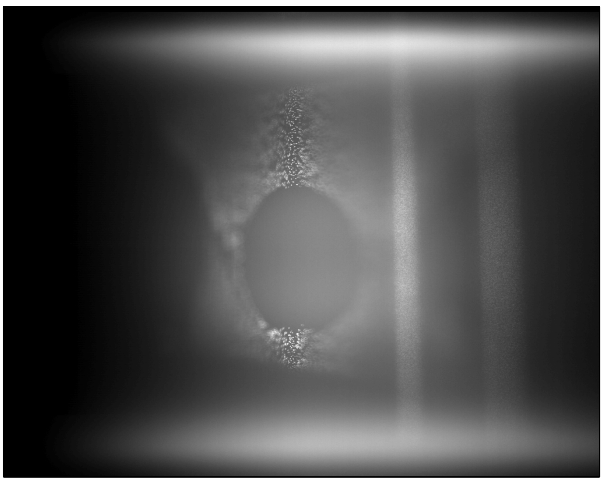

Figure 2.3: The void surrounded by a dust cloud.

Once a dust cloud is formed in a discharge, a phenomenon known as the dust void, a dust-free region, is commonly observed. The void can be observed in plasma processing discharges and plasma crystal experiments [40, 41, 65–67, 107]. In 1996, Praburam and Goree used for the first time the term "void". A cloud of 100 nm carbon particles was produced by sputtering a graphite electrode in a capacitively coupled radio frequency discharge. The void appears in the center of the discharge and it has a sharp boundary with the surrounding dusty plasma as explained by Samsonov and Goree [41]. The electron density and ionization rate are enhanced in the dust void region. Morfill *et al*. [65] observed the formation of the void using micro sized particles under micro gravity conditions. The mechanism proposed to explain the void is a force balance between the ion drag and electrostatic forces. A decrease of the electron density (electron depletion) is observed in the dust cloud due to the particle charging process. This electron depletion causes a decrease of the electron impact ionization rate in the cloud. In the other hand, a higher ionization in the void can lead to an electric field directed outward from the void center which means an inward electrostatic force on dust particles. It produces an outward ion flow, thus an outward ion drag force on the dust particles. At equilibrium, there is a balance between the outward ion drag force and the inward electrostatic force acting on dust particles. The dust particles and the

void can be clearly observed by using a laser sheet through the discharge as shown in Fig. 2.3.

2.4 Conclusion

In this Chapter, some theoretical aspects concerning plasmas and dusty plasmas have been reviewed. Dust particle charging mechanism and the various forces acting on the dust particles are described. The influence of the gravity, electrostatic force, thermophoresis, neutral drag and ion drag forces on the dust particle is presented. The last part of this Chapter is dedicated to the growth of dust particles and formation of the dust void in laboratories. In Chapter 4 and 5, the effect of dust particle growth on the plasma is studied. In Chapter 6, the void appearing in the discharge center is investigated.

2.5 French Summary

Dans ce chapitre 2, quelques notions théoriques concernant les plasmas et les plasmas poudreux ont été présentées. Les processus de charge des poudres et les forces principales agissant sur une poudre sont décrits. L'influence de la gravité, de la force électrostatique, de la thermophorèse, et des forces de friction sur les poudres sont présentés. La dernière partie de ce chapitre est consacrée à la croissance des poudres et à la formation du void. Dans les chapitres 4 et 5, l'effet de la croissance des poudres sur le plasma est étudié. Dans le chapitre 6, le void apparaissant au centre de la décharge est étudié.

Chapter 3

Experimental setups and diagnostics

The experiments analyzed in this thesis are performed in two plasma chambers: the major part of the thesis is achieved by using the PKE-Nefedov reactor located in GREMI laboratory (Orléans, France), and a part of the work is performed using the ATILA reactor located in IEAP (Kiel, Germany). Various diagnostics are used to study these plasmas: Electrical measurements, high speed imaging, Laser Induced Fluorescence and Fourier Transform InfraRed spectroscopy are detailed in this chapter.

3.1 Experimental Setups

3.1.1 PKE-Nefedov chamber

The PKE-Nefedov (Plasma Kristall Experiment) [66, 67, 108] reactor shown in Fig. 3.1 is located in GREMI Orléans. It is a capacitively coupled radio-frequency (RF 13.56 MHz) reactor operating in push-pull mode. This chamber has a volume of 10 $\times$ 10 $\times$ 5 cm^3. Four sides of the chamber are made of glass to have a clear view into the discharge. The plasma is created between two parallel electrodes with a diameter of 4.2 cm, and the gap between these electrodes is 3 cm. MPI-1 SPACE, the RF generator operating at 13.56 MHz is driven by two DC power supplies, the "ISO-TECH Dual Tracking Model IPS230300" that provides 28 V DC voltage and 0.5 A DC current, and also the "AGILENT E3610A" that delivers maximum 2.4 V. This RF generator can deliver a maximum power of about 4 W and is connected to the electrodes through an integrated matching box.

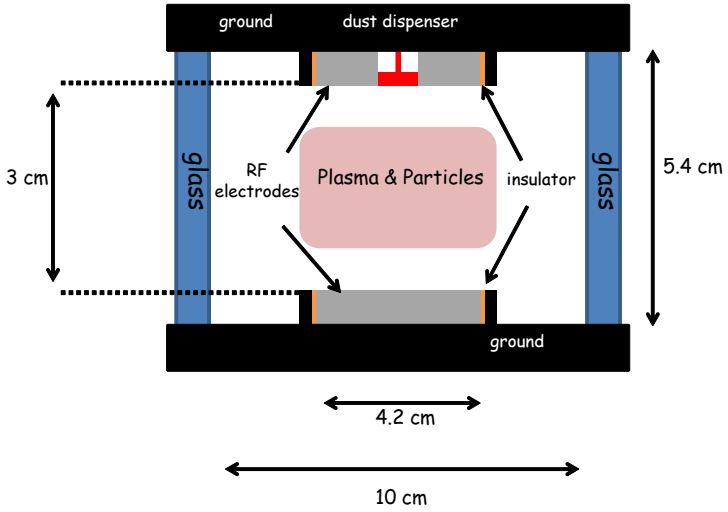

Figure 3.1: Schematic of the PKE-Nefedov reactor.

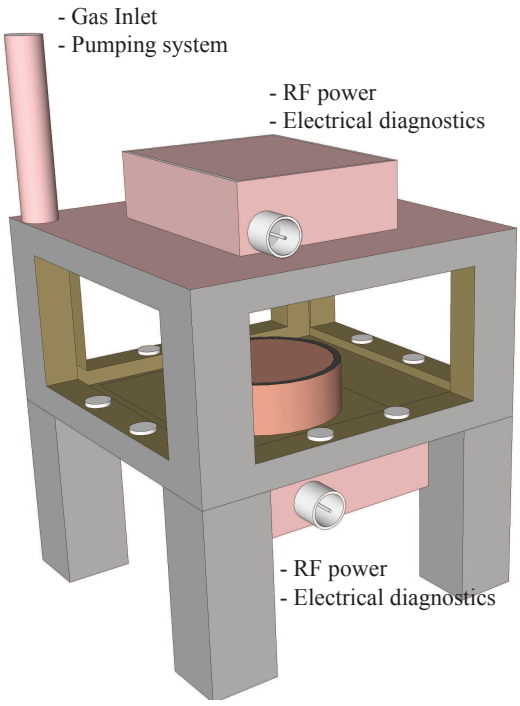

Figure 3.2: 3D view of the PKE-Nefedov reactor.

In order to pump down this chamber, a turbomolecular vacuum pump (PFEIFFER TMH 071P, 60 $L.s^{-1}$) with a fore pump (EDWARDS XDS5, 5 $m^3.h^{-1}$) are used. The pressure reached is around 10^{-6} mbar thanks to this pumping system. A full range gauge (PFEIFFER PKR 251) that gives information above 10^{-9} mbar and a capacitive gauge (MKS Baratron) showing above 10^{-4} mbar, are used to measure the pressure inside the chamber. The gas injection is controlled manually by using valves installed at the entrance of the chamber. The gas inlet and the pumping system have the same access into the reactor. Argon or krypton are used as the buffer gas for a working pressure between 1.4 and 2.4 mbar without gas flow. Dust particles are grown in the plasma by sputtering previously injected micrometer size dust particles made of polymer (melamine formaldehyde) and lying on the electrode. The injection is performed thanks to an electrically driven dust shaker located in the center of the top electrode. A 3D view of the PKE-Nefedov is shown in Fig. 3.2.

3.1.2 ATILA chamber

The ATILA reactor [36] located in Christian-Albrechts University of Kiel, at the Institute of Experimental and Applied Physics (IEAP), is an asymmetric capacitively coupled radio-frequency (RF 13.56 MHz) discharge. It is a cylindrical shape reactor with a volume of 50 dm^3, equipped with optical accesses for spectroscopy diagnostics. ATILA contains a plain electrode with a diameter of 12 cm surrounded by a grounded electrode as shown in Fig. 3.3. The powered electrode is driven by a RF generator CESAR/TM 133 from Advanced Energy Industries that can deliver an output RF power of 300 W. The RF generator is connected to the electrode through a matchbox. The pumping system consists of a turbomolecular pump (VARIAN V301, 200 $L.s^{-1}$) and a fore pump (VARIAN IDP3, 3 $m^3.h^{-1}$). The pressure is measured using pirani and baratron gauges. The pressure reached is around 0.2 Pa thanks to the pumping system. During the experiments performed in ATILA, Pascal unit is used to measure the pressure (1 Pa = 0.01 mbar). The gases used like argon and nitrogen are controlled using mass flow controllers (MFC) through a Labview interface. The chemistry of the plasma is studied using Aluminium Triisopropoxide (ATI). The ATI is a powder that is heated up to 135°C in a mini-chamber located beside the ATILA reactor shown in Fig. 3.4. The ATI pressure in the heater increases and, therefore, an ATI gas flow is initiated. In order to avoid condensation, a heated pipe has been used to connect the ATI mini-chamber to the ATILA reactor. The ATI flow can be varied by a heat resistant needle valve installed between the mini chamber and the heated pipe.

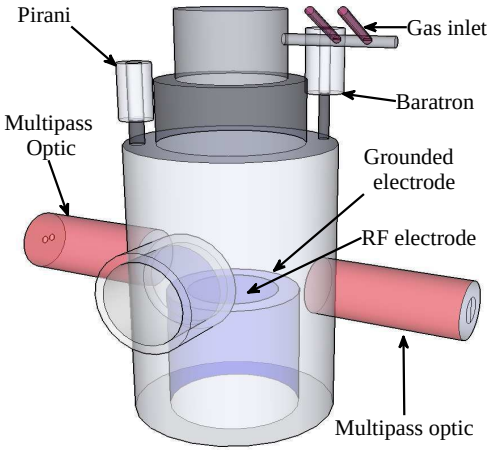

Figure 3.3: 3D view of ATILA reactor.

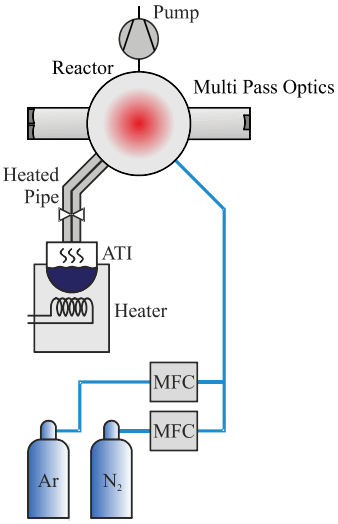

Figure 3.4: Schematic of the ATI heating system and gas connection to ATILA.

3.2 Diagnostics

3.2.1 Electrical measurements

In a capacitively coupled RF discharge, the behavior of the sheaths next to the electrodes is highly important. The sheath thickness changes with the time varying voltage due to the electrons moving toward or away from the electrode. Due to their mass, the ions cannot respond in a fast enough way and are only subject to the time-averaged fields. When the voltage on an electrode turns negative, the electrons are sent away from the electrode. The current in the discharge is the sum of the displacement and the conduction currents and is mainly transported by the electrons. In the plasma bulk, the displacement current flowing through the capacitor is smaller than the conduction current flowing through the inductance and the resistance of the plasma. Therefore, the conduction current is proportional to the plasma density. However, in the sheaths, the current flowing is dominated by the displacement current which is due to the time varying electric field [87, 109]. In the PKE-Nefedov reactor, the discharge current amplitude has been recorded with an oscilloscope in order to investigate the evolution of the dust particle growth instabilities as a function of time.

3.2.2 High speed imaging

A laser sheet is injected into the PKE-Nefedov chamber thanks to a laser diode at a wavelength $\lambda = 685$ nm located on one side of the reactor in order to illuminate the dust particles. A high speed camera (Photron SA5) is used to observe the plasma glow behavior by placing the camera in front of the reactor, or to record the scattered laser light by placing it at around 30° from the laser direction as shown in Fig. 3.5. This high speed camera can reach 1 million frames per second at low resolution (64 × 16). During the experiments performed on the PKE-Nefedov reactor, the frame rate is ranging between 10000 fps (with 1024 × 744 pixel resolution) and 20000 fps (832 × 448). At this chosen frame rate range, phenomena observed during the instabilities can be clearly detected. Above 20000 fps, the luminosity of the plasma becomes too weak and noisy to allow a correct analysis.

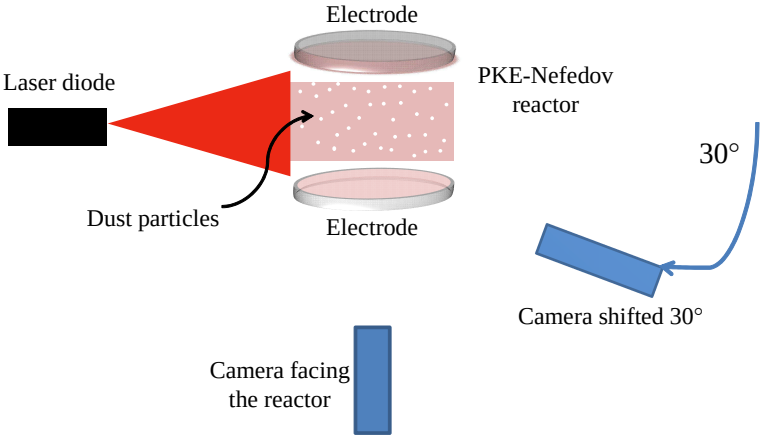

Figure 3.5: Schematic of the high speed imaging diagnostic.

3.2.3 Laser Induced Fluorescence

The understanding of the chemistry and the physics of plasmas requires information concerning the atoms, ions, electrons and molecules. This information needs to be quantitative, spatially resolved with respect to the active region of the plasma, and needs to be carried out without disturbing the plasma. Plasma glow, and much can be learned from observations of the wavelength resolved emission [110, 111]. Emission can reveal properties of the excited species, and it is generally used in UV and visible regions to observe electronically excited quantum states. Emission does not reveal the

behavior of the ground states of the species, which in most plasmas are in concentrations orders of magnitude higher than those of the excited states, and which are generally the major species responsible for the technologically important phenomena such as plasma etching or deposition. All ground state atoms, molecules and ions can absorb light in transitions between eigenstates, and therefore are detectable by this effect. Absorption measures the loss of photons. Any absorption process is followed by emission from the excited state. If the fluorescence quantum yield is reasonable, then the emission can be used as a marker for the excited species, and hence for the species in the original lower quantum level. For these purposes, Laser Induced Fluorescence (LIF) is used, because it is a non intrusive optical diagnostic, with excellent spatial and temporal resolutions. In 1975 [112], Stern used for the first time the LIF in a plasma with a single frequency argon ion laser. In 1979 [113], a tunable dye laser was used and for many years, the dye laser has been used due to its tunability, broad wavelength range and high output power. Laser diode technology has upgraded, yielding lasers in more wavelength ranges with increased power, tunability and are now cheaper than dye lasers. Usually laser induced fluorescence is used to measure the ground or metastable state populations of specific species. The LIF process is a three level procedure. Fig. 3.6 shows the energy level diagram of neutral argon used during our experiments. A laser at 667.9125 nm (beam diameter about 0.3 cm) in vacuum is used to pump the state $4s[3/2]_1$ to the $4p'[1/2]_0$. Then, the atom relaxes to the $4s'[1/2]_1$ state by emitting a photon at 750.59 nm [114, 115]. The starting state $4s[3/2]_1$ is not a ground or metastable state, however it is expected enough population for LIF due to the direct excitation from the ground state and electron impact excitation from metastable states $4s[3/2]_2$ and $4s'[1/2]_0$. The laser diode (Toptica DL100) with a bandwidth of less than 1 MHz and an output power

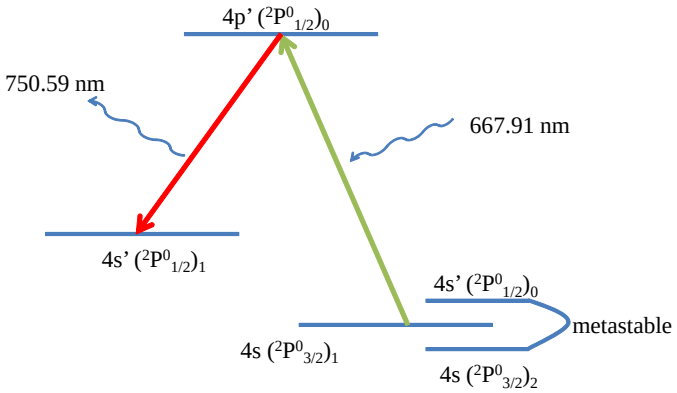

Figure 3.6: Diagram of argon LIF scheme.

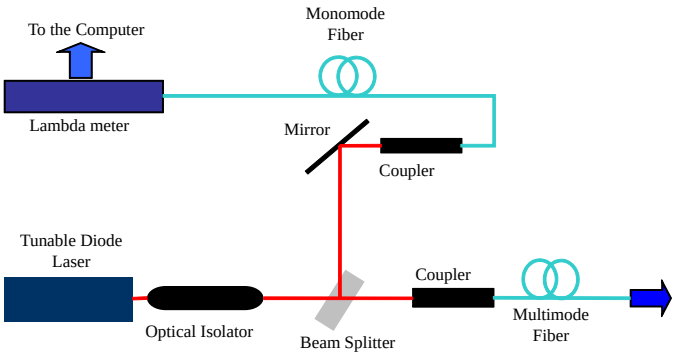

Figure 3.7: Transverse optical diagnostics. Constituents mounted on the laser table.

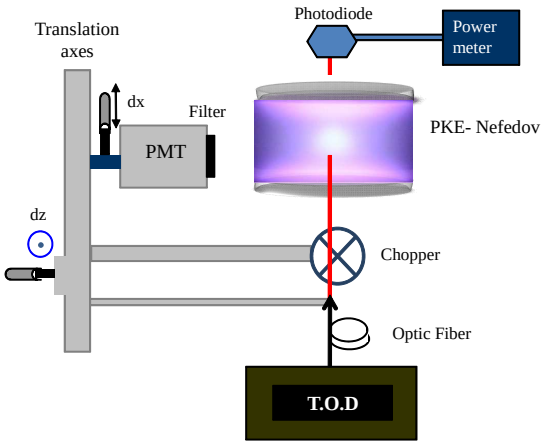

Figure 3.8: Schematic of LIF diagnostic on the PKE-Nefedov reactor. Collection system of the fluorescence.

of 30 mW is used to measure the spatial distribution of excited neutral atoms. The wavelength scanning is performed by varying the voltage on the piezoelectric controlled grating located within the laser cavity. The laser beam passes through an optical isolator which allows the transmission of light in only one direction. It is typically used to prevent unwanted feedback. Beam splitter and mirrors are mounted on the laser table in order to direct the laser beam to the lambdameter (for the control), and also toward the plasma chamber. A mechanical chopper is used to modulate the laser beam before entering into the reactor, and a lock-in amplifier is connected to eliminate the undesired signals. The fluorescence is observed through a filter by a photomultiplier (PMT) positioned perpendicularly to the entrance of the laser beam into the reactor. Figures. 3.7 and 3.8 show respectively the schematic of the transverse

optical diagnostics (a table that contains the laser and its additional components) and the collection system of the LIF. The system will be used to characterize the evolution of dust particle growth instabilities and of the void. The void appears as an enhanced luminosity region in the central part of the plasma bulk. A translation axes (Fig. 3.8) is used during the measurements performed in the void in order to move the laser and the photomultiplier simultaneously.

3.2.4 Fourier Transform Infrared spectroscopy

Infrared spectroscopy is used in several fields in research and industry. It is one of the most common spectroscopic techniques used by organic and inorganic chemists. IR spectroscopy is used for the measurements of CO_2 concentrations in green houses, for identification of functional groups in unknown substances, and for identification of molecular orientation in polymer films. IR spectrometers can accept a wide range of sample types such as solids, liquids and gases. Therefore IR spectroscopy is an important and popular tool for compound identification. Infrared radiation extents on the electromagnetic spectrum with wavenumbers from roughly 12800 to 10 cm^{-1}, or wavelengths from 0.78 to 1000 μm. It is bounded by the red end of the visible region at high frequencies and the microwave region at low frequencies. The Infrared spectrum is divided into three areas: near infrared, mid infrared and far infrared as shown in Table 3.1. The near infrared is used to excite harmonic vibrations, the mid infrared

Infrared region	Wavelength range (μm)	Wavenumber range (cm^{-1})
Near Infrared	0.78 - 2.5	12800 - 4000
Mid Infrared	2.5 - 50	4000 - 200
Far Infrared	50 - 1000	200 - 10

Table 3.1: Infrared ranges.

to investigate fundamental vibrations and the far infrared is mostly used for rotational spectroscopy. Absorption in the infrared region results in changes in rotational and vibrational status of the molecules. The absorption frequency depends on the vibrational frequency of the molecules, whereas the absorption intensity depends on how effectively the infrared photon energy can be transferred to the molecule. It depends on the change in the dipole moment that occurs as a result of molecular vibration. Therefore, a molecule will absorb infrared light only if the absorption causes a change in the dipole moment [116]. Major types of molecular vibrations are stretching and

bending. Some stretching motions are shown in Fig. 3.9. Infrared radiation is absorbed and the related energy is converted into these type of motions. The absorption involves discrete, quantized energy levels. However, the individual vibrational motion is usually accompanied by other rotational motions. These combinations lead to absorption bands commonly observed in the mid Infrared region and not to discrete lines [117].

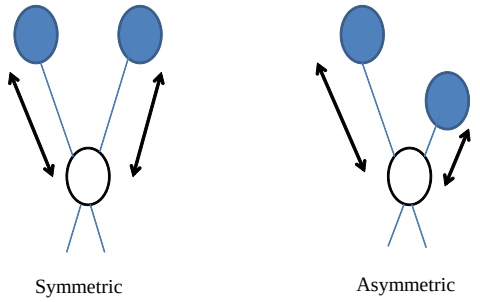

Figure 3.9: Some molecular vibrational modes.

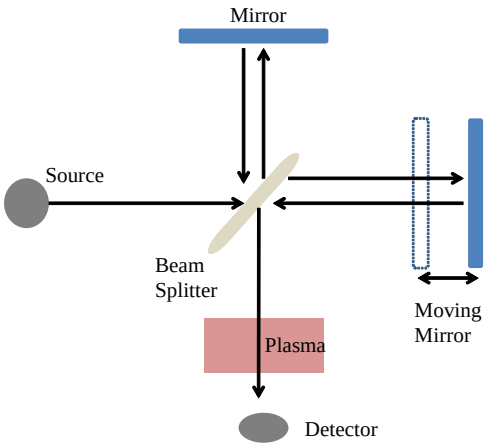

Figure 3.10: Illustration of a Michelson interferometer used in the FTIR.

Fourier transform infrared spectroscopy (FTIR) is operated at the mid infrared ranges. Michelson interferometer (Fig. 3.10) is the most common interferometer used in FTIR spectroscopy. It consists of three active components: a moving mirror, a fixed mirror, and a beamsplitter. The two mirrors are perpendicular to each other. The beamsplitter is a semireflecting device. Radiation from the broadband IR source is collimated and directed into the interferometer and hit the beamsplitter [118]. Half of the IR beam is transmitted to the fixed mirror and the other half is reflected to the moving mirror. After the divided beams are reflected from the two mirrors, they are

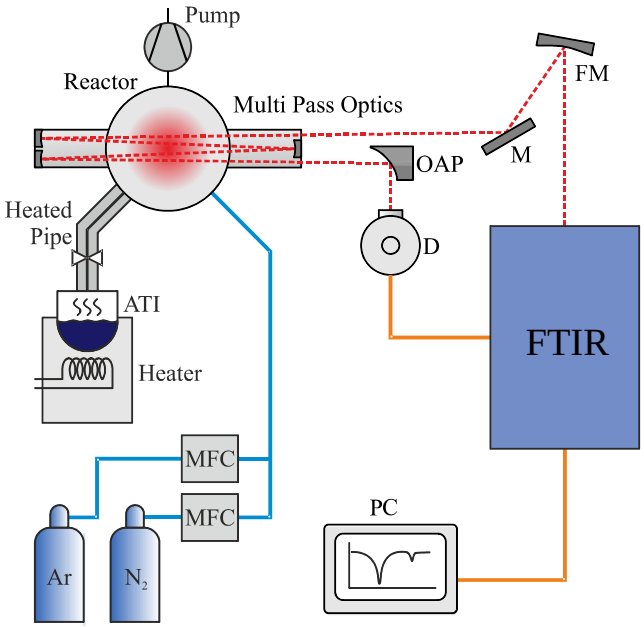

Figure 3.11: Schematic of the experimental setup: FTIR + ATILA.

recombined at the beamsplitter. Due to changes in the relative position of the moving mirror to the fixed mirror, an interference pattern is created. Then, the resulting beam passes through the sample and is focused on the detector.

FTIR spectroscopy is performed in the ATILA reactor located in Christian-Albrechts University of Kiel, at the Institute of Experimental and Applied Physics (IEAP). It is a collaboration between the GREMI (Orléans, France), IEAP (Kiel, Germany), and the Leibniz Institute for Plasma Science and Technology (Greifswald, Germany). The Fourier Transform infrared spectroscopy is brought from Greifswald to study the ATI evolution in an RF plasma.

In Fig. 3.11, a schematic of the complete setup with the FTIR connected to the reactor is presented. The beam leaving the FTIR box (Bruker Vertex 80v) is directed toward a focal mirror, $f_{FM} = 1$ m that has been used to focus the beam into the optical multi pass cell, leading to a total absorption length of $l = 17.2$ m inside the reactor chamber. The beam coming out from the reactor has been focused on the detector using an Off Axis Parabolic (OAP) mirror. For all experiments, the spectrum between 700 cm^{-1} and 4700 cm^{-1} has been scanned in order to detect the various species in our plasma.

3.3 Conclusion

In this Chapter, the various reactors used in this thesis are detailed. The PKE-Nefedov reactor located in GREMI laboratory (Orléans, France), a capacitively coupled radio-frequency discharge, is used to study dusty plasmas using argon or krypton. The ATILA reactor located in IEAP (Kiel, Germany), an asymmetric capacitively coupled radio-frequency discharge, is used to study the chemistry of the plasma using argon, nitrogen and ATI mixtures.

In the PKE-Nefedov reactor, various diagnostics (electrical measurements, high speed imaging and Laser Induced Fluorescence) detailed in this Chapter are used to investigate phenomena (dust particle growth instabilities, void appearance in the plasma center) appearing due to the presence of dust particles in the plasma. In ATILA, Fourier Transform Infrared spectroscopy is used to study the Aluminium Triisopropoxide dissociation in the plasma.

3.4 French Summary

Dans ce chapitre, les differents réacteurs utilisés dans cette thèse sont détaillés. Le réacteur PKE-Nefedov situé au laboratoire GREMI (Orléans, France), une décharge radiofréquence à couplage capacitif, est utilisé pour étudier les plasmas poudreux en utilisant l'argon ou le krypton. Le réacteur ATILA à l'IEAP (Kiel, Allemagne), une décharge radiofréquence, est utilisé pour étudier la chimie du plasma en utilisant un mélange d'argon, d'azote et d'aluminium tri-isopropoxide (ATI).

Dans le réacteur PKE-Nefedov, les différents diagnostics (mesures électriques, imagerie rapide et Fluorescence Induite par Laser) detaillés dans ce chapitre ont été utilisés pour étudier différents phénomènes (les instabilités de croissance des poudres et l'apparition du void au centre du plasma). Sur ATILA, la spectroscopie infrarouge à transformée de Fourier est utilisée pour étudier la dissociation de l'aluminium triisopropoxide dans le plasma.

Chapter 4

Electrical diagnostics of dust particle growth instabilities (DPGI)

In this Chapter, the study is mainly focused on the electrical diagnostics performed on the PKE-Nefedov reactor. Once the plasma ions sputter the polymer deposited on the electrode, a high density of dust particles is grown in the plasma. These particles acquire a negative charge by capturing plasma electrons resulting in a decrease of the discharge current as shown in Fig. 4.1 (DC component). The ignition of the plasma is detected at around 7 s after the recording start (increase of the current amplitude from 0.43 to 0.80). Then, a decrease of the signal amplitude as a function of time confirms the formation and the growth of dust particles. Sudden amplitude drops in the electrical signal are noticed when using Kr (28 s and 91 s in Fig. 4.1). These drops last for a few seconds and are evidenced just after the plasma ignition and during the first part of the instabilities. Later in the growth process, the existence of these drops is no more evidenced. As we will see in section 4.3, these drops are not (or less) observed in argon plasmas where a smaller dust particle density is obtained. Thus, these drops could be related to the formation of a high dust particle density. The exact origin of these drops is currently under investigation.

The loss of electrons during dust particle growth can lead to a disturbance of the plasma equilibrium. In these conditions, the plasma enters in an unstable state characterized by low frequency instabilities like dust particle growth instabilities (DPGI). The beginning of these instabilities is clearly observed on the electrical signal at around 62 s (55 s after the plasma ignition).

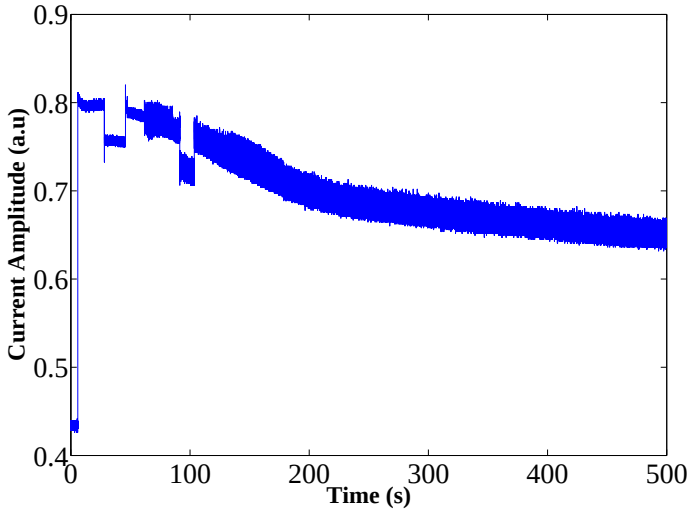

Figure 4.1: Amplitude of the RF current (DC component).

In this Chapter, DPGI are investigated by recording the amplitude of the discharge current:

- This signal reveals the temporal evolution of the instability.

- A Fourier analysis shows the existence of different instability regimes [119] and complex frequency evolutions.

- The evolution of the current is studied as a function of the gas pressure. It provides the evolution of DPGI characteristics like the appearance time, the duration and the typical frequencies [120]. These parameters are compared and discussed in connection with dust particle size and density. It is also shown that the instability parameters can be correlated to each other. The instability appearance time is the first parameter that can be easily measured during an experiment. It is shown that it can be used to estimate the instability evolution and its other main characteristics.

- The analysis of the electrical signal oscillation amplitudes also reveals the different instability regimes and their transitions. For this purpose all the peaks during DPGI are detected to emphasize these variations.

- A comparison of the instability evolution in krypton and argon plasmas is performed in order to study the effect of the gas on the formation of dust particles. The sputtering efficiency and the dust particle formation can be affected.

4.1 Evidence of different instability regimes

In order to study more precisely the evolution of the instabilities as a function of time, the oscillating part of the electrical measurement is recorded to have a better oscilloscope vertical resolution (Fig. 4.2). In order to bring to light the DPGI frequency evolution, the corresponding Fourier spectrogram is calculated and presented in Fig. 4.3. In order to emphasize small ordered domains, the spectrogram intensity has been normalized separately inside each 100 s range (from 0 to 100 s the intensity has been normalized to its maximum value inside this time domain and so on). From Figs. 4.2 and 4.3, it clearly appears that the instability is characterized by a well-defined succession of phases. These phases can be either ordered with a smoothly evolving frequency or stochastic with fast and erratic frequency variations. These phases are also well-identified in Fig. 4.2 where they are characterized by different instability amplitudes. In Fig. 4.3, when several frequencies are detected simultaneously, the color code allows to identify the dominant frequency. Indeed, the electrical measurement shows that the instability is constituted of well-defined patterns with a varying number of peaks (as it will be shown in section 4.1.1). Depending on the respective peak amplitudes, the dominant frequency corresponds either to the main frequency pattern (constituted of several peaks) or to the peak separation within the pattern.

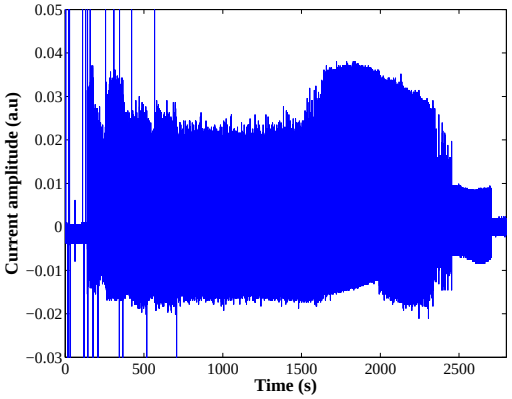

Figure 4.2: Alternative part of the discharge current amplitude evidencing DPGI.

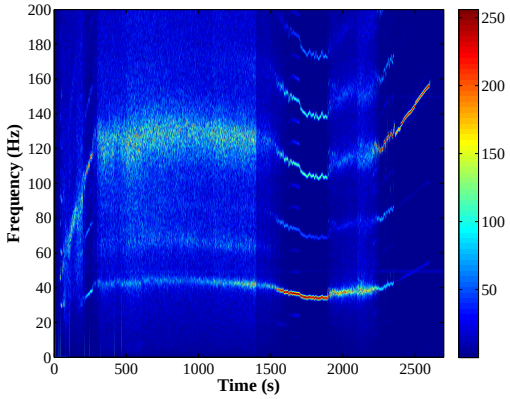

Figure 4.3: Fourier spectrogram representing the frequency evolution during DPGI.

Figures 4.2 and 4.3 evidence that dust particle growth instabilities are constituted of 4 successive main regimes:

- A fast rise of the frequencies at the beginning with ordered phases followed by an alternation of short stochastic and ordered phases (from 140 to 400 s).

- A long stochastic phase with fast and erratic frequency behavior (from 400 to 1400 s).

- A frequency drop phase constituted of ordered and slightly stochastic behaviors (from 1400 to 2400 s).

- A final high frequency ordered phase (from 2400 s till the end of the instability).

In order to better characterize DPGI, each of these phases is finely analyzed in the following sections.

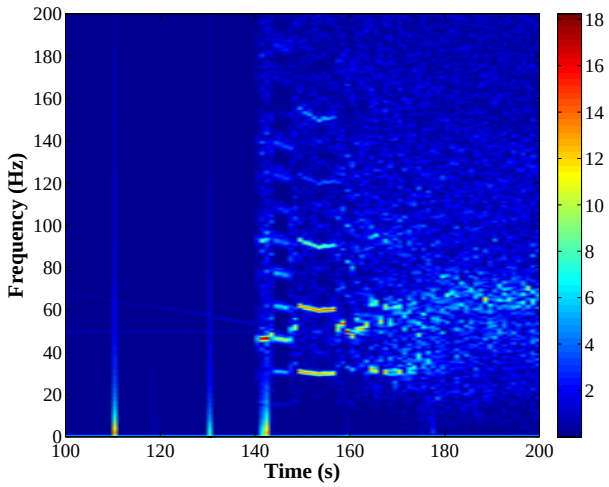

Figure 4.4: Zoom on the first part of the instability. The instability begins at 140 s (plasma ignition at 0 s) and is characterized by 4 successive ordered phases before entering into a stochastic regime.

4.1.1 Starting regimes

A zoom of the Fourier spectrogram is shown in Fig. 4.4 to study more specifically the instability beginning. The instability starts around 140 s after the plasma ignition. The ordered phases are well-observed between 140 s and 162 s. Four phases can be evidenced. The first phase from 140 s to 142 s is followed by a second one until 148 s. Then, a well-defined third phase takes place until 157 s and finally a fourth one (less clear) appears until 162 s. From 162 s to 400 s, the instability enters into a stochastic regime where a relatively fast rise of the frequency is observed.

The ordered phases show well-defined patterns containing a varying number of peaks. For the first phase (Fig. 4.5(a)), the main pattern is composed of two big peaks followed by a smaller one. For the second and third phases, respectively four (Fig. 4.5(b)) and two peaks (Fig. 4.5 (c)) of different amplitudes form the main pattern.

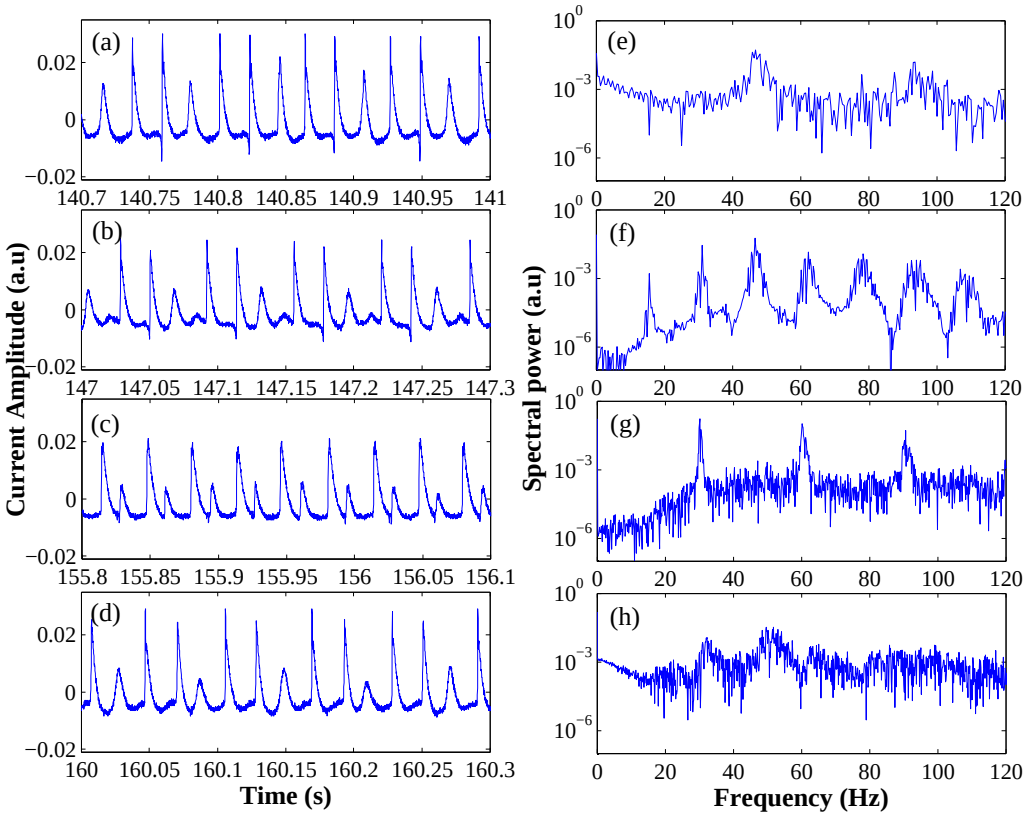

Figure 4.5: Electrical signals and their corresponding Fourier spectra for the first 4 ordered phases of the instability.

The fourth phase (Fig. 4.5 (d)) appears roughly similar to the first one with differences in the relative amplitude of the peaks. From this first insight, the transition between each phase is characterized by the appearance or disappearance of peaks and by a change in their respective amplitudes.

The frequency evolution is also quite interesting. In order to better understand and complete Fig. 4.4, the Fourier spectrum of each phase is presented in Figs. 4.5 (e)-(h). It appears that the same typical frequencies or their harmonics are globally encountered in each phase. Harmonics are easily obtained due to the non-sinusoidal shape of the signals that have similarities with sawtooth signals. The smallest detected frequency is about 15 - 16 Hz. This frequency is clearly detected in Fig. 4.5 (f), is very small in the cases corresponding to Figs. 4.5 (e) and (h) and cannot be detected in Fig. 4.5 (g). Whereas in Figs. 4.5 (e) and (h) presenting the whole frequency range this frequency cannot be easily observed, its presence has been confirmed by filtering and zooming the corresponding data around 15 Hz. In the phases where this frequency appears, it

corresponds to the main pattern frequency that is slightly similar in phases 1, 2 and 4. For phase 3, the main pattern frequency is about 30 Hz, twice the value of the other phases. This value of 30 Hz is present in all the phases, as a main frequency or as an harmonic. Another interesting value is the frequency at 45 Hz that is clearly present in phases 1, 2 and 4. In the Fourier spectra, a peak is centered at this value with a width of about 4 Hz. It appears that 45 Hz is roughly the frequency corresponding to the peak separation within the main pattern. For phase 1, three peaks at a repetition rate of 45 Hz constitute the main pattern that repeats at 15 Hz. For phase 2, the main pattern frequency is similar but with four peaks: The first two peaks appear at 45 Hz but the frequency for the two other peaks is continuously increasing with values multiple of 15 Hz. The fact that the system oscillates at very well-defined frequencies that are multiple from each others, underlines that the dynamics behind these instabilities is relatively complex. For example, the sum of two signals at 30 Hz and 60 Hz can roughly reproduce the signal of phase 3 (Figs. 4.5 (c) and (g)) but a linear combination of simple signals cannot reproduce the other phases in a satisfactory way.

These four phases appearing at the beginning of the instability cannot be observed regularly in each experiment, but are encountered in most of them.

4.1.2 Long stochastic regime

A long stochastic phase starts at 400 s up to 1400 s (Fig. 4.3). During this phase, the frequency fluctuates around 130 Hz quickly and erratically but stays within a rather small value range. The envelop amplitude of the electrical signal stays roughly at the same height (Fig. 4.2) and the dominant frequency (Fig. 4.3) corresponds to the frequency between two consecutive peaks.

In Fig. 4.6 a small part of the electrical signal during this long stochastic phase is extracted. The Fourier spectrum calculated during the entire phase is shown in Fig. 4.7. Most of the frequencies are around 130 Hz that correspond to the frequency between consecutive peaks, and less dominant frequency is also observed around 45 Hz. During the long stochastic phase, a three peak pattern can be observed infrequently in the midst of the stochastic behavior of the signal, with a main pattern frequency of about 45 Hz. These major frequencies (130 and 45 Hz) are also clearly evidenced in Fig. 4.3.

4.1.3 Frequency drop regime

After this long stochastic phase, the frequency drops to a lower level (35 Hz) at around 1400 s (Fig. 4.3). This drop appears as an increase of the signal amplitude in Fig. 4.2.

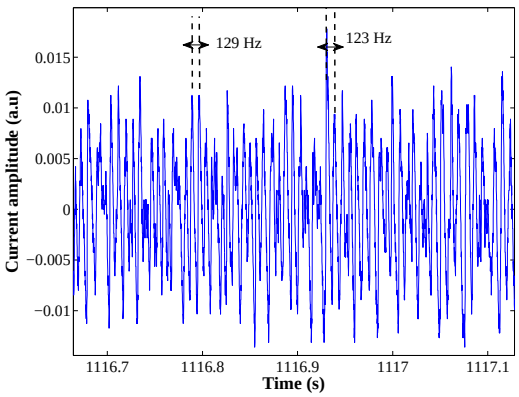

Figure 4.6: A part of the electrical signal during the long stochastic regime.

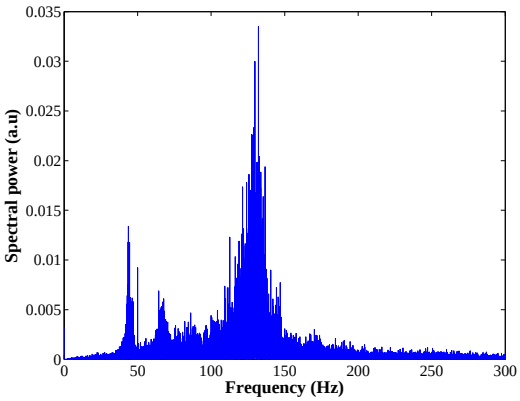

Figure 4.7: Fourier spectrum during the long stochastic regime.

A small part of the electrical signal is extracted and a pattern with three peaks can be observed during this phase (Fig. 4.8). Two peaks with high amplitudes are clearly evidenced, and a small peak around -0.002 is also taken into consideration. The Fourier spectrum is calculated during this whole phase and is shown in Fig. 4.9. A dominant frequency around 35 Hz is clearly evidenced, as the harmonics of this frequency at around 70, 105 and 140 Hz are observed. Some of the frequencies also correspond to the consecutive peak frequency. For instance, the frequency between the two big peaks is also 140 Hz. This frequency drop phase is constituted of two parts, the well-organized part presented in Fig. 4.8 and a more stochastic part. During this last part, the three peak pattern is always observed but some extra peaks can be detected disturbing the well-organized pattern.

4.1.4 Last ordered regime

Around 2400 s, the instability ends with an ordered phase characterized by a high frequency ($\approx$ 140 Hz, Fig. 4.3) and a small amplitude (Fig. 4.2). The characteristic pattern of the electrical signal changes and turns into a single sawtooth shape as shown in Fig. 4.10. The typical frequency is about 140 Hz as shown in Fig. 4.11 where the frequency harmonics are also detected at 280 and 420 Hz. The evolution of this phase (duration, frequency) will be detailed and discussed in section 4.2.2.

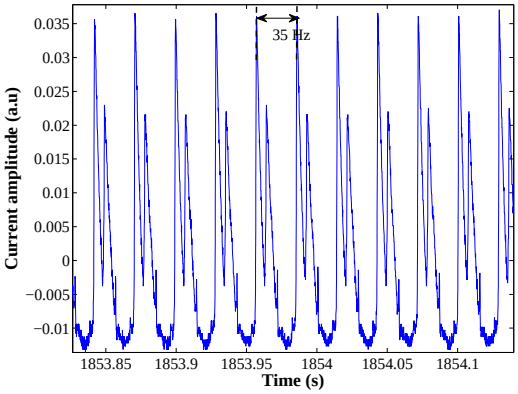

Figure 4.8: A part of the electrical signal during the frequency drop regime.

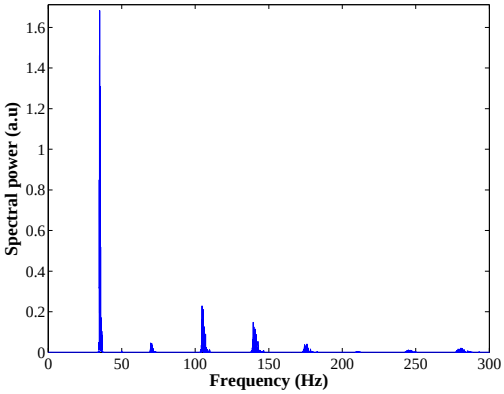

Figure 4.9: Fourier spectrum during the frequency drop regime.

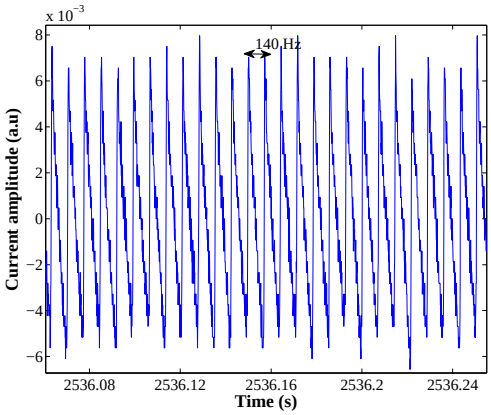

Figure 4.10: A part of the electrical signal during the last ordered regime.

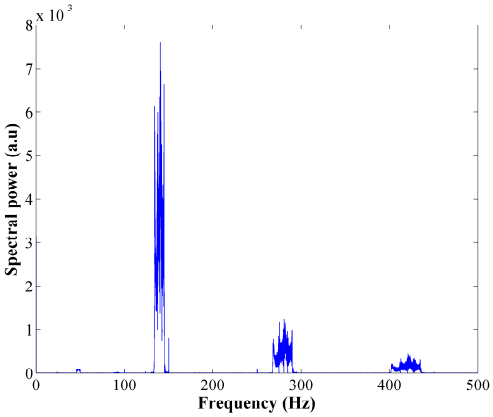

Figure 4.11: Fourier spectrum during the last ordered regime.

4.2 Pressure dependence of DPGI

In section 4.1, we have identified different phases and a complex evolution of the main frequency. In order to better understand the instability behavior, its modification as a function of the pressure is investigated. The following results are issued from a series of well-defined experiments. The dust particle growth process in our setup is very sensitive to any slight changes in the experimental conditions. It is particularly dependent on the initial base pressure before an experiment [73]. This sensitivity has also been observed in other experiments where dust particles are grown by sputtering [41]. It has been attributed to the presence of molecular impurities. Thus, to obtain conclusive

comparisons between DPGI observed at different krypton pressures, experiments have been performed by following a strict procedure. The reactor and the gas line are pumped down for almost 24 hours between each experiment. For each pressure, several experiments are performed in order to obtain statistical measurements and estimate the related error bars.

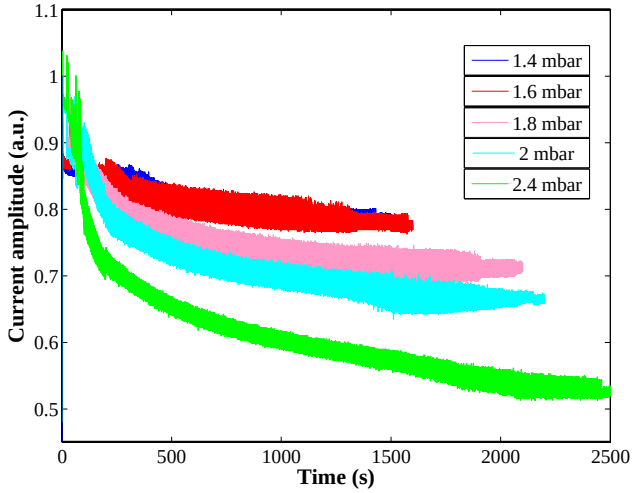

Figure 4.12: Amplitude of the RF current (DC component) as a function of time for different pressures.

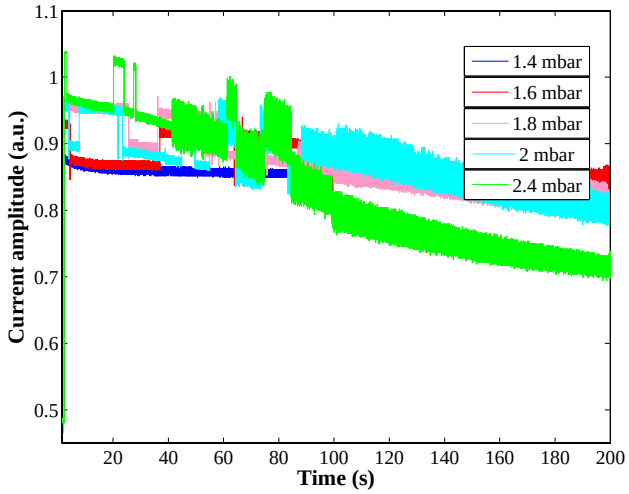

Figure 4.13: Amplitude of the RF current (DC component) as a function of time for different pressures. Zoom on the plasma ignition.

In Fig. 4.12, the evolution of the amplitude of the RF current (DC component) as a function of time is presented for different pressures from 1.4 to 2.4 mbar with a step of 0.2 mbar (excluding 2.2 mbar). The current decrease during dust particle growth is quite different as a function of the pressure. For instance, at 1.4 mbar the decrease is slow and the amplitude variation is small. At 1.6 mbar, same behavior as at 1.4 mbar is almost observed. At 1.8 mbar, the current decrease becomes faster and a clear gap can be observed between 1.6 and 1.8 mbar (around 1500 s in Fig. 4.12). Then, at 2 mbar, the current decrease is slightly faster than 1.8 mbar. The gap observed between 2 mbar and 2.4 mbar could be the place of the missing curve at 2.2 mbar. This difference shows that at higher pressure (above 1.6 mbar) the growth kinetics is faster and the dust density is higher (the bigger is the amount of formed dust particles, the bigger is the loss of electrons). In Fig. 4.13, a zoom on the plasma ignition part is shown. It is observed that the higher is the pressure, the higher is the rise of the signal at the ignition. It is also observed that the number of the electrical drops increases as a function of the pressure. It means that these drops are certainly induced by high dust particle density.

The DC component (Figs. 4.12 and 4.13) is used to study dust particle growth kinetics. However, in the following sections, the AC component is used to have a better oscilloscope vertical resolution that allows to investigate dust particle growth instability characteristics such as the appearance time, the duration, the frequencies and the peak amplitude evolution.

4.2.1 Appearance time and duration of instabilities

The appearance time and the total duration of DPGI are presented as a function of the pressure in Fig. 4.14. At 1.4 mbar, the instability appears around 220 s after the plasma ignition, while at 2.4 mbar it occurs more quickly (35 s). Increasing the pressure results in a continuous decrease of the appearance time. The appearance time trend can be easily fitted by a decreasing exponential function. It means that the necessary conditions to trigger DPGI are obtained faster at high pressure. It is consistent with the observation that higher pressures result in the growth of a higher dust density (and thus smaller dust sizes) as deduced from Fig. 4.12. These conditions seem to be more favorable to trigger DPGI than situations with a lower density of bigger dust particles obtained at low pressures [73].

Concerning the instability duration, it increases with the pressure from 1200 s at 1.4 mbar up to 2400 s at 2.4 mbar. The duration trend can also be fitted by an exponential

function in the form $a - b \cdot exp(-c \cdot P)$. It means that at high pressure, the amount of dust particles is high enough to maintain a longer instability. From these behaviors, it can be deduced that the higher the pressure, the shorter the appearance time and the longer the duration of the instability. Thus, a high dust particle density induced well-developed DPGI.

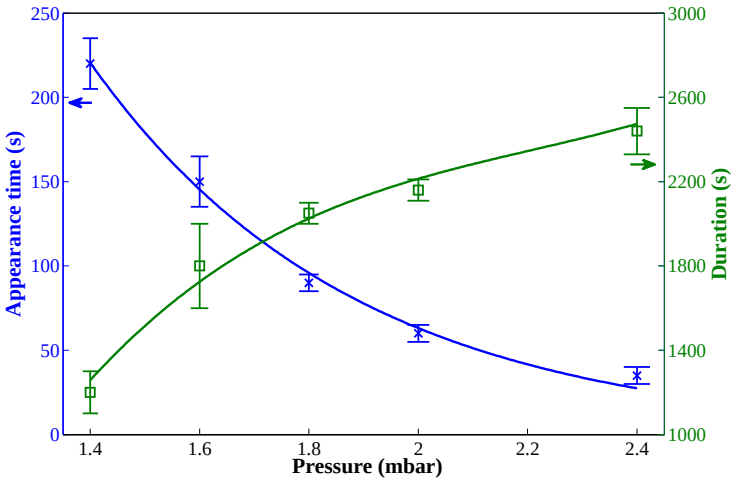

Figure 4.14: Appearance time (×) and total duration (□) of DPGI as a function of gas pressure.

4.2.2 Frequency evolution

The DPGI frequency can also provide estimations on dust particle growth kinetics. For this purpose, the starting (at the instability beginning) and final (just before the instability end) frequencies are measured as a function of the pressure (Fig. 4.15). At 1.4 mbar, the starting frequency is around 35 Hz and it increases with the pressure up to a value of about 58 Hz at 2 mbar (an increase of 1.6 times). The final frequency is around 75 Hz at 1.4 mbar, and it increases with the pressure up to 350 Hz at 2 mbar (an increase of 4.6 times). It is observed that at 1.4 mbar the final frequency (75 Hz) is twice the starting one (35 Hz), at 1.6 mbar the proportionality factor is 3, at 1.8 mbar it becomes 4.5, and finally at 2 mbar it is around 6. At 2.4 mbar, the signal is mostly dominated by a stochastic behavior, where it is difficult to identify starting and final frequencies. This study shows that a relatively small change of the starting frequency can have a big influence on the evolution of the frequencies during dust particle growth instabilities. For this purpose, the frequency evolution in different parts of the instability will be discussed in the following.

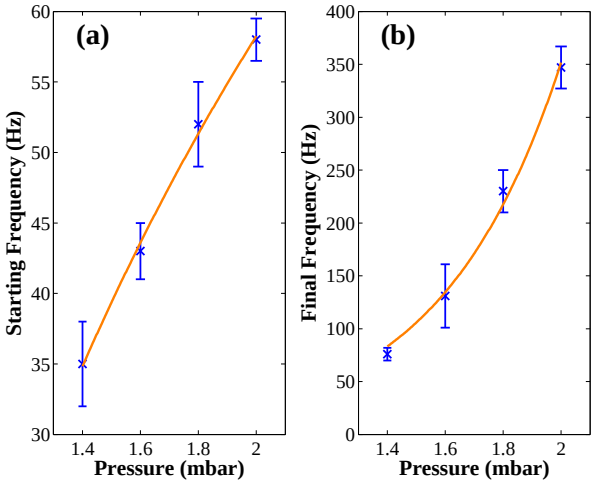

Figure 4.15: Starting and final frequencies of the instability as a function of the pressure.

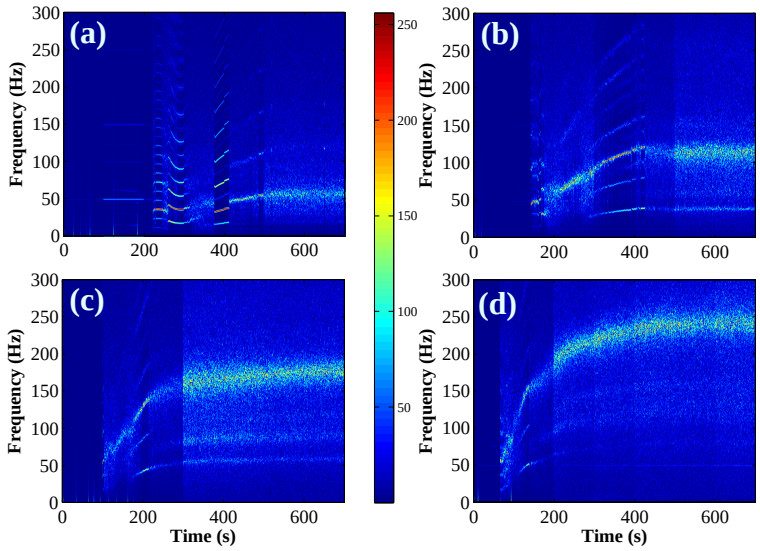

Figure 4.16: Fourier spectrogram of the first phases for different pressures, (a) 1.4 mbar, (b) 1.6 mbar, (c) 1.8 mbar and (d) 2 mbar.

First part of the instability

In Fig. 4.16, the first part of the instability is observed for four values of the pressure (1.4, 1.6, 1.8, and 2 mbar). At 1.4 mbar, many ordered phases are observed at the beginning of the instability before the long stochastic phase. The frequency increases slowly with a speed of about 0.07 Hz/s. At 1.6 mbar, the first part of the instability becomes shorter and an alternation of ordered and stochastic behavior is observed

before the beginning of the long stochastic phase at around 500 s. During this first part, the frequency increases with a speed of about 0.25 Hz/s. At 1.8 mbar, the rise of the frequency is faster with a speed of 0.5 Hz/s, and the first part of instability has mostly a stochastic behavior. At 2 mbar, the first part of the instability is a fast phase with a speed of 0.9 Hz/s. This shows that at high pressure, the frequency increases faster than at low pressure. It means that the formation of a high dust density (as shown in Fig. 4.12) can accelerate the instability frequency evolution.

Long stochastic phase

In Fig. 4.17, the long stochastic phase frequency is shown as a function of the pressure. The frequency mean value is around 55 Hz at 1.4 mbar, and increases up to 240 Hz at 2 mbar. At 2.4 mbar, the long stochastic phase frequency can vary within a rather big range. This means that it is impossible to identify a typical long stochastic frequency after several experiments at 2.4 mbar due to the stochastic behavior of the signal from the beginning of the instability. As for the starting and final frequencies (Fig. 4.15), the central stochastic frequency increases with the pressure.

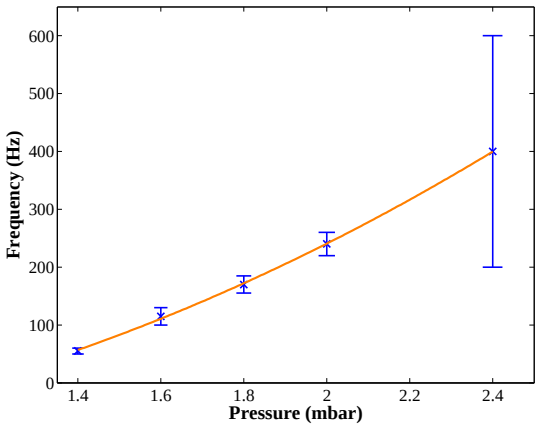

Figure 4.17: Central stochastic phase frequency as a function of the pressure.

Frequency drop phase

After this long stochastic phase, the frequency drops to a lower level (Fig. 4.18 (a) 1.4, (b) 1.6, (c) 1.8 and (d) 2 mbar). This is mainly due to the fact that for this phase, the frequency corresponds to the pattern frequency and no more to the consecutive peak frequency as shown previously in Figs. 4.8 and 4.9. The frequency drop phase is constituted of two parts, a well-ordered one and a more stochastic one. At low pressure, this phase is more ordered than at high pressure. At 1.4 mbar, the frequency drop phase begins around 1180 s (Fig. 4.18 (a)) where a frequency at 32 Hz and its

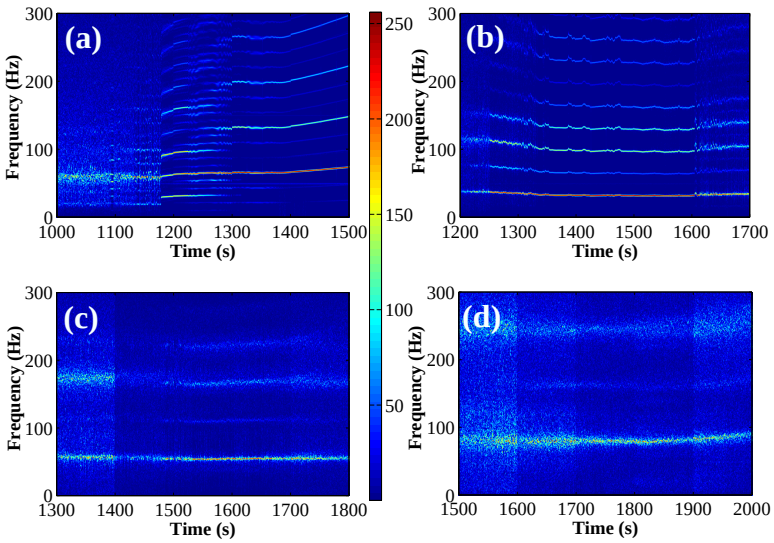

Figure 4.18: Fourier spectrogram of the frequency drop phase for different pressures, (a) 1.4 mbar, (b) 1.6 mbar, (c) 1.8 and (d) 2 mbar.

harmonics are observed for a short time until 1220 s, then the frequency at 65 Hz becomes dominant. At 1.6 mbar, this frequency drop is clearly evidenced around 1250 till 1600 s (Fig. 4.18 (b)) before turning into a more stochastic behavior. At 1.8 mbar (Fig. 4.18 (c)), the frequency drop phase is globally more stochastic. It means that a clear pattern exists, but some peaks appear infrequently during this phase disturbing the well-ordered pattern. Finally at pressures above 2 mbar, the stochastic behavior is completely dominant during the frequency drop phase. At 2.4 mbar, this frequency drop phase is the final phase before the end of the instability (ordered phases are not observed at high pressure). As the electrical signal turns into a stochastic behavior as a function of the gas pressure as observed in Fig. 4.18.

Last ordered phase

At pressures lower than 2.4 mbar, another phase occurs before the instability end. This final phase has a clear ordered behavior as shown in Fig. 4.19. At high pressure, the phase is shorter than at low pressure, and the shape of the frequency evolution is different. At 1.4 mbar, the frequency increases slowly with a speed of about 0.09 Hz/s then slightly decreases at the end. At 1.6 mbar, the frequency increases with a speed of 0.10 Hz/s and the last decrease is less marked. At 1.8 mbar, the speed is around 0.13 Hz/s and the last decrease is not observed. At 2 mbar, this phase is divided into two parts, with a rising speed of about 0.63 Hz/s. It is observed in Figs. 4.16 and 4.18 that the instability becomes more stochastic as a function of the pressure,

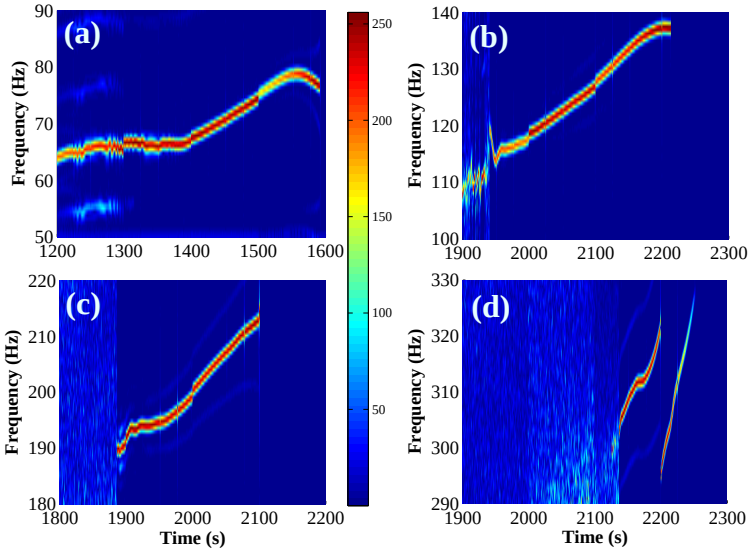

Figure 4.19: Spectrogram of the last ordered phase before the end of the instabilities, (a) at 1.4 mbar, (b) 1.6 mbar, (c) 1.8 mbar and (d) 2 mbar.

thus the separation of the last ordered phase observed in Fig. 4.19 (d) (at 2 mbar) show the disturbance of the last phase from the stochastic behavior of the signal. The frequency changes as a function of pressure (Fig. 4.19 (a) to (d)) are quite similar to the ones observed at the beginning of the instability (Fig. 4.16). The frequency evolution becomes faster as a function of the pressure.

4.2.3 Contribution of the different regimes

The relative contribution of the ordered and stochastic regimes during DPGI is now estimated for the different pressures (Fig. 4.20). The durations of all the stochastic regimes occurring during a DPGI sequence have been summed up. The same procedure has been used for the ordered regimes. At 1.4 mbar, the two types of regimes have roughly the same duration, whereas the stochastic phases become dominant as the pressure is increased. At 2.4 mbar, the ordered phases are almost absent, and DPGI are mainly stochastic during their whole duration. It means that when the dust particle density is huge (and thus the dust particle size is small), the instability cannot enter in an ordered regime. The disturbance induced by the dust particles is too strong to allow the instability to have an ordered oscillating behavior.

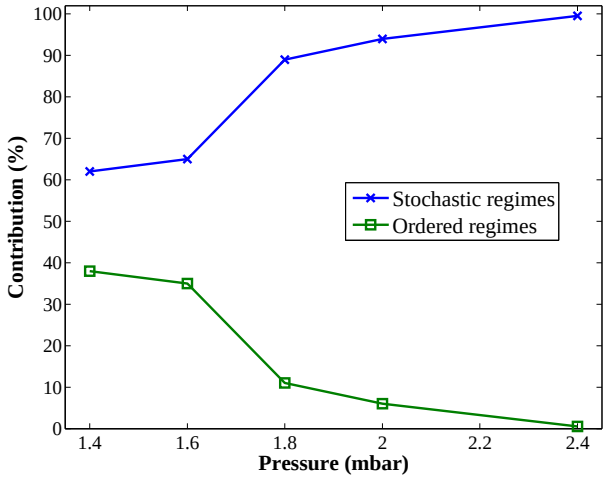

Figure 4.20: Contribution of the ordered (□) and stochastic (×) regimes as a function of the pressure.

4.2.4 Discussion

The Fourier spectrogram has been used to bring to light the temporal evolution of the frequencies during the instability. In particular, different ordered and stochastic regimes have been identified, and the instability characteristics have been measured as a function of the gas pressure. It appears that the higher the pressure, the shorter the appearance time, the longer the duration and the higher the frequencies. These results are consistent with the observation in Fig. 4.12 that at high pressure the growth kinetics is faster, the dust density is higher and the dust size is smaller. Indeed, a fast growth kinetics and a high dust density lead to a rapid appearance of DPGI. As the disturbance is strong and the discharge is saturated by dust particles, the instability can thus last longer. For the frequencies, a direct correlation is more difficult to define. Indeed, a simple approximation consists in considering that the typical DPGI frequencies are related to the dust plasma frequency [74, 121, 122] $\omega_{pd} = \sqrt{\frac{Q_d^2 n_d}{\epsilon_0 m_d}} \propto \sqrt{\frac{n_d}{r_d}}$. As n_d is higher and r_d is smaller at high pressure, it is logical to obtain a global increase of the typical DPGI frequencies with the pressure (Figs. 4.15 and 4.17). Nevertheless, this simple consideration cannot clearly explain the frequency temporal evolution. Whereas, the frequency increase at the beginning (Fig. 4.16) could be easily related to an initial increase of n_d, the stochastic phase and the last ordered phase (characterized by a frequency increase) cannot be related to ω_{pd}. In the long stochastic phase, the mean frequency is relatively constant. It is not consistent with growing dust particles. An hypothesis can be that we have a slowing down of the dust particle growth during

this regime, and then, rather constant values of n_d and r_d. The last ordered phase is characterized by a frequency increase. As n_d is not expected to increase at this stage of the dust particle growth process (no indication of a new dust particle generation is observed), the relation with ω_{pd} is rather difficult to justify. It underlines that more complex phenomena are behind DPGI and that complex plasma / dust interactions are involved.

4.2.5 Instability parameter relationship

In section 4.2, the evolution of the instability characteristics has been studied as a function of the pressure. In the present section, relations between these different characteristics will be emphasized. During an experiment, the first parameter that can be easily measured is the instability appearance time. We show that the knowledge of this parameter can provide information on the entire instability evolution. In Fig. 4.21, the instability duration is plotted as a function of the appearance time. It confirms the result of Fig. 4.14 that shows that the longer the appearance time, the shorter the instability duration. When the instability appears 35 s after the plasma ignition, it

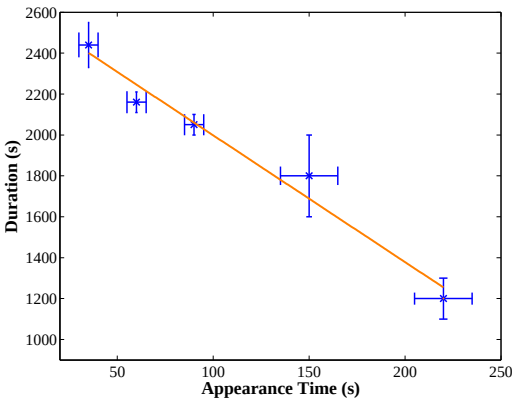

Figure 4.21: Duration of the instability as a function of the appearance time.

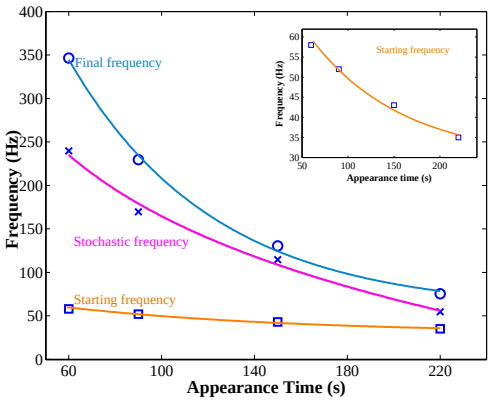

Figure 4.22: Frequencies as a function of the appearance time.

can last for 2400 s. When it starts 220 s after the plasma ignition, the total duration of the instability is only 1200 s. Figure 4.21 shows that there is roughly an inversely linear dependence between the instability duration and appearance time. The duration of DPGI can thus be roughly predicted as soon as they appear. Thanks to the appearance time, the different frequencies of the instability (starting, during the long stochastic phase, and final) can also be determined as shown in Fig. 4.22. The starting frequency as a function of the appearance time is zoomed in the upper right insert for a

better observation. The frequency trends can be fitted by decreasing exponential functions. Figure 4.22 confirms the relation between the frequencies discussed previously in Fig. 4.15. A quick start of the instability (60 s after plasma ignition) shows a noticeable evolution of the frequency (a factor of 6 between the starting and the final frequencies). At longer appearance time (220 s after plasma ignition), the factor between the starting and the final frequencies becomes just twice. It means that the earlier is the appearance of the instability, the bigger is the global increase of the frequency.

This study shows that DPGI is a relatively robust phenomenon and that small fluctuations in the starting conditions (appearance time) do not change its long term evolution. For the experimenters, the knowledge of the appearance time is enough to know rather accurately the instability evolution.

4.2.6 Oscillation amplitude investigations

In section 4.1, different phases have been identified from the beginning till the end of the instability. In section 4.2, the instability appearance time, duration, and frequencies have been discussed as a function of the gas pressure. In this section, the electrical signal is analyzed through the variation of its oscillation amplitude.

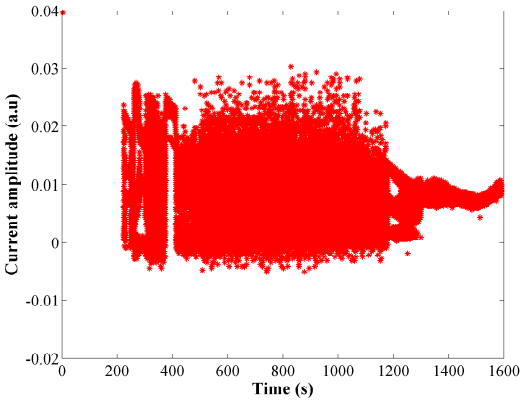

Figure 4.23: Peak detection on the discharge current amplitude at 1.4 mbar.

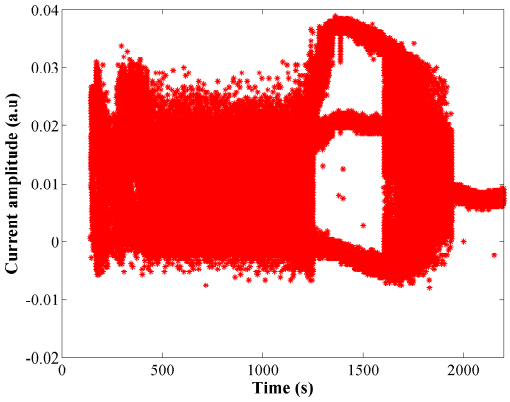

Figure 4.24: Peak detection on the discharge current amplitude at 1.6 mbar.

For this purpose, the discharge current (for example Fig. 4.2) is analyzed in order to detect all the peaks. In this kind of signal, the peaks can be easily detected due to the non-sinusoidal shape of the signals that have similarities with sawtooth signals. The peak detection criterion is adjusted in order to avoid detecting too many peaks of noise. The obtained peak amplitudes are presented in Figs. 4.23 to 4.26 for different gas pressures (1.4, 1.6, 1.8, 2 mbar). As mentioned in section 4.2.3, DPGI are characterized

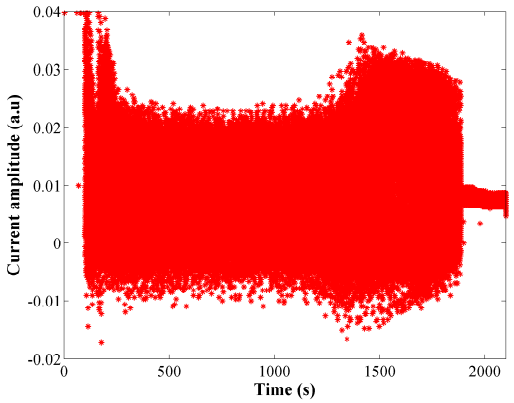

Figure 4.25: Peak detection on the discharge current amplitude at 1.8 mbar.

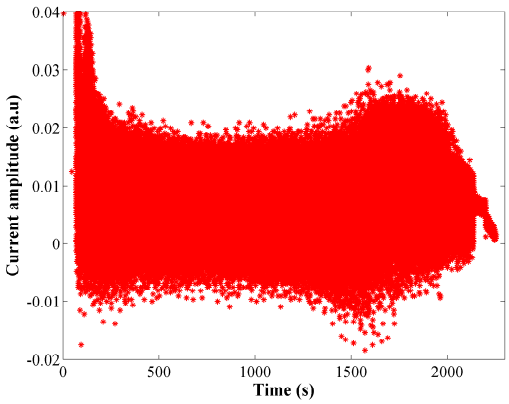

Figure 4.26: Peak detection on the discharge current amplitude at 2 mbar.

by an alternation of ordered and stochastic regimes. It has been shown in Fig. 4.20, that at higher pressure, DPGI are mainly described by stochastic regimes. The peak detection shown in Figs. 4.23 to 4.26 confirms this behavior. At 1.4 mbar (Fig. 4.23), the ordered phases appear at the beginning of the instability, between 200 and 400 s and then after 1180 s (frequency drop and last ordered phases). The remaining parts of the instability have a stochastic behavior. At 1.6 mbar, ordered phases are observed during the frequency drop phase (around 1500 s) and during the last ordered regime (after 1900 s). At pressures above 1.8 mbar, the ordered phases are mainly constituted by the last phase before the end of the instability.

In the following, the different phases are discussed with respect to the peak amplitudes.

Long stochastic phase

Figure 4.27 shows the number of detected peaks as a function of their amplitudes during the long stochastic phase for different pressures. The distributions are fitted by a Gaussian function. At 1.4 mbar, it is observed that the number of peaks having small amplitudes is low. Most of the peaks have amplitudes in between 0.008 and 0.012. Above 0.012, the number of peaks is relatively low. At 1.6 mbar, the distribution is slightly different, most of the peaks being gathered between 0.005 and 0.012. However, at higher pressure (1.8 and 2 mbar), the distribution of the peak amplitudes has a more clear Gaussian form. It means that at higher pressure, where the stochastic regime is dominant, the distribution of the peak amplitudes has a perfect Gaussian form.

Frequency drop phase

After this long stochastic regime, the frequency drop regime is observed. This phase

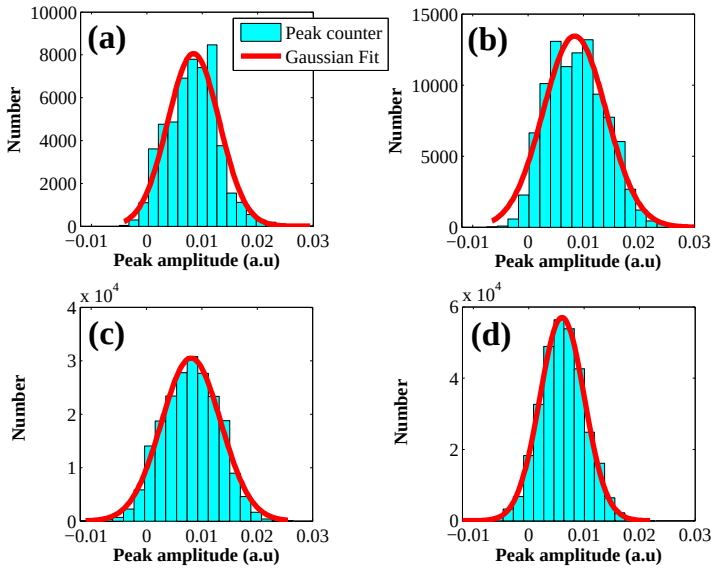

Figure 4.27: Number of peaks as a function of their amplitudes during the long stochastic phase (a) at 1.4 mbar, (b) 1.6 mbar, (c) 1.8 mbar and (d) 2 mbar.

is characterized by a decrease of the signal amplitude in Fig. 4.23 (1.4 mbar) around 1180 s, but by an increase of the signal in Figs. 4.24, 4.25 and 4.26 (1.6, 1.8 and 2 mbar) respectively around 1250, 1400 and 1600 s. The amplitude variation during the transition from the long stochastic phase to the frequency drop phase is measured (except at 1.4 mbar): At 1.6 mbar, the amplitude variation between these two phases is the bigger, and corresponds to the larger variation of the frequency (factor of 4 between the long stochastic phase frequency and the frequency drop phase) as shown also in Fig. 4.18 (b). The amplitude variation becomes smaller as the pressure increases. A similar behavior is observed on the frequency variation that becomes smaller at 1.8 and 2 mbar (Figs. 4.18 (c) and (d)) with a proportionality factor of respectively 3.3 and 3. After this transition, the frequency drop phase characterized by a three peak pattern is observed.

In Fig. 4.28, the frequency drop phase extracted from Fig. 4.23 is presented (at 1.4 mbar, from 1100 to 1400 s). A part of its electrical signal is shown in Fig. 4.29 where a clear three peak pattern is observed between 1180 and 1220 s. It explains the structure observed in Fig. 4.28 during the same period. The three peak amplitudes slightly vary until 1220 s, then they evolve more stochastically where some additional peaks can also be detected until 1300 s. The frequency drop phase clearly observed at 1.6, 1.8 and 2 mbar are zoomed and shown in Fig. 4.30 (a), (b), and (c), and a part of their

corresponding temporal signals are shown in Fig. 4.30 (d), (e), and (f). Figure 4.30 (a)

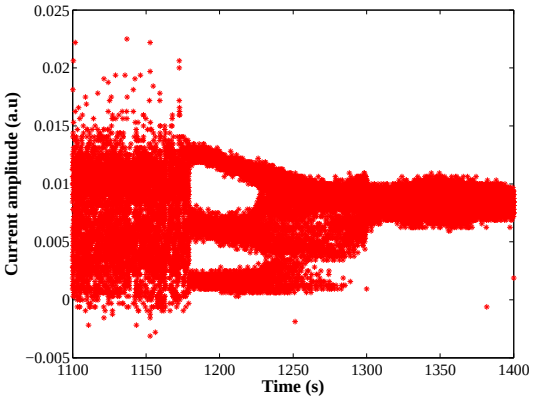

Figure 4.28: Peak detection of the transition phase at 1.4 mbar.

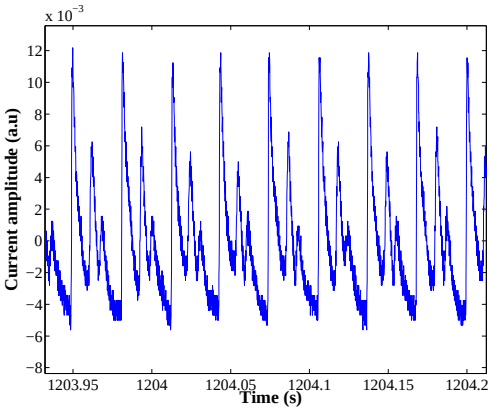

Figure 4.29: Electrical signal of the transition phase at 1.4 mbar.

extracted from Fig. 4.24 (at 1.6 mbar) shows a clear three peak pattern. During the major part of this phase, the electrical signal has a well-ordered behavior. As we know from section 4.2.3, the contribution of the stochastic phases during DPGI increases as a function of the pressure. It is confirmed at 1.8 mbar (Figs. 4.30 (b) and (e)) where the three peak pattern can be guessed but in a more stochastic way. In Fig. 4.30 (b), the two big peaks (Fig. 4.30 (e)) have amplitudes in between 0.02 and 0.03 and are difficult to separate. At 2 mbar, the same pattern is reproduced but is much more stochastic as shown in Figs. 4.30 (c) and (f).

Eye-shape form

Another interesting behavior is the evolution of the peaks in an eye-shape form (Fig. 4.31). This behavior has only been observed at 1.6 mbar, just before the last ordered phase (this electrical signal is extracted from an experiment not presented in this thesis). In Fig. 4.32, a zoom on this behavior is performed. Three peaks are clearly observed and the evolution of two of them form an eye. The peaks forming the eye are labeled as peak 1 and 3. The increase of the amplitude of peak 1 corresponds to the decrease of the amplitude of the peak 3 (2315 s in Fig. 4.32). Then, when the peak 1 reaches its maximum amplitude, it starts to decrease while the peak 3 amplitude behaves in the opposite way (around 2320 s). When the amplitudes of these two peaks become comparable, a short stochastic regime occurs, closing the eye-shape structure (at 2329 s). This phenomenon repeats several times before the last ordered phase appears. The peak 2 corresponds to the constant peak amplitude (around 0.005) during

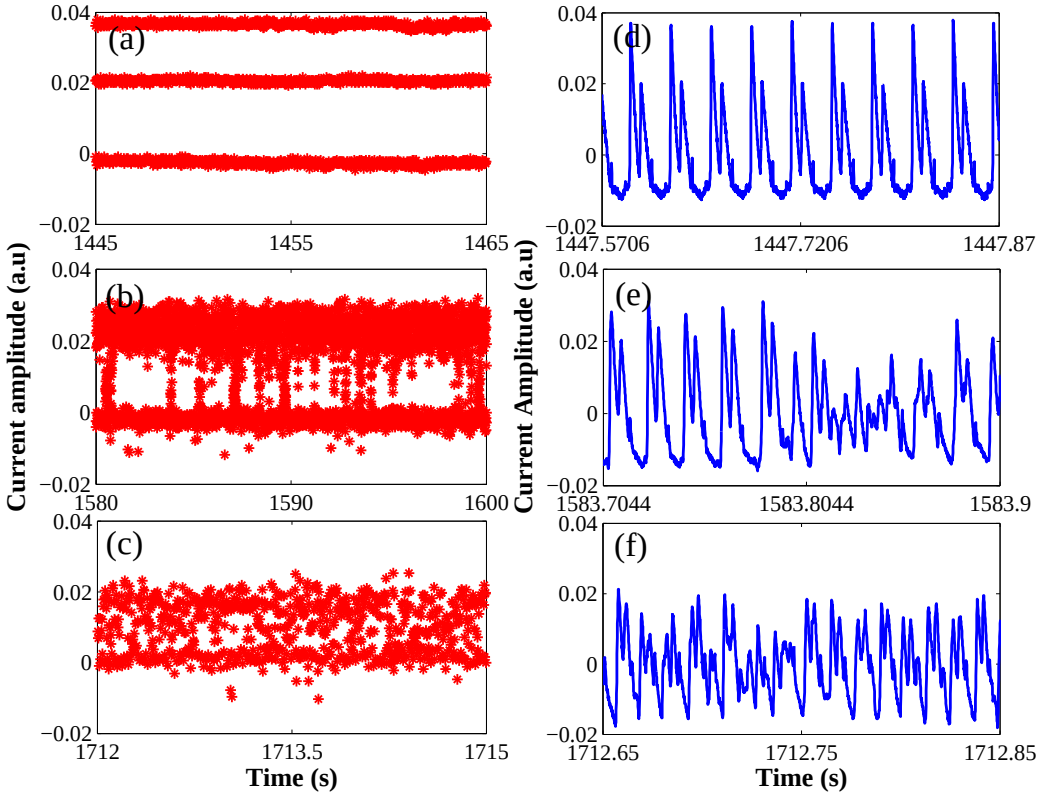

Figure 4.30: Zoom on the peak detection concerning the transition phase (frequency drop) for (a) 1.6 mbar, (b) 1.8 mbar and (c) 2 mbar and their corresponding temporal signals.

the whole duration of this phenomenon except during the short stochastic regime. In order to observe clearly the oscillation form, the electrical signal is shown in Figs. 4.33, 4.34 and 4.35. Figure 4.33 shows the pattern with three peaks, at the starting point of the eye formation where peaks 1 and 3 have almost the same height. Then, in Fig. 4.34 corresponding to the center of the eye-shape structure, a decrease of peak 3 is observed. Figure 4.35 corresponds to the eye-shape closing. When, a short stochastic regime appears around 2329 s. Then, for a short period (0.3 s) two peaks are observed (around 2329.2 s). Afterwards, the same behavior restarts and repeats for several times.

Summary

Thanks to the peak detection method, the evidence of different regimes (ordered and stochastic) can be easier. The distribution of the peak amplitudes has been studied during the long stochastic phase for different pressures (Fig. 4.27). It shows that at

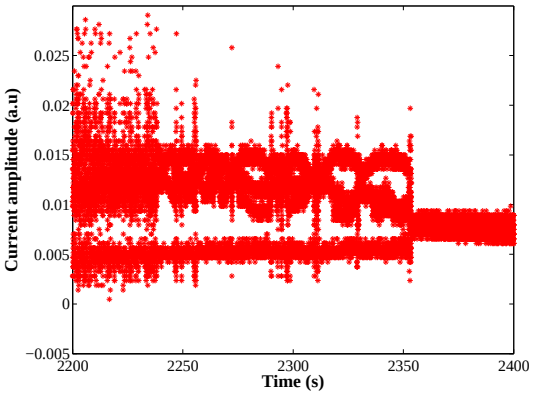

Figure 4.31: The eye-shape peak evolution at 1.6 mbar.

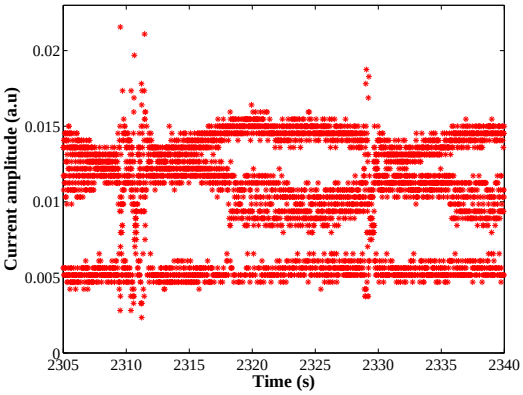

Figure 4.32: A zoom on the eye-shape peak evolution.

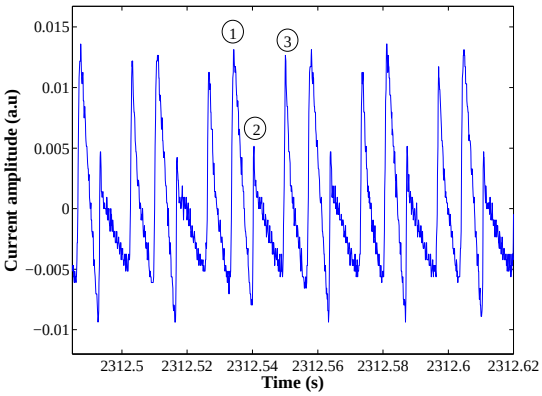

Figure 4.33: Electrical signal at the starting point of the eye-shape formation.

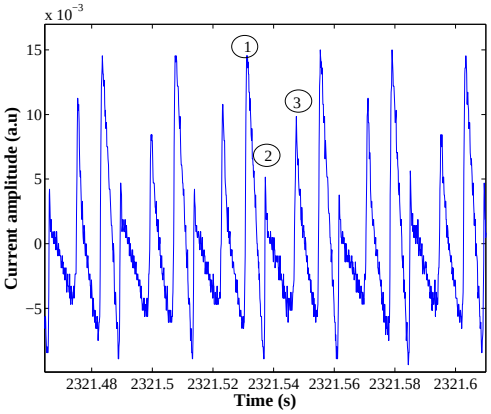

Figure 4.34: Electrical signal at the center of the eye-shape structure.

higher pressure, when the signal is clearly stochastic during its nearly whole duration, the distribution can be fitted by a perfect Gaussian function. Then, the frequency drop phase has been investigated. It is observed a decrease of the amplitude during the transition from the long stochastic phase to the frequency drop phase at 1.4 mbar. While an increase of the signal amplitude has been observed at higher pressures. Amplitude and frequency proportionality is measured during the transition from the long stochastic phase to the frequency drop phase. During the frequency drop phase, a three peak pattern has been noticed (Figs. 4.28, 4.29 and 4.30). As the pressure is increased, the frequency drop phase becomes more stochastic. At 1.6 mbar, an eye-shape form peak evolution has been analyzed .

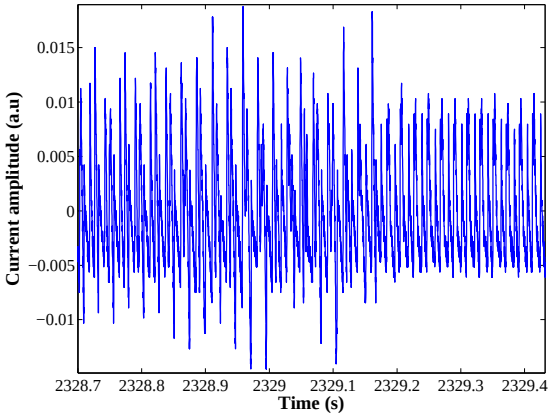

Figure 4.35: Electrical signal at the closing of the eye-shape structure.

4.3 Comparison Krypton / Argon

In this Chapter, the experiments have been performed using krypton as the sputtering gas. Argon is also used in the PKE-Nefedov reactor to study and to compare the instabilities. The sputtering efficiency and the gas phase reactions can be affected by the gas type (ionization energy of krypton 14 eV is lower than the one of argon 15.76 eV) and particularly by the ion mass (83.7u for krypton and 39.9u for argon).

In Figs. 4.36 and 4.37, the DC component of the RF current is presented in krypton and argon plasmas. The decrease of the DC component in the krypton case is faster than in the argon case. It results that the formation kinetics of dust particles is faster in a krypton plasma as also discussed in section 4.2. Some amplitude drops in the electrical signal are observed mostly in the krypton case. They could be due to the fact that higher dust densities are reached in Kr than in Ar.

In Figs. 4.38 and 4.39, the AC component is also presented. The first difference is the oscillation amplitude which is twice as high for krypton as for argon. Different phases are evidenced in both cases, but discrepancies exist in the frequency evolution as shown by the calculated Fourier spectrograms in Figs. 4.40 and 4.41. In Kr, the frequency increases very quickly and then a chaotic phase appears and lasts for a long time as shown in section 4.2.2. During this phase, the dominant frequencies can still be detected. Close to the end of the instability, the oscillation becomes more regular and the frequency starts to increase. Concerning the Ar plasma, the instability follows globally the same scheme: several regular phases followed by a chaotic regime and another more regular phase at the end. However the details of these regimes are different than in Kr. The fast increase is not observed before the chaotic regime and at

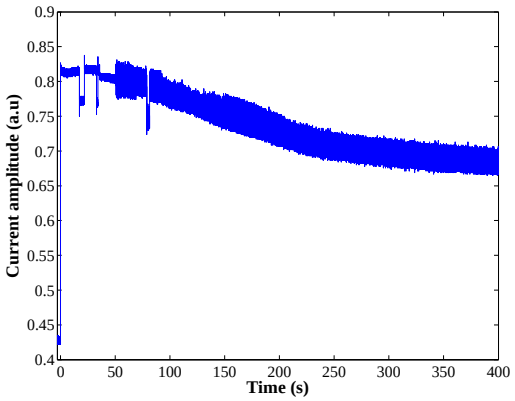

Figure 4.36: Amplitude of the RF current (DC component) for a Krypton plasma.

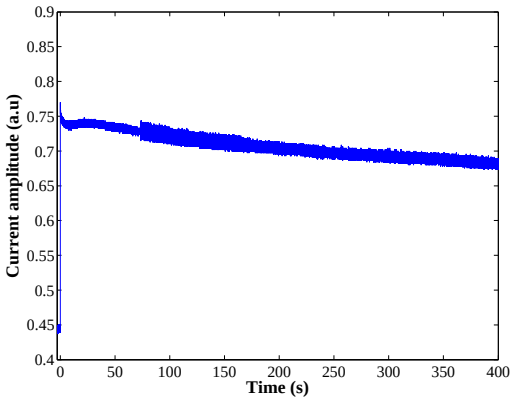

Figure 4.37: Amplitude of the RF current (DC component) for an Argon plasma.

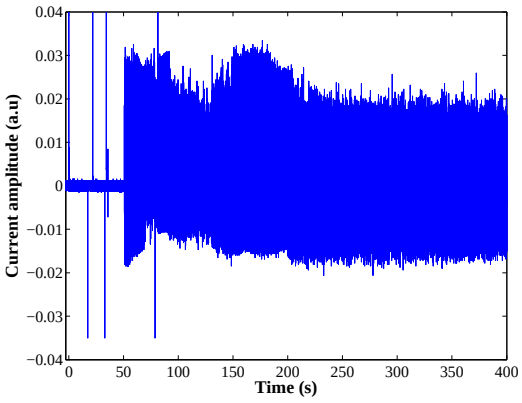

Figure 4.38: Amplitude of the RF current (AC component) for a Krypton plasma.

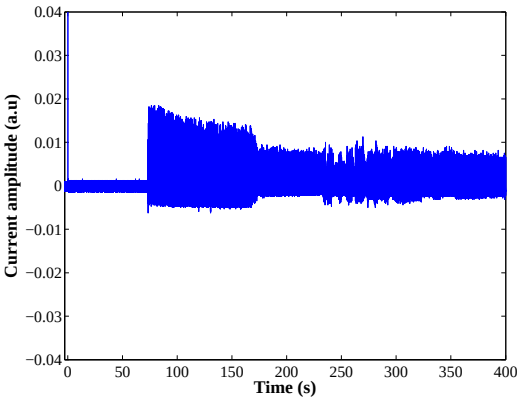

Figure 4.39: Amplitude of the RF current (AC component) for an Argon plasma.

the end a frequency decrease is observed instead of an increase as in Kr. It can also be noted that the typical frequencies are globally lower in Ar than in Kr (for instance, the final frequency in krypton is around 150 Hz, while is around 15 Hz in argon). The dust cloud can be easily observed in Ar by using laser light scattering and classical cameras. In Kr, while electrical measurements clearly attest the growth of dust particles, the dust cloud cannot be observed by our imaging system.

If we summarize all the differences between electrical measurements in Kr and Ar, we observed in the case of Kr: more drops, a higher and faster current decrease, a higher amplitude oscillation, and higher frequencies. All these observations are consistent with

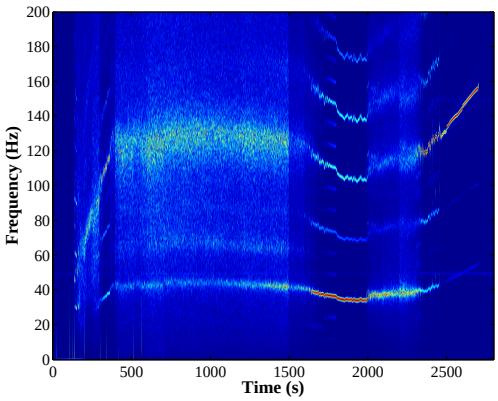

Figure 4.40: Fourier spectrogram of the AC component for a Krypton plasma.

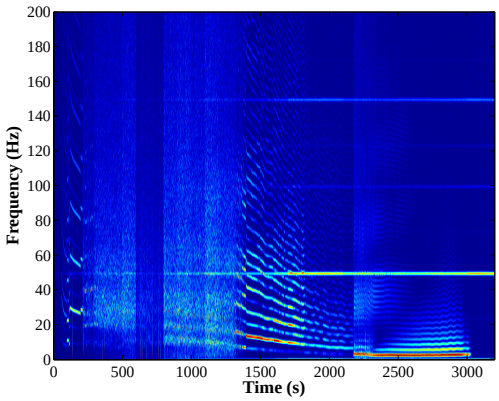

Figure 4.41: Fourier spectrogram of the AC component for an Argon plasma.

a higher dust density and a smaller dust size in the case of Kr.

4.4 Conclusion

In this Chapter, electrical measurements performed on the PKE-Nefedov are discussed. Dust particle growth instabilities are investigated by recording the amplitude of the discharge current. Different instability regimes are evidenced, from the first ordered phases to the last ordered phase, passing through stochastic phases. The electrical signal form and the frequency evolution are studied in each phase during the evolution of the instability. In general, the instability starts with 4 ordered phases followed by an increase of the frequency in a more stochastic way. Then, a long stochastic phase with fast and erratic frequency evolution (within a rather small value range) is observed. After this long stochastic phase, the frequency drops to a lower level constituted of a well-organized part and a more stochastic part. The instability ends with an ordered phase characterized by a high frequency. After the description of the different phases, an investigation is performed concerning the instability parameters as a function of the pressure. It appears that the higher the pressure, the shorter the appearance time, the longer the duration and the higher the frequencies of DPGI. These results are consistent with the observation on the DC component of the electrical signals that at high pressure the growth kinetics is faster, the dust density is higher and the dust size is smaller. Indeed, a fast growth kinetics and a high dust density lead to a rapid appearance of DPGI. The relation between different instability parameters is emphasized. It is shown that the knowledge of the appearance time is enough for the experimenters to

know rather accurately the instability evolution. In order to emphasize DPGI phases, the electrical signal is analyzed through the variation of its oscillation amplitude as a function of the pressure. The distribution of the peak amplitudes is studied during the long stochastic phase showing that at higher pressure, the distribution can be fitted by a perfect Gaussian function. Then, the frequency drop is investigated showing a three peak evolution that becomes more stochastic at high pressure. At the end, a comparison of the instability evolution is performed between argon and krypton plasmas. The evolution of the frequencies is quite different in both case. Due to the mass discrepancy between argon and krypton, the sputtering efficiency is certainly different and the gas phase reactions leading to the dust particle growth can be modified. The decrease of the DC component in the krypton case is faster than in the argon case. It results that the formation kinetics of dust particles is faster in a krypton plasma. Therefore, the frequency evolution during DPGI is also affected.

4.5 French Summary

Dans ce chapitre , les mesures électriques effectuées sur PKE- Nefedov sont discutées. Les instabilités de croissance des poudres sont étudiées à l'aide de l'amplitude du courant de décharge. Différentes phases sont ainsi mises en évidence par l'étude de la forme du signal électrique et de l'évolution de la fréquence durant les instabilités. En général, l'instabilité commence par quatre phases ordonnées suivies par une augmentation de la fréquence d'une manière plus stochastique. Ensuite, on observe une longue phase stochastique avec une évolution erratique et rapide de la fréquence. Après cette phase, la fréquence chute et l'instabilité suit un régime constitué d'une partie organisée et d'une autre plus stochastique. L'instabilité se termine par une phase ordonnée caractérisée par une fréquence élevée.

Après la description des différentes phases, l'étude porte sur l'évolution des différents paramètres de l'instabilité en fonction de la pression. Lorsque la pression est élevée, le temps d'apparition des instabilités est court, leur durée est longue, et les fréquences caractéristiques sont plus grandes. Ces résultats sont cohérents avec l'observation de la composante continue (DC) des signaux électriques confirmant qu'à haute pression, la cinétique de croissance des poudres est plus rapide, leur densité est plus élevé et leur taille plus petite. En effet, une cinétique de croissance rapide et une forte densité de poudres conduisent à une apparition rapide des instabilités. La relation entre les différents paramètres de l'instabilité est également étudiée.

Afin d'étudier plus précisément les différentes phases, le signal électrique est analysé

par le biais de la variation de son amplitude d'oscillation en fonction de la pression. La répartition des amplitudes est étudiée durant la longue phase stochastique. Il apparaît ainsi qu'à haute pression, la distribution des amplitudes à la forme d'une fonction gaussienne. La phase de chute de la fréquence est étudiée et se traduit par une structure à trois pics dont l'amplitude devient de plus en plus stochastique à haute pression.

Une comparaison de l'évolution de l'instabilité est effectuée entre l'argon et le krypton. L'évolution des fréquences est trés différente dans les deux cas. En raison de la différence de masse entre l'argon et le krypton, le taux de pulvérisation est certainement différent et les réactions en phase gazeuse conduisant à la croissance des poudres sont sans doute modifiées. La diminution de la composante continue du signal électrique dans le cas du krypton est plus rapide que dans le cas de l'argon. Il en résulte que la cinétique de formation des poudres est plus rapide dans un plasma de krypton. L'évolution de la fréquence durant les instabilités est également affectée. En krypton, la taille des poudres est plus petite qu'en argon et leur densité plus élevée. Cela entraîne que la fréquence des instabilités est globalement plus élevée en krypton.

Chapter 5

High speed imaging of dust particle growth instabilities

In the previous Chapter, dust particle growth instabilities (DPGI) have been analyzed by using an electrical diagnostic. The evolution of the phases and frequencies have been studied. In this Chapter, a high speed camera is used to study the evolution of the plasma glow during the beginning of dust particle growth instabilities, and to characterize the existence of small regions with an enhanced emission (plasma spheroids) that appear during and just after DPGI (when the plasma is in a "stable" state). Characterization of plasma spheroids that appear in the center of the discharge [123] and/or at the vicinity of the electrodes [75, 124] is performed using argon or krypton. During our experiments, it is impossible to observe these spheroids without using a high speed camera due to their small size and their high speed motions. Several types of plasma spheroid behaviors are presented in this Chapter.

In argon plasmas:

1) Single spheroid rotation along the circumference of the electrode.

2) Complex appearance and disappearance of spheroids close to the electrodes.

In krypton plasmas:

1) Splitting of spheroids at the vicinity of the electrode.

2) Interaction between spheroids in the discharge center (up and down motions, splitting and merging of spheroids).

It can be noted that the existence of localized structures with an enhanced emission is encountered in many different types of plasmas with certainly different physical mechanisms driving their creation and dynamics. Indeed, these regions are well known in magnetized plasmas, especially in the context of fusion reactors. In this field they

are called blobs and are involved in transport phenomena explaining their current intense study, both experimentally and theoretically, by many authors [125–129]. In atmospheric pressure plasmas, especially in dielectric barrier discharges, these regions are called filaments and they have been shown recently to be able to interact with each other, showing the merging or the splitting of these regions [130–132]. Similar interactions like the merging or the splitting of regions of enhanced plasma emission were also observed very recently in plasma jets where plasma streams with a comet-like shape are produced [133–135]. In these works, the well-defined comet head (sometimes called plasma bullet) has been shown to be able to split into two parts, and the merging of two bullets into a single one was also reported. In experimental conditions closer to our study, we can report on relatively similar observations by Schulze *et al.* [136] where moving plasmoids were observed.

5.1 Beginning of the instability

A high speed camera is used to observe the variation of the plasma luminosity during DPGI. The camera is positioned in front of the reactor as shown in section 3.2.2. The experiments are performed using argon as the sputtering gas. As a first step into

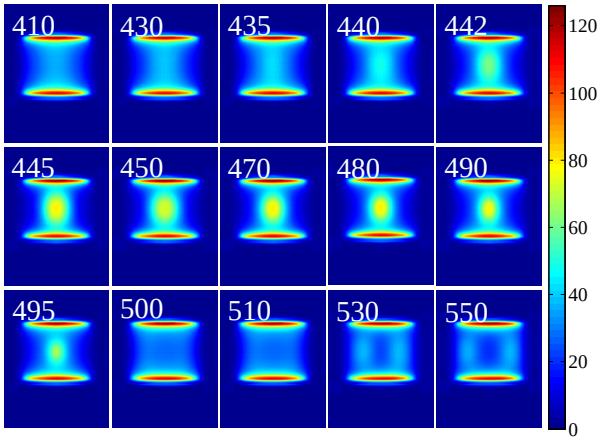

Figure 5.1: Plasma glow variation during dust particle growth instabilities.

the optical study of the instability, the beginning of the instability is investigated. The camera recording is fixed at 5000 fps and is triggered by the discharge current amplitude measured in AC. Indeed, the amplitude increase at the beginning of the instability can be easily detected as shown in Chapter 4 (for example in Figs. 4.38 and 4.39). Figure 5.1 represents the evolution of the plasma luminosity at the beginning of the DPGI. False

colors have been used in order to enhance the luminosity variations. In each image, the two parallel horizontal regions are the pre-sheaths of the discharge. On the left hand side of each image, the tagged number represents the concerned frame. At frame 410, the plasma is stable as the required dust density to trigger the instability is still not reached. Then, at frame 435, the instability beginning is visible in the center of the discharge. The luminosity in the center increases gradually until frame 470. Then, it decreases and finally disappears at frame 500. At this moment, bright regions appear at the edges of the plasma bulk as observed at frame 530. This phenomenon repeats several times during the first instability instants.

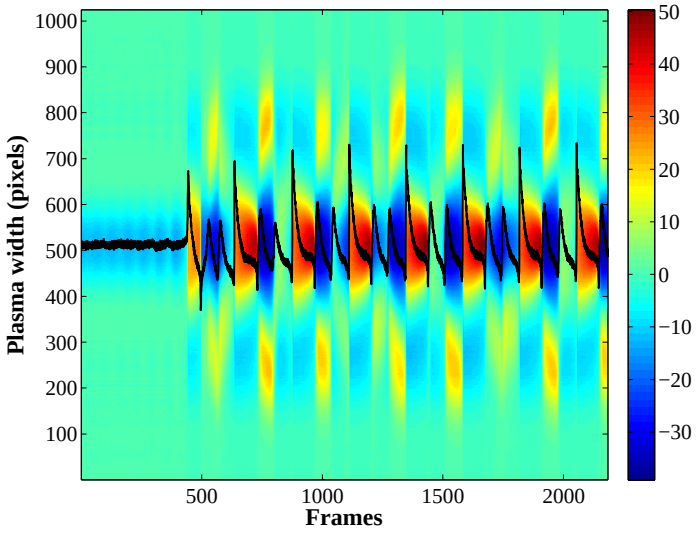

Figure 5.2: Plasma glow profile along the horizontal axis in between the two electrodes during DPGI. Correlation with the amplitude of the discharge current.

In order to better characterize this phenomenon, 2183 frames (436.6 ms) are processed during a movie recorded at 5000 fps. In Fig. 5.2, a line profile (parallel to the electrodes and passing through the discharge center) is extracted. The contrast is enhanced by subtracting a temporal average value. It represents the beginning of the DPGI as a function of time. The time is represented by the number of frames on the x-axis, and the plasma width (in pixels) is presented on the y-axis. The instability beginning is visible around frame 435 where an increase of the luminosity is observed in the center of the discharge (around 500 on the y-axis) as also shown in Fig. 5.1. Then, the bright regions appear at the edges of the plasma at frame 530 (around 200 and 800 on the y-axis). At this stage, the luminosity of the central part of the plasma bulk is at its lowest level. This phenomenon repeats several times at the beginning

of each experiment. A correlation between optical and electrical measurements at the beginning of DPGI is also presented in Fig. 5.2. The superimposed electrical signal shows the first phase of the instability discussed in Chapter 4 section 4.1.1, where the main pattern is constituted of three peaks. Here, the big amplitude peak seems to correspond to the rise of the luminosity in the center of the discharge, while the small amplitude peaks seem to be related to the bright regions appearing at the edge of the plasma bulk.

5.2 Single spheroid

In this section, a phenomenon is extracted from a video recorded at 10000 fps where a single spheroid is observed rotating along the circumference of the top electrode after DPGI. The motion of the spheroid is followed as shown in Fig. 5.3. Due to the angle of view, the top and bottom electrodes appear a little bit tilted. It allows to discriminate plasma spheroid location (foreground/background). At frames 120 and 209, the spheroid is in the foreground whereas at frames 365 and 460 it is in the background. In the present case, the spheroid is rotating anti-clockwise. A line profile close to the vicinity of the electrode is extracted. The profile is averaged over several lines in order to distinguish the spheroid position. After image processing, its rotating trajectory is represented in Fig. 5.4. The spheroid performs an electrode revolution in about 570 frames, corresponding to a rotation frequency of 17 Hz and a typical speed of about 2 $m{\cdot}s^{-1}$.

This experiment has been made with a fixed discharge power and pressure. In order to observe the influence of the discharge power on the spheroid behavior, a new experiment is performed. When a single spheroid regularly rotating around the electrode is observed, the RF power is increased and movies are taken for each value. In Fig. 5.5, the trajectory of the spheroid as a function of the discharge power is presented. All reconstructed trajectories are then compared by taking the same reference frame as the starting point. A zoom is performed on the trajectories after 2 complete rotations around the electrode and is presented on the upper left insert. A clear comparison can be performed between 3.3 and 4 W, the rotation speed slightly increasing from 7.3 $m{\cdot}s^{-1}$ at 3.3 W, to 7.8 $m{\cdot}s^{-1}$ at 4 W.

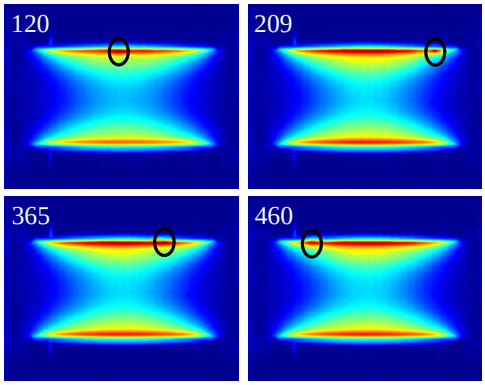

Figure 5.3: A single spheroid rotating around the top electrode.

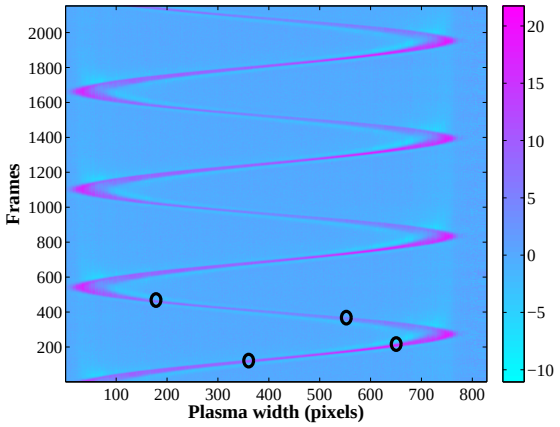

Figure 5.4: Line profile of the plasma glow in front of the top electrode. Positions of the spheroid from Fig. 5.3.

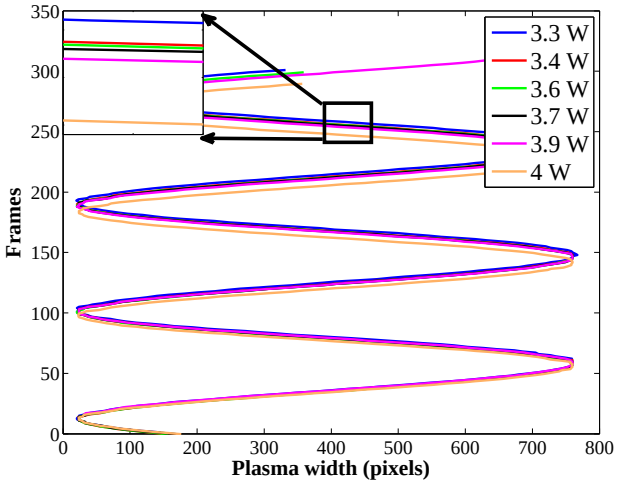

Figure 5.5: Trajectory of a spheroid as a function of discharge power.

5.3 Complex appearance and disappearance of spheroids close to the electrodes

The experiments presented in this section are performed at a pressure of 1.6 mbar with a RF power of about 3 W when plasma spheroids are observed during DPGI. Figure 5.6 shows an image where six plasma spheroids can be clearly evidenced in front of each electrode (two of them are marked with an arrow). In order to reveal more precisely this phenomenon, the regions (800 × 110 pixels) in the close vicinity of both electrodes

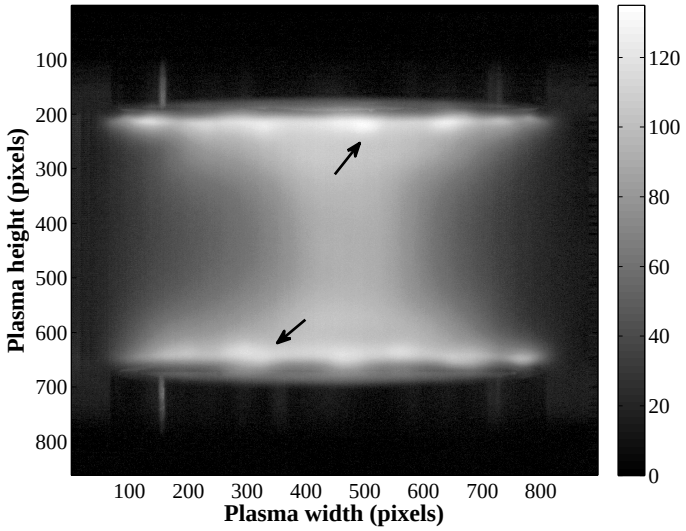

Figure 5.6: Plasma glow and detection of 6 spheroids in front of both electrodes. Two plasma spheroids are marked with an arrow.

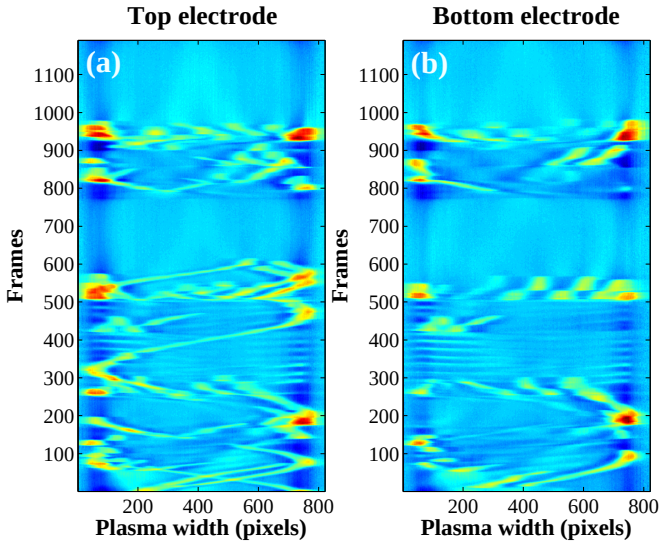

Figure 5.7: Line profile of plasma glow in front of (a) top and (b) bottom electrodes during 1190 frames. Appearance and disappearance of spheroids during DPGI (brightness variation in false colors from dark blue to red).

are extracted from the movie. Plasma luminosity is averaged on the height of each of these regions. Thus, each frame gives two lines. In Fig. 5.7, 1190 frames (170 ms) are processed during a movie recorded at 7000 fps. Three major regimes related to the

plasma spheroids can be evidenced:

- Regime I: No spheroid is observed.

- Regime II: Stochastic appearance and disappearance of spheroids characterized by bright spots.

- Regime III: Persistence of some spheroids that enter in a rotating motion along the circumference of the electrode. This regime corresponds to long spheroid paths visible in Fig. 5.7, mainly at the vicinity of the top electrode (around frame 400). This type of behavior can also be evidenced after DPGI, with many spheroids rotating close to the electrodes. This behavior with a single spheroid was presented in Fig. 5.4.

The last two regimes are not so strongly separated due to the fact that during the stochastic phase some short spheroid paths exist. These three regimes do not appear always simultaneously in front of both electrodes. In Fig. 5.7, from frame 0 to 100, regime III is observed in front of each electrode but is clearer close to the top electrode. This regime is followed by regime II until frame 300. Between frames 300 and 420, the regimes in front of each electrode are not similar. Indeed, in Fig. 5.7 (a) we observe regime III (with only one spheroid) while regime I is evidenced in Fig. 5.7 (b). Two other regimes I are clearly observed simultaneously in both figures between frames 550 and 770, and later after frame 920. The other parts of Fig. 5.7 are mainly characterized by regime II and very short spheroid paths.

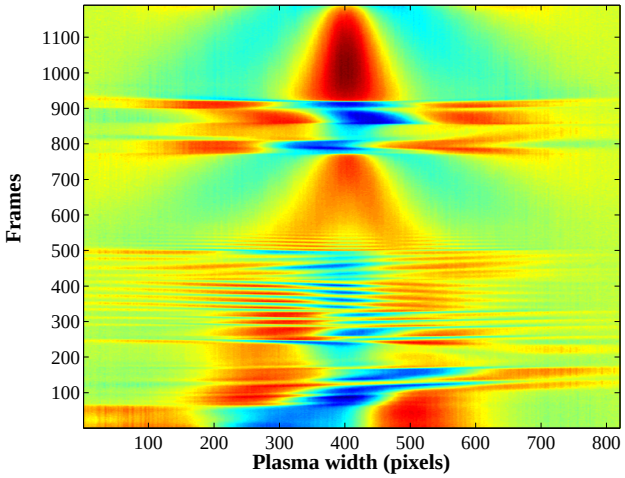

Figure 5.8: Plasma glow profile along the horizontal axis in between the two electrodes during DPGI (in false colors from dark blue to red).

In order to correlate the observed regimes with a global observation of DPGI, the evolution of the central part of the plasma glow is analyzed. Figure 5.8 is obtained by

taking the plasma glow profile along the horizontal axis in between the two electrodes for each frame. The vertical axis of symmetry of the plasma is around 400 on the x-axis. It clearly appears that during DPGI the plasma luminosity can strongly vary, not only in the center, but also toward plasma, and electrode, edges.

By comparing Figs. 5.7 and 5.8, several correlations can be made. When the plasma glow changes are mainly concentrated near the discharge center (between frames 550 and 770 or 920 and 1190 in Fig. 5.8), it corresponds principally to regime I near the electrodes but also to a lesser extent, to some short spheroid paths (Fig. 5.7). When the plasma behavior in Fig. 5.8 is much more stochastic with off-centered changes (between 0 and 300 or 770 and 920), it corresponds in Fig. 5.7 either to the stochastic appearance of the spheroids (regime II), or to their rotation (regime III). It confirms that regimes II and III can be mixed up due to the existence of some spheroid paths during the stochastic phase. The phase in between frames 300 and 420 in Fig. 5.8 is characterized by very fast changes in the plasma emission. It explains the striations observed in Fig. 5.7 at the same time.

Another behavior extracted from a video recorded at 10000 fps has also been observed. The spheroids are present all the time close to the top electrode, while several regimes are observed near the bottom electrode. These results are shown in Fig. 5.9. The paths of the plasma spheroids are clearly observed at the vicinity of the top electrode in Fig. 5.9 (a). In the beginning, three rotating spheroids (regime III) are detected and keep turning for several rounds at a speed of about 4 $m{\cdot}s^{-1}$. At frame 720 this ordered regime is interrupted by a stochastic phase with many spheroids appearing and disappearing in a fast way (regime II). This regime stops at frame 1000 where the three spheroid system is restored again until a second stochastic phase at frame 1400. At frame 1700, the regime III (rotating spheroid) is back but the number of spheroids is reduced to one, turning around the top electrode. A second spheroid appears at frame 1900 till the end of the video recording. Concerning the bottom electrode in Fig. 5.9 (b), the spheroids just appear during the stochastic phase. When a nice rotation regime is observed near the top electrode, nothing is observed close to the bottom one, except at the end (around frame 2200). As for the previous experiment, a comparison is performed between the phenomena occurring close to both electrodes and the luminosity of the middle region of the plasma (Fig. 5.10). Globally, same conclusions than in Figs. 5.7 and 5.8 can be drawn. Slow and central changes in the plasma luminosity (for example, between frames 1000 and 1400) correspond to either no spheroid (Fig. 5.9 (b)) or rotating spheroids (Fig. 5.9 (a)). Fast and off-centered plasma changes (for example, between frames 720 and 1000) are related to stochastic regimes for the spheroids.

In the two studied cases, different regimes have been clearly identified and correlated with the variation of the plasma luminosity in the discharge central part. It is found that when the plasma changes are mainly located in the close discharge center, regime I (no spheroid) or III (rotating spheroids) is observed in front of the electrodes. Regime II (stochastic appearance and disappearance of the spheroids) appears when plasma changes in between the electrodes are fast and more off-centered. The appearance of these plasma spheroids at the vicinity of the electrodes seems to be correlated with DPGI as they have been observed only during or just after DPGI. In this section, we focused on the stochastic appearance of the spheroids occurring only during DPGI. When plasma spheroids are observed after DPGI, only regime III, with spheroids rotating regularly at a few $m{\cdot}s^{-1}$, seems to exist as shown in section 5.2. Plasma spheroids are observed along the periphery of the electrodes indicating that the guard ring surrounding the electrode can play a role in this phenomenon. However, these spheroids have always been observed in dusty plasma conditions with a high density of sub-micron dust particles and a quite high pressure. We can assume that the strong disturbance induced by the dust particle presence can trigger the spheroid appearance or rotation. Thus, this behavior occurs preferentially in regions where electrical inhomogeneities exist as close to the guard rings. A similar phenomenon has been described in [136]. In this last case, the disturbance of the plasma equilibrium is not induced by dust particles

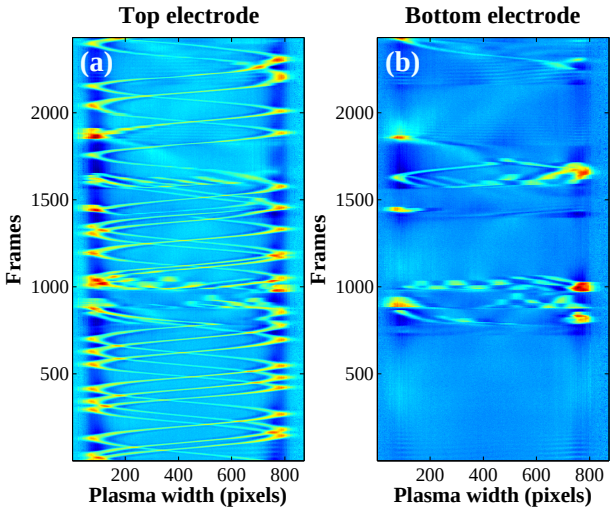

Figure 5.9: Line profile of plasma glow in front of (a) top and (b) bottom electrodes during 2431 frames. Appearance and disappearance of spheroids during DPGI (brightness variation in false colors from dark blue to red).

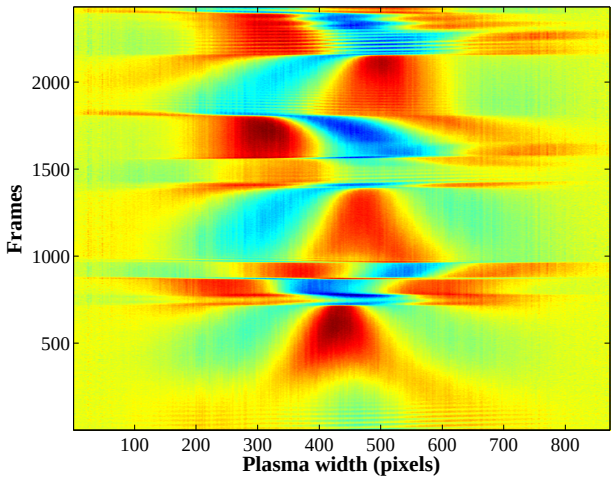

Figure 5.10: Plasma glow profile along the horizontal axis in between the two electrodes during DPGI (in false colors from dark blue to red).

but by the introduction of a glass tube into the discharge.

5.4 Splitting of spheroids at the vicinity of the electrode

In this section, the behavior of a plasma spheroid at the vicinity of the electrode is studied in a krypton plasma. Figure 5.11 shows a line profile close to the electrode extracted from a movie at 16000 fps. At frame 236, the appearance of a spheroid is evidenced (encircled in Fig. 5.11). In the following frame, this spheroid is splitting into two parts. These two new spheroids are observed on the x-axis respectively at 300 and 370. Then, at frame 238, the spheroid observed at x=300 gives birth to another spheroid at x=250. This phenomenon repeats several times and gives birth to new spheroids at the vicinity of the electrode. Here, four bright spheroids (at x=120, 210, 300 and 370) are observed and two others less bright are detected at the edge of the plasma bulk (at x=90 and 410 respectively). The four main spheroids do not move during several frames (their position stays unchanged). Around frame 250, they start rotating along the electrode. It is observed that the rotation of the spheroids along the electrode begins simultaneously. The two spheroids (positions 120 and 210) move towards the left part of the electrode, while the other two spheroids (positions 300 and 370) move towards the right hand side of the electrode.

In Fig. 5.12, another movie at 16000 fps is analyzed and a line profile is extracted. At frame 7978, two main spheroids are evidenced at positions 160 and 340 on the x-

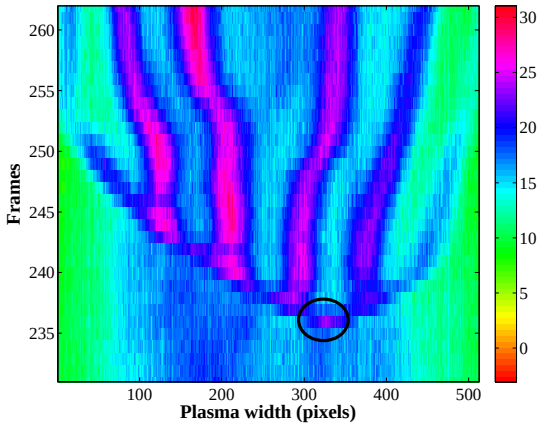

Figure 5.11: Line profile of plasma glow at the vicinity of the electrode showing the appearance of a spheroid and then its splitting (16000 fps).

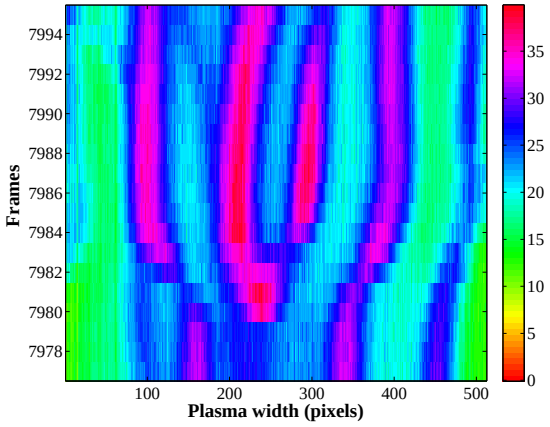

Figure 5.12: Line profile of plasma glow at the vicinity of the electrode showing spheroid appearances and their trajectories (16000 fps).

axis. The birth of a new spheroid is detected at frame 7980 (240 on the x-axis). It is clearly observed that this new spheroid pushes away the two other spheroids moving respectively from 160 to 100 and from 340 to 395. Then, at frame 7983, the new spheroid is split into two in the same way than in Fig. 5.11.

In this section, the splitting behavior of a spheroid close to the electrode is studied in a krypton plasma. Then, the influence of a new spheroid on the trajectory of other spheroids is investigated. These observations open the question on the origin of the physical phenomena that trigger the splitting of spheroids and the interaction in between them. In the following section, interaction between spheroids in the plasma center will be investigated.

5.5 Interaction between spheroids in the discharge center

When krypton is used as the sputtering gas, spheroids can be observed across the entire discharge, unlike in argon where they are mainly detected at the vicinity of the electrodes. Due to the mass discrepancy in between argon and krypton, the sputtering efficiency is certainly different and the gas phase reactions leading to the dust particle growth can be modified. It leads to slightly different characteristics for DPGI as detailed in Chapter 4.

In this section, the interaction between spheroids in the discharge center is investigated. In Fig. 5.13, a typical experiment in a krypton plasma is shown with four

frames from a movie taken at 8000 fps. The spheroids come usually from the electrode (or sheath) regions and propagate towards the plasma bulk. They have a comet-like shape, their head being brighter than their tail. Some of them seem to stay attached to their place of birth thanks to this tail, while others enter the plasma center. Most of the displacements are in the vertical plane where plasma spheroids can form chain-like structures as on the left hand side of frame 73. Horizontal motions are also observed but on shorter distances.

In the plasma center, plasma spheroids experience different motions and interactions:

- Up and down motions.
- Merging and splitting.
- Combined behaviors.

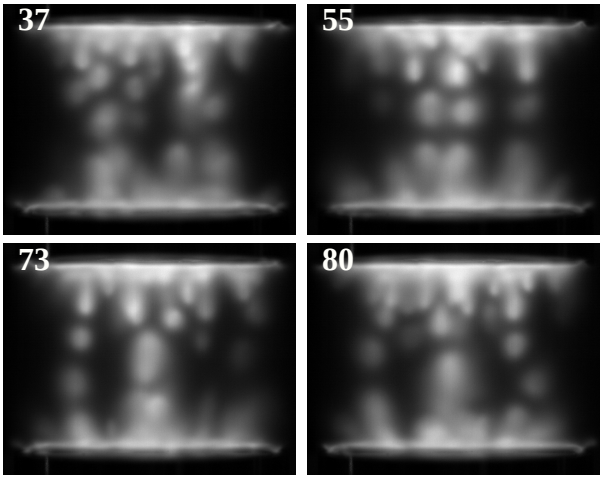

Figure 5.13: Plasma spheroids in the plasma bulk. Well-defined regions with an enhanced emission are clearly observed in between the electrodes (dark regions on the top and bottom separated by 3 cm).

5.5.1 Up and down motions

In order to better observe the interaction between the spheroids, another video taken at 16000 fps (60 μs) has been recorded. This movie also corresponds to a slightly less stochastic experiment where the number of interacting spheroids is reduced compared with the case in Fig. 5.13. It allows an easier image analysis and limit the number of interacting spheroids, thus the interaction between two isolated spheroids can be investigated. The complex motions of the plasma spheroids are evidenced in the zoom

shown in Fig. 5.14. The comet-like shape is very well evidenced in image 3552, where two plasma spheroids are getting closer. In 3555 and 3558 the upper spheroid comes off its tail and the comet head is clearly directed towards the lower spheroid. In 3564 the comet head changes its direction when the lower spheroid disappears and a new one appears on the top of the frame. The central spheroid is now going up until frame 3573. Then, when the upper spheroid disappears and a new one emerges from the bottom, a switch in the central spheroid direction occurs.

This behavior can be more easily identified by using the column profile during the interaction between the spheroids (obtained by taking the plasma glow profile along the vertical axis of the discharge). In Fig. 5.15, a column profile of all sequence frames is shown. To compensate the slight horizontal motion of the spheroids, the profile is averaged over several columns around the interaction location. It clearly shows the down-up-down motion of the central plasma spheroid as a function of the appearance of other spheroids on the top or bottom. It can also be observed that the top and bottom spheroids go back towards the electrode before disappearing. The central spheroid seems to follow them, and it gives the impression that it is just a global motion of all spheroids. In fact, an attraction between the spheroids can better explain the observed behavior. Indeed, a drastic reversal of the comet head position is detected when the top or bottom spheroid enters the plasma. For example, in frames 3561-3567 of Figs. 5.14 and 5.15, the change of the maximum intensity position of the central spheroid is clearly observed. The maximum is clearly on the top of the central spheroid

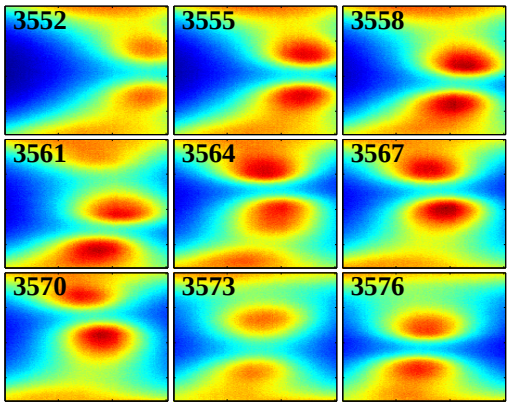

Figure 5.14: Interaction between plasma spheroids leading to the up and down motion of the central spheroid. The central spheroid moves in the direction of the other spheroids. Frames from a movie taken at 16000 fps and presented in false colors from dark blue to red. Each image is about 2.3 cm height and 1 cm width.

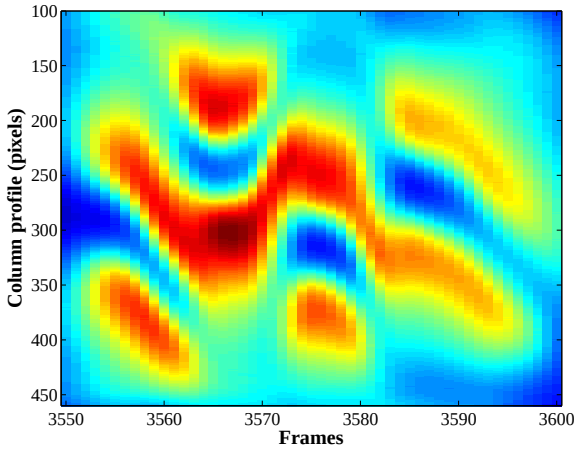

Figure 5.15: Column profile (averaged over several columns) of all frames.

when the top spheroid is on its way towards the center. This behavior confirms that an interaction really exists in between the spheroids and that the observed motions are not only related to a global plasma change affecting all spheroids.

5.5.2 Merging and splitting

Although interaction between plasma spheroids can be guessed from Figs. 5.13, 5.14 and 5.15, a clear evidence is brought to the fore by observing the merging and/or the splitting of the plasma spheroids. These phenomena are shown in Fig. 5.16, where both merging and splitting are observed during a single sequence. These zoomed frames have been extracted from a movie at 16000 fps. Two clear spheroids are observed on the top and bottom of frame 78 and they are getting closer, approaching the image center up to frame 81. At this stage the merging of the two spheroids starts and continues in frame 82. In the following frame, a single spheroid is observed with diffuse connections to the previous spheroid locations. From frame 84 up to 90, the single spheroid is nearly completely disconnected from the top and bottom parts of the frames. In frame 91 it seems that connections with top and bottom parts are activated again and the splitting starts up to frame 95 where two spheroids are again obtained. This behavior is better evidenced by using the same technique as the one shown in Fig. 5.15. The column profile in Fig. 5.17 really brings to the fore this merging-splitting sequence. It can also be observed that the two spheroids created after the splitting appear brighter, which was observed in many splitting cases. This observation and the fact that the splitting phenomenon often occurs close to the horizontal axis of symmetry of the

discharge (around 260 on the y-axis of Fig. 5.17) are currently under investigation. This symmetry is less marked when looking at Fig. 5.13, where interactions also appear out of the horizontal symmetry plane.

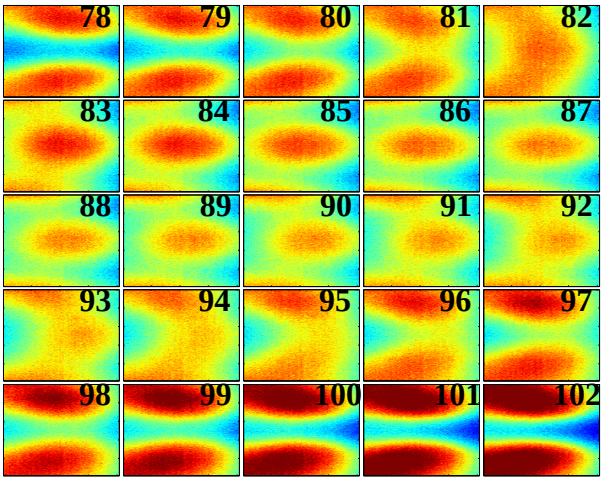

Figure 5.16: Merging of two plasma spheroids quickly followed by the splitting of the newly constituted spheroid. These zoomed frames are extracted from a movie at 16000 fps and are represented in false colors. Each image is about 1.6 cm height and 0.5 cm width.

Although getting consecutively both the merging and the splitting is quite unusual and difficult to observe, an isolated merging or splitting is more commonly encountered. Experimental proofs of these behaviors are presented in Fig. 5.18 with a splitting in (a) and a merging in (b) obtained during a movie at 16000 fps. In Fig. 5.18 (a), a spheroid at frame 5588 is split into two and these two new spheroids are brighter than the initial spheroid. In the case of merging (Fig. 5.18 (b)), the luminosity modification is not clear. The merging process is studied finely, in order to verify that the two spheroids are approaching and are merging into a single spheroid. The new spheroid resulting from the merging process is always observed at mid-distance of the two original spheroids (Fig. 5.17 from frame 75 to 85 and in Fig. 5.18 (b)). It means that a real merging process occurs between the spheroids and it is not due to the disappearance of one of them.

5.5.3 Combined behaviors

In Fig. 5.19, a movie recorded at 16000 fps shows several behaviors a spheroid can follow: its appearance from the top electrode vicinity, up and down motions and the splitting

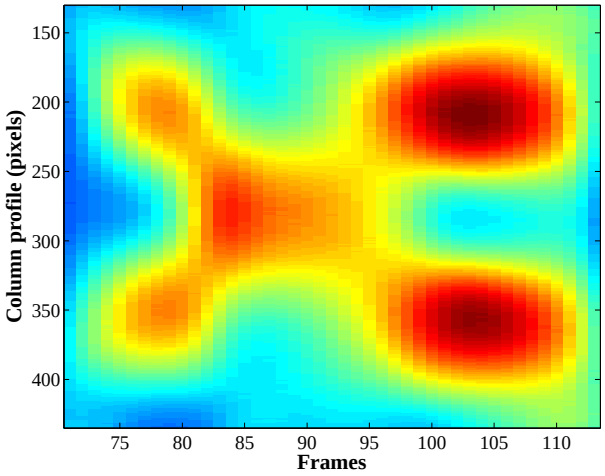

Figure 5.17: Column profile (averaged over several columns) of all frames.

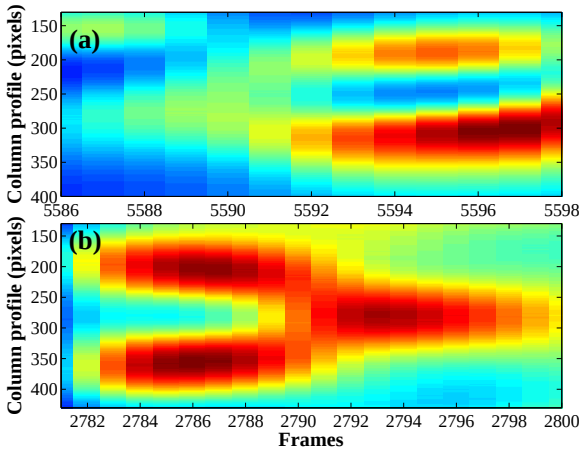

Figure 5.18: (a) Splitting and (b) merging of plasma spheroids. Column profiles (averaged over several columns) in false colors from dark blue to red.

into two. At frame 5, a spheroid appears at the top part of the discharge. It becomes brighter and bigger up to frame 10. It moves toward the bottom electrode as shown between frames 10 and 15. Then, at frame 16 a modification of the spheroid direction is evidenced due to the appearance of a new spheroid close to the top electrode. Between frames 17 and 20, the spheroid is directed toward the top electrode. A splitting of the spheroid into two is observed at frame 22 where two brighter spheroids appear in the discharge. Afterwards, up and down motions continue until frame 36.

In this section, we reported the experimental observation of the interaction of localized plasma structures (called plasma spheroids) in a dusty plasma. The case presented

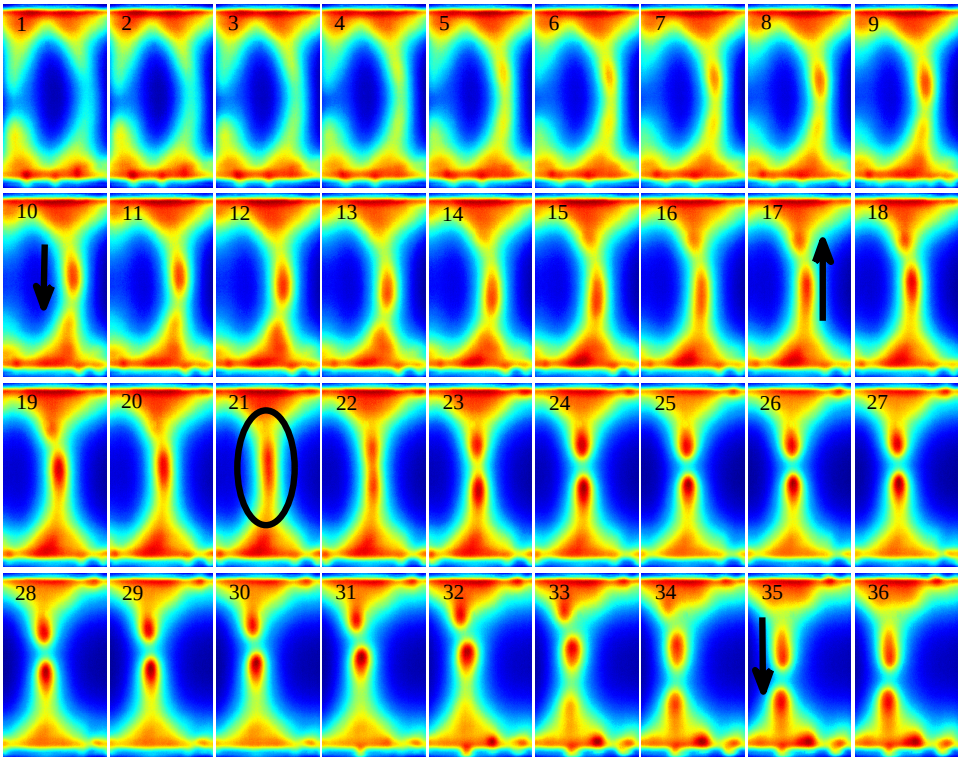

Figure 5.19: Appearance, up and down motions and splitting of spheroids in the center of the discharge. The frames are extracted from a movie at 16000 fps.

in Fig. 5.13 appears particularly rich in complex phenomena (motion, repulsion, splitting, or merging) but is difficult to analyze due to the insufficient frame rate and the too big number of plasma spheroids. Thus, easier cases have been found in order to analyze these interactions. Results show that these regions of enhanced emission emerge from the electrode vicinity and propagate towards the plasma bulk where they can interact with each other. It leads to complex motions, repulsion and attraction phenomena. A single spheroid can also be divided into two parts, giving birth to two new spheroids.

During these phenomena, the electrical characteristics of the discharge show clear instabilities. Nevertheless, a direct correlation between these measurements and the spheroid dynamics is quite difficult. First, because it would consist in comparing local behaviors (spheroids) and global electrical measurements integrating phenomena outside the camera field of view. Second, because spheroid dynamics does not necessarily change the discharge characteristics: when a spheroid is moving in between the electrodes, its charge is just transported from one place to another. In the case of merging or splitting, the situation is more complicated as the respective spheroid intensities play

a role. Similar interactions have been found in other plasma conditions like in fusion plasmas, dielectric barrier discharges, and plasma jets, for example, in the context of plasma medicine. These experimental results obtained in a dusty plasma propose a new system to study these behaviors. The experimental conditions are very different in each of these fields, leading to a certainly quite different physical origin of these behaviors. Nevertheless, it appears obvious that electrical effects (repulsion, polarization, etc.) are the common points behind all observations.

5.6 Conclusion

In this Chapter, a high speed camera is used in order to study the dust particle growth instabilities.

First, the evolution of the plasma glow at the beginning of dust particle growth instabilities is investigated. A correlation between optical evolution of the instability and the electrical measurements (three peak pattern) during DPGI is obtained. It shows that the big amplitude peak corresponds to the rise of the luminosity in the center of the discharge, while the small amplitude peaks are related to the bright regions appearing at the edges of the plasma bulk.

Second, the appearance of plasma spheroids is investigated. Several types of plasma spheroid behaviors are presented. In argon plasmas, a single spheroid is observed rotating along the circumference of the electrode. Experiments are performed in order to observe the influence of the discharge power on the spheroid behavior. It shows clearly that with the increase of the discharge power, the rotation speed (around a few $m{\cdot}s^{-1}$) is slightly increased (section 5.2). Then, a complex behavior of spheroids close to the electrodes is studied where three regimes are evidenced: A regime where no spheroids are detected, a second regime where stochastic appearance and disappearance of spheroids are observed, and a third regime where the persistence of some spheroids that enter in a rotating motion along the circumference of the electrode is observed. These regimes are correlated with the variation of the plasma luminosity in the discharge central part. It is shown that when the plasma changes are located in the discharge center, regime I or III is observed in front of the electrodes. Regime II appears when plasma changes in between the electrodes are fast and more off-centered (section 5.3). In krypton plasmas, the splitting of spheroids at the vicinity of the electrode, and the influence of the appearance of a new spheroid on the trajectory of other spheroids are studied (section 5.4). These observations show that many physical phenomena (attraction, repulsion) can be behind these behaviors. Then, many interactions between

spheroids in the discharge center are investigated such the up and down motion, the merging of spheroids and the splitting of a spheroid into two. During the up and down motion, a clear attraction between the spheroids is observed. A drastic reversal of the comet head position (in the plasma center) is detected when a spheroid from the top or bottom enters the plasma (Fig. 5.14). Concerning the splitting and the merging of spheroids, these processes have been confirmed thanks to the luminosity variation in Fig. 5.17 and the frame by frame analysis.

5.7 French Summary

Dans ce chapitre, une caméra rapide est utilisée afin d'étudier les instabilités de croissance des poudres.

En premier, l'évolution de la luminosité du plasma au début de l'instabilité de croissance des poudres est étudiée. Une corrélation entre l'évolution optique de l'instabilité et les mesures électriques (montrant une structure à trois pics) est observée. Elle montre que le grand pic correspond à l'augmentation de la luminosité au centre de la décharge, tandis que les petits pics sont liés aux régions lumineuses apparaissant sur les bords du plasma.

Ensuite, l'apparition des "sphéroides" de plasma est étudiée. Plusieurs types de comportements sont présentés. Dans les plasmas d'argon, la rotation d'un sphéroide le long de la circonférence de l'électrode est étudiée. Des expériences sont réalisées afin d'observer l'influence de la puissance de décharge sur le comportement du sphéroide. On observe clairement que l'augmentation de la puissance induit une augmentation de la vitesse de rotation du sphéroide. Ensuite, un comportement complexe de sphéroides à proximité des électrodes est étudié et plusieurs régimes sont mis en évidence: I- Un régime où aucun sphéroide n'est détecté, II- un second régime où l'apparition et la disparition stochastique des sphéroides sont observées, et III- un troisième régime durant lequel on observe la persistance de certains sphéroides qui entrent dans un mouvement de rotation tout le long de la circonférence de l'électrode. Ces régimes sont corrélés avec la variation de la luminosité du plasma au centre de décharge. Il est démontré que lorsque les changements de luminosité du plasma sont situés au centre de la décharge, le régime I ou III est observé à proximité des électrodes. Le régime II apparait lorsque les changements de luminosité du plasma sont décentrés.

En krypton, la séparation de sphéroides au voisinage de l'électrode, et l'influence de l'apparition d'un nouveau sphéroide sur la trajectoire des autres sphéroides sont étudiés. Ces observations montrent que de nombreux phénomènes physiques (attrac-

tion, répulsion) peuvent être à l'origine de ces comportements. Ensuite, de nombreuses interactions entre les sphéroides au centre de la décharge sont étudiées: des déplacements verticaux, la fusion de deux sphéroides et la séparation d'un sphéroide en deux. Des phénomènes d'attraction entre les sphéroides sont observés durant les déplacements verticaux. En ce qui concerne la séparation et la fusion de sphéroides, ces processus ont été confirmés grâce à la variation de la luminosité, et à l'analyse image par image de ces comportements.

Chapter 6

Laser Induced Fluorescence investigations in a dusty plasma

The Laser Induced Fluorescence (LIF) diagnostic is used in the PKE-Nefedov reactor to investigate two different phenomena occurring in an argon dusty plasma. First, as in Chapters 4 and 5, a particular attention is paid on the plasma evolution during dust particle growth instabilities. The second phenomenon concerns the appearance of a dust-free region, called the void, in the plasma center [137]. The theory of the void formation was detailed in Chapter 2. Many theoretical works have been devoted to the formation and the behavior of the void in dusty plasmas [81, 138–140]. Indeed, the void is the place of many complex phenomena (dynamics, self excited oscillations [79, 141], growth of dust successive generations [77, 142]). Indeed, under some conditions, it was reported that the void can be disturbed and exhibits oscillations. This instability is named the heartbeat instability consisting in successive contractions and expansions of the void size [137, 143–146]. During our investigations, the void is in a stable situation. This region of enhanced luminosity is easily observed by looking at the plasma light emission [147] (Fig. 6.1) or by using a thin laser sheet produced with a laser diode to detect the dust cloud. As the characteristics inside the void are completely different than those in the surrounding dust cloud, the LIF can be useful to reveal the void particularities. For this purpose the horizontal and vertical profiles of the LIF intensity are measured in the presence of a void.

The experimental setup related to the LIF diagnostic is detailed in section 3.2.3. In Fig. 6.2, an image of the PKE-Nefedov reactor is presented showing the laser passing through the dusty plasma. The laser is continuously probing the wavelength region around $\lambda_0 = 667.9125$ nm with a scan, i.e. with a cycle from $\lambda_0 - d\lambda$ up to $\lambda_0 + d\lambda$

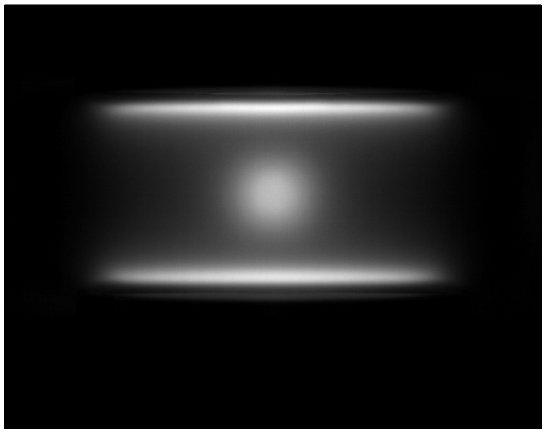

Figure 6.1: An image of the plasma glow showing the "void" in the center of the discharge.

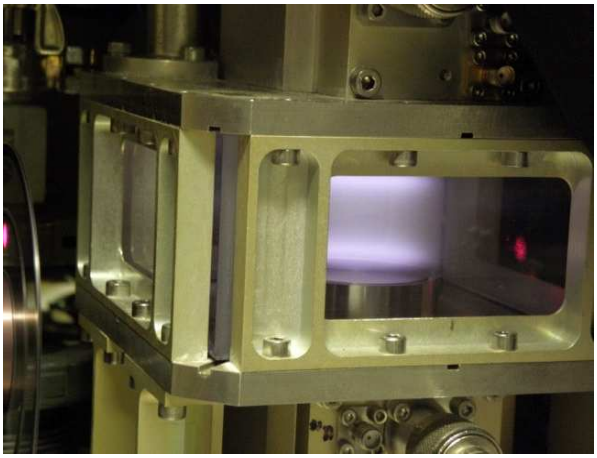

Figure 6.2: The laser (LIF) observed on the PKE-Nefedov reactor window.

and then down to $\lambda_0 - d\lambda$. By repeating this procedure, LIF signal as a function of λ can be recorded for different locations as shown in Fig. 6.3.

6.1 DPGI investigation using LIF

In this section, DPGI evolution is investigated. For this purpose, the laser crosses the plasma center in between the two electrodes and the photomultiplier records the LIF signal coming from the central part of the plasma. Figures 6.4, 6.5 and 6.6 represent the LIF signal and the electrical measurements during DPGI. The beginning of the instability is detected around 70 s after the plasma ignition (clearly observed in Fig. 6.5

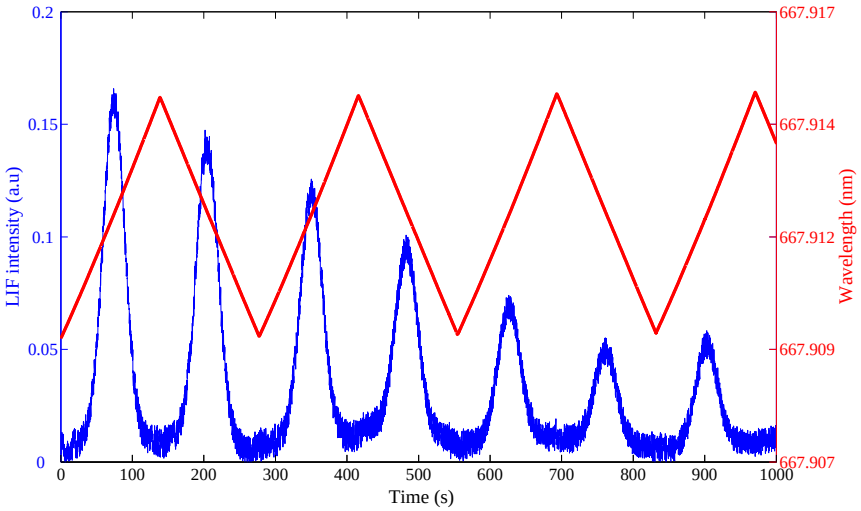

Figure 6.3: Evolution of the fluorescence as a function of the wavelength, for different positions with different properties in the bulk.

where the amplitude of the RF current is recorded in AC). During dust particle growth, an increase of the LIF signal (Fig. 6.4) is observed until 500 s. At the same time, modifications on the electrical signals (AC and DC components) are detected. In Fig. 6.5 fast amplitude variations are observed, while in Fig. 6.6 a fast decrease of the DC component is clearly observed (confirming dust particle growth as discussed in Chapter 4). Afterwards, the LIF intensity is stable until 1200 s (Fig. 6.4). During this phase, slight modifications are evidenced on the AC component without big changes on the amplitude variation. For the DC component, a slow decrease of the electrical current is observed. Then, a slight decrease of the LIF signal starts at 1200 s and continues even after the end of the instability (1550 s). During this phase of DPGI, a decrease of the instability frequency is noticed as shown in Chapter 4 section 4.3 (argon plasma). It means that the bright regions (Chapter 5) observed during the last phase of DPGI are moving at a slower rate. Therefore, less intensity coming from the plasma is detected by the photomultiplier during each laser scan, explaining the LIF decrease from 1200 to 1550 s. The LIF decrease after DPGI could be due to the absence of regions of enhanced emission or to a slight continuous pollution of the gas.

Another experiment is presented in Fig. 6.7 where the wavelength scan is the same as in Fig. 6.4 but the speed of the scan is much more higher (around 2.5 s for a scan, whereas 95 s in Fig. 6.4). It clearly shows that after the plasma is switched on, the LIF signal slowly increases as dust particles are growing. Around 100 s (80 s after plasma ignition), dust particles start to disturb the plasma equilibrium and DPGI are triggered.

This effect is well observed in the LIF signal that continues to globally increase but with clear disturbances. In these measurements, the wavelength scan duration is much longer than the instability typical timescale. The LIF signal cannot follow the unstable phenomena but its perturbation is clearly observed. After a few minutes, the plasma is switched off during 1 minute in order to let enough time to the dust particles to fall down on the bottom electrode. The gas inside the reactor is not renewed in order to keep roughly the same discharge conditions and the plasma is switched on anew (around 320 s in Fig. 6.7). It appears that the LIF signal is much smaller than just before the extinction. Its value is close to the one just after the first plasma ignition.

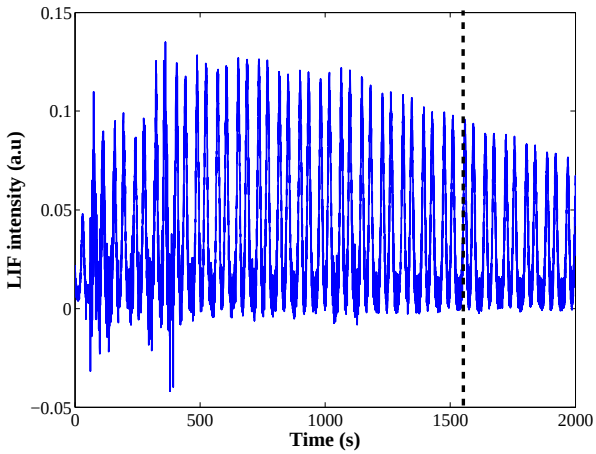

Figure 6.4: Evolution of the fluorescence peak during dust particle growth instabilities.

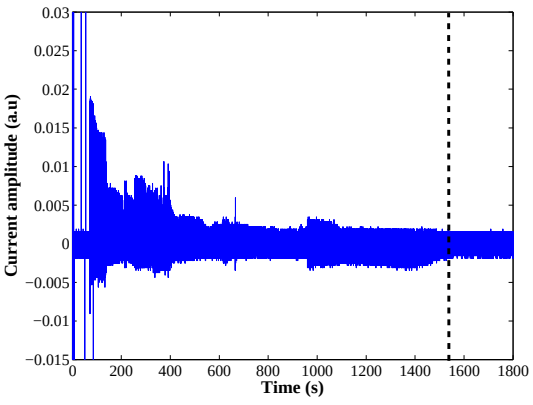

Figure 6.5: Amplitude of the RF current (AC component).

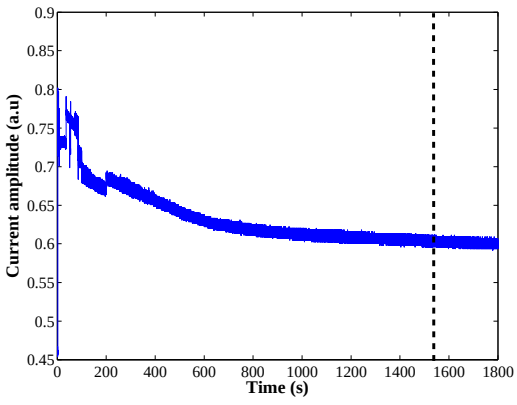

Figure 6.6: Amplitude of the RF current (DC component).

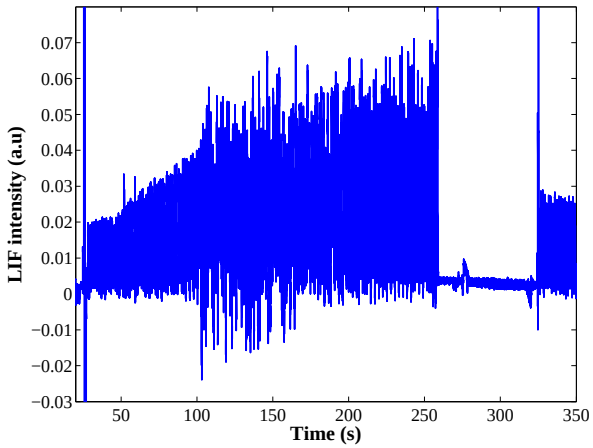

Figure 6.7: LIF measurements during dust particle growth instabilities.

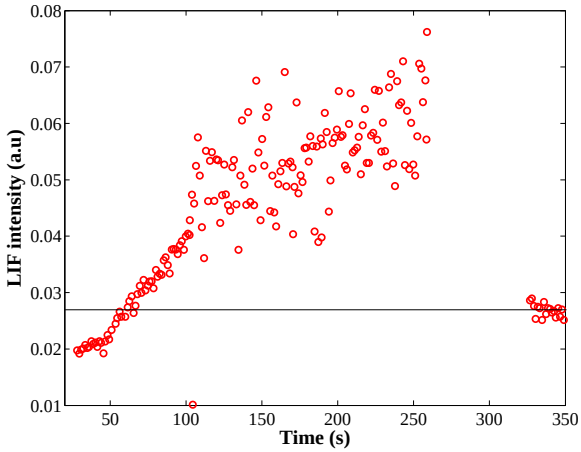

Figure 6.8: Envelope of the LIF measurements. The horizontal line allows to compare the LIF amplitudes of the two consecutive plasmas.

This experiment shows an interesting result: the global increase observed during dust particle growth and DPGI is really induced by the dust particles and is not due to any other effect. It confirms previous works [140, 148] showing an enhanced excitation rate when dust particles are growing inside a plasma. This is mainly due to a higher electron temperature in a dusty plasma than in a dust-free plasma. These analyses are better observed in Fig. 6.8 where a peak detection has been performed on the LIF signal of Fig. 6.7. It roughly shows the signal envelope and confirms the continuous increase related to the dust particle growth and the clear evidence of DPGI. It also shows that the amplitude of the LIF signal after the re-ignition at 320 s is slightly higher than for

the first plasma ignition.

6.2 Void investigations

LIF measurements are performed inside and outside the void in order to study its characteristics. First of all, a measurement is performed along the x-axis of the reactor, from the void center to the plasma edge (Fig. 6.9). A clear enhancement of the excited neutral atom emission is observed in the void center. The emission is continuously decreasing when moving towards the plasma edge. The transition between the void and the dusty plasma region is not well-marked as it could be expected. It could be due to the too large size of the region observed by the photomultiplier. Indeed, as the light is integrated on a region of a few mm it leads to a smoothing of the emission gradient. Figure 6.10 shows the vertical measurement locations. LIF signal is measured at 9 positions on the vertical axis starting from the void center towards the bottom electrode. Then the same vertical measurements are performed at 2 and 4 mm (along the horizontal axis) from the void center. As shown in Fig. 6.11, the vertical profile has a slightly different behavior than in Fig. 6.9. Indeed, in this direction the plasma is strongly confined by the electrodes. It leads to the formation of well-defined sheaths in front of each electrode. It is well-known that a region of enhanced emission appears at the transition between the plasma and the sheath. This is the place where plasma electrons gain energy [149]. Three main regions are evidenced in Fig. 6.11. The first one is the void with and enhanced excitation. In comparison with the horizontal profile, the void is clearly marked between 0 and 0.4 cm. Indeed, for the vertical profile, the integration region is reduced because it is limited by the laser width. The second region is the plasma bulk with a rather constant emission, between 0.4 and 1.3 cm. The last region is the pre-sheath where the excitation steeply increases (above 1.3 cm). These three curves show a big decrease of LIF intensity in the void. The decrease is sharper in the center of the void, while in the other 2 positions (at 2 and 4 mm from the void center) the decrease is smoother.

We briefly presented preliminary results on the void characteristics using a Laser Induced Fluorescence platform currently under improvement in GREMI. It has been shown that the excited neutral density is higher in the void than in the rest of the plasma bulk containing dust particles (except the pre-sheath regions). Some improvements will be performed as for example an increase of the spatial resolution. The neutral gas temperature can also be estimated from LIF measurements. Nevertheless, uncertainties on the temperature were rather important during our experimental campaign and no

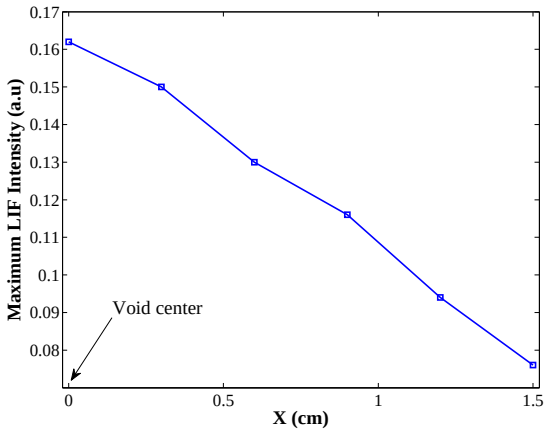

Figure 6.9: Horizontal profile for LIF maximum intensity from the void center towards the plasma edge.

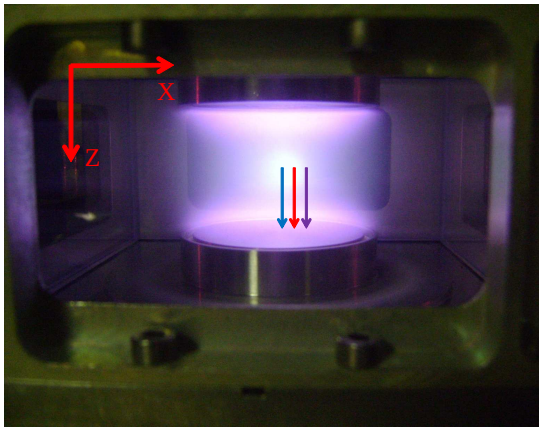

Figure 6.10: Enhanced emission of the central void in an argon plasma. The three arrows show the measurement positions and directions.

clear conclusions can be drawn for the moment on this interesting parameter.

It would have been also interesting to study the ion density distribution inside and outside the void. For this purpose, a laser was used at 668.61 nm to pump a level of Ar II and observe the de-excitation signal at 442.7 nm. After several experiments, we were unable to observe a clear LIF signal. Perhaps, another wavelength for Ar II should be used. Unfortunately, it was not possible to perform this work. It would be interesting to obtain results concerning the ions as they create the ion drag force directly involved in the void formation. This force is still actively studied, both experimentally and theoretically [150] and any new data on this aspect could be useful.

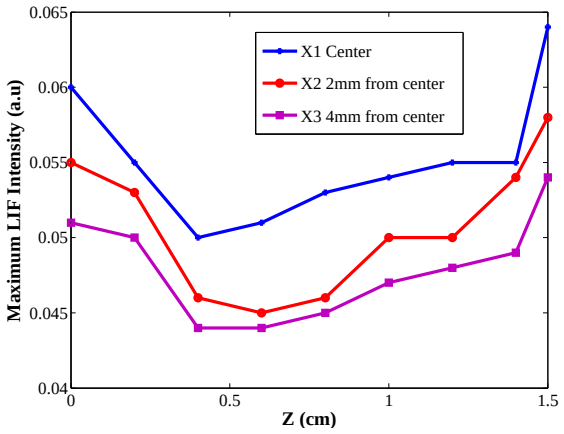

Figure 6.11: Maximum LIF intensity profile in the vertical direction for 3 different horizontal positions.

6.3 Conclusion

In this Chapter, Laser Induced Fluorescence is used in order to investigate dust particle growth instabilities and the void. The evolution of DPGI is compared to the electrical measurements (AC and DC components). At the beginning of the instability, a fast increase of LIF signal is observed on the electrical signals, it corresponds to strong variations of the AC and DC components. Afterwards, the LIF signal becomes stable and no huge change on the electrical signals is evidenced during this phase. At the end a decrease of the LIF signal is noticed. This decrease can be related to the decrease of the instability frequency and thus to a reduction of the luminosity coming from the moving bright regions characterizing DPGI.

The effect of the dust particles on the LIF signal is studied by comparing 2 consecutive plasmas (Fig. 6.7). It is observed that after the re-ignition of the plasma, the LIF signal is roughly similar to the one just after the first plasma ignition. It confirms that the LIF signal increase during the first plasma is really due to dust particle growth.

It has also been shown that the excited neutral density is higher in the void than in the rest of the plasma bulk containing dust particles (except the pre-sheath regions). In the future, some improvements will be performed in order to study the ion density inside and outside the void, as the void is a result of a balance between ion drag force and electrostatic force.

6.4 French Summary

Dans ce chapitre, la fluorescence induite par laser est utilisée afin d'étudier les instabilités de croissance des poudres et le void.

L'évolution des instabilités mesurée par LIF est comparée aux mesures électriques (composantes alternatives et continues). Au début de l'instabilité, une augmentation rapide du signal de LIF est observée, ce qui correspond à de fortes variations des composantes continues et alternatives du courant de décharge. Ensuite, le signal du LIF est stable et aucun grand changement sur les signaux électriques n'est observé durant cette phase. Vers la fin, une diminution du signal du LIF est remarquée. Cette diminution peut être liée à la diminution de la fréquence de l'instabilité et donc à une réduction de la luminosité provenant des régions lumineuses en mouvement caractéristiques des instabilités.

L'effet des poudres sur le signal du LIF est étudié en comparant 2 plasmas consécutifs. Il a également été démontré que la densité des neutres excités est plus élevée dans le void que dans le reste du plasma contenant des poudres (sauf dans les régions de pré-gaine). Dans l'avenir, des améliorations seront effectuées afin d'étudier la densité ionique à l'intérieur et à l'extérieur du void. Cela pourrait fournir des précieuses informations, puisque le void est le résultat d'un équilibre entre la force ionique et la force électrostatique.

Chapter 7

FTIR spectroscopy investigations using ATI

In Chapters 4, 5 and 6, the effect of dust particles on the plasma was investigated. In particular, the instabilities triggered by the presence of the particles have been studied using different diagnostics. In this Chapter, the experiments are performed in a vacuum chamber called ATILA where aluminium tri-isopropoxide (ATI) is injected at gas phase in the plasma. The aim of the study is to present fundamental results about the dissociation of ATI and the formation of the reaction products in the plasma [151]. These experiments are performed in IEAP Kiel in collaboration with INP Greifswald and GREMI Orléans.

7.1 Aluminium Tri Isopropoxide

Aluminium tri-isopropoxide is odorless, cheap but water sensitive powder. It is characterized by the formula $[Al(O-i-Pr)_3]_n$, where i-Pr is an isopropyl group ($CH(CH_3)_2$), n changes due to thermal, physical and storage conditions [152, 153]. In Table 7.1 some physical and chemical properties of ATI are presented.

Metal organic precursors are frequently used in plasma processes for the deposition of metal oxide layers, where hardness, wear resistance, thermal and chemical stability are requested. First investigations on aluminum tri-isopropoxide (ATI) were made by Daasch and Fales [154] in the late 1960s. They used mass spectrometry to determine the components of hot ATI gas. As a conclusion of this work, several species have been found with the formula $(Al(OC_3H_7)_3)_n$ (Fig. 7.1), where n can vary from 1 to 7. In the late 1970s, many studies have given information on the crystal structure of solid ATI

Chemical formula	$C_9H_{21}O_3Al$
Other names	Aluminium triisopropanolate Triisopropoxyaluminium Aluminium triisopropylate 2-Propanol
Molar mass	$204.25 g/mol$
Density	$1.035\ g/cm^3$
Melting point	118 - 138 $°C$
Boiling point	140 - 150 $°C$
Solubility	Decomposes in water
Appearance	White powder
Safety	Flammable, irritates skin and eyes gastrointestinal irritation with nausea
Conditions to avoid	exposure to moist air or water high temperatures ignition sources
Dangerous decomposition products	Carbon monoxide Carbon dioxide Aluminum oxide
Chemical stability	Stable under normal conditions Isopropanol: susceptible to autoxidation

Table 7.1: Chemical and physical properties of ATI.

using X-ray diffraction [155]. In the 90s, Folting *et al.* [156] also explained the occurrence of several oligomers and the crystal structure. The ATI molecule is studied due its presence in different applications: as a catalyst in the reduction of carbonyl containing compounds, as a component of catalytic compositions in polymerization reactions and also as a main source for oxide films used in electronics [157, 158]. An important use of ATI is the deposition of Al_xO_y by chemical vapor deposition (CVD) processes. In the field of gas diffusion barriers like organic light emitting devices (OLED), atomic layer

deposition is used [159]. The OLED is a light emitting diode with a film of organic compound. A layer of organic semiconductor is positioned in between the two electrodes. Despite its high efficiency and low drive voltage, this device can be easily damaged due to the presence of the water and oxygen. Most of the studies are performed to replace the current capping method with the aim to reduce the weight, costs, and amount of materials used.

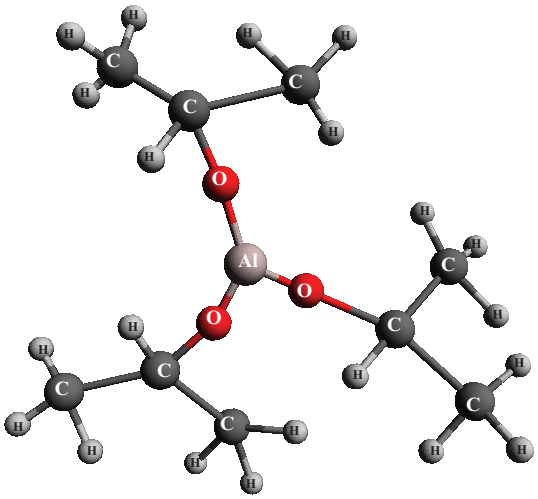

Figure 7.1: Monomeric structure of aluminium tri-isopropoxide.

The stability of deposited aluminium layers is an important aspect regarding the applications. Huntz *et al.* made in-situ investigations on growing Al_xO_y films by X-ray diffraction and scanning electron microscopy focusing on the phase transformations occurring in Al_xO_y layers during heat-treatment [160]. In the 1980s, Saraie *et al.* measured the deposition rate of Al_xO_y formed by using ATI in CVD processes [161]. Sovar *et al.* found that despite the ageing of ATI, it can principally be used in process plasmas for depositing stable Al_xO_y layers [153].

Although ATI containing plasmas are used in PECVD processes [162], the chemical reactions are far from being completely understood. The knowledge about the fragmentation and reaction processes in the ATI plasma, which are induced by electron impact processes, is an essential presumption for the optimization of Al_xO_y deposition. Information about the absolute ground state concentration of molecular precursors, fragments and products including transient species like radicals in relation to the discharge parameters such as gas mixture, absolute pressure and discharge power would be very helpful to achieve further insight into this complex plasma type.

Previous work has been done by Niemietz *et al.* [163] and Lopatik *et al.* [164]

getting first information about chemical phenomena in ATI containing plasmas by using mass spectrometry (MS) and quantum cascade laser absorption spectroscopy (QCLAS). Possible reactions were proposed by the authors. Polymerization process and formation of hydrocarbons were studied.

In the present work, the evolution of the concentration of the precursor gas (ATI) and of a group of molecular reaction products is analyzed under various experimental conditions. Additionally, the fragmentation efficiencies and rates of ATI are determined.

7.2 FTIR investigation

The experiments are performed in an asymmetric capacitively coupled RF (13.56 MHz) discharge called ATILA described in section 3.1.2. The initial gas mixtures were controlled using mass flow controllers for argon and nitrogen. The ATI is initially a powder and has to be heated up to 135 °C to be injected into the reactor in gas phase. The flow of ATI can be varied thanks to a heat resistant needle valve installed at the vicinity of the heating system. The total pressure is in the Pa range (1 Pa = 0.01 mbar). The composition of the plasma is investigated by a Fourier Transform Infrared spectrometer.

For all experiments, the spectrum between 700 cm^{-1} and 4700 cm^{-1} has been scanned. In total, seven species have been detected, i.e. ATI, CH_4, C_2H_2, C_2H_4, C_2H_6, CO and HCN. The spectral identification and quantification were performed with the help of the PNNL database [165]. In order to calculate absolute ATI number densities, the FTIR spectra were calibrated with ATI vapor at known pressure values using the ideal gas law. For that purpose, the spectral range between 3050 cm^{-1} and 2800 cm^{-1} was used (Fig. 7.2). For the calculations of the concentrations, a gas temperature of 300 K was used since this value was found to be a good average for the gas temperature over the line of sight (constituted of the active zone over the discharge electrode and the afterglow surrounding them). The band strength S(T) depending on the temperature T is defined as

$$\frac{1}{L}\int_{band} \ln\left(\frac{I_0}{I}\right) \mathrm{d}\nu = n_{ATI} \cdot S(T) \tag{7.1}$$

where L is the absorption length, I_0 is the introduced intensity and I the transmitted intensity of the FTIR system. n_{ATI} is the number density and ν denotes the wavenumber scale of the spectra.

The measured spectrum of gaseous ATI at a pressure of p= 2 Pa is given in Fig. 7.2.

The strongest absorption was identified at a spectral region around 3000 cm^{-1}. The small CO_2 absorption at 2300 cm^{-1} was caused by atmospheric traces in the beam path and was neglected in the further analysis. The integration (eq. 7.1) was done over the ATI band, i.e. from 3050 cm^{-1} to 2800 cm^{-1} giving a band strength of $5.8 \cdot 10^{-16}$ cm^{-1}/molecules cm^{-2} used for the calculation of absolute number densities of ATI .

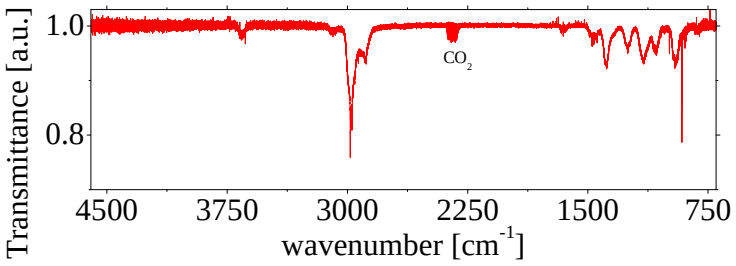

Figure 7.2: Spectrum of ATI measured at 2 Pa with a resolution of 0.075 cm^{-1}.

7.2.1 Determination of ATI flow

The ATI pressure is controlled through a needle valve placed right after the heater. Therefore, in order to have an estimation of the ATI flow, some calculations have to be performed. The vacuum pump system is running at its maximum performance, no reducing or stabilizing components are placed in the output gas flow. The needle valve is used to set a fixed ATI flow which leads to a stable ATI pressure in the reactor, $p_{(t=0)} = p_{ini}$. At $t = 0$, the pump is isolated from the vacuum chamber and the pressure increases depending on the gas flow. Consequently, the time dependent increase of the pressure is proportional to the gas flow. Using the ideal gas law (eq. 7.2) and its time derivation (eq. 7.3), the gas flow can be calculated.

$$pV = Nk_BT \tag{7.2}$$

$$\frac{dp}{dt} = \frac{k_BT}{V}\frac{dN}{dt} \tag{7.3}$$

In eq. 7.2 and eq. 7.3, p is the pressure, V is the volume of the reactor, N is the number of molecules in V and T the gas temperature.

Using this approach, with a constant Ar flow of 5 and 10 sccm, controlled by mass flow controllers, the reactor volume has been measured to be 60391 +/− 4500 cm^3. Once the reactor volume is known, the ATI flow can be determined from the initial pressure. Figure 7.3 shows the ATI flow as a function of the initial ATI pressure p_{ini},

exhibiting an expected linear slope. This function allows to calculate the ATI flow from the initial ATI pressure.

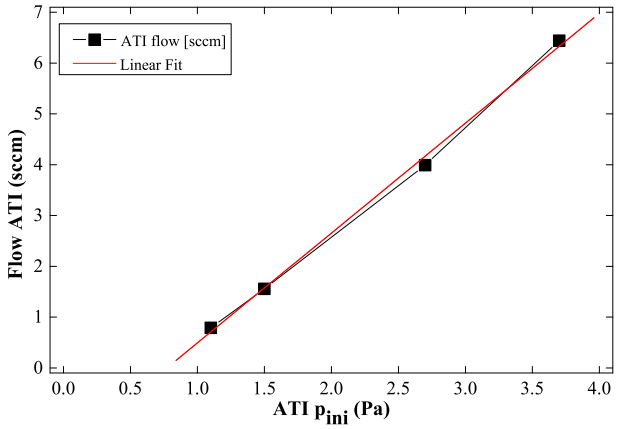

Figure 7.3: Curve used to calculate the flow of ATI by measuring the ATI pressure in the reactor. The curve has been calculated using eq. 7.3 and the temporal change of the pressure.

7.2.2 Determination of analysis parameters

A typical FTIR spectrum obtained with a Ar/N_2/ATI plasma is given in Fig. 7.4. In the following, ϕ_X indicates the gas flow of the species X in molecules per min. $2.69 \cdot 10^{19}$ molecules min^{-1} corresponds to 1 sccm gas flow. The power coupled into the plasma is P_{plasma} (in W). The concentration n_X of the species X is in molecules cm^{-3}. Table 7.2 lists the species and the spectral range used for spectral analysis.

An important parameter is the degree of dissociation of the ATI-molecules (D_{ATI}) which has been calculated using

$$D_{ATI} = \left[1 - \frac{n_{ATI_{Plasma}}}{n_{ATI_{input}}}\right] \cdot 100\% \tag{7.4}$$

with $n_{ATI_{plasma}}$ is the ATI concentration during the plasma phase and $n_{ATI_{input}}$ is the ATI-concentration of the input gas mixture.

Further insight into the chemical processes in the plasma is possible by calculating absolute ATI fragmentation efficiency and rate. The fragmentation efficiency F_E of the

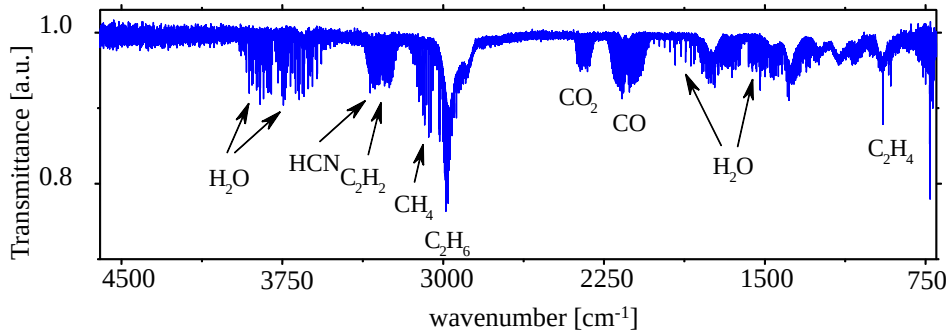

Figure 7.4: Typical spectrum for an RF plasma at 80 W and a pressure of 8 Pa. The flow of the precursor gas is Ar: 2.2 sccm, N_2: 5 sccm, ATI: 2.65 sccm. The concentration of H_2O and CO_2 are due to the atmosphere.

ATI molecules is calculated by analogy with [166] as

$$F_E = \phi_{ATI} \frac{1}{P\,(_{Plasma})} \frac{D_{ATI}}{100\%} \tag{7.5}$$

The fragmentation rate can be determined using

$$F_R = \phi_{ATI} \frac{D_{ATI}}{100\%} \tag{7.6}$$

7.2.3 Argon-ATI plasma

In this section, experiments are performed to study the behavior of ATI in an Ar/ATI gas mixture with the ratio 2/1. The initial pressure is constant at 6 Pa. The applied RF power varies between 0 and 100 W.

FTIR spectroscopy is a line-of-sight method. Inside the reactor the measured concentration is the sum of the ATI concentrations (i) in the plasma volume and (ii) in the volume outside the plasma, i.e. the volume between the plasma and the mirrors or windows of the long path cell. Since the present work focuses on the processes in the active plasma volume, the measured concentration had to be corrected in order to exclude the ATI concentration outside the plasma volume.

The measured initial concentration of ATI of $5 \cdot 10^{14}$ molecules cm^{-3} and the concentration at the constant level of about $2 \cdot 10^{14}$ molecules cm^{-3} at P= 100 W (not shown), was used to estimate the diameter of the active plasma volume. With a mirror distance of 78 cm, the diameter of the active plasma volume could be estimated to be $78\text{cm}\cdot(5 \cdot 10^{14} - 2 \cdot 10^{14})/5 \cdot 10^{14} = 47\text{cm}$ at p=6 Pa.

Species	Spectral range (cm^{-1})
ATI	3050 - 2800
CH_4	3115.21 - 3112.13 3096.77 - 3093.69 3087.73 - 3084.65
C_2H_2	3274.05 - 3272.85 3254.29 - 3252.48 3283.51 - 3282.55
C_2H_4	951.264 - 947.468
C_2H_6	2997.74 - 2995.99 2994.3 - 2992.56 2987.49 - 2985.75
CO	2092.11 - 2089.18 2096.63 - 2093.7 2201.03 - 2198.83
HCN	3345.83 - 3344.8 3354.14 - 3352.64 3284.66 - 3283.63

Table 7.2: Identified species and the spectral position used for the calculation of the absolute number density. A calibrated database was used [165]. In case several positions are listed, averaging has been applied. The error of absolute densities is in the order of about 15 %. No temperature effects were taken into account.

Figure 7.5 shows the concentrations and the degree of dissociation of the ATI precursor corrected for the plasma volume. As a function of the applied RF power, the initial concentration of about $3.2 \cdot 10^{14}$ molecules cm^{-3} decreases to about zero.

Using the corrected ATI concentrations, properties related to the plasma volume were calculated. The degree of dissociation shows a continuous increase and reaches 100 % at P= 100 W of applied power. The gas mixture contains ATI and chemical inert Ar. Therefore, the main channel for the dissociation of ATI can be supposed to be electron

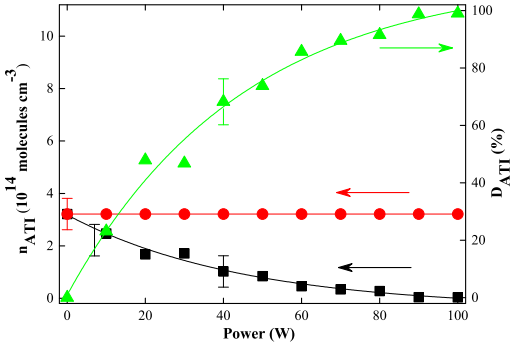

Figure 7.5: Concentration of ATI with - ■ and without - ● plasma operation as well as the degree of dissociation - ▲ as a function of the discharge power in an Ar/ATI plasma, p= 6 Pa, ratio Ar/ATI= 2/1.

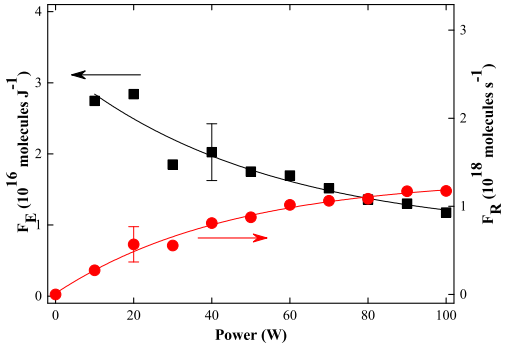

Figure 7.6: Fragmentation efficiency F_E - ■ and fragmentation rate F_R - ● of ATI as a function of the discharge power in an Ar/ATI plasma. p_{total} = 6 Pa, ratio Ar/ATI= 2/1.

impact dissociation. This process is influenced by the ATI density. Figure 7.6 shows the fragmentation efficiency and fragmentation rate, both calculated from the ATI concentration, power values and the gas flows using eq. 7.5 and 7.6. The fragmentation efficiency clearly indicates that the efficiency decreases as the power is increasing. The fragmentation rate shows a similar behavior as the degree of dissociation, see Fig. 7.5.

The next experiment is performed as a function of the pressure. The initial pressure, i.e. the pressure before plasma ignition, is varied between 3 and 10.5 Pa while the mixing gas ratio of Ar/ATI = 2/1 is kept constant. In Figure 7.7 the concentrations of ATI with and without plasma operation as well as the degree of dissociation as a function of the total pressure in an Ar/ATI plasma are shown. Inside the plasma volume the concentration of ATI was below the detection limit for pressures below p= 6 Pa and reaches about $3.4 \cdot 10^{14}$ molecules cm^{-3} for an pressure of about p= 10.5 Pa. The degree of dissociation was found to be 100% for a pressure below p= 6 Pa and decreases to about 25% for a pressure of p= 10.5 Pa. The fragmentation efficiency and rate are presented in Fig. 7.8. Both increase between p= 3 Pa and about p= 7 Pa. A maximum appeared at around p= 7 Pa. For pressure higher than p= 7 Pa the fragmentation efficiency and rate decrease, presumably caused by a lower mean free path length of the electrons at higher pressures leading to a reduced efficiency of the fragmentation process.

In the following, experiments are performed varying the Ar/ATI mixing gas ratio in

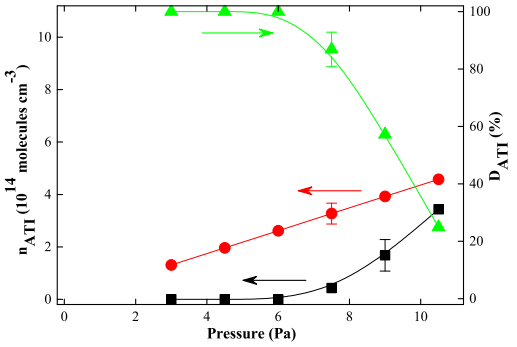

Figure 7.7: Concentration of ATI with - ■ and without - ● plasma operation as well as the degree of dissociation - ▲ as a function of the total pressure in an Ar/ATI plasma. P_{Plasma} = 80 W, gas ratio Ar/ATI= 2/1.

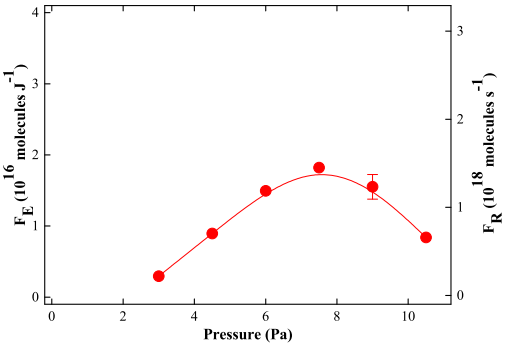

Figure 7.8: Fragmentation efficiency and fragmentation rate, both - ●, of ATI as a function of the total pressure in an Ar/ATI plasma. P_{Plasma} = 80 W, gas ratio Ar/ATI= 2/1.

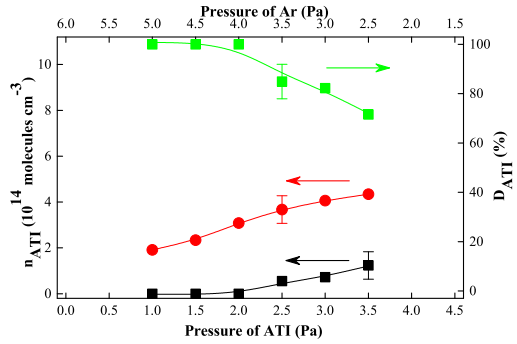

Figure 7.9: Concentration of ATI with - ■ and without - ● plasma operation as well as the degree of dissociation - ▲ as a function of the mixing gas ratio of Ar and ATI, given in pressure values. p_{total}= 6 Pa, P_{Plasma}= 80 W.

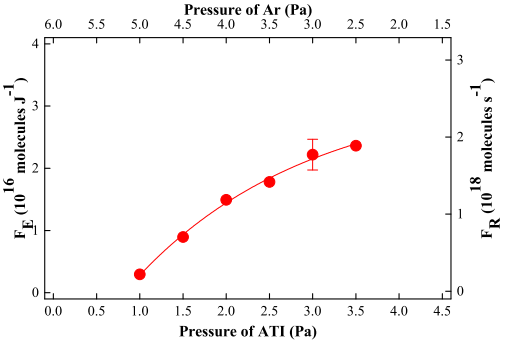

Figure 7.10: Fragmentation efficiency and fragmentation rate, both - ●, of ATI as a function of the mixing gas ratio of Ar and ATI. p_{total} = 6 Pa and P_{plasma} = 80 W.

the range of Ar/ATI = 5/1 to Ar/ATI = 2.5/3.5 keeping the total pressure constant at 6 Pa. The RF power is 80 W. The concentration and the degree of dissociation of ATI as a function of the mixing ratio is given in Fig. 7.9. For an ATI partial pressure lower than p= 2 Pa, the ATI concentration was found to be again below the detection limit in the plasma region. But it reveals nearly a linear increasing for an increasing ATI

pressure. Therefore, the degree of dissociation of ATI can be considered to be about 100% for an ATI pressure below p=2 Pa. At higher ATI pressures D_{ATI} decreases to about 72% at p= 3.5 Pa. Both, the fragmentation efficiency and rate show nearly a linear increase as the ATI partial pressure increases (Fig. 7.10). It means, that for a higher ATI partial pressure more aluminium tri-isopropoxide is fragmented but also more energy is needed for this process. This may be caused by a lower plasma density correlated to the decreased Ar partial pressure.

7.2.3.1 By-product formation

Figure 7.11 shows the concentration of the detected reaction products as a function of power. In general, the concentrations of CH_4, C_2H_6, C_2H_4 and CO increase with power. It is interesting to note, that in this experiment the concentration of C_2H_2 showed a different behavior compared to the other produced molecular species. At lower power values the acetylene concentration increase is less pronounced but it exceeds the concentration of the other products at higher power values. Compared to the concentration of CH_4, C_2H_6, C_2H_4 and CO, no constant level of the C_2H_2 concentration is observed for P $>$ 80 W.

Figure 7.12 shows the concentration of the reaction products for an Ar/ATI ratio of 2/1 at constant power of P = 80 W. The concentrations of CH_4, C_2H_2, C_2H_4 and C_2H_6 increase with the pressure. It is interesting to note that the concentration of CO is nearly constant over the entire pressure range.

Figure 7.13 shows the concentration of the reaction products with a varying Ar/ATI mixing ratio while the pressure and the power have been kept constant at p= 6 Pa and P = 80 W. All concentrations show an increase as the ATI pressure increases which is a similar behavior to the one seen in Fig. 7.12.

The FTIR measurements show the presence of several hydrogen carbon compounds, as CH_4, C_2H_2, C_2H_4 and C_2H_6, resulting from fragmentation and following polymerization processes in the plasma region. Generally, methyl groups can be considered to be detached from ATI molecules [163, 164] and react with hydrogen or other radicals containing carbon and hydrogen, forming C_nH_m molecules in several steps. The following general polymerization processes are discussed in literature [163]:

$$CH_3 + H \rightarrow CH_4 \tag{7.7}$$

$$CH_3 + CH_3 \rightarrow C_2H_2 + 4H \tag{7.8}$$

$$CH_3 + CH_3 \rightarrow C_2H_4 + 2H \tag{7.9}$$

$$CH_3 + CH_3 \rightarrow C_2H_6 \tag{7.10}$$

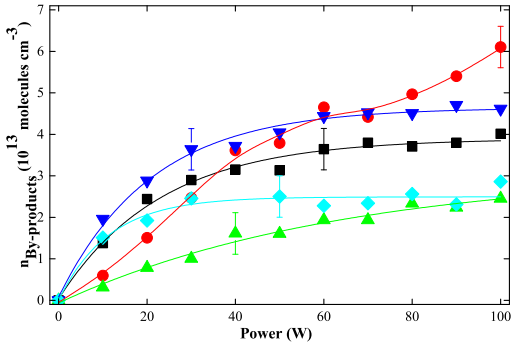

Figure 7.11: Concentration of CH_4 - ■, C_2H_2 - ●, C_2H_4 - ▲, C_2H_6 - ▼ and CO - ♦ as a function of the discharge power in an Ar/ATI plasma, p_{total} = 6 Pa, ratio Ar/ATI = 2/1.

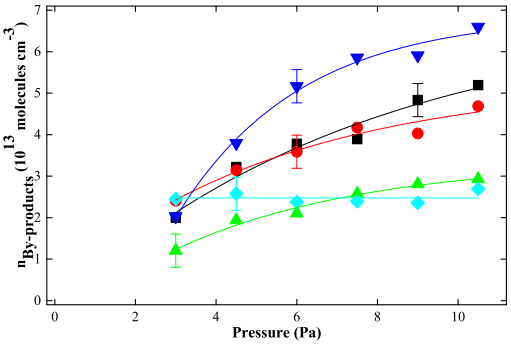

Figure 7.12: Concentration of CH_4 - ■, C_2H_2 - ●, C_2H_4 - ▲, C_2H_6 - ▼ and CO - ♦ as a function of the total pressure in an Ar/ATI plasma P_{Plasma}= 80 W, gas ratio Ar/ATI= 2/1.

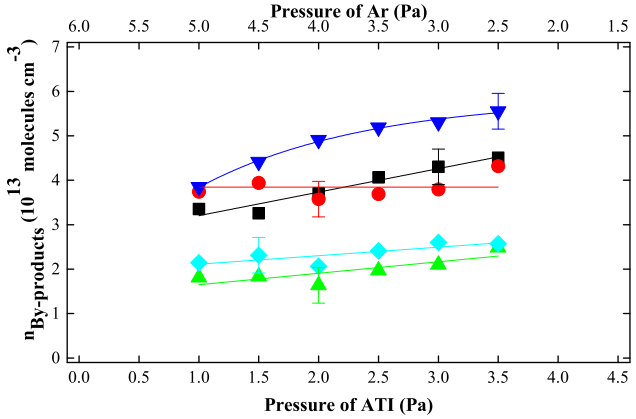

Figure 7.13: Concentration of CH_4 - ■, C_2H_2 - ●, C_2H_4 - ▲, C_2H_6 - ▼ and CO - ♦ as a function of the mixing gas ratio of Ar and ATI. given in pressure values, p_{total}= 6 Pa, P_Plasma= 80 W.

As shown in Fig. 7.11 the density of the hydrocarbons increases with increasing RF power. According to the decreasing ATI concentration for higher discharge power (Fig. 7.5) the growth of C_nH_m concentrations became less pronounced reaching a nearly constant value at higher powers. For P= 80 W the number of molecules per volume is in the range of 3.5 to $5 \cdot 10^{13}$ molecules cm^{-3} for CH_4, C_2H_2 and C_2H_6. The density

of C_2H_4 is generally lower, at about $2.2 \cdot 10^{13}$ molecules cm^{-3}.

As the total pressure increases, keeping the power and gas ratio constant (P= 80 W, Ar/ATI= 2/1), the number of hydrogen carbon product molecules increases according to the increasing ATI concentration, as presented in Fig. 7.12. Ethylene (C_2H_4) shows the lowest concentration while C_2H_6 shows the highest values. Generally, the concentration of CH_4, C_2H_2, C_2H_4 and C_2H_6 increases while the partial pressure of aluminium tri-isopropoxide increases as shown Fig. 7.13. As obtained in Fig. 7.12, C_2H_6 has the higher concentration and C_2H_4 the lowest density.

7.2.4 Argon-Nitrogen-ATI plasma

In this section, experiments are performed using Ar/N_2/ATI gas mixture. At first, a ratio of the partial pressure of Ar/N_2/ATI = 1/1/1 has been used at an initial total pressure of 6 Pa. Figure 7.14 shows the ATI concentration and the degree of dissociation while Fig. 7.15 shows the fragmentation rate and efficiency as a function of the power. The results are comparable to the measurements without nitrogen (Figs. 7.5 and 7.6). The only identified difference is the fragmentation efficiency for low power values. At P= 10 W, $F_E = 2.8 \cdot 10^{16}$ molecules J^{-1} for an Ar/ATI mixture while for an Ar/N_2/ATI mixture, $F_E = 4 \cdot 10^{16}$ molecules J^{-1}. Both evolve to $1.2 \cdot 10^{16}$ molecules J^{-1} at P= 100 W.

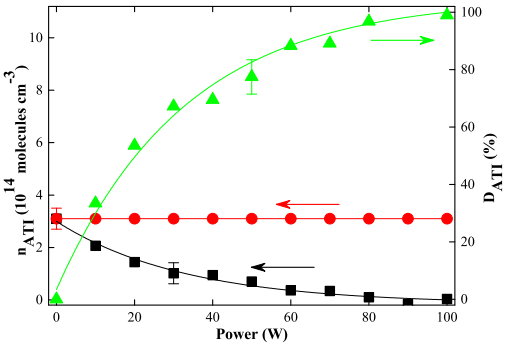

Figure 7.14: Concentration of ATI with - ■, and without - ● plasma operation as well as the degree of dissociation - ▲ of ATI as a function of the discharge power in an Ar/N_2/ATI plasma. p_{total}= 6 Pa, gas ratio Ar/N_2/ATI= 1/1/1.

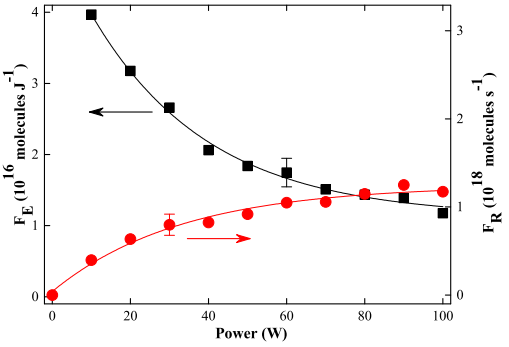

Figure 7.15: Fragmentation efficiency and fragmentation rate, both - ●, of ATI as a function of the discharge power in an Ar/N_2/ATI plasma. p_{total}= 6 Pa, gas ratio Ar/N_2/ATI= 1/1/1.

An Ar/N_2/ATI mixture with varying N_2/ATI gas ratio has also been studied. The

total initial pressure has been kept at 6 Pa and the RF power at 80 W. The pressure of Ar has been kept constant at 2 Pa. Figure 7.16 shows the ATI concentration and the degree of dissociation as a function of the N_2/ATI mixing ratio. The degree of dissociation reached a value of about 100% for low ATI partial pressures, i.e. p < 2 Pa, and decreases down to 76% for higher ATI pressure values. At an ATI pressure of p= 3 Pa, D_{ATI} exhibits a constant level up to an ATI pressure of p= 4 Pa. The fragmentation efficiency and rate (Fig. 7.17) show a linear increase over the entire range of the mixing ratio. The fragmentation efficiency increases linearly from $0.2 \cdot 10^{16}$ molecules J^{-1} to $3 \cdot 10^{16}$ molecules J^{-1}, whereas the fragmentation rate increases linearly from $0.2 \cdot 10^{18}$ molecules s^{-1} to $2.3 \cdot 10^{18}$ molecules s^{-1}. Taking into account the reduced absolute number of the ATI density in the Ar/N_2/ATI plasma. Figs. 7.16 and 7.17 are similar to Figs. 7.9 and 7.10 obtained in an Ar/ATI plasma.

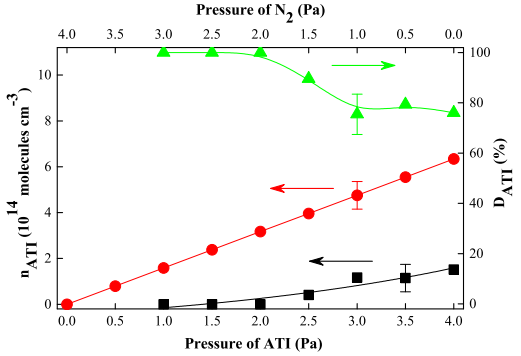

Figure 7.16: Concentration of ATI with - ■ and without - ● plasma operation as well as the degree of dissociation - ▲ of ATI as a function of the mixing gas ratio of N_2 and ATI, given in pressure values. p_{total}= 6 Pa, p_{Ar}= 2 Pa, P_{Plasma}= 80 W.

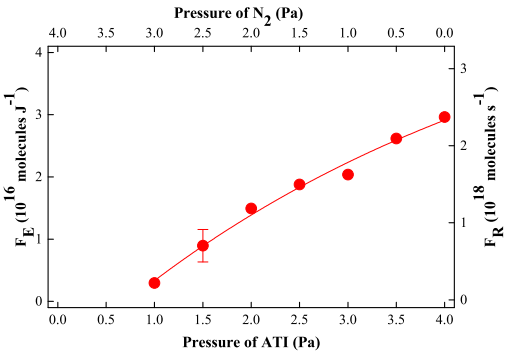

Figure 7.17: Fragmentation efficiency and fragmentation rate, both - ●, of ATI as a function of the mixing gas ratio of N_2 and ATI, given in pressure values. p_{total} = 6 Pa, p_{Ar}= 2 Pa and P_{plasma} = 80 W.

7.2.4.1 By-product formation

Figure 7.18 shows the concentrations of the by-products of an Ar/N_2/ATI plasma. Basically, the same hydrocarbons are formed as in an Ar/ATI plasma (Fig. 7.11) except HCN that starts to be detectable at P= 20 W, with a concentration of $0.8 \cdot 10^{13}$ molecule cm^{-3}. Despite a reduced absolute number density of ATI compared to the Ar/ATI plasma (Fig. 7.11), the concentrations of CH_4, C_2H_4, C_2H_6 and CO show nearly the same behavior.

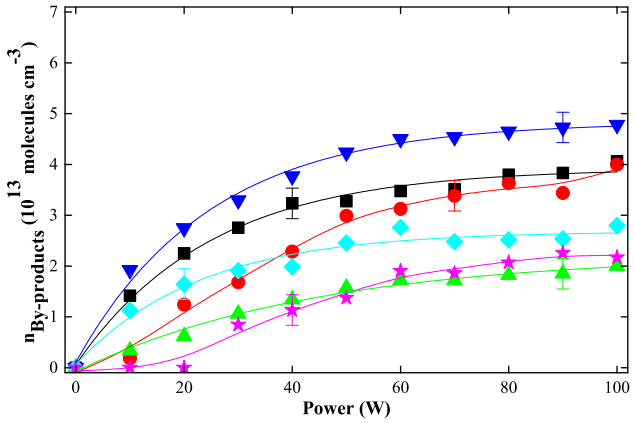

Figure 7.18: Concentration of CH_4 - ■, C_2H_2 - ●, C_2H_4 - ▲, C_2H_6 - ▼ and CO - ♦ and HCN - ★ as a function of the discharge power in an Ar/N_2/ATI plasma. p_{total} = 6 Pa and gas ration Ar/N_2/ATI= 1/1/1.

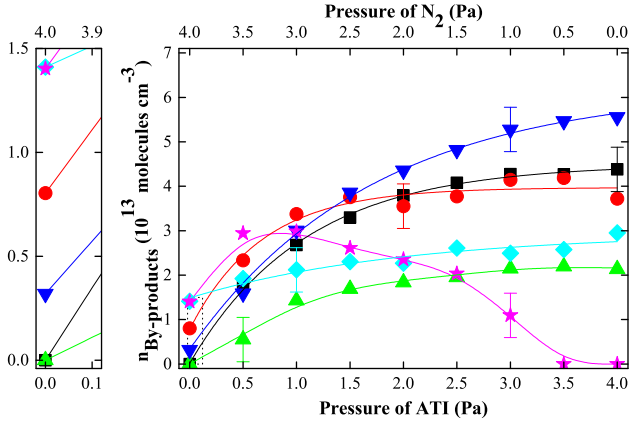

Figure 7.19: Concentration of CH_4 - ■, C_2H_2 - ●, C_2H_4 - ▲, C_2H_6 - ▼ and CO - ♦ and HCN - ★ as a function of the mixing gas ratio of N_2 and ATI. p_{total} = 6 Pa, p_{Ar}= 2 Pa and P_{plasma} = 80 W.

The concentrations of the by-products of an Ar/N_2/ATI plasma as a function of the mixing ratio are given in Fig. 7.19. The species concentrations of CH_4, C_2H_2, C_2H_4 and C_2H_6 show an increase as a function of the ATI pressure while the behavior of HCN is characterized by a maximum at a partial pressure of about p= 1 Pa. In contrast, the concentration of CO increases only slightly. Its concentration starts at $1.5 \cdot 10^{13}$ molecules cm^{-3} without ATI admixed and growths linearly up to $3 \cdot 10^{13}$ molecules cm^{-3} for P= 4 Pa, i.e. for the maximum partial pressure of ATI. It is interesting to note, that the reaction products C_2H_2, C_2H_6, CO and HCN show already a distinct level

of concentration even without supplying any ATI to the plasma chamber, i.e. at p= 0 Pa partial pressure of ATI. Therefore, under these conditions another source for the by-products had to be considered. It can be supposed, that mainly ATI or fragments of ATI deposited at the inner surfaces of the reactor act as a source for the production of by-products in this case.

7.3 Conclusion

In this Chapter, some preliminary results are presented from a campaign of experiments performed in Kiel using Fourier Transform Infrared spectroscopy. Aluminium triisopropoxide is injected into the ATILA reactor in the gas phase and its dissociation in the plasma is investigated using many gas mixtures. The density, the dissociation, the fragmentation rate and efficiency are studied as a function of the pressure and the discharge power. The density evolution of the formed by-products is also detailed. It is shown that the dissociation of ATI increases with the power. However, the degree of dissociation decreases with the total pressure at constant power and gas ratio. When the gas ratio (Ar/ATI) is varied, the degree of ATI dissociation is higher when the partial ATI pressure is higher. It is shown that nitrogen does not have an influence on the dissociation of the ATI. The hydrocarbon compound evolution is also detailed. These compounds can be at the origin of dust particle formation [167, 168] that can be investigated in a future work. Most of these analyses are performed by Dr. Marko Hübner (INP Greifswald). Some calculations are still in progress such as the carbon balance. Since the precursor gas contains a lot of carbon, the carbon balance allows one to study the deposition process and, therefore, the quality of the layers.

7.4 French Summary

Dans ce chapitre, quelques résultats préliminaires sont présentés issus d'expériences réalisées à Kiel en utilisant la spectroscopie infrarouge à transformée de Fourier.

L'aluminium triisopropoxide est injectée dans le réacteur ATILA en phase gazeuse et sa dissociation dans le plasma est analysée en utilisant de nombreux mélanges de gaz. La densité, la dissociation, le taux et l'efficacité de fragmentation sont étudiés en fonction de la pression et de la puissance de décharge. Par exemple, il est montré que la dissociation de l'ATI augmente avec la puissance. Cependant, le degré de dissociation diminue avec la pression totale à puissance et rapport de gaz constants. L'évolution des composants hydrocarbonés formés est également détaillée. Ces composants peuvent

être à l'origine de la formation de poudres, processus qui pourra être étudié dans l'avenir. La plupart des analyses présentées ont été effectuées par Dr. Marko Hübner (INP Greifswald). Certains calculs sont toujours en cours comme le bilan carbone.

Chapter 8

General Conclusion

Plasmas are strongly present in the universe (the Sun, stars and lightning) and become more and more present in many fields of research, industry and technology. For instance nowadays, one of the major concerns is to create a clean energy. For this purpose, an international facility called ITER is under construction with the objective to prove the practicability of continuous fusion energy production at the industrial scale. Plasma medicine is also an emerging field that combines plasma physics, life sciences and clinical medicine to use physical plasma for therapeutic applications. Beside these "ordinary" plasmas, dusty plasmas are characterized by an additional charged component: dust particles. Astrophysicists are highly interested in this field due to the presence of dusty plasmas in many astrophysical environments like comet tails, planetary nebulae and rings. In the late 80s, during the microelectronics fabrication process, engineers encountered a significant problem due to the presence of these dust particles in the plasma. Once the discharge is switched off, dust particles fall on wafers and can affect seriously semiconductor device performances. In fact, these particles are grown in the plasma itself, either by using reactive gases, surface sputtering or etching. The presence of dust particles in a plasma, besides electrons, positive and negative ions, has a big effect on the system and can change its properties like the electron density and temperature. During their growth, dust particles acquire a negative charge by capturing electrons and can experience several forces such as gravity, electrostatic force, thermophoresis, neutral drag and ion drag forces.

In the main part of this thesis, carbonaceous dust particles are created by sputtering a polymer layer deposited on the bottom electrode of a capacitively coupled radio-frequency discharge. The formation of a high dust density in the plasma can cause an important loss of free electrons leading to a disturbance of the plasma equilibrium. Unstable behaviors can be observed like dust particle growth instabilities

(DPGI). Different diagnostics are used in order to characterize these phenomena resulting from complex plasma-dust particle interactions: Electrical measurements, high speed imaging and Laser Induced Fluorescence. In order to estimate the role of the ion mass, argon or krypton are used as the sputtering gas. Thanks to the electrical measurements, the amplitude of the discharge current is studied during DPGI. Different instability regimes are evidenced, from the first ordered phases to the last ordered one, passing through stochastic phases. The electrical signal form and the frequency evolution are studied in each phase during the evolution of the instability. DPGI evolution as a function of the pressure is detailed. It appears that the higher the pressure, the shorter the appearance time, the longer the duration and the higher the frequencies. These results are consistent with the conclusions deduced from the DC component of the electrical signals: at high pressure the growth kinetics is faster, the dust density is higher and the dust size is smaller. The fact that a high dust density is connected to a small dust particle size is also confirmed by direct visual observations. The frequency drop phase is investigated showing the three peak evolution that becomes more stochastic at high pressure.

A comparison of the instability evolution is performed between argon and krypton plasmas. The evolution of the frequencies is quite different in both case. The decrease of the DC component in the krypton case is faster than in the argon case. In particular, it appears that DPGI frequencies are globally higher in Kr than in Ar. In addition, due to the mass discrepancy in between argon and krypton, the sputtering efficiency is certainly different and the gas phase reactions leading to the dust particle growth can be modified. These results show that with Kr, the dust particle density is much higher than in Ar (and therefore the dust size is smaller). A conclusive proof would consist in the measuring dust particle size and density during their growth. Unfortunately, for the moment, in situ diagnostics cannot be easily implemented on our experimental setup.

Thanks to the high speed imaging, the evolution of the plasma glow at the beginning of dust particle growth instabilities is investigated. A correlation between optical and electrical measurements is discussed. It shows that a big amplitude peak corresponds to the rise of the luminosity in the plasma center, while a small amplitude peak is related to bright regions appearing at the edges of the plasma bulk.

The appearance of plasma spheroids in the discharge is also investigated. Several types of plasma spheroid behaviors are presented in argon and krypton plasmas. Experiments on the rotation of a single spheroid along the circumference of the electrode show that the increase of the discharge power induces a slight increase of the rotation

speed. The spheroid appearance and behavior at the vicinity of the electrode is then correlated with the variation of the plasma luminosity in the discharge central part.

Complex interactions between spheroids in the discharge center are observed and investigated. These interactions consist of up and down motions, merging of two spheroids into a single one and the splitting of a spheroid into two. These behaviors show phenomenological similarities with some phenomena observed in other types of plasmas. they open very interesting questions about possible attraction or repulsion between these small plasma regions.

Thanks to the Laser Induced Fluorescence diagnostic, DPGI evolution as a function of time is described and compared to the electrical measurements. The increase of the LIF signal during dust particle growth is evidenced. It is related to the increase of the electron temperature expected in the presence of dust particles. The excited neutral density distribution inside and outside the void is also determined. Results show that the LIF signal is higher in the void region. This effect corresponds to an higher electron density in the void. Some improvements will be performed in order to study the ion density inside and outside the void, as the void is due to a balance between ion drag force and electrostatic force.

In the last Chapter, an investigation is performed on a capacitively coupled radio-frequency discharge located in Kiel. The chemistry of the plasma is studied using Fourier Transform Infrared spectroscopy. The dissociation and fragmentation of aluminium triisopropoxide is studied as a function of the discharge power and mixing ratio pressures. Hydrocarbon compounds are formed in the plasma. These compounds can be source of dust particle formation that can be investigated in a future work.

8.1 French Summary

Les plasmas sont très présents dans l'univers (le soleil, les étoiles et la foudre) et deviennent de plus en plus présents dans de nombreux domaines de la recherche, de l'industrie et de la technologie. De nos jours, l'une des principales préoccupations est de créer une énergie propre. Pour cela, un complexe international appelé ITER est en cours de construction dans le but de démontrer la possibilité de la production de l'énergie de fusion à l'échelle industrielle. La "médecine plasma" est également un domaine émergent qui combine la physique des plasmas, les sciences de la vie et la médecine clinique afin d'utiliser le plasma physique pour des applications thérapeutiques. En plus de ces plasmas "ordinaires", les plasmas poudreux se caractérisent par une com-

posante supplémentaire chargée: les poudres. Les astrophysiciens sont très intéressés par ce domaine du fait de la présence des plasmas poudreux dans de nombreux environnements astrophysiques comme les queues de comètes, les nébuleuses et les anneaux planétaires. Vers la fin des années 80, durant le processus de fabrication des composants microélectroniques, les ingénieurs ont rencontré un problème en raison de la présence de ces poudres dans le plasma. Une fois que la décharge est éteinte, les poudres tombent sur les wafers et peuvent affecter sérieusement les performances des dispositifs semiconducteurs. En fait, ces poudres sont formées dans le plasma lui-même, soit du fait de l'utilisation de gaz réactifs, soit à cause de la pulvérisation des surfaces exposées au plasma. La présence des poudres perturbe et modifie les propriétés du plasma. Durant leur croissance, les poudres aquièrent une charge négative en capturant des électrons et elles peuvent être influencées par différentes forces.

Dans une grande partie de cette thèse, les poudres à base de carbone sont créées par pulvérisation d'une couche de polymère déposée sur l'électrode inférieure d'une décharge radio fréquence à couplage capacitif. La croissance d'une forte densité de poudres dans le plasma peut causer une importante perte d'électrons conduisant à une perturbation du plasma. Des comportements instables peuvent être observés comme les instabilités de croissance des poudres. Differents diagnostics sont utilisés pour caractériser les phénomènes résultant des interactions plasma/poudres: mesures électriques, imagerie rapide et la fluorescence induite par laser.

A l'aide des mesures électriques, l'amplitude du courant de décharge est étudiée durant les instabilités. Différents régimes d'instabilité sont mis en évidence, depuis les premières phases ordonnées jusqu'à la dernière phase, en passant par des phases stochastiques. La forme du signal électrique et l'évolution de la fréquence durant les instabilités sont étudiées notamment en fonction de la pression du gaz. On conclut que quand la pression est élevée, le temps d'apparition des instabilités est court, leur durée est longue, et leurs fréquences caractéristiques sont plus grandes. Ces résultats sont cohérents avec l'observation de la composante continue (DC) des signaux électriques confirmant qu'à forte pression la cinétique de croissance des poudres est plus rapide, leur densité est plus élevé et leur taille est plus petite. La relation entre la forte densité de poudres et leur petite taille est aussi confirmée par une observation visuelle.

Une comparaison de l'évolution de l'instabilité est effectuée entre l'argon et le krypton. L'évolution des fréquences est trés différente dans les deux cas. la diminution de la composante continue (DC) dans le cas du krypton est plus rapide que dans le cas de l'argon. En particulier, il apparait que les fréquences de l'instabilité sont globalement plus élevées en Kr qu'en Ar. En raison de la difference de masse entre l'argon et le

krypton, le taux de pulvérisation est certainement different et les réactions en phase gazeuse conduisant à la croissance des poudres peuvent être modifiées. Des mesures de la taille et de la densité des poudres durant leur croissance apporteraient de précieuses informations. Malheureusement, pour le moment, un diagnostic in situ ne peut pas être facilement mis en place sur notre dispositif expérimental.

A l'aide de l'imagerie rapide, l'évolution de la luminosité du plasma au début des instabilités de croissance des poudres est étudiée. Une corrélation entre l'évolution optique de l'instabilité et les mesures électriques (suivant une structure à trois pics) est observée. Elle montre que le grand pic correspond à l'augmentation de la luminosité au centre de la décharge, tandis que les petits pics sont liés aux régions lumineuses apparaissant sur les bords du plasma.

Durant l'instabilité, l'apparition de petites "boules" de plasma (sphéroides) dans la décharge est également étudiée. Plusieurs types de comportements sont présentés. Dans les plasmas d'argon, la rotation d'un sphéroide le long de la circonférence de l'électrode est étudiée. Des expériences sont réalisées afin d'observer l'influence de la puissance de décharge sur le comportement du sphéroide. Une augmentation de la vitesse de rotation est observée avec l'augmentation de la puissance. Le comportement des sphéroides au voisinage de l'électrode est corrélé avec la variation de la luminosité du plasma au centre de la décharge. Des interactions complexes entre les sphéroides au centre du plasma ont été observées et analysées. Des mouvements verticaux des sphéroides, la fusion de deux sphéroides en un seul, et la séparation d'un sphéroide en deux sont observés. Ces comportements présentent des similarités avec certains phénomènes observés dans d'autres types de plasmas. Cela soulève de nombreuses questions sur les phénomènes physique à l'origine de l'attraction et de la répulsion entre ces petites régions de plasma.

A l'aide de la fluorescence induite par laser, l'évolution de l'instabilité en fonction du temps est analysée et comparée aux mesures électriques. L'augmentation du signal de LIF pendant la croissance des poudres est mis en évidence. Elle est liée à l'augmentation de la température des électrons attendue en présence de poudres. La répartition de densité des neutres excités à l'intérieur et à l'extérieur du void est également déterminée. Les résultats montrent que le signal de LIF est plus élevé dans la région de void. Cet effet correspond à une densité d'électrons supérieure dans le void. Certaines améliorations seront effectuées afin d'étudier la densité ionique. En effet, le void étant dû à l'équilibre entre la force ionique et la force électrostatique, une mesure de la population ionique est fondamentale.

Dans le dernier chapitre, une étude est effectuée sur une décharge radiofréquence située à Kiel en Allemagne. La chimie du plasma est étudiée à l'aide de la Spectro-

scopie Infrarouge à Transformée de Fourier. La dissociation et la fragmentation de l'aluminium triisopropoxide sont étudiées en fonction de la puissance de décharge et du mélange des gaz. Des composants d'hydrocarbures sont alors formés dans le plasma. Ces composants peuvent être à l'origine de la formation des poudres, processus qui pourra être étudié dans l'avenir.

References

[1] P. Bradu. *L'Univers des Plasmas*. Flammarion, 1999. 1

[2] N. F. Ness. Observed properties of the interplanetary plasma. *Annu. Rev. Astron. Astrophys.*, 6:79, 1968. 1

[3] I. Langmuir. Positive ion currents from the positive column of mercury arcs. *Science*, 58:290, 1923. 2

[4] I. Langmuir. The interaction of electron and positive ion space charges in cathode sheaths. *Phys. Rev.*, 33:954, 1929. 2

[5] L. Tonks and I. Langmuir. Oscillations in ionized gases. *Phys. Rev.*, 33:195, 1929. 2

[6] V. A. Nemchinsky and W. S. Severance. What we know and what we do not know about plasma arc cutting. *J. Phys. D: Appl. Phys*, 39:R423, 2006. 2

[7] M. Vandamme, E. Robert, S. Pesnel, E. Barbosa, S. Dozias, J. Sobilo, S. Lerondel, A. Le Pape, and J.-M. Pouvesle. Antitumor Effect of Plasma Treatment on U87 Glioma Xenografts: Preliminary Results. *Plasma Process. Polym.*, 7:264, 2010. 2

[8] P. K. Shukla and A. A. Mamun. *Introduction to Dusty Plasma Physics*. IOP Publishing, Bristol, 2002. 2

[9] C. K. Goertz and G. E. Morfill. A model for the formation of spokes in Saturn's ring. *Icarus*, 53:219, 1983. 2, 3

[10] C. J. Mitchell, M. Horányi, O. Havnes, and C. C. Porco. Saturn's spokes: Lost and found. *Science*, 311:1587, 2006. 2, 3

[11] J. R. Hill and D. A. Mendis. On the braids and spokes in Saturn's ring system. *Earth, Moon, and Planets*, 24:431, 1981.

[12] B. A. Smith, L. Soderblom, R. Beebe, J. Boyce, G. Briggs, A. Bunker, S. A. Collins, C. J. Hansen, T. V. Johnson, J. L. Mitchell, R. J. Terrile, M. Carr, A. F. Cook II, J. Cuzzi, J. B. Pollack, G. E. Danielson, A. Ingersoll, M. E. Davies, G. E. Hunt, H. Masursky, E. Shoemaker, D. Morrison, T. Owen, C. Sagan, J. Veverka, R. Strom, and V. E. Suomi. Encounter with Saturn: Voyager 1 imaging science results. *Science*, 212:163, 2012.

[13] E. Grün, G. E. Morfill, R. J. Terrile, T. V. Johnson, and G. Schwehm. The evolution of spokes in Saturn's B ring. *Icarus*, 54:227, 1983. 3

[14] I. Langmuir, C. G. Found, and A. F. Dittmer. A new type of electric discharge: the streamer discharge. *Science*, 60:392, 1924. 3

[15] A. C. Breslin and K. G. Emeleus. The distinction between negative ions and charged dust in plasmas. *Int. J. Electron.*, 31:189, 1971. 3

[16] K. G. Emeleus and A. C. Breslin. Note on dust in positive columns. *Int. J. Electron.*, 30:273, 1971. 3

[17] T. C. Anestos and C. D. Hendricks. Injection of small macroscopic particles into plasmas as a diagnostic technique. *J. Appl. Phys.*, 43:1176, 1974. 3

[18] G. S. Selwyn, J. E. Heidenreich, and K. L. Haller. Particle trapping phenomena in radio frequency plasmas. *Appl. Phys. Lett.*, 57:1876, 1990. 4

[19] G. S. Selwyn, J. Singh, and R. S. Bennett. In situ laser diagnostic studies of plasma generated particulate contamination. *J. Vac. Sci. Technol. A*, 7:2758, 1989. 4

[20] G. S. Selwyn. Optical characterization of particle traps. *Plasma Sources Sci. Technol.*, 3:340, 1994. 4

[21] A. Bouchoule, A. Plain, L. Boufendi, J. Ph. Blondeau, and C. Laure. Particle generation and behavior in a silane-argon low-pressure discharge under continous or pulsed radio-frequency excitation. *J. Appl. Phys.*, 70:1991, 1991. 4

[22] K. Narihara, K. Toi, Y. Hamada, K. Yamauchi, K. Adachi, I. Yamada, K. N. Sato, K. Kawahata, A. Nishizawa, S. Ohdachi, K. Sato, T. Seki, T. Watari,

J. Xu, A. Ejiri, S. Hirokura, K. Ida, Y. Kawasumi, and M. Kojima. Observation of dust particles by a laser scattering method in the JIPPT-IIU tokamak. *Nucl. Fusion*, 37:1177, 1997. 4

[23] J. Winter. Dust in fusion devices - experimental evidence, possible sources and consequences. *Plasma Phys. Control. Fusion*, 40:1201, 1998.

[24] V. N. Tsytovich and J. Winter. On the role of dust in fusion devices. *Phys. Usp.*, 41:815, 1998.

[25] J. Winter, V. E. Fortov, and A. P. Nefedov. Radioactive dust levitation and its consequences for fusion devices. *J. Nucl. Mater.*, 290-293:509, 2001. 4

[26] J. D. Martin, M. Coppins, and G. F. Counsell. Motion and lifetime of dust grains in a tokamak plasma. *J. Nucl. Mater.*, 337-339:114, 2005.

[27] C. Castaldo, S. Ratynskaia, V. Pericoli, U. de Angelis, K. Rypdal, L. Pieroni, E. Giovannozzi, G. Maddaluno, C. Marmolino, A. Rufoloni, A. Tuccillo, M. Kretschmer, and G. E. Morfill. Diagnostics of fast dust particles in tokamak edge plasmas. *Nucl. Fusion*, 47:L5, 2007. 4

[28] P. Roca i Cabarrocas, R. Cariou, and M. Labrune. Low temperature plasma deposition of silicon thin films: From amorphous to crystalline. *J. Non-Cryst. Solids*, 358:2000, 2012. 4

[29] A. Dutta, Y. Hayafune, and S. Oda. Single electron memory devices based on plasma-derived silicon nanocrystals. *Jpn. J. Appl. Phys.*, 39:L855, 2000. 4

[30] E. Stoffels, W. W. Stoffels, G. Ceccone, R. Hasnaoui, H. Keune, and G. Wahl. MoS_2 nanoparticle formation in a low pressure environment. *J. Appl. Phys.*, 86: 3442, 1999. 4

[31] T. Ishigaki, T. Sato, Y. Moriyoshi, and M. I. Boulos. Influence of plasma modification of titanium carbide powder on its sintering properties. *J. Mater. Sci. Lett.*, 14:1694, 1995. 4

[32] A. A. Howling, Ch. Hollenstein, and P. J. Paris. Direct visual observation of powder dynamics in rf plasma - assisted deposition. *Appl. Phys. Lett.*, 59:1409, 1991. 4

[33] S. Hong, J. Berndt, and J. Winter. Growth precursors and dynamics of dust particle formation in the Ar/CH_4 and Ar/C_2H_2. *Plasma Sources Sci. Technol.*, 12:46, 2003.

[34] E. Kovačević, J. Berndt, T. Strunskus, and L. Boufendi. Size dependent characteristics of plasma synthesized carbonaceous nanoparticles. *J. Appl. Phys.*, 112: 013303, 2012.

[35] M. Calafat, P. Yuryev, A. Drenik, A. Slim, and R. Clergereaux. Carbon Nanoparticle/Hydrogenated amorphous carbon composite thin films formed in ECR plasma. *Plasma Process. Polym.*, 8:401, 2011.

[36] M. Hundt, P. Sadler, I. Levchenko, M. Wolter, H. Kersten, and K. Ostrikov. Real-time monitoring of nucleation-growth cycle of carbon nanoparticles in acetylene plasmas. *J. Appl. Phys.*, 109:123305, 2011. 27

[37] B. Despax, K. Makasheva, and H. Caquineau. Cyclic powder formation during pulsed injection of hexamethyldisiloxane in an axially asymmetric radiofrequency argon discharge. *J. Appl. Phys.*, 112:093302, 2012.

[38] F. Greiner, J. Carstensen, N. Kohler, I. Pilch, H. Ketelsen, S. Knist, and A. Piel. Imaging Mie ellipsometry: dynamics of nanodust clouds in an argon-acetylene plasma. *Plasma Sources Sci. Technol.*, 21:065005, 2012. 4

[39] A. Michau, G. Lombardi, L.C. Delacqua, M. Redolfi, C. Arnas, P. Jestin, X. Bonnin, and K. Hassouni. Field reversal and particle growth in dc discharge. *Plasma Chem. Plasma Process*, 32:451, 2012. 4

[40] G. Praburam and J. Goree. Experimental observation of very low-frequency macroscopic modes in a dusty plasma. *Phys. Plasmas*, 3:1212, 1996. 6, 23

[41] D. Samsonov and J. Goree. Instabilities in a dusty plasma with ion drag and ionization. *Phys. Rev. E*, 59:1047, 1999. 6, 23, 44

[42] C. Arnas and A. A. Mouberi. Thermal balance of carbon nanoparticles in sputtering discharges. *J. Appl. Phys.*, 105:063301, 2009. 4

[43] H. Kersten, P. Schmetz, and G. M. W. Kroesen. Surface modification of powder particles by plasma deposition of thin metallic films. *Surf. Coat. Tech.*, 108:507, 1998. 4

[44] H. Thomas, G. E. Morfill, V. Demmel, J. Goree, B. Feuerbacher, and D. Möhlmann. Plasma crystal: Coulomb crystallization in a dusty plasma. *Phys. Rev. Lett.*, 73:652, 1994. 5

[45] G. E. Morfill, H. M. Thomas, U. Konopka, and M. Zuzic. The plasma condensation: Liquid and crystalline plasmas. *Phys. Plasmas*, 6:1769, 1999.

[46] M. Schwabe, L.-J. Hou, S. Zhdanov, A. V. Ivlev, H. M. Thomas, and G. E. Morfill. Convection in a dusty radio-frequency plasma under the influence of a thermal gradient. *New. J. Phys.*, 13:083034, 2011.

[47] V. Land, J. Carmona-Reyes, J. Creel, J. Schmoke, M. Cook, L. Matthews, and T. Hyde. The effect of electrode heating on the discharge parameters in complex plasma experiments. *Plasma Sources Sci. Technol.*, 20:015026, 2011.

[48] S. Iwashita, E. Schüngel, J. Schulze, P. Hartmann, Z. Donkó, G. Uchida, K. Koga, M. Shiratani, and U. Czarnetzki. Transport control of dust particles via the electrical asymmetry effect: experiment, simulation and modelling. *J. Phys. D: Appl. Phys.*, 46:245202, 2013. 4

[49] L. Boufendi and A. Bouchoule. Industrial developments of scientific insights in dusty plasmas. *Plasma Sources Sci. Technol.*, 11:A211, 2002. 4

[50] A. Bouchoule and L. Boufendi. Particle formation and dusty plasma behaviour in argon-silane rf discharge. *Plasma Sources Sci. Technol.*, 2:204, 1993. 4

[51] L. Boufendi, A. Plain, J. Ph. Blondeau, A. Bouchoule, C. Laure, and M. Toogood. Measurements of particle size kinetics from nanometer to micrometer scale in a low pressure argon silane radiofrequency discharge. *Appl. Phys. Lett.*, 60:169, 1992.

[52] E. Stoffels, W. W. Stoffels, G. M. W. Kroesen, and F. J. de Hoog. Dust formation and charging in an Ar/SiH_4 radio-frequency discharge. *J. Vac. Sci. Technol. A*, 14:556, 1996. 4

[53] N. N. Rao, P. K. Shukla, and M. Y. Yu. Dust–acoustic waves in dusty plasmas. *Planet. Space Sci.*, 38:543, 1990. 5

[54] A. Barkan, R. L. Merlino, and N. D′Angelo. Laboratory observation of the dust acoustic wave mode. *Phys. Plasmas*, 2:3563, 1995.

[55] J. B. Pieper and J. Goree. Dispersion of plasma dust acoustic waves in the strong coupling regime. *Phys. Rev. Lett.*, 77:3137, 1996.

[56] P. K. Kaw and A. Sen. Low frequency modes in strongly coupled dusty plasmas. *Phys. Plasmas*, 5:3552, 1998.

[57] C. Thompson, A. Barkan, N. D′Angelo, and R. L. Merlino. Dust acoustic waves in a direct current glow discharge. *Phys. Plasmas*, 4:2331, 1997.

[58] E. Thomas Jr, R. Fisher, and R. L. Merlino. Observations of dust acoustic waves driven at high frequencies: Finite dust temperature effects and wave interference. *Phys. Plasmas*, 14:12701, 2007.

[59] M. Schwabe, K. Jiang, S. Zhdanov, T. Hagl, P. Huber, A. M. Lipaev A. V. Ivlev, V. I. Molotkov, V. N. Naumkin, K. R. Sütterlin, H. M. Thomas, V. E. Fortov, G. E. Morfill, A. Skvortsov, and S. Volkov. Direct measurement of the speed of sound in a complex plasma under microgravity conditions. *Europhys. Lett.*, 96: 55001, 2011. 5

[60] A. Melzer, T. Trottenberg, and A. Piel. Experimental determination of the charge on dust particles forming coulomb lattices. *Phys. Lett. A*, 191:301, 1994. 5

[61] V. E. Fortov, A. P. Nefedov, V. M. Torchinsky, V. I. Molotkov, O. F. Petrov, A. A. Samarian, A. M. Lipaev, and A. G. Khrapak. Crystalline structures of strongly coupled dusty plasmas in dc glow discharge strata. *Phys. Lett. A*, 229: 317, 1997. 5

[62] V. E. Fortov, A. P. Nefedov, V. M. Torchinskii, V. I. Molotkov, A.G. Khrapak, O. F. Petrov, and K. F. Volykhin. Crystallization of a dusty plasma in the positive column. *JEPT Lett.*, 64:86, 1996. 5

[63] V. E. Fortov, A. P. Nefedov, V. I. Vladimirov, L. V. Deputatova, V. I. Molotkov, V. A. Rykov, and A. V. Khudyakov. Dust particles in a nuclear induced plasma. *Phys. Lett. A*, 258:305, 1999. 5

[64] N. Reinke and D. Gonzalez. TEXUS - DLR, 2009. URL `http://www.dlr.de/rd/desktopdefault.aspx/tabid-2282/3421_read-5228/`. 5

[65] G. E. Morfill, H. M. Thomas, U. Konopka, H. Rothermel, M. Zuzic, A. Ivlev, and J. Goree. Condensed Plasmas under Microgravity. *Phys. Rev. Lett.*, 83:1598, 1999. 5, 23

[66] A. P. Nefedov, G. E. Morfill, V. E. Fortov, H. M. Thomas, H. Rothermel, T. Hagl, A. Ivlev, M. Zuzic, B. A. Klumov, A. M. Lipaev, V. I. Molotkov, O. F. Petrov, Y. P. Gidzenko, S. K. Krikalev, W. Shepherd, A. I. Ivanov, M. Roth, H. Binnenbruck, J. Goree, and Y. P. Semenov. PKE-Nefedov: plasma crystal experiments on the International Space Station. *New J. Phys.*, 5:33, 2003. 5, 6, 25

[67] M. Mikikian, L. Boufendi, A. Bouchoule, H. M. Thomas, G. E. Morfill, A. P. Nefedov, V. E. Fortov, and the PKE-Nefedov Team. Formation and behaviour of dust particle clouds in a radio-frequency discharge: results in the laboratory and under microgravity conditions. *New J. Phys.*, 5:19, 2003. 5, 6, 23, 25

[68] H. M. Thomas, G. E. Morfill, V. E. Fortov, A. V. Ivlev, V. I. Molotkov, A. M. Lipaev, T. Hagl, H. Rothermel, S. A. Khrapak, R. K. Sütterlin, M. Rubin-Zuzic, O. F. Petrov, V. I. Tokarev, and S. K. Krikalev. Complex plasma laboratory PK-3 plus on the International Space Station. *New. J. Phys.*, 10:033036, 2008. 5

[69] M. H. Thoma, H. Höfner, M. Kretschmer, S. Ratynskaia, G. E. Morfill, A. Usachev, A. Zobnin, O. Petrov, and V. Fortov. Parabolic flight experiments with PK-4. *Microgravity Sci. Technol.*, 18:47, 2006. 5

[70] A. V. Ivlev, M. H. Thoma, C. Räth, G. Joyce, and G. E. Morfill. Complex plasmas in external fields: The role of non-hamiltonian interactions. *Phys. Rev. Lett.*, 106:155001, 2011.

[71] L. Wörner. *Tuning the interaction potential in complex plasmas.* PhD thesis, 2012.

[72] S. Mitic, B. A. Klumov, S. A. Khrapak, and G. E. Morfill. Three dimensional complex plasma structures in a combined radio frequency and direct current discharge. *Phys. Plasmas*, 20:043701, 2013. 5

[73] M. Mikikian, M. Cavarroc, L. Couëdel, and L. Boufendi. Low frequency instabilities during dust particle growth in a radio-frequency plasma. *Phys. Plasmas*, 13:092103, 2006. 6, 44, 46

[74] M. Mikikian, L. Couëdel, M. Cavarroc, Y. Tessier, and L. Boufendi. Dusty plasmas: synthesis, structure and dynamics of a dust cloud in a plasma. *Eur. Phys. J. Appl. Phys.*, 49:13106, 2010. 6, 52

[75] M. Mikikian, L. Couëdel, Y. Tessier, and L. Boufendi. Carousel instability in a capacitively-coupled rf dusty plasma. *IEEE Trans. Plasma Sci.*, 39:2748, 2011. 6, 65

[76] M. Mikikian, M. Cavarroc, L. Couëdel, Y. Tessier, and L. Boufendi. Dust particles in low-pressure plasmas: Formation and induced phenomena. *Pure Appl. Chem.*, 82:1273, 2010. 6

[77] L. Couëdel, M. Mikikian, A. A. Samarian, and L. Boufendi. Self-excited void instability during dust particle growth in a dusty plasma. *Phys. Plasmas*, 17: 083705, 2010. 6, 85

[78] M. Mikikian and L. Boufendi. Experimental investigations of void dynamics in a dusty discharge. *Phys. Plasmas*, 11:3733, 2004. 6

[79] M. Mikikian, L. Couëdel, M. Cavarroc, Y. Tessier, and L. Boufendi. Threshold phenomena in a throbbing complex plasma. *Phys. Rev. Lett.*, 105:075002, 2010. 6, 85

[80] K. Avinash, A. Bhattacharjee, and S. Hu. Nonlinear theory of void formation in colloidal plasmas. *Phys. Rev. Lett.*, 90:075001, 2003. 6

[81] V. N. Tsytovich, S. V. Vladimirov, and G. E. Morfill. Theory of dust and dust-void structures in the presence of the ion diffusion. *Phys. Rev. E*, 70:066408, 2004. 6, 85

[82] M. R. Akdim and W. J. Goedheer. Modeling of voids in colloidal plasmas. *Phys. Rev. E*, 65:015401, 2001. 6

[83] A. Gleizes, M. M. Sovar, D. Samélor, and C. Vahlas. Low temperature MOCVD-processed alumina coatings. *Advances in Science and Technology*, 45:1184, 2006. 6

[84] S. Blittersdorf, N. Bahlawane, K. Kohse-Höinghaus, B. Atakan, and J. Müller. CVD of Al_2O_3 thin films using aluminium tri-isopropoxide. *Chem. Vap. Deposition*, 9:194, 2003.

[85] H. Kersten, G. Thieme, M. Fröhlich, D. Bojic, D. H. Tung, M. Quaas, H.Wulff, and R. Hippler. Complex (dusty) plasmas: Examples for applications and observation of magnetron induced phenomena. *Pure Appl. Chem.*, 77:415, 2005.

[86] D. Samélor, A-M. Lazar, M. Aufray, C. Tendero, L. Lacroix, J-D. Béguin, B. Caussat, H. Vergnes, J. Alexis, D. Poquillon, N. Pébère, A. Gleizes, and C. Vahlas. Amorphous alumina coatings: Processing, structure and remarkable barrier properties. *J. Nanosci. Nanotechnol.*, 11:1, 2011. 6

[87] M. A. Lieberman and A. J. Lichtenberg. *Principles of Plasma Discharges and Materials Processing.* John Wiley and Sons, Inc., Hoboken, New Jersey, 2nd edition, 2005. 13, 28

[88] A. Piel. *Plasma Physics, An Introduction to laboratory, Space, and Fusion Plasmas.* Springer, 2010. 13, 14, 16, 18

[89] I. B. Bernstein and I. N. Rabinowitz. Theory of electrostatic probes in a low density plasma. *Phys. Fluids*, 2:112, 1959. 15

[90] H. M. Mott-Smith and I. Langmuir. The theory of collectors in gaseous discharges. *Phys. Rev.*, 28:727, 1926.

[91] J. E. Allen. Probe theory - the orbital motion approach. *Phys. Scr.*, 45:497, 1992.

[92] J. G. Laframboise and L. W. Parker. Probe design for orbit limited current collection. *Phys. Fluids*, 16:629, 1973. 15

[93] A. Piel and A. Melzer. Dynamical processes in complex plasmas. *Plasma Phys. Control. Fusion*, 44:R1, 2002. 16

[94] K. De Bleecker. *Modeling of the formation and behavior of nanoparticles in dusty plasmas.* PhD thesis, 2006. 18

[95] S. Hamagushi and R. T. Farouki. Polarization force on a charged particulate in a nonuniform plasma. *Phys. Rev. E*, 49:4430, 1994. 19

[96] J. E. Daugherty, R. K. Porteous, and D. B. Graves. Electrostatic forces on small particles in low-pressure discharges. *J. Appl. Phys.*, 73:1617, 1993. 19

[97] G. M. Jellum and D. B. Graves. Particle plasma interactions in low pressure discharges. *Appl. Phys. Lett.*, 57:2077, 1990. 20

[98] G. M. Jellum, J. E. Daugherty, and D. B. Graves. Particle thermophoresis in low pressure glow discharges. *J. Appl. Phys.*, 69:6923, 1991. 20

[99] O. Arp, D. Block, A. Piel, and A. Melzer. Dust coulomb balls: Three-dimensional plasma crystals. *Phys. Rev. Lett.*, 93:165004, 2004. 20

[100] L. Couëdel, M. Mikikian, L. Boufendi, and A. A. Samarian. Residual dust charges in discharge afterglow. *Phys. Rev. E*, 74:026403, 2006. 20

[101] D. B. Graves, J. E. Daugherty, M. D. Kilgore, and R. K. Porteous. Charging, transport and heating of particles in radiofrequency and electron cyclotron resonance plasmas. *Plasma Sources Sci. Technol.*, 3:433, 1994. 20

[102] U. Konopka, D. Samsonov, A. V. Ivlev, J. Goree, and V. Steinberg. Rigid and differential plasma crystal rotation induced by magnetic fields. *Phys. Rev. E*, 61: 1890, 2000. 21

[103] M. S. Barnes, J. H. Keller, J. C. Forster, J. A. O'Neill, and D. K. Coultas. Transport of dust particles in glow-discharge plasmas. *Phys. Rev. Lett.*, 68:313, 1992. 21

[104] M. D. Kilgore, J. E. Daugherty, R. K. Porteous, and D. B. Graves. Ion drag on an isolated particulate in a low-pressure discharge. *J. Appl. Phys.*, 73:7195, 1993. 22

[105] S. A. Khrapak, A. V. Ivlev, G. E. Morfill, and H. M. Thomas. Ion drag force in complex plasmas. *Phys. Rev. E*, 66:046414, 2002. 22

[106] A. Bouchoule. *Dusty Plasmas: Physics, Chemistry and Technological impacts in Plasma Processing.* Wiley, New York, 1999. 22

[107] B. M. Annaratone, S. A. Khrapak, P. Bryant, G. E. Morfill, H. Rothermel, H. M. Thomas, M. Zuzic, V. E. Fortov, V. I. Molotkov, A. P. Nefedov, S. Krikalev, and Yu. P. Semenov. Complex-plasma boundaries. *Phys. Rev. E*, 66:056411, 2002. 23

[108] H. M. Thomas, D. D. Goldbeck, T. Hagl, A. V. Ivlev, U. Konopka, G. E. Morfill, H. Rothermel, R. Sütterlin, and M. Zuzic. Complex plasmas under microgravity conditions: parabolic flights. *Phys. Scr.*, T89:16, 2001. 25

[109] Y. P. Raizer. *Gas discharge physics.* Springer-Verlag, 1991. 28

[110] R. W. Dreyfus, J. M. Jasinski, R. E. Walkup, and G. S. Selwyn. Optical diagnostics of low pressure plasmas. *Pure & Appl. Chem.*, 57:1265, 1985. 29

[111] T. G. M. Freegarde and G. Hancock. A Guide to Laser-Induced Fluorescence Diagnostics in Plasmas. *J. Phys. IV France*, 7:C4, 1997. 29

[112] R. A. Stern and J. A. Johnson. Plasma ion diagnostics using resonant fluorescence. *Phys. Rev. Lett.*, 34:1548, 1975. 30

[113] H. C. Meng and H. J. Kunze. Investigation of the diffusion of impurity atoms in plasmas by laser fluorescence. *Phys. Fluids*, 22:1082, 1979. 30

[114] A. M. Keesee. *Neutral Density Profiles in Argon Helicon Plasmas*. PhD thesis, 2006. 30

[115] A. M. Keesee and E. E. Scime. Neutral density profiles in argon helicon plasmas. *Plasma Sources Sci. Technol.*, 16:742, 2007. 30

[116] D. Skoog, J. Holler, and S. Crouch. *Principles of instrumental analysis*. Belmont, CA: Brooks/Cole., 2007. 32

[117] C. P. Sherman Hsu. *Handbook of Instrumental Techniques for Analytical Chemistry*. 1997. 33

[118] P. Tschida and T. Lawson. *FT-IR Instrument Instructions*. URL http://instrumentalanalysis.community.uaf.edu/files/2013/01/Group2InstrumentInstructionsFT-IR-1.pdf. 33

[119] H. Tawidian, T. Lecas, and M. Mikikian. Zoom into dusty plasma instabilities. *IEEE Trans. Plasma Sci.*, 41:754, 2013. 38

[120] H. Tawidian, T. Lecas, and M. Mikikian. Evolution of low frequency instabilities in a dusty plasma. *To be Submitted*, 2013. 38

[121] P. K. Shukla and B. Eliasson. Colloquium: Fundamentals of dust-plasma interactions. *Rev. Mod. Phys.*, 81:25, 2009. 52

[122] M. Cavarroc, M. C. Jouanny, K. Radouane, M. Mikikian, and L. Boufendi. Self-excited instability occurring during the nanoparticle formation in an Ar - SiH_4 low pressure radio frequency plasma. *J. Appl. Phys.*, 99:064301, 2006. 52

[123] M. Mikikian, H. Tawidian, and T. Lecas. Merging and splitting of plasma spheroids in a dusty plasma. *Phys. Rev. Lett.*, 109:254007, 2012. 65

[124] H. Tawidian, M. Mikikian, L. Couëdel, and T. Lecas. Plasma inhomogeneities near the electrodes of a capacitively-coupled radio-frequency discharge containing dust particles. *Eur. Phys. J. Appl. Phys.*, 56:24018, 2011. 65

[125] S. I. Krasheninnikov. On scrape off layer plasma transport. *Phys. Lett. A*, 283: 368, 2001. 66

[126] D. Jovanovic, U. de Angelis, R. Fedele, and F. Pegoraro. Effects of dust particles on the dynamics of blobs in the scrape off layer. *Phys. Plasmas*, 14:083704, 2007.

[127] R. J. Maqueda, D. P. Stotler, S. J. Zweben, and the NSTX team. Intermittency in the scrape-off layer of the National Spherical Torus experiment during H-mode confinement. *J. Nucl. Mater.*, 415:S459, 2011.

[128] D. A. D'Ippolito, J. R. Myra, and S. J. Zweben. Convective transport by intermittent blob-filaments: Comparison of theory and experiment. *Phys. Plasmas*, 18:060501, 2011.

[129] J. R. Angus, M. V. Umansky, and S. I. Krasheninnikov. Effect of drift waves on plasma blob dynamics. *Phys. Rev. Lett.*, 108:215002, 2012. 66

[130] I. Brauer, M. Bode, E. Ammelt, and H.-G. Purwins. Traveling pairs of spots in a periodically driven gas discharge system: Collective motion caused by interaction. *Phys. Rev. Lett.*, 84:4104, 2000. 66

[131] L. Stollenwerk. Interaction of current filaments in dielectric barrier discharges with relation to surface charge distributions. *New. J. Phys.*, 11:103034, 2009.

[132] J. P. Boeuf, B. Bernecker, Th. Callegari, S. Blanco, and R. Fournier. Generation, annihilation, dynamics and self-organized patterns of filaments in dielectric barrier discharge plasmas. *Appl. Phys. Lett.*, 100:244108, 2012. 66

[133] E. Robert, V. Sarron, D. Riés, S. Dozias, M. Vandamme, and J.-M. Pouvesle. Characterization of pulsed atmospheric-pressure plasma streams (PAPS) generated by a plasma gun. *Plasma Sources Sci. Technol.*, 21:034017, 2012. 66

[134] Z. Bonaventura, M. Duarte, and A. Bourdon. Derivation of a merging condition for two interacting streamers in air. *Plasma Sources Sci. Technol.*, 21:052001, 2012.

[135] Z. Xiong, E. Robert, V. Sarron, J.-M. Pouvesle, and M. J. Kushner. Dynamics of ionization wave splitting and merging of atmospheric-pressure plasmas in branched dielectric tubes and channels. *J. Phys. D: Appl. Phys.*, 45:275201, 2012. 66

[136] J. Schulze, D. Luggenhölscher, and U. Czarnetzki. Instabilities in capacitively coupled radio-frequency discharges. *IEEE Trans. Plasma Sci.*, 36:1402, 2008. 66, 73

[137] J. Goree, G. E. Morfill, V. N. Tsytovich, and S. V. Vladimirov. Theory of dust voids in plasmas. *Phys. Rev. E*, 59:7055, 1999. 85

[138] S. V. Vladimirov, V. N. Tsytovich, and G. E. Morfill. Stability of dust voids. *Phys. Plasmas*, 12:052117, 2005. 85

[139] Y. H. Liu, Z. Y. Chen, M. Y. Yu, and A. Bogaerts. Multiple void formation in plasmas containing multispecies charged grains. *Phys. Rev. E*, 74:056401, 2006.

[140] V. Land and W. J. Goedheer. The plasma inside a dust free void: hotter, denser, or both? *New J. Phys.*, 9:246, 2007. 85, 89

[141] M. Mikikian, M. Cavarroc, L. Couëdel, Y. Tessier, and L. Boufendi. Mixed mode oscillations in complex plasma instabilities. *Phys. Rev. Lett.*, 100:225005, 2008. 85

[142] M. Cavarroc, M. Mikikian, Y. Tessier, and L. Boufendi. Successive generations of dust in complex plasmas: A cyclic phenomenon in the void region. *Phys. Rev. Lett.*, 100:045001, 2008. 85

[143] M. Mikikian, L. Couëdel, M. Cavarroc, Y. Tessier, and L. Boufendi. Self-excited void instability in dusty plasmas: plasma and dust cloud dynamics during the heartbeat instability. *New J. Phys.*, 9:268, 2007. 85

[144] L. Couëdel. *Nanoparticle formation and dynamics in a complex (Dusty) plasma: From the plasma ignition to the Afterglow.* PhD thesis, 2008.

[145] R. J. Heidemann, L. Couëdel, S. K. Zhdanov, K. R. Sütterlin, M. Schwabe, H. M. Thomas, A. V. Ivlev, T. Hagl, G. E. Morfill, V. E. Fortov, V. I. Molotkov, O. F. Petrov, A. I. Lipaev, V. Tokarev, T. Reiter, and P. Vinogradov. Comprehensive experimental study of heartbeat oscillations observed under microgravity conditions in the PK-3 plus laboratory on board the international space station. *Phys. Plasmas*, 18:053701, 2011.

[146] M. Y. Pustylnik, A. V. Ivlev, N. Sadeghi, R. Heidemann, S. Mitic, H. M. Thomas, and G. E. Morfill. On the heterogeneous character of the heartbeat instability in complex (dusty) plasmas. *Phys. Plasmas*, 19:103701, 2012. 85

[147] M. Mikikian, L. Couëdel, M. Cavarroc, Y. Tessier, and L. Boufendi. Plasma emission modifications and instabilities induced by the presence of growing dust particles. *IEEE Trans. Plasma Sci.*, 36:1012, 2008. 85

[148] I. Denysenko, K. Ostrikov, M. Y. Yu, and N. A. Azarenkov. Behavior of the electron temperature in nonuniform complex plasmas. *Phys. Rev. E*, 74:036402, 2006. 89

[149] M. R. Akdim and W. J. Goedheer. Modeling of dust in a silane/hydrogen plasma. *J. Appl. Phys.*, 94:104, 2003. 90

[150] V. V. Yaroshenko, S. A. Khrapak, and G. E. Morfill. Relationship between the ion drag and electric forces in dense dust clouds. *Phys. Plasmas*, 20:043703, 2013. 91

[151] M. Hübner, M. Fröhlich, H. Tawidian, M. Mikikian, J. Röpcke, and H. Kersten. On the plasma chemistry of a RF discharge containing aluminium triisopropoxide studied by FTIR spectroscopy. *To be Submitted*, 2013. 95

[152] M. M. Sovar. *Du Tri-isopropoxide aux oxydes d'aluminium par dépôt chimique en phase vapeur: procédé, composition et propriétés des revêtements obtenus.* PhD thesis, 2006. 95

[153] M. M. Sovar, D. Samélor, A. N. Gleizes, and C. Vahlas. Aluminium tri-iso-propoxide: Shelf life, transport properties, and decomposition kinetics for the low temperature processing of aluminium oxide-based coatings. *Surf. Coat. Tech.*, 201:9159, 2007. 95, 97

[154] L. W. Daasch and H. M. Fales. The mass spectra of aluminum isopropoxide. *Org. Mass. Spectrom.*, 2:1043, 1969. 95

[155] N. Ya. Turova, V. A. Kozunov, A. I. Yanovskii, N. G. Bokii, Yu. T. Struchkov, and B. L. Tarnopol'skii. Physico-chemical and structural investigation of aluminium isopropoxide. *J. Inorg. Nucl. Chem.*, 41:5, 1979. 96

[156] K. Folting, W. E. Streib, K. G. Caulton, O. Poncelet, and L. G. Hubert-Pfalzgraf. Characterization of aluminium isopropoxide and aluminosiloxanes. *Polyhedron*, 10:1639, 1991. 96

[157] V. J. Shiner and D. Whittaker. The mechanism of the Meerwein-Ponndorf-Verley reaction. *J. Am. Chem. Soc.*, 85:2337, 1963. 96

[158] E. C. Ashby, A. B. Goel, and J. N. Argypoulos. Evidence supporting a single electron transfer pathway in the reduction of aromatic ketones by metal alkoxides. lithium isopropoxide, an excellent reducing agent for aromatic ketones. *Tetrahedron Lett.*, 23:2273, 1982. 96

[159] W. Keuning, P. Van de Weijer, H. Lifka, W. M. M. Kessels, and M. Creatore. Cathode encapsulation of organic light emitting diodes by atomic layer deposition Al_2O_3 films and Al_2O_3 /a-SiNx:H stacks. *J. Vac. Sci. Technol. A*, 30:01A131, 2012. 97

[160] A. M. Huntz, M. Andrieux, C. Vahlas, M. M. Sovar, D. Samélor, and A. N . Gleizes. Phase transformations of metallorganic chemical vapor depositon processed alumina coatings investigated by in situ deflection. *J. Electrochem. Soc.*, 154:P63, 2007. 97

[161] J. Saraie, J. Kwon, and Y. Yodogawa. Chemical vapor deposition of Al_2O_3 thin films under reduced pressures. *J. Electrochem. Soc.*, 132:890, 1985. 97

[162] H. Kersten, R. Wiese, G. Thieme, M. Fröhlich, A. Kopitov, D. Bojic, F. Scholze, H. Neumann, M. Quaas, H. Wulff, and R. Hippler. Examples for application and diagnostics in plasma-powder interaction. *New J. Phys.*, 5:93.1, 2003. 97

[163] S. Niemietz, M. Fröhlich, and H. Kersten. Mass spectrometric investigations on aluminum isopropoxide containing plasmas. *Plasma Process. Polym.*, 9:904, 2012. 97, 105

[164] D. Lopatik, S. Niemietz, M. Fröhlich, J. Röpcke, and H. Kersten. Plasma chemical study of a RF discharge containing aluminum tri-isopropoxide using MIR absorption spectroscopy based on external-cavity Quantum Cascade Lasers. *Contrib. Plasma Phys.*, 52:864, 2012. 97, 105

[165] S. W. Sharpe, T. J. Johnson, R. L. Sams, P. M. Chu, G. C. Rhoderick, and P. A. Johnson. Gas-phase databases for quantitative infrared spectroscopy. *Applied Spectroscopy*, 58:1452, 2004. 98, 102

[166] F. Hempel, P. B. Davies, D. Loffhagen, L. Mechold, and J. Röpcke. Diagnostic studies of $H_2 - Ar - N_2$ microwave plasmas containing methane or methanol

using tunable infrared diode laser absorption spectroscopy. *Plasma Sources Sci. Technol.*, 12:S98, 2003. 101

[167] J. Berndt, S. Hong, E. Kovačević, I. Stefanović, and J. Winter. Dust particle formation in low pressure Ar/CH_4 and Ar/C_2H_2 discharges used for thin film deposition. *Vacuum*, 71:377, 2003. 110

[168] F. Hempel, D. Lopatik, B. Sikimic, I. Stefanović, J. Winter, and J. Röpcke. Monitoring of hydrocarbon concentrations in dust–producing RF plasmas. *Plasma Sources Sci. Technol.*, 21:055001, 2012. 110

Published articles

Publications related to this thesis:

• H. Tawidian, M. Mikikian, L. Couëdel, and T. Lecas. "Plasma inhomogeneities near the electrodes of a capacitively-coupled radio-frequency discharge containing dust particles", Eur. Phys. J. Appl. Phys., **56**, 24018 (2011)

• M. Mikikian, H. Tawidian, and T. Lecas. "Merging and splitting of plasma spheroids in a dusty plasma", Phys. Rev. Lett., **109**, 254007 (2012)

• H. Tawidian, T. Lecas, and M. Mikikian. "Zoom into dusty plasma instabilities", IEEE Trans. Plasma Sci., **41**, 754 (2013)

Additional publication:

• V. Massereau-Guilbaud, I. Géraud-Grenier, J. F. Lagrange, H. Tawidian and M. Mikikian. "Electron temperature evolution in a low pressure dusty RF nitrogen-rich methane plasma". IEEE Trans. Plasma Sci. **41**, 816 (2013)

To be submitted:

• H. Tawidian, T. Lecas and M. Mikikian. "Evolution of low frequency instabilities in a dusty plasma".

• M. Hübner, M. Fröhlich, H. Tawidian, M. Mikikian, J. Röpcke and H. Kersten. "On the plasma chemistry of a RF discharge containing aluminium triisopropoxide studied by FTIR spectroscopy".

Eur. Phys. J. Appl. Phys. **56**, 24018 (2011)
DOI: 10.1051/epjap/2011110163

THE EUROPEAN PHYSICAL JOURNAL
APPLIED PHYSICS

Regular Article

Plasma inhomogeneities near the electrodes of a capacitively-coupled radio-frequency discharge containing dust particles

H. Tawidian[a], M. Mikikian[b], L. Couëdel[c], and T. Lecas

GREMI, Groupe de Recherches sur l'Energétique des Milieux Ionisés, UMR 6606, CNRS/Université d'Orléans, 14 rue d'Issoudun, BP6744, 45067 Orléans Cedex 2, France

Received: 15 April 2011 / Received in final form: 25 July 2011 / Accepted: 3 August 2011
Published online: 28 October 2011 –

Abstract. Small plasma spheroids are evidenced and analyzed in front of the electrodes of a capacitively-coupled radio-frequency discharge in which dust particles are growing. These regions are characterized by a spherical shape, a slightly enhanced luminosity and are related to instabilities induced by the presence of dust particles. Several types of behaviors are identified and particularly their chaotic appearance or disappearance and their rotational motion along the electrode periphery. Correlations with the unstable behavior of the global plasma glow are performed. These analyses are obtained thanks to high-speed imaging which is the only diagnostics able to evidence these plasma spheroids.

1 Introduction

Solid particles from a few nanometers to centimeters can be found in laboratories and industrial plasma processes. In the late 1980s, dust particle formation was discovered in industrial reactors [1,2] and became a huge problem, particularly in microelectronics. Indeed, these particles can fall on wafers and affect semiconductor devices performances. Since then, scientists and engineers involved in this field must take into account this potential problem. Lately, with the big achievement concerning electronic devices miniaturization, these dust particles could be used in many industrial applications related to nanotechnology. Dusty plasmas [3,4] can also be found in astrophysical environments [5], like almost everywhere (comet tails, planetary nebulae, atmospheres [6] and rings) or in fusion devices [7] like the future ITER.

In laboratory reactors, there are many methods to create dust particles, mainly using reactive gases [8–14] or material sputtering [15–18]. In the present work, material sputtering is used to grow a high density of sub-micron dust particles. In the plasma, dust particles acquire a negative charge by capturing electrons. This huge loss of free electrons [19,20] can strongly disturb the plasma stability. It can give birth to unstable behaviors [15] like dust particle growth instabilities (DPGI) [21,22].

In this paper, we analyze a new phenomenon occurring during DPGI and consisting of the appearance of small plasma spheroids in the vicinity of discharge electrodes. These regions are characterized by a slightly enhanced luminosity and seem to appear and disappear in a quite chaotic way. In some conditions, they can rotate regularly along the circumference of the electrodes as recently observed [23]. In the following, we focus more precisely on the chaotic phase related to their appearance.

2 Experimental setup

The work presented in this paper is performed in the PKE-Nefedov reactor (Plasma Kristall Experiment) that was designed for microgravity experiments [18,24]. This reactor is a capacitively-coupled radio-frequency (rf at 13.56 MHz in push-pull mode) discharge in argon. The plasma is created between two electrodes (separated by 3 cm and with a diameter of 4 cm, surrounded by a guard ring) with a rf power around 3 W and a pressure around 1.6 mbar (a pressure above 1.5 mbar is required to observe the spheroids). Dust particles are grown by sputtering a polymer layer previously deposited on the electrodes [18] and composed of injected micrometer particles (melamine formaldehyde). At the end of each experiment, the grown dust particles settle on the electrodes. This additional material, mainly composed of carbon, is also sputtered and involved in the growth process. After plasma ignition, we can observe many instabilities due to the dust presence [25,26], like DPGI [21,22] or the heartbeat instability [27,28] consisting of successive contractions and expansions of a central dust-free region named

[a] e-mail: hagop.tawidian@univ-orleans.fr
[b] e-mail: maxime.mikikian@univ-orleans.fr
[c] Present address: Laboratoire de Physique des Interactions Ioniques et Moléculaires, UMR 6633 CNRS/Université de Provence, 13397 Marseille, France

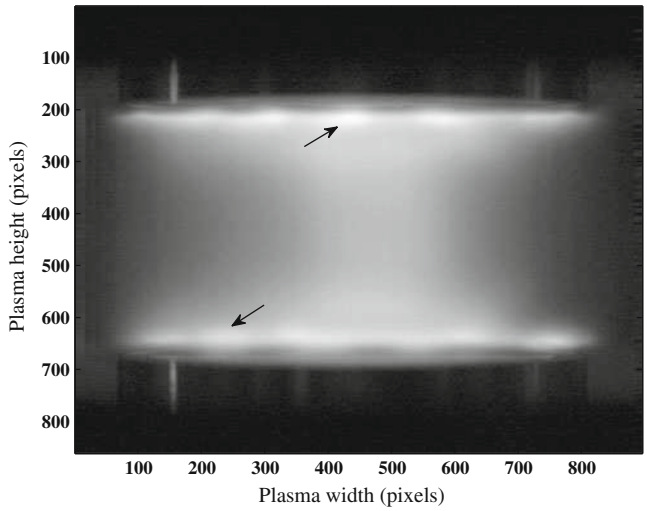

Fig. 1. Plasma glow and detection of spheroids in front of both electrodes. Two plasma spheroids are marked with an arrow.

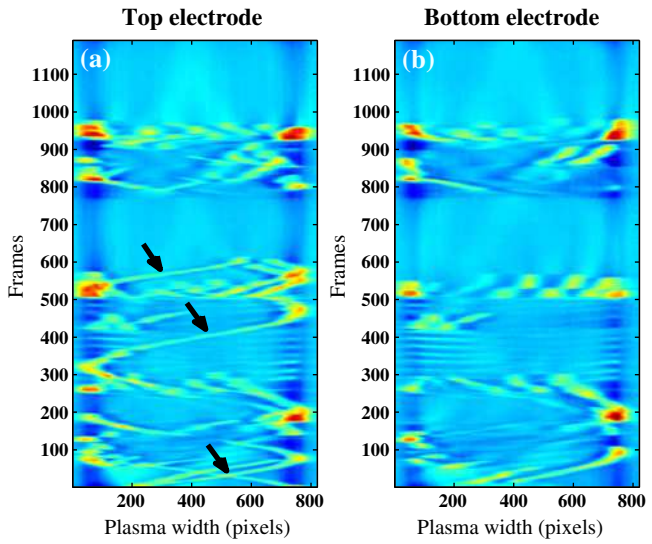

Fig. 2. (Color online) Line profile of plasma glow in front of (a) top and (b) bottom electrodes during 1190 frames. Appearance and disappearance of spheroids during DPGI (brightness variation in false colors from dark blue to red). Some short spheroid paths are marked with arrows.

void. The void region is due to the equilibrium between two major counteracting forces, the electric and ion drag forces [29–31]. All these instabilities are characterized by a strong nonlinear behavior [28,32]. To observe the small plasma spheroids appearing during DPGI, we used a high-speed camera "Photron FASTCAM SA5" at 7000 or 10000 frames per second (fps). The camera was positioned directly in front of the reactor at a distance of about 50 cm to detect and record the plasma glow during the phenomenon. It is noteworthy to mention that, while the other unstable phenomena are quite easily observed, the spheroids discussed in this paper are only visible and detectable thanks to high-speed imaging.

3 Appearance and behavior of plasma spheroids

A typical image showing this phenomenon on the plasma glow is presented in Figure 1. This frame is extracted from a movie recorded at 10000 fps during DPGI. Plasma spheroids appear in front of each electrode and are localized on their periphery. They consist of well-defined regions of about a few mm with a slightly enhanced luminosity. In Figure 1 about six plasma spheroids can be evidenced in front of each electrode. Two of them are marked with an arrow. Due to the angle of view, the top and bottom electrodes appear a little bit tilted. It allows to discriminate plasma spheroids in the foreground from those in the background. In order to reveal more precisely this phenomenon, the regions in the close vicinity of both electrodes (800 × 110 pixels) are extracted from the movie. Plasma luminosity is averaged on the height of each of these regions. Thus, each frame gives two lines (one for each region).

The behavior of the small plasma spheroids in front of both electrodes is analyzed in two different cases. In Figure 2, 1190 frames (170 ms) are processed during a movie recorded at 7000 fps. A spatiotemporal image of the plasma spheroid behavior is obtained. Contrast is enhanced by subtracting a temporal average value and by using false colors [27]. From Figure 2, three different regimes related to the plasma spheroids can be evidenced:

– Regime I: No spheroid is observed.
– Regime II: Chaotic appearance and disappearance of spheroids characterized by bright spots.
– Regime III: Persistence of some spheroids that enter in a rotating motion along the circumference of the electrode. This regime corresponds to long spheroids path visible in Figure 2.

The last two regimes are not so strongly separated due to the fact that during the chaotic phase some short spheroids paths exist. These three regimes do not appear always simultaneously in front of both electrodes. From frame 0 to 100, regime III is observed in front of each electrode but is clearer close to the top electrode (some paths are marked by arrows in Fig. 2a). This regime is followed by regime II until frame 300. Between frames 300 and 420, the regimes in front of each electrode are not similar. Indeed, in Figure 2a we observe regime III (with only one spheroid) while regime I is evidenced in Figure 2b. The striations observed in both figures are not related to spheroids and their origin will be explained later in this paper. Two other regimes I are clearly observed simultaneously in both figures between frames 550 and 770, and later after frame 920. The other parts of Figure 2 are mainly characterized by regime II and very short spheroids paths. In order to correlate the observed regimes with DPGI, the evolution of the central plasma glow is analyzed. It is performed by taking the plasma glow profile along the horizontal axis in between the two electrodes for each frame (Fig. 3). The vertical axis of symmetry of the plasma is

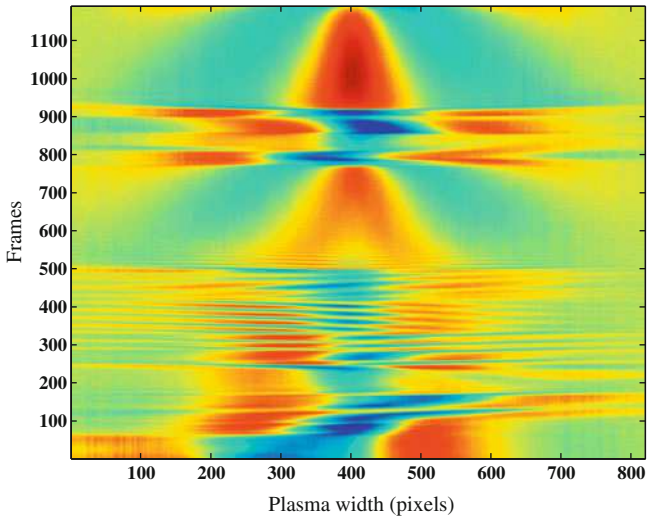

Fig. 3. (Color online) Plasma glow profile along the horizontal axis in between the two electrodes during DPGI (in false colors from dark blue to red).

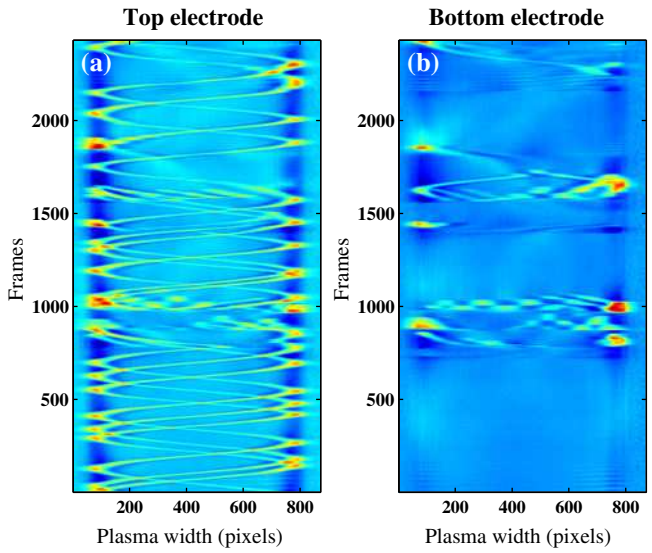

Fig. 4. (Color online) Line profile of plasma glow in front of (a) top and (b) bottom electrodes during 2431 frames. Appearance and disappearance of spheroids during DPGI (the brightness variation in false colors from dark blue to red).

around 400 on the x-axis. It clearly appears that during DPGI the plasma luminosity can strongly vary not only in the center but also toward plasma, and electrode, edges (left and right). Different time scales can also be evidenced with fast and slow changes. By comparing Figures 2 and 3, several correlations can be made. When the plasma glow changes are mainly concentrated near the discharge center (between frames 550 and 770 or 920 and 1190 in Fig. 3) it corresponds principally to regime I near the electrodes but also to a lesser extent, to some short spheroids paths (Fig. 2). When the plasma behavior in Figure 3 is much more chaotic with off-centered changes (between 0 and 300 or 770 and 920), it corresponds in Figure 2 either to the chaotic appearance of the spheroids (regime II), or to their rotation (regime III). It confirms that regimes II and III can be confused due to the existence of some spheroids paths during the chaotic phase. The phase in between frames 300 and 420 in Figure 3 is characterized by very fast changes in the plasma emission. It explains the striations observed in Figure 2 at the same time.

In the second case we studied, the camera speed was fixed at 10000 fps. The spheroids are present all the time close to the top electrode, while many regimes occur near the bottom electrode. These results are shown in Figure 4 obtained using the same procedure as in Figure 2. For the top electrode the spheroids paths clearly appear (Fig. 4a). In the beginning three rotating spheroids (regime III) are detected and keep turning for several rounds at a speed of about 4 m s^{-1}. At frame 720 this regime is interrupted by a chaotic phase with many spheroids appearing and disappearing quickly (regime II). This regime stops at frame 1000 where a three spheroid system is back again until the second chaotic phase at frame 1400. Once again regime III is back but the number of spheroids is reduced to one, turning around the top electrode. A second spheroid joins it at frame 1900 till the end of the video

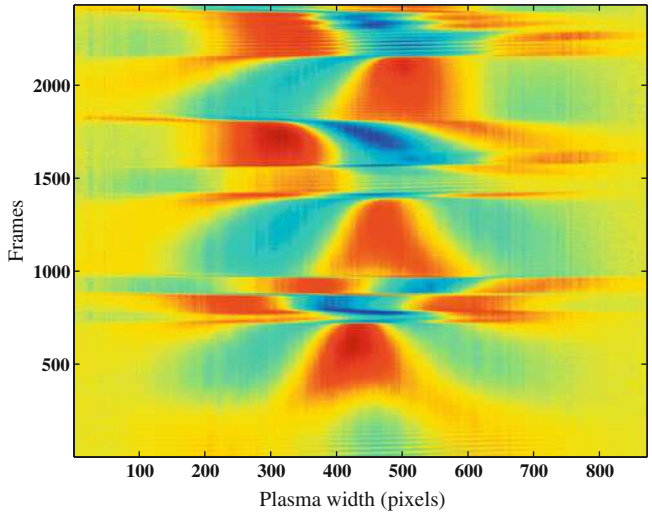

Fig. 5. (Color online) Plasma glow profile along the horizontal axis in between the two electrodes during DPGI (in false colors from dark blue to red).

recording. Concerning the bottom electrode (Fig. 4b), the spheroids just appear during the chaotic phase. When a nice rotation regime is observed near the top electrode, nothing is observed close to the bottom one except at the end (around frame 2200). By comparing the phenomena happening close to both electrodes with the luminosity of the middle region of the plasma (Fig. 5), same behaviors as in Figures 2 and 3 are observed. Slow and central changes in the plasma luminosity (for example, between frames 1000 and 1400) correspond to either no spheroid (Fig. 4b) or rotating spheroids (Fig. 4a). Fast and off-centered plasma changes (for example, between frames 720 and 1000) are related to chaotic regimes for the spheroids.

4 Discussion and conclusion

In this paper, we have characterized and analyzed a new phenomenon occurring during DPGI and consisting of the appearance of small plasma spheroids in front of the discharge electrodes. In the studied cases, different regimes have been clearly identified and correlated with the variation of the plasma luminosity in the discharge central part. We found that when the plasma changes are mainly located in the close discharge center, regime I (no spheroid) or III (rotating spheroids) is observed in front of the electrodes. Regime III (chaotic appearance and disappearance of the spheroids) appears when plasma changes in between the electrodes are fast and more off-centered.

The origin of these plasma spheroids is not well elucidated. Their appearance in front of the electrodes seems to be correlated with DPGI as they have been observed only during or after DPGI. In this paper we focused on the chaotic appearance of the spheroids which occurs only during DPGI. When plasma spheroids are observed after DPGI, only regime III, with spheroids rotating regularly at a few m s^{-1}, has been observed until now (Carousel instability [23]). In this last case, DPGI seem to be finished or are no more detectable.

These spheroids are observed along the periphery of the electrodes indicating that the guard ring surrounding the electrode can play a role in this phenomenon. However, these spheroids have always been observed in dusty plasma conditions with a high density of sub-micron dust particles and a quite high pressure (>1.5 mbar). We can assume that the strong disturbance induced by the dust particle presence can trigger the spheroid appearance or rotation. Thus, this behavior occurs preferentially in regions where electrical inhomogeneities exist as close to the guard rings. A similar phenomenon has been described in [33]. In this last case, the disturbance of the plasma equilibrium is not induced by dust particles but by the introduction of a glass tube into the discharge.

The authors would like to thank L. Boufendi for supporting this project. B. Dumax is acknowledged for electronic support and J.-M. Bauchire and H. Rabat for providing the high-speed camera. The PKE-Nefedov chamber has been made available by the Max-Planck-Institute for Extraterrestrial Physics, Germany, under the funding of DLR/BMBF under Grant No. 50WM9852.

References

1. R.M. Roth, K.G. Spears, G.D. Stein, G. Wong, Appl. Phys. Lett. **46**, 253 (1985)
2. G.S. Selwyn, J. Singh, R.S. Bennett, J. Vac. Sci. Technol. A **7**, 2758 (1989)
3. P.K. Shukla, B. Eliasson, Rev. Mod. Phys. **81**, 25 (2009)
4. M. Mikikian, L. Couëdel, M. Cavarroc, Y. Tessier, L. Boufendi, Eur. Phys. J. Appl. Phys. **49**, 13106 (2010)
5. C.K. Goertz, Rev. Geophys. **27**, 271 (1989)
6. E. Sciamma-O'Brien, N. Carrasco, C. Szopa, A. Buch, G. Cernogora, Icarus **209**, 704 (2010)
7. S.I. Krasheninnikov et al., Plasma Phys. Control. Fusion **50**, 124054 (2008)
8. J. Berndt, E. Kovačević, I. Stefanović, O. Stepanovic, S.H. Hong, L. Boufendi, J. Winter, Contrib. Plasma Phys. **49**, 107 (2009)
9. M. Mikikian, M. Cavarroc, L. Couëdel, Y. Tessier, L. Boufendi, Pure Appl. Chem. **82**, 1273 (2010)
10. J. Benedikt, J. Phys. D: Appl. Phys. **43**, 043001 (2010)
11. J. Pereira, V. Massereau-Guilbaud, I. Géraud-Grenier, A. Plain, J. Appl. Phys. **103**, 033301 (2008)
12. M. Cavarroc, M. Mikikian, Y. Tessier, L. Boufendi, Phys. Rev. Lett. **100**, 045001 (2008)
13. J. Berndt, E. Kovačević, I. Stefanović, L. Boufendi, J. Appl. Phys. **106**, 063309 (2009)
14. S. Dap, D. Lacroix, F. Patisson, R. Hugon, L. de Poucques, J. Bougdira, New J. Phys. **12**, 093014 (2010)
15. D. Samsonov, J. Goree, Phys. Rev. E **59**, 1047 (1999)
16. C. Dominique, C. Arnas, J. Appl. Phys. **101**, 123304 (2007)
17. A. Michau, G. Lombardi, L.C. Delacqua, M. Redolfi, C. Arnas, X. Bonnin, K. Hassouni, Plasma Phys. Control. Fusion **52**, 124014 (2010)
18. M. Mikikian, L. Boufendi, A. Bouchoule, H.M. Thomas, G.E. Morfill, A.P. Nefedov, V.E. Fortov, the PKE-Nefedov Team, New J. Phys. **5**, 19 (2003)
19. W.W. Stoffels, E. Stoffels, G.M.W. Kroesen, F.J. de Hoog, J. Appl. Phys. **78**, 4867 (1995)
20. H. Kersten, H. Deutsch, M. Otte, G.H.P.M. Swinkels, G.M.W. Kroesen, Thin Solid Films **377–378**, 530 (2000)
21. M. Mikikian, M. Cavarroc, L. Couëdel, L. Boufendi, Phys. Plasmas **13**, 092103 (2006)
22. M. Mikikian, L. Couëdel, M. Cavarroc, Y. Tessier, L. Boufendi, IEEE Trans. Plasma Sci. **36**, 1012 (2008)
23. M. Mikikian, L. Couëdel, Y. Tessier, L. Boufendi, IEEE Trans. Plasma Sci. (in press), DOI: http://dx.doi.org/10.1109/TPS.2011.2155675
24. A.P. Nefedov et al., New J. Phys. **5**, 33 (2003)
25. S.K. Zhdanov et al., New J. Phys. **12**, 043006 (2010)
26. L. Couëdel, M. Mikikian, A.A. Samarian, L. Boufendi, Phys. Plasmas **17**, 083705 (2010)
27. M. Mikikian, L. Couëdel, M. Cavarroc, Y. Tessier, L. Boufendi, New J. Phys. **9**, 268 (2007)
28. M. Mikikian, L. Couëdel, M. Cavarroc, Y. Tessier, L. Boufendi, Phys. Rev. Lett. **105**, 075002 (2010)
29. J. Goree, G.E. Morfill, V.N. Tsytovich, S.V. Vladimirov, Phys. Rev. E **59**, 7055 (1999)
30. Z. Hu, Y. Chen, X. Zheng, F. Huang, G.-F. Shi, M.Y. Yu, Phys. Plasmas **16**, 063707 (2009)
31. C. Schmidt, O. Arp, A. Piel, Phys. Plasmas **18**, 013704 (2011)
32. M. Mikikian, M. Cavarroc, L. Couëdel, Y. Tessier, L. Boufendi, Phys. Rev. Lett. **100**, 225005 (2008)
33. J. Schulze, D. Luggenhölscher, U. Czarnetzki, IEEE Trans. Plasma Sci. **36**, 1402 (2008)

Merging and Splitting of Plasma Spheroids in a Dusty Plasma

Maxime Mikikian,* Hagop Tawidian, and Thomas Lecas
GREMI, Groupe de Recherches sur l'Energétique des Milieux Ionisés, UMR7344 CNRS/Université d'Orléans, 14 rue d'Issoudun, BP6744, 45067 Orléans Cedex 2, France
(Received 10 September 2012; published 14 December 2012)

Dust particle growth in a plasma is a strongly disturbing phenomenon for the plasma equilibrium. It can induce many different types of low-frequency instabilities that can be experimentally observed, especially using high-speed imaging. A spectacular case has been observed in a krypton plasma where a huge density of dust particles is grown by material sputtering. The instability consists of well-defined regions of enhanced optical emission that emerge from the electrode vicinity and propagate towards the discharge center. These plasma spheroids have complex motions resulting from their mutual interaction that can also lead to the merging of two plasma spheroids into a single one. The reverse situation is also observed with the splitting of a plasma spheroid into two parts. These results are presented for the first time and reveal new behaviors in dusty plasmas.

DOI: 10.1103/PhysRevLett.109.245007 PACS numbers: 52.27.Lw, 52.35.−g

Dusty (or complex) plasmas [1] are systems where many peculiar behaviors can be experimentally observed. The presence of dust particles as an additional species in the plasma induces new behaviors like a wide variety of instabilities that appear to be strongly nonlinear [2–4]. It is important to well characterize and understand these unstable phenomena because dusty plasmas are relatively often encountered in nature and industry. They are observed in astrophysics where they are involved, for example, in interstellar materials [5] or planetary atmospheres [6]. They are also found in industry, where after being considered only as unwanted situations, they are now more involved in useful applications [7]. Nevertheless, the presence of dust particles in fusion reactors [8] like the future ITER (Cadarache, France) is still a very critical issue.

To experimentally create a dusty plasma containing a huge density of dust particles (huge means that the dust particle density is not negligible with respect to electron and ion densities), the most efficient way is to grow them. Dust particles can be grown from reactive gases [9–14] or material sputtering [15–18]. In both cases, molecular precursors are injected in the reactor and are at the origin of chemical reactions initiating the growth of solid bodies in the plasma. During this growth phase, dust particles capture plasma free electrons and thus change the plasma characteristics [19–21]. When the dust particle density is huge and thus the effect on the electron population is strong, low-frequency instabilities can be observed. This phenomenon has been analyzed during dust particle growth [15,16,22,23] where spatiotemporal oscillations of the plasma luminosity have been evidenced. More recently, the use of high-speed imaging improved the characterization of these instabilities and allowed us to detect new behavior. Particularly, it evidences the existence of small regions (plasma spheroids) with an enhanced emission that appear in the vicinity of the electrodes and move around the discharge [24,25].

In this Letter we show that plasma spheroids can also be observed in the dusty plasma center (Fig. 1) and, for the first time to the best of our knowledge, that they have complex interactions. Indeed, their mutual interaction gives rise to complex motions and in some cases to the merging of two plasma spheroids into a single one. The reverse situation is also encountered with the splitting of a plasma spheroid into two parts. These behaviors are observed in a capacitively coupled radio frequency discharge (width 4 cm, height 3 cm) in Kr at low pressure (1–2 mbar) and power (∼ 3 W). This plasma is used to sputter a polymer material deposited on the electrodes that provides the molecular precursors, giving birth to a huge density of dust particles. With respect to our previous experiments where argon was used [26], we use Kr as the sputtering gas. It appears that with Kr the density of grown

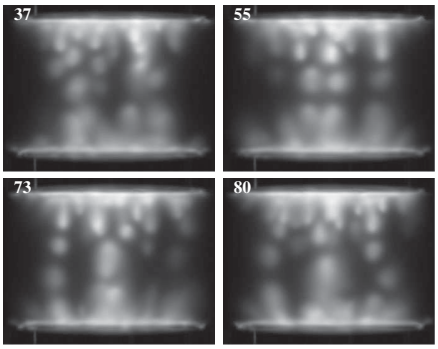

FIG. 1. Plasma spheroids in the plasma bulk. Well-defined regions with an enhanced emission are clearly observed in between the electrodes (dark regions on the top and bottom separated by 3 cm). The numbered frames are from a movie taken at 8000 fps [27].

dust particles is much higher than with Ar and that the dust particle size stays relatively small (certainly below 100 nm due to the difficulty of observing them with laser light scattering). The dust particle formation triggers instabilities [22,23] during which plasma spheroids are observed only near the electrodes [24,25] or also in the plasma bulk (when dust particle density is very high) with new complex behaviors. The question of the plasma spheroid composition is posed: they can contain just plasma (as for the void [18]) or plasma and dust particles. At the moment, no clear experimental indication allows us to select one of these possibilities. The plasma spheroid analyses have been performed thanks to a high-speed camera. The plasma luminosity is clearly detected up to a maximum speed of about 20000 frames per second (fps). A typical example is shown in Fig. 1 with four frames from a movie taken at 8000 fps.

From this figure and the movie [27], some general trends can be defined. The plasma spheroids have a rather homogeneous size of about a few mm and a cometlike shape. They come from the electrode (or sheath) regions and propagate towards the plasma bulk, their head being brighter than their comet tail. Some of them seem to stay ''attached'' to their place of birth thanks to this tail, while others seem to come off their tail and enter the plasma center. In Fig. 1 and in the related movie [27], some interactions between the plasma spheroids can be slightly guessed. Indeed, complex dynamics, merging, and splitting of the plasma spheroids can be observed and will be more precisely highlighted in the following.

Before going deeper in the analysis of this phenomenon in dusty plasmas, it can be noted that the existence of localized structures with an enhanced emission is encountered in many different types of plasmas with certainly different physical mechanisms driving their creation and dynamics. Indeed, these regions are well known in magnetized plasmas, especially in the context of fusion reactors. In this field they are called ''blobs'' and are involved in transport phenomena explaining their current intense study, both experimentally and theoretically, by many authors [28–32]. In atmospheric pressure plasmas, especially in dielectric barrier discharges, these regions are called filaments and they have been shown recently to be able to interact with each other, showing the merging or the splitting of these regions [33–35]. These works show phenomenological similarities with our previous observation of rotating plasma spheroids [24,25] and with the present Letter on the interaction between these structures. Similar interactions like the merging or the splitting of regions of enhanced plasma emission were also observed very recently in plasma jets where plasma streams with a cometlike shape are produced [36–39]. In these works, the well-defined comet head (sometimes called plasma bullet) has been shown to be able to split into two parts, and the merging of two bullets into a single one was also reported. In experimental conditions closer to the present study, we can report on relatively similar observations by Schulze *et al.* [40] where moving ''plasmoids'' are observed during their experiments.

In order to better observe the interactions between our plasma spheroids, another movie taken at 16000 fps (60 μs per frame) has been recorded. At this speed, the plasma emission appears less bright and thus the movie contrast has to be enhanced. However, this speed allows us to better follow the three main interactions (dynamics, merging, splitting) of interest. This movie also corresponds to a slightly less stochastic experiment where the number of interacting spheroids is reduced compared with the case of Fig. 1, allowing an easier image analysis. The complex motions of the plasma spheroids are evidenced in the zoom shown in Fig. 2 represented in false colors (from dark blue to red). The cometlike shape is very well evidenced in image 3552, where two plasma spheroids are getting closer. In 3555 and 3558 the upper spheroid comes off its tail and the comet head is clearly directed towards the lower spheroid. In 3564 the comet head changes its direction when the lower spheroid disappears and a new one appears on the top of the frame. The central spheroid is now going up until frame 3573, where the upper spheroid in turn disappears and a new one emerges from the bottom. Once again, a switch in the central spheroid direction occurs.

This behavior is well observed in Fig. 3 where the column profile of all sequence frames is shown. To compensate the slight horizontal motion of the spheroids, the profile is averaged over several columns around the interaction location. The temporal mean value of the plasma emission has also been subtracted to better evidence slight emission changes. This figure clearly shows the down-up-down motion of the central plasma spheroid as a function of the appearance of other spheroids on the top or bottom. It can also be observed that the top and bottom spheroids

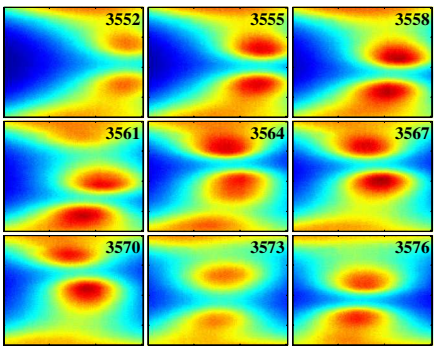

FIG. 2 (color online). Interaction between plasma spheroids leading to the up and down motion of the central spheroid. The central spheroid moves in the direction of the other spheroids. Frames from a movie taken at 16000 fps and presented in false colors from dark blue to red. Each image is about 2.3 cm height and 1 cm width.

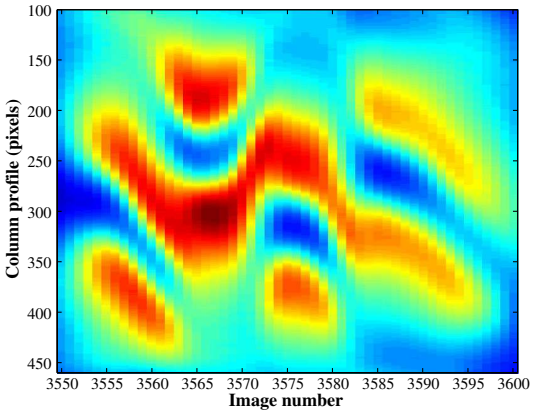

FIG. 3 (color online). Column profile (averaged over several columns) of all frames from the movie partly shown in Fig. 2.

go back towards the electrode before disappearing. The central spheroid seems to follow them, and it gives an impression that it is just a global motion of all spheroids. In fact, an attraction between the spheroids can better explain the observed behavior. Indeed, a drastic reversal of the comet head position is detected when the top or bottom spheroid enters the plasma. For example, in frames 3561–3567 of Figs. 2 and 3, the change of the maximum intensity position of the central spheroid is clearly observed. The maximum is clearly on the top of the central spheroid when the top spheroid is on its way towards the center. This behavior confirms that an interaction really exists in between the spheroids and that the observed motions are not only related to a global plasma change affecting all spheroids.

Although interaction between plasma spheroids can be guessed from Figs. 1–3, a clear evidence is brought to the fore by observing the merging and/or the splitting of the plasma spheroids. These phenomena are shown in Fig. 4, where both merging and splitting are observed during a single sequence. These zoomed frames have been extracted from a movie at 16000 fps [27]. Two clear spheroids are observed on the top and bottom of frame 78 and they are getting closer, approaching the image center up to frame 81. At this stage the merging of the two spheroids starts and continues in frame 82. In the following frame, a single spheroid is observed with diffuse connections to the previous spheroid locations. From frame 84 up to 90 the single spheroid is nearly completely disconnected from the top and bottom parts of the frames. In frame 91 it seems that connections with top and bottom parts are activated again and the splitting starts up to frame 95 where two spheroids are again obtained. This behavior is better evidenced by using the same technique as the one shown in Fig. 3. The column profile in Fig. 5 really brings to the fore this merging-splitting sequence. It can also be observed that the two spheroids created after the splitting appear brighter, which was observed in many splitting cases. This observation and the fact that the splitting phenomenon often occurs close to the horizontal axis of symmetry of the discharge (around 260 on the y axis of Fig. 5) are currently under investigation. This symmetry is less marked when looking at Fig. 1 and Ref. [27], where interactions also appear out of the horizontal symmetry plane.

Although getting consecutively both the merging and the splitting is quite unusual and difficult to find in the obtained movies, isolated merging or splitting is more commonly encountered. Experimental proofs of these behaviors are presented in Fig. 6 with a splitting in 6(a) and a merging in 6(b) obtained during a movie at 16000 fps.

In this Letter, we reported for the first time the experimental observation of the interaction of localized plasma structures (called plasma spheroids) in a dusty plasma. The case presented in Fig. 1 appears particularly rich in complex phenomena (motion, repulsion, splitting, or merging) but is difficult to analyze due to the insufficient frame rate

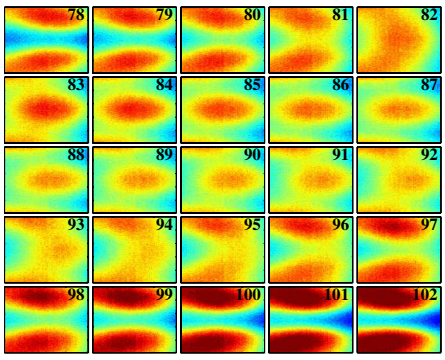

FIG. 4 (color online). Merging of two plasma spheroids quickly followed by the splitting of the newly constituted spheroid. These zoomed frames are extracted from a movie at 16000 fps [27] and are represented in false colors. Each image is about 1.6 cm height and 0.5 cm width.

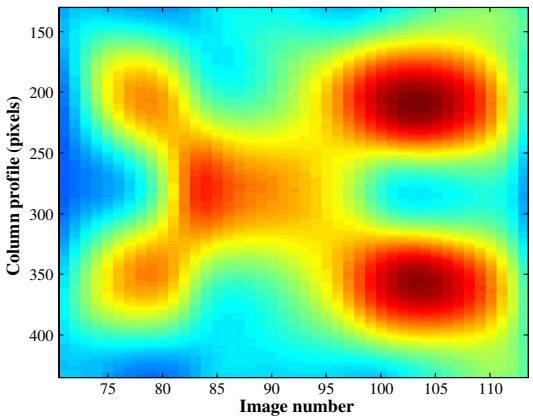

FIG. 5 (color online). Column profile (averaged over several columns) of all frames from the movie partly shown in Fig. 4.

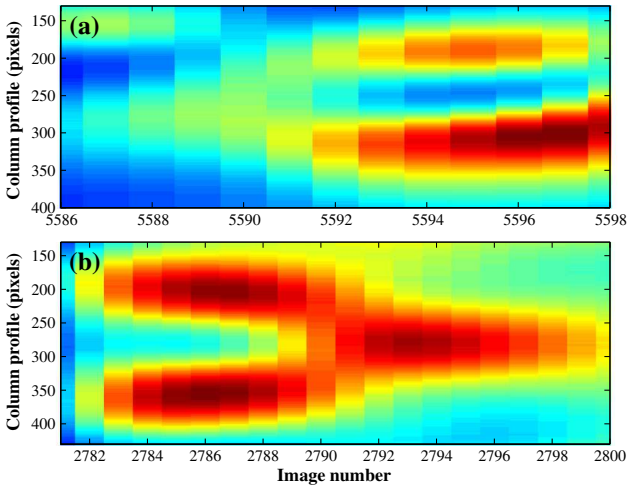

FIG. 6 (color online). (a) Splitting and (b) merging of plasma spheroids. Column profiles (averaged over several columns) in false colors from dark blue to red.

and the too big number of plasma spheroids. Thus, easier cases have been found in order to analyze these interactions. Results show that these regions of enhanced emission emerge from the electrode vicinity and propagate towards the plasma bulk where they can interact with each other, leading to complex motions, repulsion phenomena, or the merging of spheroids. A single spheroid can also be divided into two parts, giving birth to two new spheroids. During these phenomena, the electrical characteristics of the discharge show clear instabilities. Nevertheless, a direct correlation between these measurements and the spheroid dynamics is quite difficult. First, because it would consist in comparing local behaviors (spheroids) and global electrical measurements integrating phenomena outside the camera field of view. Second, because spheroid dynamics does not necessarily change the discharge characteristics: when a spheroid is moving in between the electrodes, its ''charge'' is just transported from one place to another. In the case of merging or splitting, the situation is more complicated as the respective spheroid ''intensities'' play a role.

Similar interactions have been found in other plasma conditions like in fusion plasmas, dielectric barrier discharges, and plasma jets, for example, in the context of plasma medicine. These experimental results obtained in a dusty plasma propose a new system to study these behaviors. The experimental conditions are very different in each of these fields, leading to a certainly quite different physical origin of these behaviors. Nevertheless, it appears obvious that electrical effects (repulsion, polarization, etc.) are the common points behind all observations. Future works will be conducted to find the physical origin of the present results obtained in dusty plasmas. These new investigations could be useful for the other fields concerned with localized plasma structures.

The authors would like to thank B. Dumax for electronic support, and J.-M. Bauchire and H. Rabat for providing the high-speed camera. The PKE-Nefedov chamber has been made available by the Max-Planck-Institute for Extraterrestrial Physics, Germany, under the funding of DLR/BMBF Grant No. 50WM9852. This work was partly supported by the French National Research Agency (ANR), Project INDIGO No. ANR-11-JS09-010-01.

*maxime.mikikian@univ-orleans.fr

[1] P. K. Shukla and B. Eliasson, Rev. Mod. Phys. **81**, 25 (2009).
[2] M. Mikikian, M. Cavarroc, L. Couëdel, Y. Tessier, and L. Boufendi, Phys. Rev. Lett. **100**, 225005 (2008).
[3] M. Mikikian, L. Couëdel, M. Cavarroc, Y. Tessier, and L. Boufendi, Phys. Rev. Lett. **105**, 075002 (2010).
[4] S. K. Zhdanov, M. Schwabe, R. Heidemann, R. Sütterlin, H. M. Thomas, M. Rubin-Zuzic, H. Rothermel, T. Hagl, A. V. Ivlev, G. E. Morfill, V. I. Molotkov, A. M. Lipaev, O. F. Petrov, V. E. Fortov, and T. Reiter, New J. Phys. **12**, 043006 (2010).
[5] E. Kovačević, I. Stefanović, J. Berndt, Y. J. Pendleton, and J. Winter, Astrophys. J. **623**, 242 (2005).
[6] E. Sciamma-O'Brien, N. Carrasco, C. Szopa, A. Buch, and G. Cernogora, Icarus **209**, 704 (2010).
[7] P. Roca i Cabarrocas, T. Nguyen-Tran, Y. Djeridane, A. Abramov, E. Johnson, and G. Patriarche, J. Phys. D **40**, 2258 (2007).
[8] S. I. Krasheninnikov *et al.* (LHD Experimental Group), Plasma Phys. Controlled Fusion **50**, 124054 (2008).
[9] J. Berndt, E. Kovačević, I. Stefanović, O. Stepanovic, S. H. Hong, L. Boufendi, and J. Winter, Contrib. Plasma Phys. **49**, 107 (2009).
[10] V. Massereau-Guilbaud, J. Pereira, I. Géraud-Grenier, and A. Plain, J. Appl. Phys. **105**, 033302 (2009).
[11] J. Berndt, E. Kovačević, I. Stefanović, and L. Boufendi, J. Appl. Phys. **106**, 063309 (2009).
[12] M. Hundt, P. Sadler, I. Levchenko, M. Wolter, H. Kersten, and K. Ostrikov, J. Appl. Phys. **109**, 123305 (2011).
[13] M. Calafat, P. Yuryev, A. Drenik, A. Slim, and R. Clergereaux, Plasma Processes Polym. **8**, 401 (2011).
[14] I. Géraud-Grenier, R. Jaffiol, V. Massereau-Guilbaud, and A. Plain, Appl. Phys. Lett. **99**, 091503 (2011).
[15] G. Praburam and J. Goree, Phys. Plasmas **3**, 1212 (1996).
[16] D. Samsonov and J. Goree, Phys. Rev. E **59**, 1047 (1999).
[17] C. Arnas, A. Mouberi, K. Hassouni, A. Michau, G. Lombardi, X. Bonnin, F. Bénédic, and B. Pégourié, J. Nucl. Mater. **390–391**, 140 (2009).
[18] M. Mikikian, L. Couëdel, M. Cavarroc, Y. Tessier, and L. Boufendi, Eur. Phys. J. Appl. Phys. **49**, 13 106 (2010).
[19] S. Mitic, M. Y. Pustylnik, and G. E. Morfill, New J. Phys. **11**, 083020 (2009).
[20] S. Hübner and A. Melzer, Phys. Rev. Lett. **102**, 215001 (2009).
[21] I. Goertz, F. Greiner, and A. Piel, Phys. Plasmas **18**, 013703 (2011).
[22] M. Mikikian, M. Cavarroc, L. Couëdel, and L. Boufendi, Phys. Plasmas **13**, 092103 (2006).

[23] M. Mikikian, L. Couëdel, M. Cavarroc, Y. Tessier, and L. Boufendi, IEEE Trans. Plasma Sci. **36**, 1012 (2008).
[24] M. Mikikian, L. Couëdel, Y. Tessier, and L. Boufendi, IEEE Trans. Plasma Sci. **39**, 2748 (2011).
[25] H. Tawidian, M. Mikikian, L. Couëdel, and T. Lecas, Eur. Phys. J. Appl. Phys. **56**, 24 018 (2011).
[26] M. Mikikian, L. Boufendi, A. Bouchoule, H. M. Thomas, G. E. Morfill, A. P. Nefedov, V. E. Fortov, and (the PKE-Nefedov Team), New J. Phys. **5**, 19 (2003).
[27] See Supplemental Material at http://link.aps.org/supplemental/10.1103/PhysRevLett.109.245007 for the corresponding movies.
[28] S. I. Krasheninnikov, Phys. Lett. A **283**, 368 (2001).
[29] D. Jovanovic, U. de Angelis, R. Fedele, and F. Pegoraro, Phys. Plasmas **14**, 083704 (2007).
[30] R. Maqueda, D. P. Stotler, S. J. Zweben, and (The NSTX team), J. Nucl. Mater. **415**, S459 (2011).
[31] D. A. D'Ippolito, J. R. Myra, and S. J. Zweben, Phys. Plasmas **18**, 060501 (2011).
[32] J. R. Angus, M. V. Umansky, and S. I. Krasheninnikov, Phys. Rev. Lett. **108**, 215002 (2012).
[33] I. Brauer, M. Bode, E. Ammelt, and H.-G. Purwins, Phys. Rev. Lett. **84**, 4104 (2000).
[34] L. Stollenwerk, New J. Phys. **11**, 103034 (2009).
[35] J. P. Boeuf, B. Bernecker, T. Callegari, S. Blanco, and R. Fournier, Appl. Phys. Lett. **100**, 244108 (2012).
[36] E. Robert, V. Sarron, D. Riès, S. Dozias, M. Vandamme, and J.-M. Pouvesle, Plasma Sources Sci. Technol. **21**, 034017 (2012).
[37] C. Douat, G. Bauville, M. Fleury, M. Laroussi, and V. Puech, Plasma Sources Sci. Technol. **21**, 034010 (2012).
[38] Z. Bonaventura, M. Duarte, A. Bourdon, and M. Massot, Plasma Sources Sci. Technol. **21**, 052001 (2012).
[39] Z. Xiong, E. Robert, V. Sarron, J.-M. Pouvesle, and M. J. Kushner, J. Phys. D **45**, 275201 (2012).
[40] J. Schulze, D. Luggenhölscher, and U. Czarnetzki, IEEE Trans. Plasma Sci. **36**, 1402 (2008).

Zoom Into Dusty Plasma Instabilities

Hagop Tawidian, Thomas Lecas, and Maxime Mikikian

***Abstract*—In a krypton plasma, the growth of dust particles can strongly affect the plasma characteristics by inducing many types of instabilities. These unstable phenomena are studied by analyzing their frequency evolution as a function of time and by emphasizing the appearance of plasma spheroids. Different phases are evidenced due to a detailed analysis of the form and the frequency of the discharge current. Concerning the plasma spheroids, interesting motions in the plasma bulk are evidenced.**

***Index Terms*—Complex plasma, dust particle growth, dusty plasma, Fourier analysis, instabilities, plasma spheroids.**

I. Introduction

PLASMAS ARE present in nature and also in many industrial processes. When favorable conditions are encountered, dust particles can be grown in these plasmas. The formation of dust particles has been intensively studied since their discovery in plasma processing reactors [1], [2], particularly in microelectronics. These particles can fall on wafers and affect semiconductor device performances. However, these nanometer size dust particles can be useful in some industrial applications such as solar cells [3] or memories. More recently, the existence of dust particles in fusion reactors [4] such as the future ITER is the subject of special attention. In nature, particularly in the astrophysics field, dusty plasmas are found in comet tails and planetary atmospheres [5].

In the laboratory, dust particles can be grown using reactive gases [6]–[13] or material sputtering [14]–[16]; molecular precursors resulting from both methods launch a succession of chemical reactions leading to the growth of dust particles. In this paper, material sputtering is used to grow a high density of dust particles in a Kr plasma. During their growth, they acquire a negative charge by capturing electrons [17]–[19]. This loss of free electrons [20] can lead to a disturbance of the plasma equilibrium. Many types of unstable behaviors can be observed such as the heartbeat instability [21], [22], dust particle growth instabilities (DPGIs) [23], [24], or rotating plasma spheroids close to the electrodes [25], [26]. To study the evolution of the instabilities as a function of time, the amplitude of the discharge current fundamental harmonic is recorded and analyzed using different methods such as the Fourier spectrogram, the Fourier spectrum, and the peak detection. Several regimes are identified with different frequencies and signal forms. One of the objectives of this paper is to find a way to correlate the instability characteristics and the time evolution of the dust particle size and density. It can open new perspectives for dust particle growth monitoring with an easily implemented diagnostics. A good characterization of these instabilities has to be performed as a first step. In this paper, this characterization is explored. Due to a high-speed camera, a new phenomenon has been also observed by recording the plasma glow. Plasma spheroids characterized by a slightly enhanced luminosity stochastically appear in the plasma bulk. These spheroids can have up and down motions and sudden changes in their directions.

Manuscript received July 23, 2012; revised October 2, 2012; accepted October 23, 2012. Date of publication November 26, 2012; date of current version April 6, 2013. This work was supported in part by the DLR/BMB under Grant 50WM9852 and in part by the French National Research Agency (ANR) under Project INDIGO n° ANR-11-JS09-010-01.

The authors are with Groupe de Recherches sur l'Energétique des Milieux Ionisés, UMR7344, Centre National de la Recherche Scientifique/Université d'Orléans, 45067 Orléans Cedex 2, France (e-mail: hagop.tawidian@univ-orleans.fr; maxime.mikikian@univ-orleans.fr).

Color versions of one or more of the figures in this paper are available online at http://ieeexplore.ieee.org.

Digital Object Identifier 10.1109/TPS.2012.2226756

II. Experimental Setup

Experiments are performed in the PKE-Nefedov reactor [15], [27], where the plasma is created by a capacitively coupled radio-frequency (RF; 13.56 MHz in push–pull mode) discharge in krypton. The two electrodes are separated by 3 cm and have a diameter of 4 cm. The injected RF power is around 3 W for a pressure of 1.6 mbar. Dust particles are grown by sputtering previously injected micrometer size particles made of polymer (melamine formaldehyde) and lying on the electrodes. After each experiment, the grown dust particles fall down on the electrodes, and this additional material is also sputtered and involved in the growth process. In previous experiments with argon, the dust cloud was observed by laser light scattering using a thin laser sheet injected through the reactor by a laser diode at 685 nm. However, when using Kr, the dust cloud is not observed except in the afterglow phase, meaning that, probably, the dust particle size does not exceed 100 nm. Indeed, in Kr, the final size of the grown dust particles appears much smaller than in Ar, while their number density is much higher. The Kr mass being twice higher than the Ar one, it can change the sputtering efficiency of the deposited material and also the dust particle erosion in the plasma volume. It can contribute to explain the higher dust particle density and the smaller final size leading to new behaviors not observed in Ar. To monitor dust particle growth, the amplitude of the discharge current fundamental harmonic is recorded. The plasma glow is observed due to a high-speed camera (Photron Fastcam SA5) at 16 000 frames per second.

III. DPGIs and Their Different Phases

To obtain a sufficiently high dust density, the reactor was pumped down to a very low base pressure around 10^{-6} mbar before each experiment. Once the plasma is switched on, the

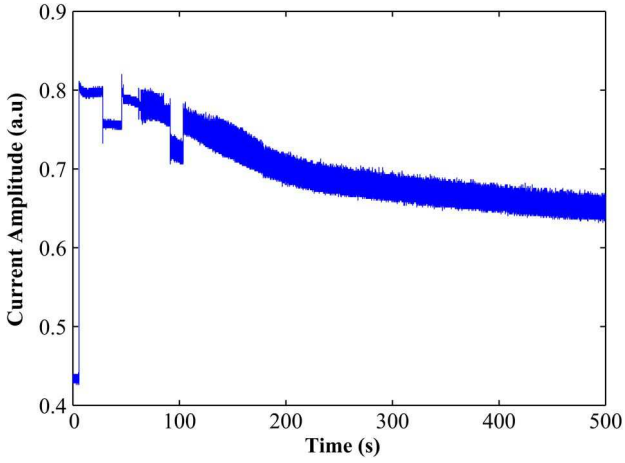

Fig. 1. Time evolution of the amplitude of the discharge current during dust particle growth (dc component). DPGIs begin at 62 s. Sudden drops are observed at 28 and 91 s and could be related to the high dust particle density.

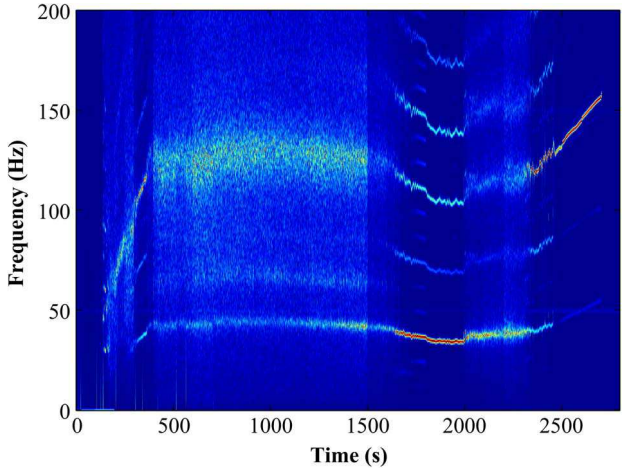

Fig. 2. Fourier spectrogram of the electrical measurements showing the frequency evolution as a function of time.

sputtering process begins, and after a few tens of seconds, the instability beginning is observed. The loss of free electrons on the dust particle surface is observed on the amplitude of the discharge current that is decreasing during the dust particle formation and growth (see Fig. 1). Sudden amplitude drops in the electrical signal are noticed when using Kr. These drops last for a few seconds and are evidenced just after the plasma ignition and during the first part of the instabilities. Later in the growth process, the existence of these drops is no more evidenced. Their origin is currently under investigation and could be related to the huge density of grown dust particles.

To more precisely study the evolution of the instabilities as a function of time, the oscillating part of the electrical measurements is recorded to have a better oscilloscope vertical resolution. This measurement is performed during a new experiment, different than the one presented in Fig. 1. The Fourier spectrogram of the signal is calculated to distinguish different phases in DPGI (see Fig. 2). To highlight the importance of the different frequencies, the Fourier spectrogram intensity has been normalized on each 100-s range. The instability begins around 140 s after the plasma ignition and consists of a succession of regular and chaotic phases. In a global way, a scenario tends to repeat. Several ordered phases are detected just after the instability beginning and are followed by a long chaotic phase (between 162 and 1400 s) briefly interrupted by a short ordered phase (between 300 and 370 s). Then, a regular phase occurs with a decreasing frequency, and finally, the instability stops after another short chaotic phase that becomes more and more regular.

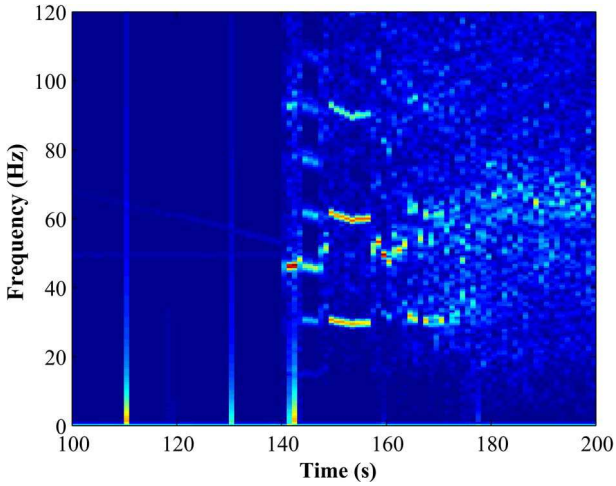

Fig. 3. Zoom of Fig. 2 on the first part of the instability. The instability begins at 140 s and is characterized by four successive ordered phases before entering in a chaotic regime.

In Fig. 3, a zoom of the Fourier spectrogram is made to more specifically study the instability beginning; the vertical lines around (110 and 130 s) correspond to electrical drops similar to the ones observed in Fig. 1. The ordered phases are well observed between 140 and 162 s. Four phases can be clearly evidenced. The first phase from 140 to 142 s is followed by a second one until 148 s. Then, a well-defined third phase takes place until 157 s, and finally, a fourth one (less clear) exists until 162 s where the system enters in the chaotic regime.

In order to better characterize these phases, the corresponding electrical signals and their Fourier spectra are presented in Fig. 4. All the phases show well-defined patterns containing a varying number of peaks. For the first phase [see Fig. 4(a)], the main pattern is composed of two big peaks followed by a smaller one, while for the second and third phases, four and two peaks [see Fig. 4(b) and (c), respectively] of different amplitudes form the main pattern. The fourth phase [see Fig. 4(d)] appears roughly similar to the first one with differences in the relative amplitude of the peaks. From this first insight, the transition between each phase is characterized by the appearance or disappearance of peaks. The frequency evolution is also quite interesting. In order to better understand and complete Fig. 3, the Fourier spectrum of each phase is presented in Fig. 4(e)–(h). It appears that the same typical frequencies or their harmonics are globally encountered in each phase. Harmonics are easily obtained due to the nonsinusoidal shape of the signals that have similarities with sawtooth signals. The smallest detected frequency is about 15–16 Hz. This frequency is clearly detected in Fig. 4(f), is very small in the cases corresponding to Fig. 4(e) and (h), and cannot be detected in Fig. 4(g). Whereas, in

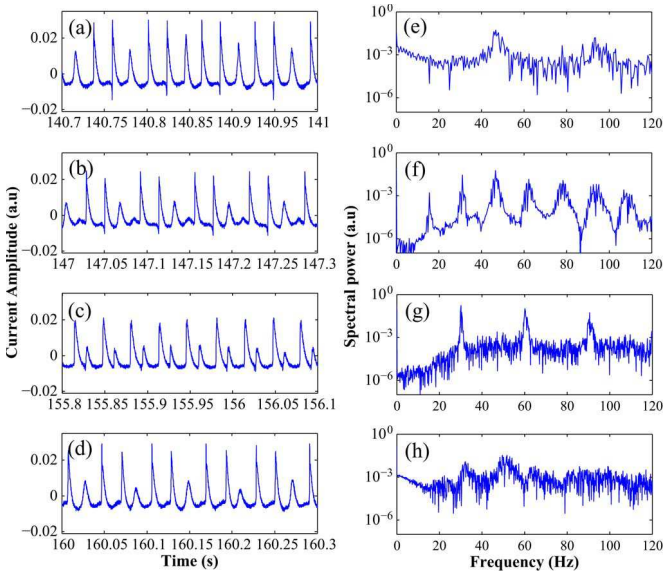

Fig. 4. Electrical signals and their corresponding Fourier spectra for the first four ordered phases of the instability.

Fig. 4(e) and (h) presenting the whole frequency range, this frequency cannot be observed, its presence has been confirmed by filtering and zooming the corresponding data around 15 Hz. In the phases where this frequency appears, it corresponds to the main pattern frequency that is slightly similar in phases 1, 2, and 4. For phase 3, the main pattern frequency is about 30 Hz, which is twice the value of the other phases. This value of 30 Hz is present in all the phases, as a main frequency or as a harmonic. Another interesting value is the frequency at 45 Hz that is clearly present in phases 1, 2, and 4. In the Fourier spectra, a peak is centered at this value with a width of about 4 Hz. It appears that 45 Hz is roughly the frequency corresponding to the peak separation within the main patterns. For phase 1, three peaks at a repetition rate of 45 Hz constitute the main pattern that repeats at 15 Hz. For phase 2, the main pattern frequency is similar but with four peaks: The first two peaks appear at 45 Hz, but the frequency for the two other peaks is continuously increasing with values that are multiple of 15 Hz. The fact that the system oscillates at very well-defined frequencies that are multiple from each other underlines that the dynamics behind these instabilities is relatively complex. For example, the sum of two signals at 30 and 60 Hz can roughly reproduce the signal of phase 3 [see Fig. 4(c) and (g)], but a linear combination of simple signals cannot reproduce the other phases in a satisfactory way. Additional experiments and analyses will be performed in order to better understand the frequency dependence of the signals and the occurrence and the evolution of defined frequencies.

During the instabilities, the electrical signal can be also analyzed through the variations of its oscillation amplitude. The same time series data used to obtain Fig. 2 and to derive the results in Figs. 3 and 4 is also used to analyze the electrical signal data. To analyze this signal, the peak maxima and minima are measured. One part of the instability that appears particularly interesting corresponds to the region between 2360 and 2460 s. The peak detection of this region is shown in

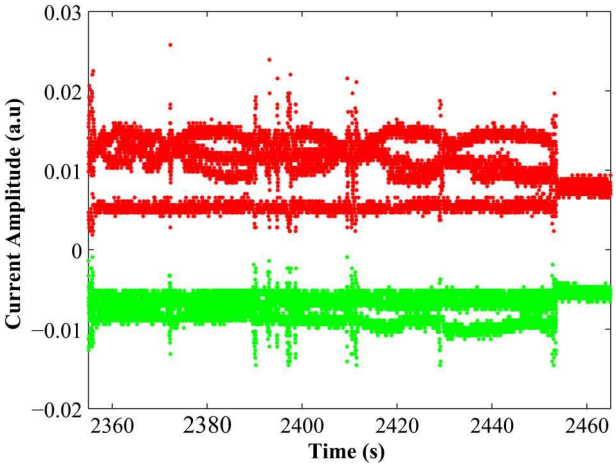

Fig. 5. Peak detection on the electrical measurements showing the evolution of the peak amplitudes. The maxima (> 0) and minima (< 0) are represented.

Fig. 5, where the maxima and the minima are represented. On the time series, this region is characterized by a three-peak pattern and occurs just before the last ordered phase at the end of the instabilities. In Fig. 5, the maxima evolution shows a very particular behavior. It is particularly clear at 2420 s, where the amplitude evolution of the different peaks follows an eye-shape form. An increase in the amplitude of the main peak corresponds to the decrease in the amplitude of the second peak. Then, when the main peak reaches its maximum amplitude, it starts to decrease, while the second peak amplitude behaves in the opposite way. When the amplitude of these two peaks becomes comparable, a short "chaotic" regime occurs, which concludes the eye-shape oscillation. This phenomenon repeats several times during the instability. It is noteworthy to mention that the third peak keeps a constant amplitude during the whole duration of this phenomenon. Concerning the amplitude of the peak minima, its variation is not very clear, and its analysis will be further examined. From these new analyses based on the amplitude variations, it appears that the resulting measured signal can be a complex combination of signals and plasma behaviors. They can simultaneously evolve or interact with each other; this interaction can be the consequence of the short chaotic regime occurring at the end of the eye-shape form when the two maxima have close amplitudes.

IV. Plasma Glow Behavior

In the previous section, an analysis has been performed on the electrical measurements during the instabilities. In order to better understand the plasma evolution during DPGI, the plasma glow has been also analyzed by high-speed imaging. An interesting phenomenon consisting of the appearance of plasma spheroids in the plasma bulk is observed. These spheroids are well-defined regions of about a few millimeters with a slightly enhanced luminosity. In a previous paper [26] where experiments were performed in Ar, these spheroids were shown to appear and disappear near the electrodes. Their behavior was either "chaotic" or regular with clear rotations along the circumference of the electrodes [25], [26]. In this paper where Kr is used, these plasma spheroids are also evidenced in the

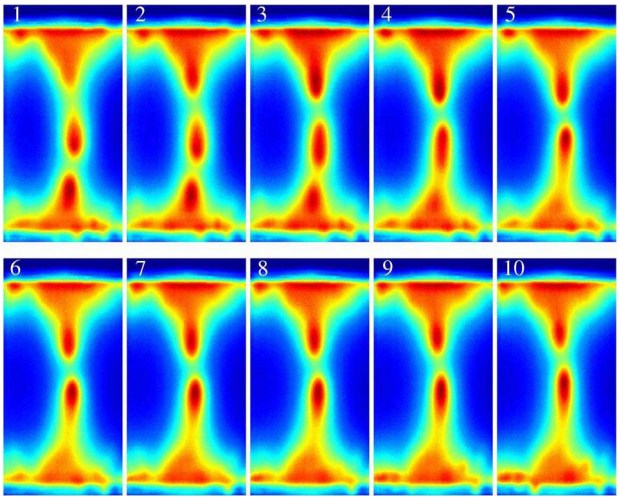

Fig. 6. Up and down motions of plasma spheroids in between the electrodes. Interactions between plasma spheroids can be detected. Images are extracted from a video recorded at 16 000 frames per second.

plasma bulk, as shown in Fig. 6, where ten successive images are extracted from a video recorded at 16 000 images per second. False colors are used to enhance the luminosity contrast in different regions of the plasma. The top and bottom regions of each frame correspond to the electrodes. As for Ar, many plasma spheroids appear in the vicinity of the electrodes. In the plasma bulk, these plasma spheroids have a comet-like shape, as clearly shown, for example, in the first image in Fig. 6. The spheroid in the plasma center is heading toward the lower electrode, where another spheroid seems to attract it, as observed in the first two frames. Then, a sudden change in the spheroid direction occurs. Another spheroid emerges from the top presheath region and moves toward the plasma center. This new spheroid seems to impact the central spheroid as confirmed by looking at its comet-like shape. The comet head is now on the spheroid top (image 4 in Fig. 6). The central spheroid is now moving toward the top electrode up to image 10. These up and down motions can repeat several times. The composition of these spheroids is still unknown; they can be composed of just plasma or of plasma containing dust particles. Similar behaviors have been observed in a Kr plasma without dust particles [28] but with the insertion of an object in the plasma. As dust particles, this object can strongly disturb the free electron density, and it can be suggested that similar instabilities with plasma spheroids can be also obtained. The origin of these plasma spheroids and particularly of their motion is currently under investigation. It raises interesting questions about the type of interaction between these regions of enhanced emission.

The correlation between the electrical measurements presented in Section III and the plasma spheroids is difficult for several reasons. The electrical measurements are a global measurement and are thus representative of the changes occurring in the whole plasma. Frames in Fig. 6 show a part of the plasma and do not give information on the possible presence of other spheroids in the plasma regions outside the camera field of view. Thus, a direct correlation would need to perfectly identify all spheroids appearing in the discharge. Concerning the spheroid motions, the correlation is even more difficult as a spheroid moving in the plasma does not necessarily change the discharge current. Indeed, if the "charge" transported by the spheroid is just displaced in the plasma, it does not change the global current, except, of course, if the spheroid size and brightness are changing.

V. Conclusion

In this paper, instabilities triggered by the presence of dust particles have been studied in a Kr plasma. These instabilities appear when a high density of grown dust particles is achieved. These instabilities have been characterized by electrical measurements and high-speed imaging. The amplitude of the discharge current decreases due to the loss of free electrons on the dust particle surface. Some electrical drops have been also evidenced and are currently under investigation. A Fourier analysis of the electrical measurements shows the existence of different phases during DPGI. The first four ordered phases have been more precisely studied using the Fourier spectrum and by observing the signal shape. After these regular phases, the instability enters into a long chaotic regime followed by a regular phase with a decreasing frequency. The instability ends with a short chaotic phase that becomes more and more regular. In comparison with Ar results [23], some preliminary comparisons can be made. Similarities are found in the succession of the different phases. As in Ar, in Kr, we have observed that DPGI start with several regular regimes followed by a long chaotic regime and finish by a more regular phase. Concerning the frequency values, in Kr, the frequencies are slightly higher than in Ar. This is consistent with the fact that the dust particle size is smaller and the dust particle density is higher in Kr. A deeper comparison is currently ongoing. The instability amplitude has been also analyzed by using peak detection. This method shows that, during some time periods, the peak maxima and minima follow a well-defined pattern consisting of the appearance of an eye-shape form. These various analyses show that the measured electrical signal is a complex combination of plasma behaviors with different typical frequencies.

In order to better investigate the plasma evolution during DPGI, the plasma glow has been analyzed by a high-speed camera evidencing the appearance of plasma spheroids in the plasma bulk. These spheroids have a comet-like shape with a slightly enhanced luminosity, and they can move. Sudden changes in their direction appear to be due to the appearance of other nearby spheroids. The origin of the spheroid motions and interactions is currently under investigation and can reveal very interesting phenomena related to interaction models.

Acknowledgment

The authors would like to thank B. Dumax for electronic support, and J.-M. Bauchire and H. Rabat for providing the high-speed camera. The PKE-Nefedov chamber has been made available by the Max-Planck-Institute for Extraterrestrial Physics, Germany.

REFERENCES

[1] R. M. Roth, K. G. Spears, G. D. Stein, and G. Wong, "Spatial dependence of particle light scattering in an RF silane discharge," *Appl. Phys. Lett.*, vol. 46, no. 3, pp. 253–255, Feb. 1985.

[2] G. S. Selwyn, J. Singh, and R. S. Bennett, "*In situ* laser diagnostic studies of plasma-generated particulate contamination," *J. Vac. Sci. Technol. A*, vol. 7, no. 8, pp. 2758–2765, Jul. 1989.

[3] P. Roca i Cabarrocas, P. Gay, and A. Hadjadj, "Experimental evidence for nanoparticle deposition in continuous argon-silane plasmas: Effects of silicon nanoparticles on film properties," *J. Vac. Sci. Technol. A*, vol. 14, no. 2, pp. 655–664, Mar. 1996.

[4] S. I. Krasheninnikov, A. Y. Pigarov, R. D. Smirnov, M. Rosenberg, Y. Tanaka, D. J. Benson, T. K. Soboleva, T. D. Rognlien, D. A. Mendis, B. D. Bray, D. L. Rudakov, J. H. Yu, W. P. West, A. L. Roquemore, C. H. Skinner, J. L. Terry, B. Lipschultz, A. Bader, R. S. Granetz, C. S. Pitcher, N. Ohno, S. Takamura, S. Masuzaki, N. Ashikawa, M. Shiratani, M. Tokitani, R. Kumazawa, N. Asakura, T. Nakano, A. M. Litnovsky, and R. Maqueda, "Recent progress in understanding the behavior of dust in fusion devices," *Plasma Phys. Control. Fusion*, vol. 50, no. 12, pp. 124 054-1–124 054-13, Dec. 2008.

[5] E. Sciamma-O'Brien, N. Carrasco, C. Szopa, A. Buch, and G. Cernogora, "Titan's atmosphere: An optimal gas mixture for aerosol production?" *Icarus*, vol. 209, no. 2, pp. 704–714, Oct. 2010.

[6] J. Berndt, E. Kovacevic, I. Stefanovic, O. Stepanovic, S. H. Hong, L. Boufendi, and J. Winter, "Some aspects of reactive complex plasmas," *Contrib. Plasma Phys.*, vol. 49, no. 3, pp. 107–733, Apr. 2009.

[7] K. De Bleecker, A. Bogaerts, and W. Goedheer, "Detailed modeling of hydrocarbon nanoparticle nucleation in acetylene discharges," *Phys. Rev. E Stat. Nonlinear Soft Matter Phys.*, vol. 73, no. 2, pp. 026405-1–026405-16, Feb. 2006.

[8] V. Massereau-Guilbaud, J. Pereira, I. Géraud-Grenier, and A. Plain, "Influence of the power on the particles generated in a low pressure radio frequency nitrogen-rich methane discharge," *J. Appl. Phys.*, vol. 105, no. 3, pp. 033302-1–033302-8, Feb. 2009.

[9] J. Berndt, E. Kovacevic, I. Stefanovic, and L. Boufendi, "Controlled dust formation in pulsed RF plasmas," *J. Appl. Phys.*, vol. 106, no. 6, pp. 063309-1–063309-8, Sep. 2009.

[10] M. Mikikian, M. Cavarroc, L. Couëdel, Y. Tessier, and L. Boufendi, "Dust particles in low-pressure plasmas: Formation and induced phenomena," *Pure Appl. Chem.*, vol. 82, no. 6, pp. 1273–1282, 2010.

[11] M. Hundt, P. Sadler, I. Levchenko, M. Wolter, H. Kersten, and K. Ostrikov, "Real-time monitoring of nucleation-growth cycle of carbon nanoparticles in acetylene plasmas," *J. Appl. Phys.*, vol. 109, no. 12, pp. 123305-1–123305-7, Jun. 2011.

[12] M. Calafat, P. Yuryev, A. Drenik, A. Slim, and R. Clergereaux, "Carbon nanoparticle/hydrogenated amorphous carbon composite thin films formed in ECR plasma," *Plasma Process Polym.*, vol. 8, no. 5, pp. 401–408, May 2011.

[13] I. Géraud-Grenier, R. Jaffiol, V. Massereau-Guilbaud, and A. Plain, "Photoluminescence of hydrogen amorphous carbon nitrile particles obtained in a 13.56 MHz dusty plasma," *Appl. Phys. Lett.*, vol. 99, no. 9, pp. 091503-1–091503-3, Aug. 2011.

[14] D. Samsonov and J. Goree, "Instabilities in a dusty plasma with ion drag and ionization," *Phys. Rev. E*, vol. 59, no. 1, pp. 1047–1058, Jan. 1999.

[15] M. Mikikian, L. Boufendi, A. Bouchoule, H. M. Thomas, G. E. Morfill, A. P. Nefedov, and V. E. Fortov, "Formation and behavior of dust particle clouds in a radio-frequency discharge: results in the laboratory and under microgravity conditions," *New J. Phys.*, vol. 5, no. 1, p. 19, Mar. 2003.

[16] C. Arnas, A. Mouberi, K. Hassouni, A. Michau, G. Lombardi, X. Bonnin, F. Bénédic, and B. Pégourié, "Carbon dust formation in a cold plasma from cathode sputtering," *J. Nucl. Mater.*, vol. 390/391, pp. 140–143, Jun. 2009.

[17] A. Melzer, T. Trottenberg, and A. Piel, "Experimental determination of the charge on dust particles forming Coulomb lattices," *Phys. Lett. A*, vol. 191, no. 3/4, pp. 301–308, 1994.

[18] B. Walch, M. Horanyi, and S. Robertson, "Measurement of the charging of individual dust grains in a plasma," *IEEE Trans. Plasma Sci.*, vol. 22, no. 2, pp. 97–102, Apr. 1994.

[19] C. Arnas, M. Mikikian, and F. Doveil, "Micro-sphere levitation in a sheath of a low pressure continuous discharge," *Phys. Scr.*, vol. 2001, no. T89, pp. 163–167, 2001.

[20] H. Kersten, H. Deutsch, M. Otte, G. H. P. M. Swinkels, and G. M. W. Kroesen, "Micro-disperse particles as probes for plasma surface interaction," *Thin Solids Films*, vol. 377/378, pp. 530–536, Dec. 2000.

[21] M. Mikikian, M. Cavarroc, L. Couëdel, Y. Tessier, and L. Boufendi, "Mixed-mode oscillations in complex plasma instabilities," *Phys. Rev. Lett.*, vol. 100, no. 22, pp. 225 005-1–225 005-4, Jun.2008.

[22] M. Mikikian, L. Couëdel, M. Cavarroc, Y. Tessier, and L. Boufendi, "Threshold phenomena in a throbbing complex plasma," *Phys. Rev. Lett.*, vol. 105, no. 7, pp. 075002-1–075002-4, Aug. 2010.

[23] M. Mikikian, M. Cavarroc, L. Couëdel, and L. Boufendi, "Low frequency instabilities during dust particle growth in a radio-frequency plasma," *Phys. Plasmas*, vol. 13, no. 9, pp. 092103-1–092103-8, Sep. 2006.

[24] M. Mikikian, L. Couëdel, M. Cavarroc, Y. Tessier, and L. Boufendi, "Plasma emission modifications and instabilities induced by the presence of growing dust particles," *IEEE Trans. Plasma Sci.*, vol. 36, no. 4, pp. 1012–1013, Aug. 2008.

[25] M. Mikikian, L. Couëdel, Y. Tessier, and L. Boufendi, "Carousel instability in a capacitively-coupled RF dusty plasma," *IEEE Trans. Plasma Sci.*, vol. 39, no. 11, pp. 2748–2749, Nov. 2011.

[26] H. Tawidian, M. Mikikian, L. Couëdel, and T. Lecas, "Plasma inhomogeneities near the electrodes of a capacitively-coupled radio-frequency discharge containing dust particles," *Eur. Phys. J. Appl. Phys.*, vol. 56, no. 2, pp. 24 018-1–24 018-4, 2011.

[27] A. P. Nefedov, G. E. Morfill, V. E. Fortov, H. M. Thomas, H. Rothermel, T. Hagl, A. Ivlev, M. Zuzic, B. A. Klumov, A. M. Lipaev, V. I. Molotkov, O. F. Petrov, Y. P. Gidzenko, S. K. Krikalev, W. Shepherd, A. I. Ivanov, M. Roth, H. Binnenbruck, J. Goree, and Y. P. Semenov, "PKE-Nefedov: plasma crystal experiments on the international space station," *New J. Phys.*, vol. 5, no. 1, p. 33, Apr. 2003.

[28] J. Schulze, D. Luggenhölscher, and U. Czarnetzki, "Instabilities in capacitively coupled radio-frequency discharges," *IEEE Trans. Plasma Sci.*, vol. 36, no. 11, pp. 1402–1403, Nov. 2011.

Hagop Tawidian was born in Mdawar, Lebanon, in 1986. He received the M.S. degree in microwave, electromagnetism, and optoelectronic from the Université Paul Sabatier, Toulouse, France, in 2010. He is currently working toward the Ph.D. degree in Groupe de Recherches sur l'Energétique des Milieux Ionisés, Centre National de la Recherche Scientifique/Université d'Orléans, Orléans, France.

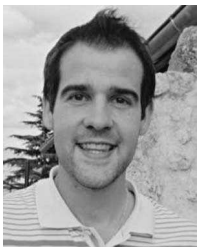

Thomas Lecas was born in 1986, in Orléans, France. He received the Associate degree in electronics in 2006.

Since 2010, he has been a Centre National de la Recherche Scientifique (CNRS) Assistant Engineer in instrumentation with Groupe de Recherches sur l'Energétique des Milieux Ionisés, CNRS/Université d'Orléans, Orléans.

Maxime Mikikian was born in Marseille, France, in 1973. He received the Ph.D. degree in radiation and plasmas from the Université de Provence, Marseille, in 1999 and the Habilitation in physics from the Université d'Orléans, Orléans, France, in 2008.

Since 2004, he has been a Centre National de la Recherche Scientifique (CNRS) researcher with Groupe de Recherches sur l'Energétique des Milieux Ionisés, CNRS/Université d'Orléans, Orléans. His research interests include dusty plasmas and particularly instabilities, dust particle formation, dust cloud structure, and dust charging.

Electron Temperature Evolution in a Low-Pressure Dusty RF Nitrogen-Rich Methane Plasma

Véronique Massereau-Guilbaud, Isabelle Géraud-Grenier, Jean-François Lagrange, Hagop Tawidian, and Maxime Mikikian

***Abstract*— Particles are generated in a classical planar RF (13.56-MHz) reactor in nitrogen-rich methane at low pressure (120 Pa). The gas decomposition leads to particle generation and growth. During their formation, the particles become negatively charged. The electrical and the optical parameters of the discharge are disturbed. The presence of particles in the plasma is put in evidence by laser light scattering and is correlated to the DC self-bias voltage. A small quantity of argon is introduced in the gas mixture in order to estimate the electron temperature. The temporal evolutions of both the electron temperature and the optical emission intensities of excited argon are correlated with the particle growth and behavior in the plasma.**

***Index Terms*— Dust particle growth, dusty plasma, plasma diagnostics.**

I. INTRODUCTION

DUSTY particle formation in plasmas was first observed and highlighted by Langmuir *et al.* [1]. At the beginning of particle formation and growth studies, particles were considered as contaminants in deposition or etching processes [2], [3]. At present, particles can be incorporated in layers for the improvement of films, for example, Au and Ag deposition on silicon surfaces for a reduction of solar cell reflectivity [4], [5]. Moreover, particles appearing in methane or methane-nitrogen plasmas are of interest in astrophysics such as in the study of Titan's atmosphere [6], [7]. In hydrocarbon plasmas, several investigations [8]–[11] have been made on dust particle formation, particle behavior within plasmas, and also the electrical and optical perturbations due to the particles. Amorphous carbon nitride films from those plasmas are used for their good physical and chemical properties [12]. Moreover, nitrogen addition in the diamond-like carbon is expected to lead to the formation of the hypothetical superhard compound β-C_3N_4 [13] or the creation of fullerene-like bonding structures [14].

In low-pressure plasmas, excitation, ionization, and dissociation phenomena are induced essentially by electron collisions. The tracking of the electron temperature and of the electron energy distribution function (EEDF) is important to control coating and/or particle growth. Studies have shown that the quality of diamond and diamond-like carbon depositions depends on the electron temperature [15].

In this paper, we deal with the generation of particles by plasma-enhanced CVD (PECVD) in nitrogen-rich methane plasma. Previous studies have been carried out in the laboratory in order to understand a particular behavior of the particles within the plasma [16] and to analyze the particle properties, their structure, and their composition [17]–[20]. In this paper, we focus on the temporal evolutions of the electrical characteristics of the discharge, of the optical emission line intensities of the excited Ar, and of the electron temperature, during particle growth. The phenomenon of particle multigeneration is described and explained. EEDF and electron temperature modifications during particle growth are investigated.

II. EXPERIMENTAL SETUP

The particles are generated by PECVD in a classical RF 13.56-MHz reactor made of stainless steel with a parallel-plate electrode configuration as described previously [21]. The upper electrode is capacitively coupled with an RF generator, and a constant incident RF power of 100 W is applied. The lower electrode and the reactor walls are grounded. The capacitive coupling induces a negative DC self-bias voltage V_{dc} relative to ground. The pumping group allows to achieve a residual pressure lower than 10^{-3} Pa. The operational pressure is equal to 120 Pa. Between each experiment, the reactor is cleaned in order to obtain particle formation and reproducible results. The gas mixture (9% CH_4-82% N_2-9% Ar) is injected within the reactor's enclosure with a constant flow rate of 6.2 sccm (0.01 $Pa.m^3.s^{-1}$). At the end of each experiment, the particles fall onto the grounded electrode, they are collected and then analyzed.

The plasma study by optical emission spectroscopy (OES) is realized through a glass window with a lens focusing the light onto a quartz optical fiber. The fiber is connected to a spectrometer which is coupled with a charge-coupled device (CCD) camera. In this paper, the optical fiber collects the light coming from the RF sheath boundary. In a previous study [21], we have shown that the strongest intensities of the emission lines are observed in this discharge zone. The optical detection system is calibrated by a tungsten lamp to determine the correction factors for the different emission line intensities of excited species.

Manuscript received July 3, 2012; revised March 5, 2013; accepted March 6, 2013. Date of publication April 6, 2013; date of current version April 6, 2013. This work was supported in part by a FEDER Contract and a FSE Contract n 24/18/2/96/040 from the European Community, the "Conseil Général du Cher," and the French National Research Agency under Project INDIGO n ANR-11-JS09-010-01.

The authors are with Groupe de Recherches Sur l'Energétique des Milieux Ionisés, UMR 7344, CNRS/Université d'Orléans, Bourges 18000, France (e-mail: veronique.massereau@univ-orleans.fr; isabelle.geraud@bourges.univ-orleans.fr; jean-francois.lagrange@univ-orleans.fr; hagop.tawidian@univ-orleans.fr; maxime.mikikian@univ-orleans.fr).

Color versions of one or more of the figures in this paper are available online at http://ieeexplore.ieee.org.

Digital Object Identifier 10.1109/TPS.2013.2252025

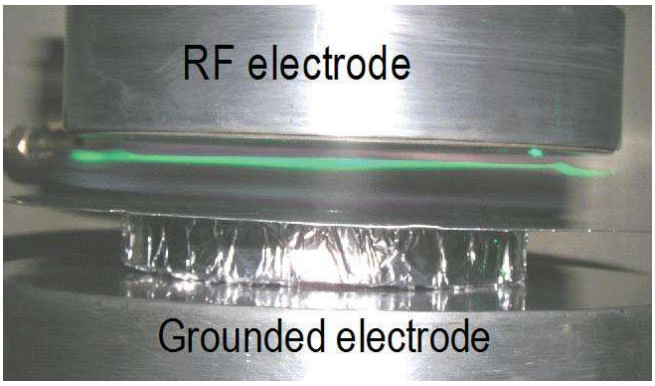

Fig. 1. Laser light scattering in the particle cloud under the RF electrode.

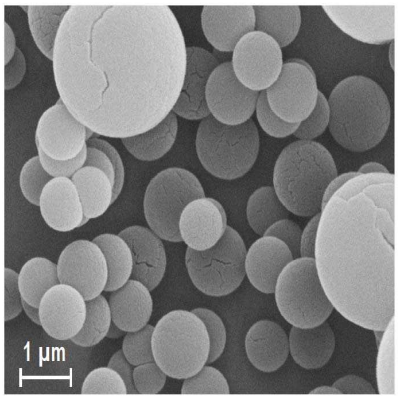

Fig. 2. SEM micrograph of particles. Observation realized in "Institut Universitaire de Technologie" at Bourges (France) in "Mesures Physiques" department.

The presence particles in the reactor is highlighted using the light scattering of an argon ion laser ($\lambda = 514.5$ nm). The laser beam parallel to the electrode surfaces is directed through the reactor at the boundary between the RF sheath and the plasma bulk. The temporal scattered light from particles at 514.5 nm is detected via the OES device at an angle of 135°. When the particles reach a critical size superior to 50 nm (≈10% of the wavelength of the laser), they scatter the laser beam light. The signal recorded by the CCD camera begins to increase.

The OES device is used both for light scattering and emission line intensity measurements. These measurements will be carried out during different experiments.

III. Results and Discussion

A. Particle Multigeneration

The decomposition of CH_4 and N_2 gases allows both the particle generation and coating deposition on the electrodes. Nevertheless, in our case, there is no coating on the electrodes. In nitrogen-rich methane plasma, the CH_4 precursors are not enough to contribute both to the particle and the deposition growth. Moreover, the coating could also be sputtered. The CH_4 precursors firstly participate in the particle formation within the plasma. In low-pressure plasmas, the electron mobility is higher than the ion one due to the lower mass of the electrons compared with the ion mass [22]. Therefore, the particle charge quickly becomes negative. The particles are submitted to different forces [21], [23]. The force action on the particles leads to specific particle behaviors in the discharge and to their trapping in different regions of the plasma bulk [24]–[26]. In our case, the forces that push the particles toward the grounded electrode are the gravitational force, the thermophoretic force, and the electrical force. The particles are pushed out of the plasma bulk toward the reactor wall by the thermophoretic and the electrostatic forces. Only one force drags the particles toward the RF electrode: the ion drag force. A previous study has shown that the neutral drag force can be neglected in our reactor [21]. At the beginning of the experiment, the forces are in equilibrium and the particles levitate in a cloud parallel to the RF electrode at the sheath boundary, as can be seen in Fig. 1. When the temperature difference between the electrodes increases, and when the particles have reached a sufficient size, the equilibrium between the forces is broken and the particles fall through the discharge. They are trapped again above the grounded electrode in a cloud. They continue to grow and then fall onto the grounded electrode [16].

The particle growth follows three phases [22], [27].

1) *Nucleation Phase:* the origin of the nucleation phase is either the formation of germs within the plasma bulk or the ejection of germs coming from the sputtering of the RF electrode. Afterward, the germs grow and form clusters in the discharge. Several experiments have been carried out in the laboratory in pure CH_4 plasmas [21], [25], [28] and in CH_4-N_2 ones [24], [29]. In our case, the nucleation phase seems to begin with the sputtering of the RF electrode. The RF electrode state becomes a very important parameter to obtain the germ formation and reproducible results [30]. In this paper, the RF electrode is sputtered with N_2^+ ions coming from the plasma bulk: germs are ejected and clusters grow.
2) A cluster coagulation leading to the formation of small particles.
3) A particle growth by deposition.

The particles present a spherical shape and an orange-peel surface with cracks as can be seen in Fig. 2. We have shown in a previous study that cracks and rough surface are due to a columnar growth during the deposition phase [29]. The particle size ranges from 0.5 to 2–3 μm.

Simultaneous measurements of the DC self-bias voltage V_{dc} and of the laser light scattering are carried out, in order to follow the particle growth and behavior at the boundary between the plasma bulk and the RF sheath. Fig. 3 shows the temporal evolutions of the absolute value of the DC self-bias voltage $|V_{dc}|$ and of the laser light scattering. The laser light scattering values change with the particle number density and/or their size. The particle formation and growth lead to an increase of the laser light scattering. In the same time, the $|V_{dc}|$ decreases, because electrons are trapped by the particles. In our case, the coagulation phase of the first particle generation begins around 10 s after the discharge is on [29], as also shown in C_2H_2-Ar mixture dusty plasma [31]. After that, particles become negatively charged. Thus, in the following, the particle charge will be considered as negative.

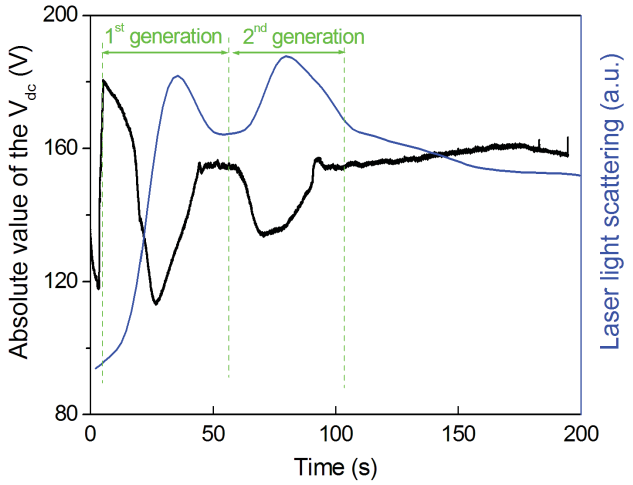

Fig. 3. Temporal evolutions of the absolute value of the DC self-bias voltage and of the laser light scattering.

The decrease of the laser light scattering means that particles leave the RF sheath boundary and migrate toward the grounded electrode. Therefore, fewer electrons are trapped and the $|V_{dc}|$ increases. The successive increases and decreases both of laser light scattering and $|V_{dc}|$ show that two particle generations occur.

The particle multigeneration phenomenon has also been observed in different dusty plasmas [8], [11], [31], and can be associated to void appearance in particle clouds [32], [33]. In our case, the particle multigeneration phenomenon could be explained from the different forces acting on the particles and from the cloud formation under the RF electrode. At the beginning of the experiment, the first particle generation growth follows the three previous phases (nucleation, coagulation, and deposition). The particles are trapped in a dense cloud under the RF electrode [24]. The particles are submitted to physical and chemical bombardments by N_2^+ ions, allowing nitrogen incorporation in the particles [34]. Thus, the screen formed by the particles prevents the N_2^+ ion bombardment of the RF electrode. The measurements of the ion flux reduction and the ion energy have not been estimated yet. Then, fewer germs are ejected and no new particles are generated. The present particles continue to grow certainly by deposition and end up falling onto the grounded electrode through the plasma; it is the end of the first particle generation. As there are fewer particles under the RF electrode, N_2^+ ions can reach the RF electrode again. New germs are sputtered from the RF electrode, they grow and form clusters. The second particle generation appears. The end of particle generations could be explained by a modification of the RF electrode surface due to nitrogen incorporation. Therefore, no more germs are ejected, allowing cluster growth and consequently particle growth.

B. Optical Emission Spectroscopy

The optical emission spectroscopy (OES) study of the plasma is carried out at the RF sheath boundary where the laser light scattering has been measured and where the particles are firstly trapped. In order to show the influence of the particle presence on the optical characteristics of the plasma, the emission line intensities of excited species are measured. Then, the electron temperature of the plasma is calculated from the intensity values using the corona balance simplified model [35].

During the two particle generations, the emission line intensities of excited species, such as CH*, N_2*, and so on, vary with time. Their temporal evolutions are due both to electron energy distribution function (EEDF) modifications and to the participation of the excited species in the particle growth. In order to obtain information concerning the EEDF and to calculate the electron temperature of the plasma, the noble gas Ar is introduced in the CH_4-N_2 gas mixture. The Ar atoms do not participate in the particle growth. Therefore, the temporal variations of the Ar* line intensities are due only to the EEDF modifications. The Ar* line intensities have been measured for different wavelengths whose energy of excited levels ranges from 13 to 15 eV. Their evolutions during the particle formation and growth are the same (not shown). Fig. 4 shows the temporal evolutions of the excited Ar* ($\lambda = 750.3$ nm) intensity and the $|V_{dc}|$ one.

At the beginning of each particle generation, the $|V_{dc}|$ decreases as the Ar intensity increases. The Ar intensity variations show that the EEDF is disturbed by the particles in the energy range from 13 to 15 eV. In low-pressure dusty plasmas, the electron number density decreases during the particle formation and growth [36]. Indeed, the trapping of electrons by the particle leads to a decrease of the electron number density within the plasma. Moreover, the energy of trapped electrons must be superior to the surface potential of the particles [37]. Thus, the EEDF is depleted of these electrons. In our case, the electron number density whose energies are between 13 and 15 eV, increases during particle formation and growth at the beginning of each particle generation. This result shows that the energy of the trapped electrons by particles is not in the range 13–15 eV. In a previous study in the same experimental conditions, Ar gas was replaced by helium [29]. The He emission line intensity at 501.5 nm, whose threshold excitation energy is 23 eV, decreases at the beginning of each particle generation. The EEDF is thus depleted of electrons with energies around 23 eV. If we compare our results with the theoretical study carried out by Ostrikov *et al.* [38], we can make the following assumptions: the EEDF is depleted with midenergy electron density (around 23 eV) whereas low-energy electron density (<15 eV) increases. Moreover, in order to sustain the discharge, high-energy electron density in the EEDF tail increases.

The electron temperature (T_e) is calculated using the corona balance simplified model. The corona balance model is used to determine the electron temperature in low pressure plasmas. In low-pressure plasmas, this temperature is likely an average energy of electrons. A Maxwellian distribution for the electron velocity and a Boltzmann distribution for the excited-state populations are supposed. In this model, the populating mechanism of an excited state mainly due to electron collisions from the ground state and is balanced by the depopulation process by radiative emission [39], [40]. Excitation and de-excitation processes such as atom–atom,

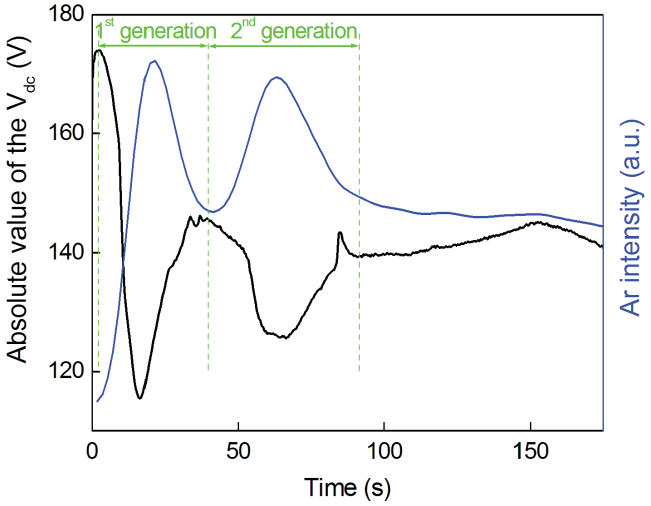

Fig. 4. Temporal evolutions of the absolute value of the DC self-bias voltage and of the Ar line intensity ($\lambda = 750.3$ nm).

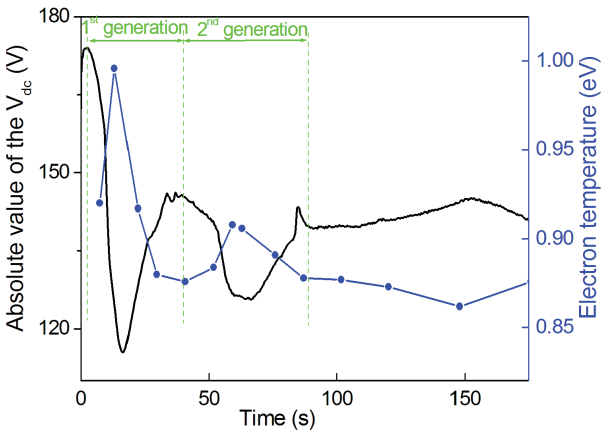

Fig. 5. Temporal evolutions of the absolute value of the DC self-bias voltage and of the electron temperature.

ion–atom, and quenching collisions are neglected. The electron temperature is calculated using the following equation:

$$\ln\left(\frac{I_{ij}\sum\limits_{i>j}A_{ij}}{A_{ij}\,h\,\nu_{ij}\,b_{1i}}\right) = -\frac{E_{1i}}{kT_e} + C \tag{1}$$

with

$$b_{1i} = k_{1i}\exp\left(-\frac{E_{1i}}{kT_e}\right) \tag{2}$$

where I_{ij}, ν_{ij}, and A_{ij} are the intensity, the transition frequency, and the transition probability, respectively, between the excited level i and the lower level j; h and k are the Planck and the Boltzmann constants, respectively; E_{1i} is the excitation energy between the fundamental level and the excited one i; k_{1i} is the electron impact excitation rate coefficient from the fundamental to the excited level i; and C is a constant.

In this paper, the electron temperature at low pressure should be calculated using the Druyvesten-like electron energy probability function [41]. Otherwise, Tachibana *et al.* [42] have shown that in argon dusty plasma containing injected carbon particles, the EEDF is close to a Maxwellian distribution because of the EEDF modifications due to the presence of particles in the plasma. This result has also been evidenced in [37], in argon dusty plasma with particles spreading over the plasma bulk. The electron collisions with particles and their trapping by particles lead to an electron thermalization. In our case, as the particles fill the plasma bulk and the EEDF is modified during the particle formation and growth, we will suppose that the EEDF is close to a Maxwellian distribution for the electron velocity.

While using (1), the validity of corona balance has to be checked using the following expression [35], [39], [43], [44]:

$$\frac{N_i(p_i)}{g_i(p_i)} \propto p_i^{-x} \tag{3}$$

where $(N_i(p_i)/g_i(p_i))$ is the relative population density of the energy levels i of argon. $g_i(p_i)$ is the statistic weight of excited level i, and p_i is the effective principal quantum number for excited states of species used, whose expression is [45]

$$p_i = \sqrt{\frac{E_H}{E_\infty - E_i}} \tag{4}$$

where E_H is the Rydberg constant (13.6 eV), E_∞ and E_i are the ionization energy of the species considered and the energy of the excited state i, respectively.

x is the power law and is equal to 0.5 for a density of 10^6 cm^{-3}. Equation (3) is valid for p_i values up to ~20. While electron density goes up, corona is only probable for lower excited state values p_i. Thus, the x value increases up to 3 for an electron density of 10^{10} cm^{-3} in corona balance with p_i values up to 7. At a higher electron density such as 10^{12} cm^{-3}, the boundary lies between $p_i = 3$ and 4.

In our experimental conditions, argon lines studied (750.3, 737.21, and 735.3 nm) give p_i values between 2.44 and 3.72, that is, x values between 0.5 and 0.8, which are in accordance with non-LTE plasma where excited levels are in corona equilibrium under an electron density of 10^9 and 10^{10} cm^{-3} [39], [44].

The electron impact excitation rate coefficients are determined from the oscillator strength values of Ar* [46], [47]. The left-hand side of (1) is plotted versus the energy E_{1i}. The points are fitted with a linear curve whose slope is equal to the inverse of the electron temperature.

In this paper, the electron temperature (T_e) is calculated from the above-mentioned Ar* line intensities. The temporal evolutions of the electron temperature and the absolute value of the DC self-bias voltage are shown in Fig. 5. The calculated values of the electron temperature are around 1 eV. These values are comparable to calculated or measured ones in low-pressure plasmas [36], [48], [49]. The absolute value of the DC self-bias voltage and the electron temperature of the plasma vary in opposite phase. During the particle formation and growth under the RF electrode, we have shown that the electron trapping by particles leads to EEDF modifications. Therefore, the electron temperature values vary. They increase when the particles grow under the RF electrode and decrease when particles leave the cloud at the RF sheath boundary.

The increase of the electron temperature during the electron trapping by the particles shows that the average energy of the electron is enhanced: this increase allows to sustain the discharge.

IV. Conclusion

The presence of particles in an RF reactor disturbed the electrical parameters of the discharge and the optical characteristics of the plasma. The perturbations were due to electron trapping by the particles during their growth. The OES and the laser light scattering measurements were performed at the boundary between the RF sheath and the plasma bulk.

The different forces acting on the particles trapped them firstly in a dense cloud at the RF sheath boundary. The cloud forms a screen for the N_2^+ ions that sputter the RF electrode. The bombardment of the RF electrode led to a germ ejection which allows particle formation. The screen effect under the RF electrode avoided a continuous bombardment of the RF electrode. Therefore, the particle formation was not regular, and the phenomenon of particle multigeneration appears.

The simultaneous measurements of the laser light scattering and the absolute value of the DC self-bias voltage put in evidence the particle presence in the discharge. The electron trapping by the particles during their formation and growth induced a decrease of the absolute value of the DC self-bias voltage, whereas the laser light scattering increased. The absolute value of the DC self-bias voltage increased when particles leave the RF sheath boundary.

The study of the plasma by OES showed the optical perturbations within the plasma when the particles are trapped under the RF electrode. The temporal evolutions of the Ar* line intensities and of the electron temperature follow the particle multigeneration. In this paper, we showed the modifications of the electron energy distribution function due to the trapping of electrons by the particles. We found that the electron number density with an energy in the range 13–15 eV and the electron temperature increase at the same time and these increases allow to sustain the discharge.

Acknowledgment

The authors would like to thank G. Rouzic and J. Bedernjak for their technical assistance, and J.-C. Hargé of the Institut Universitaire de Technologie of Bourges (France) for his help in the SEM analyses.

References

[1] I. Langmuir, C. G. Found, and A. F. Dittmer, "A new type of electric discharge: The streamer discharge," *Science*, vol. 60, no. 1557, pp. 392–394, Oct. 1924.

[2] G. M. Jellum and D. B. Graves, "Particulates in aluminum sputtering discharge," *J. Appl. Phys.*, vol. 67, no. 10, pp. 6490–6496, Feb. 1990.

[3] M. M. Smadi, G. Y. Kong, R. N. Carlile, and S. E. Beck, "Particle contamination on a silicon substrate in a SF6/Ar plasma," *J. Vac. Sci. Technol. B, Microelectron. Nanometer Struct.*, vol. 10, no. 1, pp. 30–36, Jan. 1992.

[4] K. Nishioka, S. Horita, K. Ohdaira, and H. Matsumura, "Antireflection subwavelength structure of silicon surface formed by wet process using catalysis of single nano-sized gold particle," *Solar Energy Mater. Solar Cells*, vol. 92, no. 8, pp. 919–922, Aug. 2008.

[5] K. Nishioka, T. Sueto, and N. Saito, "Formation of antireflection nanostructure for silicon solar cells using catalysis of single nano-sized silver particle," *Appl. Surf. Sci.*, vol. 255, no. 23, pp. 9504–9507, Sep. 2009.

[6] C. Szopa, G. Cernogora, L. Boufendi, J. J. Correia, and P. Coll, "PAMPRE: A dusty plasma experiment for Titan's tholins production and study," *Planetary Space Sci.*, vol. 54, pp. 394–404, Apr. 2006.

[7] C. D. Pintassilgo and J. Loureiro, "Kinetic study of a N_2-CH_4 afterglow plasma for production of N-containing hydrocarbon species of Titan's atmosphere," *Adv. Space. Res.*, vol. 46, pp. 657–671, Sep. 2010.

[8] E. Kovacevic, L. Stefanovic, J. Berndt, and J. Winter, "Infrared fingerpronts and periodic formation of nanoparticles in Ar/C_2H_2 plasmas, *J. Appl. Phys.*, vol. 93, no. 5, pp. 2924–2930, Mar. 2003.

[9] H. Kersten, H. Deutsch, and G. M. W. Kroesen, "Charging of microparticles in plasma-dust interaction, *Int. J. Mass Spectr.*, vol. 233, nos. 1–3, pp. 51–60, Apr. 2004.

[10] J. Beckers and G. M. W. Kroesen, "Surprising temperature dependence of the dust particles growth rate in low pressure Ar/CH_4 RF discharges," *Appl. Phys. Lett.*, vol. 99, no. 18, pp. 1181503-1–1181503-3, Nov. 2011.

[11] M. Hundt, P. Sadler, I. Levchenko, M. Wolter, H. Kersten, and K. Ostrikov, "Real time monitoring of nucleation-growth cycle of carbon nanoparticles in acetylene plasmas," *J. Appl. Phys.*, vol. 109, no. 12, pp. 123305-1–123305-7, Jun. 2011.

[12] A. Richardt and A. M. Durand, *Le Vide, Les Couches Minces, Les Couches Dures*. Paris, France: In Fine, 1994, p. 444.

[13] A. Y. Liu and M. L. Cohen, "Structural properties and electronic structure of low-compressibility materials: β-Si_3N_4 and hypothetical β-C_3N_4," *Phys. Rev. B*, vol. 41, no. 15, pp. 10727–10734, May 1990.

[14] B. Kleinsorge, A. C. Ferrari, J. Robertson, W. I. Milne, S. Waidmann, and S. Hearne, "Bonding regimes of nitrogen in amorphous carbon," *Diamond Relat. Mater.*, vol. 9, nos. 3–6, pp. 643–648, Apr.–May 2000.

[15] J. Emi and S. Iizuka, "Characteristics of carbon-related materials deposited in electron-energy controlled CH_4/H_2 RF discharge plasmas," *Diamond Relat. Mat.*, vol. 20, no. 4, pp. 568–572, Apr. 2011.

[16] I. Géraud-Grenier, V. Massereau-Guilbaud, and A. Plain, "Particulate growth in 13.56 MHz radiofrequency methane plasma: Influence of the flow rate and the incident rf power," *Eur. Phys. J. Appl. Phys.*, vol. 14, pp. 187–192, Jun. 2001.

[17] J. Pereira, I. Géraud-Grenier, V. Massereau-Guilbaud, A. Plain, and V. Fernandez, "Characterization of a-CN_x:H particles and coatings prepared in a CH_4/N_2 r.f. plasma," *Eur. Mater. Res. Soc. Spring Meeting*, vol. 200, nos. 22–23, pp. 6414–6419, Jun. 2006.

[18] J. Pereira, I. Géraud-Grenier, V. Massereau-Guilbaud, and A. Plain, "Characterization of hydrogenated amorphous carbon nitride particles and coatings obtained in a CH_4/N_2 radiofrequency discharge," *Thin Solid Films*, vol. 482, nos. 1–2, pp. 226–231, Jun. 2005.

[19] J. Pereira, V. Massereau-Guilbaud, I. Géraud-Grenier, and A. Plain, "CH and CN radical contribution in the particle formation generated in a radio-frequency CH_4/N_2 plasma," *Plasma Process. Polymer*, vol. 2, no. 8, pp. 633–640, Oct. 2005.

[20] I. Géraud-Grenier, R. Jaffiol, V. Massereau-Guilbaud, and A. Plain, "Photoluminescence of hydrogen amorphous carbon nitrile particles obtained in a 13.56 MHz dusty plasma," *Appl. Phys. Lett.*, vol. 99, no. 9, pp. 091503-1–091503-3, Sep. 2011.

[21] I. Géraud-Grenier, V. Massereau-Guilbaud, and A. Plain, "Analysis of particulates generated in a radiofrequency methane plasma by laser light scattering and optical spectroscopy," *Eur. Phys. J., Appl. Phys.*, vol. 8, pp. 53–59, Jul. 1999.

[22] Y. A. Mankellevich, M. A. Olevanov, and T. V. Rakhimova, "Dust particle coagulation mechanism in low-pressure plasma: Rapid growth and saturation stage modeling," *Plasma Sources Sci. Technol.*, vol. 17, no. 1, p. 015013, Jan. 2008.

[23] C. Zafiu, A. Melzer, and A. Piel, "Ion drag and thermophoretic forces acting on free falling charged particles in an rf-driven complex plasma," *Phys. Plasmas*, vol. 9, no. 11, pp. 4794–4803, Nov. 2002.

[24] J. Pereira, V. Massereau-Guilbaud, I. Géraud-Grenier, and A. Plain, "Nitrogen effect on the dust presence and behavior in a radio frequency CH_4/N_2 discharge," *J. Appl. Phys.*, vol. 103, no. 3, pp. 033301-1–033301-9, Feb. 2008.

[25] V. Massereau-Guilbaud, I. Géraud-Grenier, and A. Plain, "Influence of particulates generated in a CH_4 low pressure radiofrequency discharge on dc self bias voltage," *Eur. Phys. J., Appl. Phys.*, vol. 11, pp. 71–76, Jul. 2000.

[26] M. Mikikian, L. Couëdel, M. Cavarroc, Y. Tessier, and L. Boufendi, "Dusty plasmas: Synthesis, structure and dynamics of a dust cloud in a plasma," *Eur. Phys. J., Appl. Phys.*, vol. 49, no. 1, p. 13106, Jan. 2010.

[27] L. Boufendi, J. Gaudin, S. Huet, G. Viera, and M. Dudemaine, "Detection of particles of less than 5 nm in diameter formed in a argon-silane capacitively coupled radio-frequency discharge," *Appl. Phys. Lett.*, vol. 79, no. 26, pp. 4301–4303, Dec. 2001.

[28] V. Massereau-Guilbaud, I. Géraud-Grenier, and A. Plain, "Determination of the electron temperature by optical emission spectroscopy in a 13.56 MHz dusty methane plasma: Influence of the power," *J. Appl. Phys.*, vol. 106, no. 11, pp. 113305-1–113305-7, Dec. 2009.

[29] V. Massereau-Guilbaud, J. Pereira, I. Géraud-Grenier, and A. Plain, "Influence of the power on the particles generated in a low pressure radio frequency nitrogen-rich methane discharge," *J. Appl. Phys.*, vol. 105, no. 3, pp. 033302-1–033302-8, Feb. 2009.

[30] C. Deschenaux, "Etude de l'origine et de la croissance de particules submicrometriques dans les plasmas radiofréquence réactifs," Ph.D. dissertation, Swiss Univ. Ecole Polytechnique of Lausanne, Switzerland, 2002.

[31] J. Beckers, W. W. Stoffels, and G. M. W. Kroesen, "Temperature dependence of nucleation and growth of nanoparticles in low pressure Ar/CH_4 RF discharges," *J. Phys. D, Appl. Phys*, vol. 42, no. 15, pp. 155206-1–155206-10, Jul. 2009.

[32] M. Mikikian, L. Boufendi, A. Bouchoule, H. M. Thomas, G. E. Morfill, A. P. Nefedov, and V. E. Fortov, "Formation and behaviour of dust particle clouds in a radio-frequency discharge: Results in the laboratory and under microgravity conditions," *New J. Phys.*, vol. 5, pp. 19.1–19.12, Mar. 2003.

[33] M. Mikikian, M. Cavarroc, L. Couëdel, Y. Tessier, and L. Boufendi, "Dust particles in low-pressure plasmas: Formation and induced phenomena," *Pure Appl. Chem.*, vol. 82, pp. 1273–1282, Apr. 2010.

[34] T. Schwarz-Selinger, C. Hopf, C. Sun, and W. Jacob, "Growth and erosion of amorphous carbon (a-C:H) filmsby low-temperature laboratory plasmas containing H and N mixtures," *J. Nucl. Mater.*, vol. 363, pp. 174–178, Jun. 2007.

[35] T. Fujimoto, "Kinetics of Ionization-recombination of a plasma and population density of excited ions. II. ionizing plasma," *J. Phys. Soc. Jpn.*, vol. 47, pp. 273–281, Nov. 1979.

[36] A. Chingsungnoen, J. I. B. Wilson, V. Amornkitbamrung, C. Thomas, and T. Burinprakhon, "Spatially resolved atomic excitation temperatures in CH_44/H_2 and C_3H_8/H_2 RF discharges by optical emission Spectroscopy," *Plasma Sources Sci. Technol.*, vol. 16, no. 3, pp. 434–440, May 2007.

[37] I. Denysenko, M. Y. Yu, K. Ostrikov, N. A. Azarenkov, and L. Stenflo, "A kinetic model for an argon plasma containing dust grains," *Phys. Plasma*, vol. 11, no. 11, pp. 4959–4967, Nov. 2004.

[38] K. Ostrikov, I. Denysenko, M. Y. Yu, and S. Xu, "Electron energy distribution function in low-pressure complex plasmas," *J. Plasma Phys.*, vol. 71, no. 2, pp. 217–224, Apr. 2005.

[39] J. A. M. Van der Mullen, "Excitation equilibria in plasmas; A classification," *Phys. Rep.*, vol. 191, nos. 2–3, pp. 109–220, Jul. 1990.

[40] L. E. Kline, W. D. Partlow, and W. E. Bies, "Electron and chemical kinetics in methane RF glow-discharge deposition plasmas," *J. Appl. Phys.*, vol. 65, no. 1, pp. 70–78, Jan. 1989.

[41] V. A. Godyak, R. B. Piejak, and B. M. Alexandrovich, "Probe diagnostics of non-Maxwellian plasmas," *J. Appl. Phys.*, vol. 73, no. 8, pp. 3657–3663, Apr. 1993.

[42] K. Tachibana, Y. Hayashi, T. Okuno, and T. Tatsuta, "Spectroscopic and probe measurements of structures in a parallel-plates RF discharge with particles," *Plasma Sources Sci. Technol.*, vol. 3, no. 3, pp. 314–319, Aug. 1994.

[43] T. Fujimoto, "Kinetics of ionization-recombination of a plasma and population density of excited ions. I. Equilibrium plasma," *J. Phys. Soc. Jpn.*, vol. 47, no. 1, pp. 265–272, Jul. 1979.

[44] F. J. Gordillo-Vazquez, "Spectroscopic measurements of the electron temperature in low pressure radiofrequency $Ar/H_2/C_2H_2$ and $Ar/H_2/CH_4$ plasmas used for the synthesis of nanocarbon structures," *Plasma Sour. Sci. Technol.*, vol. 15, no. 1, pp. 42–51, Dec. 2006.

[45] G. Herzberg, *Atomic Spectra an Atomic Structure*. New York, USA: Dover, 1944.

[46] C. M. Lee and K. T. Lu, "Spectroscopy and collision theory. II. The Ar absorption spectrum," *Phys. Rev. A*, vol. 8, no. 3, pp. 1241–1257, Sep. 1973.

[47] W. F. Chan, G. Cooper, X. Guo, G. R. Burton, and C. E. Brion, "Erratum: Absolute optical oscillator strengths for electronic excitation of atoms at high resolution. III. The photoabsorption of argon, krypton and xenon," *Phys. Rev. A*, vol. 48, no. 1, pp. 858–860, Jul. 1993.

[48] H. Park and W. Choe, "Parametric study on excitation temperature and electron temperature in low pressure plasmas," *Current Appl. Phys.*, vol. 10, no. 6, pp. 1456–1460, May 2010.

[49] M. Shimozuma, G. Tochitani, and H. Tagashira, "Optical emission diagnostics of H_2+CH_4 50 Hz-13.56 MHz plasmas for chemical vapor deposition," *J. Appl. Phys.*, vol. 70, no. 2, pp. 645–648, Apr. 1991.

Authors' biographies and photographs not available at the time of publication.

Hagop-Jack TAWIDIAN

Formation et comportement de nanoparticules dans un plasma: Instabilités dans les plasmas poudreux.

Résumé:

L'objectif de cette thèse est l'étude de la formation de nanoparticules carbonées dans un plasma basse pression. Les poussières sont créées par pulvérisation d'une couche de polymère déposée sur l'électrode d'une décharge radio-fréquence à couplage capacitif. La présence des poudres perturbe et modifie les propriétés du plasma. La croissance des poudres peut notamment déclencher des instabilités basse fréquence qui évoluent avec la taille et la densité des poudres. Au centre du plasma, une région sans poudre, appelée void, est souvent observée. Cette région se caractérise en particulier par une forte luminosité. Différents diagnostics (mesures électriques, imagerie video rapide, Fluorescence Induite par Laser) sont utilisés afin d'analyser ces différents comportements résultant des interactions entre le plasma et les poussières. L'analyse approfondie des instabilités a permis de mettre en évidence plusieurs régimes et d'extraire leurs principales caractéristiques comme leur durée et l'évolution de leurs fréquences. Ces instabilités se traduisent par la formation de petites "boules" de plasma qui se déplacent et interagissent au sein de celui-ci. Des phénomènes particulièrement surprenants de fusion et de division de ces boules ont été mis en évidence. Concernant le void, nos travaux ont confirmé la forte excitation présente dans cette zone. Dans la dernière partie de la thèse, la dissociation de l'aluminium triisopropoxide (ATI) est étudiée dans un plasma à l'aide de la Spectroscopie Infrarouge à Transformée de Fourier. Ce diagnostic nous a permis de mettre en évidence l'évolution de la densité d'ATI en fonction des paramètres de la décharge. Nous avons également quantifié les différents composants hydrocarbonés formés par polymérisation.

Mots clés: RF, décharge capacitive, plasma, poussières, instabilités, void, mesures électriques, imagerie video rapide, Fluorescence Induite par Laser, ATI, Spectroscopie Infrarouge à Transformée de Fourier.

Formation and behavior of nanoparticles in a plasma: Dusty plasma instabilities.

Abstract:

The objective of this thesis is to study the formation of carbonaceous nanoparticles in a low pressure plasma. Dust particles are created by sputtering a polymer layer deposited on the bottom electrode of a capacitively coupled radio-frequency discharge. The presence of dust particles disturbs and changes the plasma properties. The growth of dust particles can trigger low frequency instabilities that evolve with the dust particle size and density. In the center of the discharge, the void, a dust-free region, is observed. It is characterized by an enhanced luminosity. Different diagnostics (electrical measurements, high speed imaging, Laser Induced Fluorescence) are used in order to understand these different behaviors resulting from plasma-dust particle interactions. Dust particle growth instabilities are investigated showing the existence of different instability regimes. Their main characteristics are extracted such as their duration and their evolution frequency. These instabilities are characterized by the formation of small plasma spheroids moving and interacting in the discharge. Several interesting phenomena are evidenced such as the merging and splitting of these plasma spheroids. Concerning the void, our investigations confirmed the high excitation occurring in this region. In the last part of the thesis, the dissociation of aluminium triisopropoxide (ATI) is studied in a plasma using Fourier Transform InfraRed spectroscopy. Thanks to this diagnostic, the evolution of ATI density has been studied as a function of the discharge parameters. We have also quantified the different hydrocarbon compounds formed by polymerization.

Keywords: RF, capacitive discharge, plasma, dust particles, instabilities, void, electrical measurements, high speed imaging, Laser Induced Fluorescence, ATI, Fourier Transform InfraRed spectroscopy.

GREMI UMR7344 CNRS - Université d'Orléans
14, rue d'Issoudun - BP6744
45067 Orléans Cedex 2